

IRE Transactions



on ANTENNAS and PROPAGATION

Volume AP-7

APRIL, 1959

Number 2

Published Quarterly

TABLE OF CONTENTS

CONTRIBUTIONS

A 215-Mile 2720-MC Radio Link.....	<i>L. H. Doherty and G. Neal</i>	117
Preliminary Results of 400-MC Radar Investigations of Auroral Echoes at College, Alaska.....	<i>R. L. Leadabrand, L. Dolphin, and A. M. Peterson</i>	127
Correlation Function and Power Spectra of Radio Links Affected by Random Dielectric Noise.....	<i>Dimitri S. Bugnolo</i>	137
Aperture-to-Medium Coupling on Line-of-Sight Paths: Fresnel Scattering.....	<i>E. Levin, R. B. Muchmore, and A. D. Wheelon</i>	142
The Inverse Scattering Problem in Geometrical Optics and the Design of Reflectors.....	<i>Joseph B. Keller</i>	146
On Scattering by Large Conducting Bodies.....	<i>Roger F. Harrington</i>	150
Asymmetrical Trough Waveguide Antennas.....	<i>W. Rotman and A. A. Oliner</i>	153
A Contribution to the Theory of Cylindrical Antennas—Radiation Between Parallel Plates.....	<i>L. Lewin</i>	162
Radiation from Ring Sources in the Presence of a Semi-Infinite Cone.....	<i>Leopold B. Felsen</i>	168
The Equiangular Spiral Antenna.....	<i>John D. Dyson</i>	181
The Influence of Gain and Current Attenuation on the Design of the Rhombic Antenna.....	<i>R. P. Decker</i>	188

COMMUNICATIONS

Directivity of a Broadside Array of Isotropic Radiators.....	<i>H. E. King</i>	197
Modification of "Simplified Method for Computing Knife Edge Diffraction in the Shadow Region".....	<i>L. J. Anderson and L. G. Trolese</i>	198
Effect of Surface Reflections on Rain Cancellation of Circularly Polarized Radars.....	<i>R. McFee and T. M. Maher</i>	199
Laboratory Development Notes—Omnidirectional Vertically Polarized Paraboloid Antenna.....	<i>E. O. Willoughby and E. Heider</i>	201
Contributors.....		204

PUBLISHED BY THE

Professional Group on Antennas and Propagation

Administrative Committee

R. L. Mattingly, *Chairman*

Arthur Dorne, *Vice-Chairman*

K. S. Kelleher, *Secretary*

S. Bowhill

J. W. Herbstreit

W. H. Radford

J. W. Findlay

E. C. Jordan

K. M. Siegel

F. T. Haddock, Jr.

S. M. King

O. G. Villard, Jr.

R. K. Moore

Ex-Officio Members

J. I. Bohnert

D. C. Ports

H. G. Booker

Honorary Member

L. C. Van Atta

IRE TRANSACTIONS® PGAP IS A PUBLICATION DEVOTED TO
EXPERIMENTAL AND THEORETICAL PAPERS ON RADIO ANTENNAS,
ON GUIDED OR UNGUIDED PROPAGATION OF RADIO WAVES, AND
ON ALLIED FIELDS OF RADIO PHYSICS SUCH AS RADIO ASTRONOMY

MANUSCRIPTS should be submitted to John B. Smyth, Editor, Smyth Research Associates, 3555 Aero Court, San Diego 11, Calif. Manuscripts should be original typewritten copy, double spaced, plus one carbon copy. References should appear as footnotes and include author's name, title, journal, volume, initial and final page numbers, and date. Each paper must have a summary of not more than 200 words. News items concerning PGAP members and group activities should be sent to the News Editor, Mr. Arthur Dorne, Dorne and Margolin, Inc., 30 Sylvester Street, Westbury, L.I., N.Y.

ILLUSTRATIONS should be submitted as follows: All line drawings (graphs, charts, block diagrams, cutaways, etc.) should be inked uniformly and ready for reproduction. If commercially printed grids are used in graph drawings, author should be sure printer's ink is of a color that will reproduce. All half-tone illustrations (photographs, wash, airbrush, or pencil renderings, etc.) should be clean and ready to reproduce. Photographs should be glossy prints. Call-outs or labels should be marked on a registered tissue overlay, not on the illustration itself. No illustration should be larger than 8 x 10 inches.

Copies can be purchased from
THE INSTITUTE OF RADIO ENGINEERS
1 East 79 St., New York 21, N.Y.

PRICE PER COPY: members of the Professional Group on Antennas and Propagation, \$1.75;
members of the IRE, \$2.60; nonmembers, \$5.25.

ANNUAL SUBSCRIPTION PRICE: PGAP members, included in PGAP fee of \$4.00; IRE members, \$8.50; Colleges and public libraries, \$10.00; nonmembers, \$17.00.

IRE TRANSACTIONS ON ANTENNAS AND PROPAGATION
Copyright © 1959, by The Institute of Radio Engineers, Inc.

Printed in U.S.A.

Entered as second-class matter, at the post office at Menasha, Wisconsin, under the act of August 24, 1912. Acceptance for mailing at a special rate of postage is provided for in the act of February 28, 1925, embodied in Paragraph 4, Section 412, P. L. & R., authorized October 26, 1927.

contributions

A 215-Mile 2720-MC Radio Link*

L. H. DOHERTY† AND G. NEAL†

Summary—The results from the operation of a 215-mile, 2720-mc radio link are discussed. The link was operated for a period of twenty months. The yearly median signal level was 79 db below free space with a seasonal variation between 12 and 14 db in the hourly medians. If attention is confined to a single season the hourly medians have a log-normal distribution. No diurnal variation was observed. Probability distributions of signal amplitude based on 30-second samples were most commonly Rayleigh although some significant departures from this law did occur. A study of the time variation of the 30-second median shows the standard deviation of these medians five minutes apart to be about 1 db, and thirty minutes apart to be 2.6 db. The same type of analysis is also performed on the hourly medians. A diurnal variation is observed in the fading, with the midafternoon rate being almost twice that recorded during the early morning. Pulse distortion and meteorological correlations are discussed qualitatively.

I. INTRODUCTION

IN April, 1955, the National Research Council of Canada established a radio link between Ottawa and Toronto. The link was operated on a frequency of 2720 mc from April, 1955, to December, 1956. The purpose of the link was to determine some of the parameters involved in the transmission of radio waves at a

microwave frequency to distances far beyond the horizon. No attempt was made to transmit information over the link.

In this paper are reported data on hourly median-signal level and its variation with time of day and with the season, and on the probability distribution of fading amplitudes. The time variation of median levels of two different time bases is shown. The fading-rate distribution and its diurnal variation are also reported. Finally, a brief discussion of pulse shape and meteorological correlations are included.

A considerable experimental effort was made with an antenna array of variable aperture. This feature of the experiment will form the subject of a later paper.

II. THE TRANSMISSION PATH

The transmitter was located at Ottawa (45° 26' 9" N, 75° 36' 42" W) and the receivers at Toronto (43° 42' 44" N, 79° 14' 04" W) 215 miles away. The intervening land is rolling, heavily wooded, and well interspersed with lakes. The last 15 miles of the path are over water. The path lies over Lake Ontario and parallel to the shoreline for this distance.

The path profile is shown in Fig. 1. The transmitter was located on an 85-foot tower and the path is clear of obstructions. The tangent to the earth's surface is about

* Manuscript received by the PGAP, June 13, 1958; revised manuscript received, January 19, 1959.

† Radio and Elec. Eng. Div., National Res. Council, Ottawa, Can.

3 minutes of arc below the horizontal. During the first five months (April to September, 1955) of the experiment, the receiving antennas were mounted about 30 feet above the immediate ground level. A grove of trees about 500 feet in front of the antenna presented an obstruction such that the unobstructed line was about 1° above the horizontal. Early in September, 1955, the receiving equipment was moved about 300 feet south towards Lake Ontario. From this vantage point an unobstructed line of sight out over Lake Ontario was obtained. The antennas were mounted about 6 feet above the ground and about 50 feet back from the cliff overlooking the lake. From this point the land falls off at a steep angle to lake level, 350 feet below. The tangent to the earth's surface from this second receiving location is below the horizontal, and the tangent lines from the transmitter and receiver intersect at 4600 feet above the general ground level at midpoint.

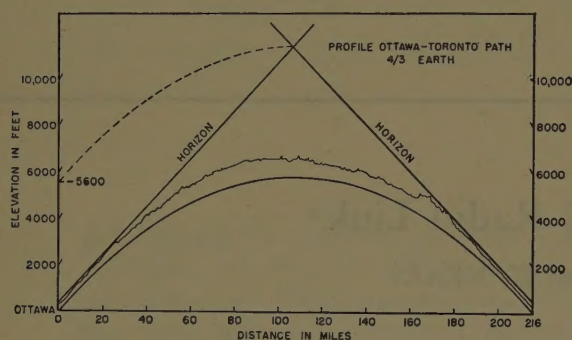


Fig. 1—The Ottawa-Toronto path profile.

III. EQUIPMENT

The transmitter was located in Ottawa on an 85-foot tower on the grounds of the Radio and Electrical Engineering Building of NRC (Fig. 2). The transmitter used a 4J35 magnetron with a nominal output of 500-kw peak pulse power. The pulse was $1 \mu\text{sec}$ long and was emitted at a repetition frequency of 600 cps. The only modifications made to the original and conventional radar transmitter were the addition of an automatic control to turn the transmitter off for two minutes every half-hour for signal identification, and replacement of the original free-running multivibrator with a tuning fork to supply an accurate pulse repetition frequency.

The transmitting antenna was a 6-foot diameter paraboloid with a double dipole waveguide feed. The antenna beamwidth was 4° . It was oriented to transmit horizontally-polarized waves.

The receiving sites were located at the Scarborough Field Station of the National Research Council on the eastern edge of Toronto. At the site used during most of the experiment, the antennas were mounted with their centers about 6 feet above the immediate ground level (Fig. 3). The receiving equipment was located in a small hut about 50 feet from the center of the antenna array. Two different types of receiver were used during

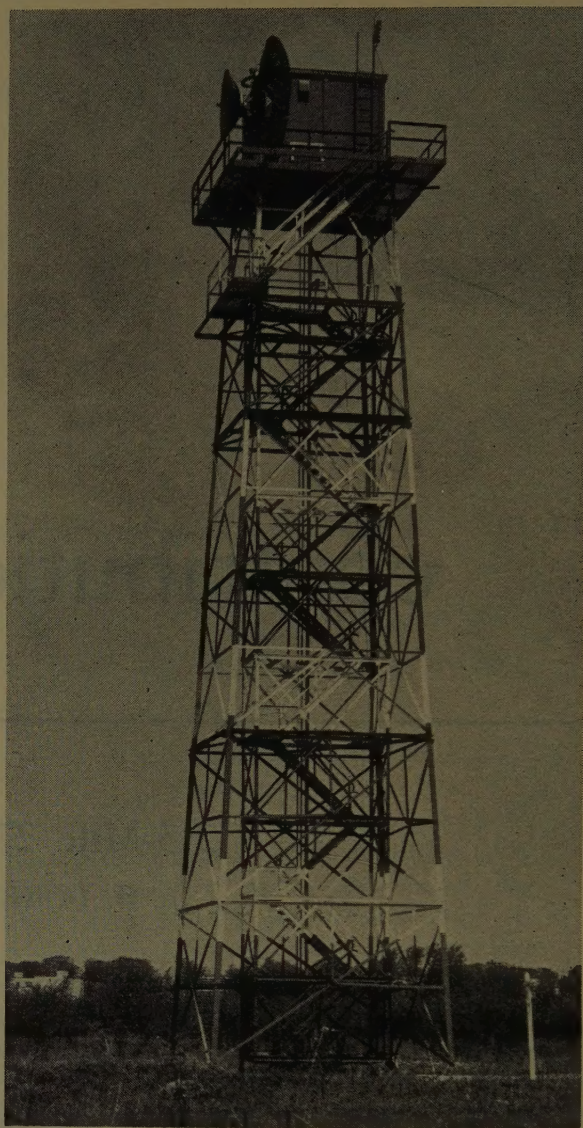


Fig. 2—The 85-foot transmitter tower. The 6-foot paraboloid on the left is directed towards Toronto.

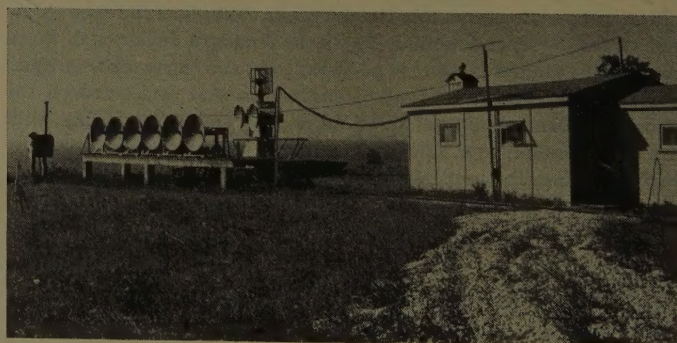


Fig. 3—The receiving site. Two adjacent antennas in the array of six were paralleled to form the receiving antenna.

the experiment, although both had a crystal mixer, 30-mc IF amplifier, diode detector, pulse stretcher, narrow-band 600-cycle amplifier (the pulse repetition frequency) dc amplifier, and recording meter driver. Only one receiver of the first type was available. Two receivers of the second design were used, and these differed

from the first in the addition of a low-noise 30-mc pre-amplifier situated at the antennas, and various minor improvements.

During the period from April, 1956, to September, 1956, the antennas and receiving equipment were mounted on the roof of the main building at the Scarborough Field Station. This was about 30 feet above immediate ground level. As mentioned above, there was a reduction in signal level due to trees located about 500 feet in front of the antennas. A number of experiments were performed to determine the difference in median signal level between these two locations. Results varied between 3 and 5 db, and consequently, a correction of 4 db has been applied to values of median-signal level obtained at this first site. The only results of measurements made at this first site and reported here are those of hourly median signal level.

TABLE I

Site	Receiver Type I	Receiver Type II
I	April 1, 1955 September 11, 1955	—
II	September 11, 1955 November 30, 1955	November 30, 1955 November 30, 1956

Table I shows the periods covered by the various combinations of two sites and two receiver types. It may be seen that a full year's operation was obtained at the second site with the second type of receiver.

The receiving antenna array consisted of six 4-foot paraboloids with double dipole waveguide feeds. They were placed in a line horizontally at right angles to the propagation path (see Fig. 2). Any number of these antennas could be connected together through a specially designed paralleling unit. The result was that an antenna was obtained whose aperture could be varied in one dimension in 4-foot steps between 4 and 24 feet. For the routine measurements of median-signal level, two antennas in parallel were used, providing an antenna of dimensions 4 feet by 8 feet.

The routine measurements were made with an output time constant of 4 seconds on an Esterline-Angus recorder operating at a speed of 3 inches per hour. A two-channel Brush recorder was operated from time-to-time throughout the experiment; and between about the middle of July, 1956, and November 30, it operated automatically, 40 seconds every half-hour. A totalizer, which determined the percentage of time each of 15 preset levels was exceeded during a 10-minute interval, was also operated automatically every half-hour during most of this same period.

Transmitter power was measured daily during the initial stages of the experiment. At no time was the power found to vary as much as 1 db, and the power was measured only once or twice a week. Receiver calibrations were performed at least once a day, and for the greater part of the experiment were taken twice a day.

IV. HOURLY MEDIAN OBSERVATIONS

Hourly median-signal levels were taken from the Esterline-Angus charts for every hour of observation. These hourly medians were estimated by eye from the chart record. As mentioned earlier, these recordings were made with a 4-second time constant to reduce the amplitude of fading. The estimates of the median were repeatable at different times and with different observers to better than 0.5 db under most circumstances. The exceptions were at times of signals near noise where the decibel scale is compressed, and at times of rapid signal level change. During times of rapid change in signal level, the concept of the hourly median is of little value. On rare occasions, short-term median-signal levels were observed to change by as much as 15 db within the period of an hour.

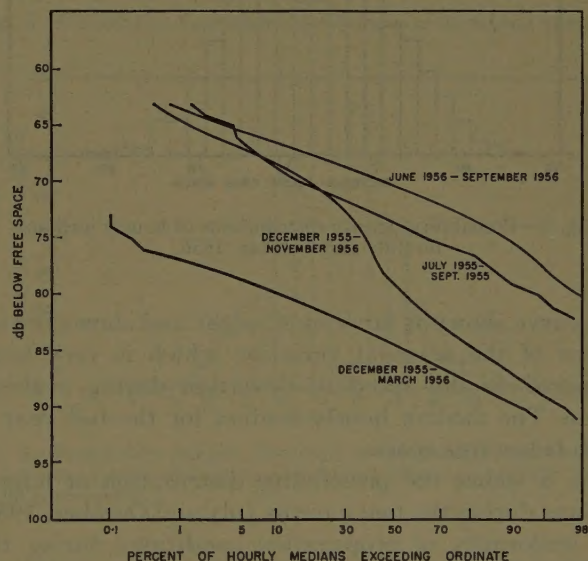


Fig. 4—Cumulative distributions of hourly medians.

The cumulative distribution of hourly medians is shown in Fig. 4. The curves are plotted on normal probability paper with "decibels below free space" as the abscissas. Consequently a straight line is indicative of a log normal distribution. The three curves representing Summer 1955, Summer 1956, and Winter 1955-56, are approximately straight lines of the same slope. The standard deviation for each of these curves is about 3.5 db. The seasonal variation as measured from these curves at the 50 per cent values is 11 db between the summer of 1955 and the following Winter, and 14 db between the same Winter and the following Summer. As mentioned previously, the data for the Summers of 1955 and 1956 were taken with different receivers at different sites. Greater assurance may be placed on the value of 14 db for the seasonal variation although it is believed that the difference between these values is a real one. The medians of the hourly medians are 71 and 74 db below free space for the Summer months and 84 db below free space for the Winter months. The single full-

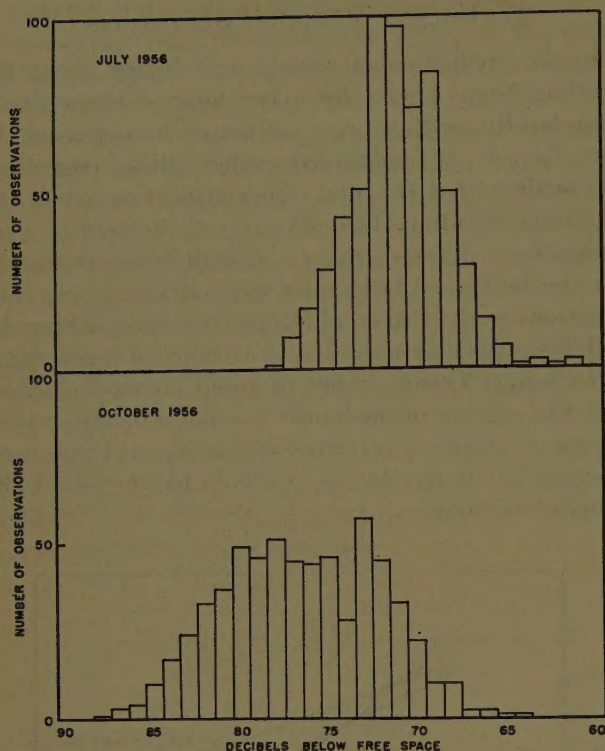


Fig. 5—Probability density distributions of hourly medians for July and October, 1956.

year curve shown is far from straight and shows the influence of the seasonal variation which is very large compared to the standard deviation during a single season. The median hourly median for the full year is 79 db below free space.

Fig. 5 shows the probability distribution of hourly medians during the two months July and October, 1956. The uniformity of propagation conditions during the summer months is evident in the narrow probability curve. The transition month, October, shows evidence of the intermingling of winter and summer conditions in the suggestion of a double peak in the probability curve.

The diurnal variation of hourly median signal level is shown in Fig. 6 and Fig. 7. It is evident from these figures that there is no significant diurnal variation of hourly medians within the percentile range 10–90 per cent. A slight dip in the June to September data during the middle hours of the day may be observed. It is not more than 1 db and probably is not significant. Since the diurnal variation is an outstanding characteristic of superrefraction, it is reasonably safe to draw the conclusion from these curves that superrefraction plays no significant part in the propagation over the path discussed here. It is to be expected, of course, that if superrefraction ever is present on this link, it will make its presence felt at high percentile values. Fig. 6 and Fig. 7 go only to the 10 per cent level, but the 5 and 3 per cent levels show—less positively because of a greater scatter—the same lack of diurnal variation. In spite of the failure to show up in the statistics, it did appear that occasionally a superrefraction signal was received. Seven

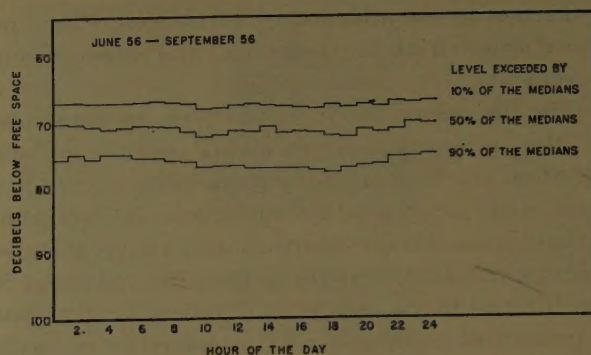


Fig. 6—Diurnal variation of hourly medians during Summer 1956.

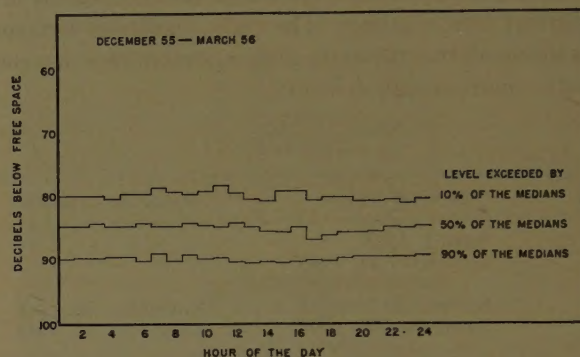


Fig. 7—Diurnal variation of hourly medians during Winter 1955–56.

times during the Summer of 1956 the receiver was saturated continuously for periods ranging from 15 minutes to 1.5 hours. This represented a signal level greater than 58 db below free space. These few periods occurred without exception during the hours of darkness, or within two hours after sunrise.

V. PROBABILITY DISTRIBUTIONS OF THE SIGNAL AMPLITUDE

Analysis of some short intervals (30 to 40 seconds), and of some medium intervals (10 minutes) was performed to determine the probability distribution of the amplitude of the received signals. The 30-second distributions were obtained from a small number of Brush recorder tapes. Many more are available but have not been analyzed. The 10-minute distributions were obtained from the totalizer mentioned earlier. In this case about one-half of the available records were analyzed.

A) 30-Second Distributions

The length of the records discussed here varied slightly;—the shortest is 27 seconds long, the longest 39 seconds. Only ten days, distributed over nine months, are involved in this analysis, but it includes 106 separate 30-second intervals. The Brush recorder tapes were not originally taken for the purpose of obtaining probability distributions, and consequently the amplitude range reliably covered is limited, in some cases. It should be recognized that some of the data used here did not extend beyond the 20 and 80 percentiles.

The cumulative distributions were plotted on Rayleigh probability paper. Approximately 70 per cent of the graphs were such that a straight line could be fitted to them with confidence. The remaining graphs showed either evidence of two straight lines or an irregular scatter of points. Examples are shown in Fig. 8.

If attention is confined to those graphs to which a straight line may easily be fitted, the majority have a slope near that of the Rayleigh distribution;—that is, the difference between the 10 and 90 percentiles differs by no more than 1.0 db from 13.4 db. On two of the ten days, however, the slope departed appreciably from the Rayleigh slope. The above-mentioned fading range fell to between 10 and 11 db in one case and between 9 and 10 db in the other. A few isolated curves yielded fading ranges greater than 13.4 db. These apparently were the result of rapid change in the average signal level. The records taken a minute or two before, and a minute or two after, were in each case Rayleigh-distributed, but different in median level by two or three decibels.

Only a few cases have been observed when the cumulative distribution curve could best be fitted with two straight lines, but in each case the order of the two slopes is such that the composite curve is concave upwards.

B) 10-Minute Distributions

A time totalizer was operated on one of the receivers from July, 1956, through the middle of October, 1956. It was not operated on a continuous schedule but was turned on automatically every 30 minutes for a period of 10 minutes. At the end of the 10-minute sampling period each of the 15 channels was read automatically and the readings recorded in turn on an Esterline-Angus recorder. Only the records made during the month of July and the first 18 days of August have been analyzed.

The totalizer is an analog device and hence of limited accuracy. It cannot be used safely for indication of levels outside the 10 and 90 percentiles. It was used consequently for determining the median-signal level and the fading range (the number of decibels between the 10 and 90 percentiles).

The cumulative distribution curves plotted on Rayleigh paper appear on the whole to be straight lines within the 10 to 90 percentiles. The percentages of graphs showing either an irregular scatter of points or evidence of two straight lines is considerably less than for the 30-second distributions.

Fig. 9 shows the observed frequency distribution of fading ranges. The extremes observed are 7.5 db and 18.5 db, while the median value of these 530 observations is 13.4 db. This figure of 13.4 is identical with the fading range to be expected with a Rayleigh distributed signal. It is believed that a few of the very large fading ranges may be due to faulty operation of the totalizer. A more important number is probably due to aircraft reflections. Slow components of fading; *i.e.*, fading components of period of the order of 10 minutes, of sufficient

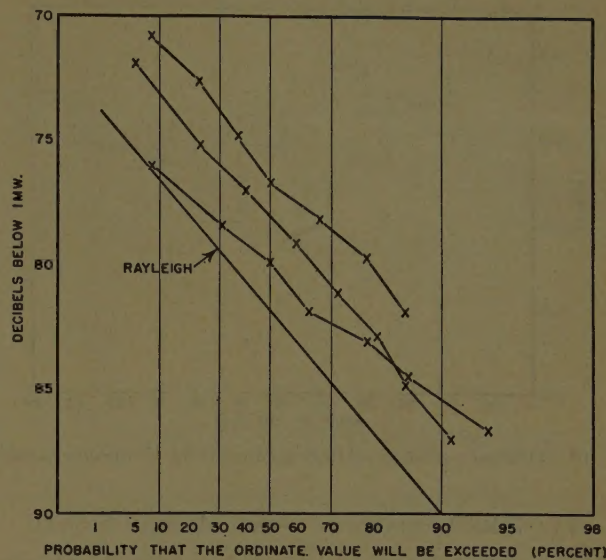


Fig. 8—Cumulative amplitude distributions of 30-second samples.

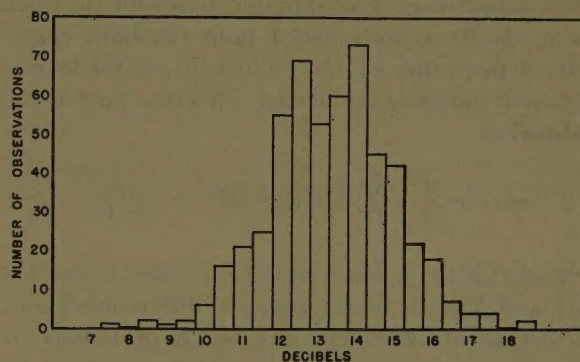


Fig. 9—Probability density distributions of fading range from 10-minute samples (fading range = decibel difference between 10 and 90 percentiles).

amplitude, would also result in fading ranges in excess of 13.4 db. Section VI-A gives evidence of such components with amplitudes of the order of 1 to 2 db.

The occurrence of fading ranges less than 13.4 db is normally explained in terms of the addition to a Rayleigh distributed signal of a component of steady signal. Fig. 10 has some bearing on this point. In this figure the 10-minute median fading range has been plotted as a function of the time of day. Each straight line segment in this figure is the median value of the fading ranges observed on all days for which analyzed records are available during the two-hour period indicated. Some indication of diurnal variation of fading range is present. Statistically, a lower fading range was observed during the afternoon and early evening hours than during the night and early morning. If the data for the period 0000–1000 hours are combined the median fading range is 13.8 db. For the period 1200–2000 hours it is 12.7 db. The number of fading range observations included in these evaluations of the median are 243 and 163, respectively. If this is a significant variation then the steady signal is more commonly present during the afternoon hours.

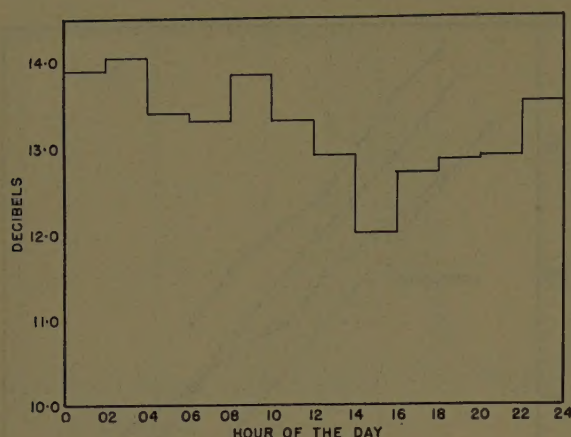


Fig. 10—Diurnal variation of fading range from 10-minute samples.

VI. TIME VARIATION OF THE MEDIAN SIGNAL

Some analysis has been undertaken with the object of determining the nature of the variation with time of the median signal level. Two different bases for the medians were used; 30 seconds and 1 hour. In both cases the standard deviation of the change in signal level as a function of time was calculated. This standard deviation is defined as

$$\sigma(\tau) = \left\{ \frac{1}{N} \sum [M(t) - M(t + \tau)]^2 \right\}^{1/2}$$

where $M(t)$ is the median signal expressed in decibels at time t , and N is the total number of differences summed. This method of correlation was used in preference to the more conventional product correlation, in part because the nature of the 30-second median data did not lend itself readily to the latter calculation, but primarily because it was desired to have a direct measure in decibels of signals spaced in time.

A) The 30-Second Median

Median signal levels were determined from Brush recorder tapes 30 and 40 seconds long. These recordings were taken for another purpose, and consisted of sixteen series of recordings taken on sixteen days over a period of nine months. Each series consisted of a number of 30-second recordings. The number of such recordings varied from a low of four to a high of twenty. The individual recordings were separated by intervals ranging from one minute to ten minutes, and no series of recordings occupied more than 83 minutes, and most were completed within 30 minutes.

The difference, in decibels, in median-signal level, was obtained between each recording and every other recording of the same series. Each such difference had associated with it a time difference which was the interval between the two readings. The standard deviation of these differences was then obtained as described above. The resulting standard deviations are then plotted vs time in Fig. 11. Starting with an interval of ten minutes, the data for two minutes were combined so

that each point had very approximately the same weight.

With only sixteen series of tapes included, the data, of course, are not necessarily representative. Only seven of the series were longer than 15 minutes, and only five were longer than 40 minutes.

A curve has been drawn, by eye, through the points. It may be noted that 5 minutes must elapse before the 30-second median changes by one decibel. Even 30 minutes later the median has changed by only 2.7 db. This, it must be remembered, is the standard deviation, and greater changes do occur on occasion.

The data here are all derived from the same antenna and the same receiver. Consequently, as the time difference forming the abscissas of Fig. 11 tends to zero, σ must tend to zero, since it is derived from the difference between two medians which in the limit become the same median. However, it is not unreasonable to assume that for sufficiently large time differences the same curve would have been obtained if one of the medians had been derived from a second spaced antenna and receiver—the same time difference being maintained. For such a curve, however, the extension back to zero time interval would result in a nonzero intercept; *i.e.*, the medians recorded on spaced antennas are not necessarily equal. It is therefore suggested that the apparently natural extrapolation of the curve of Fig. 11 back to zero time yields a standard deviation, for the ensemble of 30-second medians, of 0.4 db.

B) The Hourly Median

The same general procedure was followed in determining a measure of the time variation of the hourly median as was used for the 30-second median. A great deal of data were available for this calculation and consequently it could be done in more detail. The summation was originally taken over periods of one month, but in some cases two months data were combined. A total of seven months of data is shown in Fig. 12. For all months there is a considerable stability in the signal level over short periods, and a remarkable similarity between the months. The difference between hourly-median signals one hour apart has a standard deviation of between 1.5 and 1.8 db for those months shown. A marked difference between the months shows up with greater time separations. The July–August curve reaches a plateau at about 12 hours. The February curve has very much the same characteristic, although the maximum standard deviation is somewhat higher. In each case, of course, the plateau indicates no correlation between hourly medians greater than 12 hours apart, and the value of standard deviation agrees, as it must, with the standard deviation calculated for all hourly medians for the month. The December–January curve shows the presence of correlation in the hourly medians to time separations of the order of 48 hours. The plateau reached here is significantly higher. The data for March (not shown) are very similar to those for December–January.

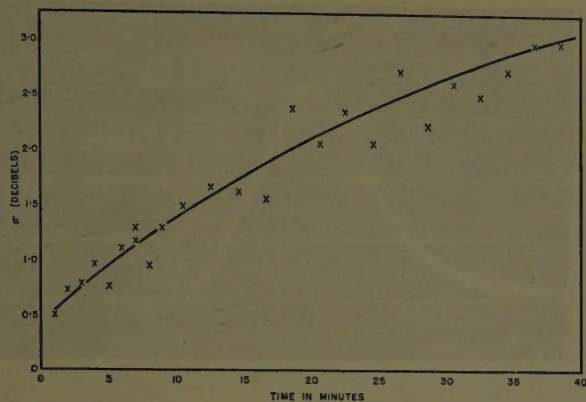


Fig. 11—Standard deviation of 30-second medians as a function of time separation.

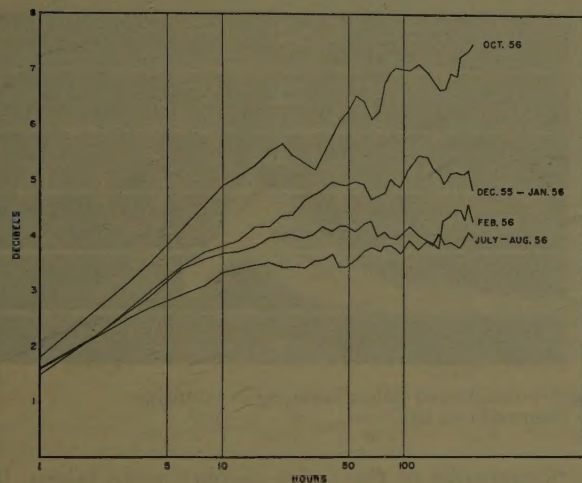


Fig. 12—Standard deviation of hourly medians as a function of time separation.

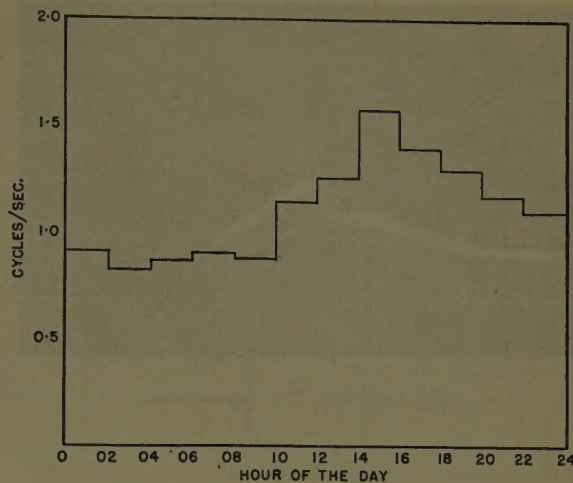


Fig. 13—Diurnal variation of fading rate (one-half the average number of crossings of the median during a 40-second period).

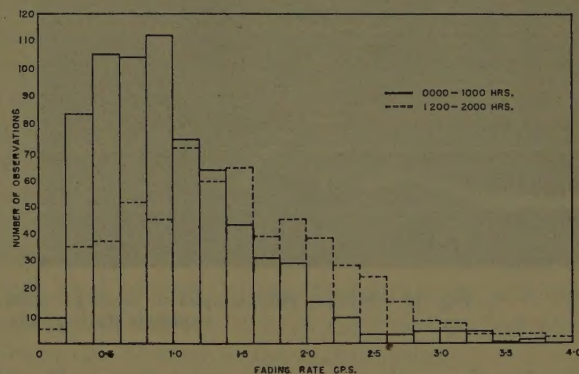


Fig. 14—Probability density distribution of fading rate.

The October curve shows no sign of leveling-off at a time separation of 240 hours. October is a transition month when the signal fluctuates, in a period of a few days, between Summer and Winter values. There is no evidence of a regular diurnal variation in these curves.

VII. FADING RATE OF THE RECEIVED SIGNAL

During the period July through November, 1956, a high-speed Brush recorder was in more or less continuously programmed operation. It was turned on automatically for 40 seconds every 30 minutes. This sampling period was arranged to fall within the 10-minute operation of the totalizer. The recorder was operated at a chart speed of 25 millimeters per second. It was a two-channel recorder and the outputs of the two receivers were recorded simultaneously. For fading rate investigations the record of a particular receiver was used whenever it was available. However, if for any reason the record of this receiver was unavailable or unreliable, the other receiver record was read without making any distinction in the data presented here. A total of 1699 of these records has been analyzed for fading rate. This amounts to 23 per cent of the total half-hour periods during these five months. The data analyzed do, how-

ever, vary in quantity from the separate months, ranging from a high of 36 per cent of the total half-hour periods during August to only 12 per cent during November.

The fading rate as used in this analysis is defined as one-half the average number of crossings of the median-signal level during one second. The 40-second interval was chosen as a result of some experimentation with the sampling period. It is a generally satisfactory period for the fading rate observed, but is short for the lower 10 per cent of the observations.

The fading rates recorded during these five months show a strong diurnal variation, with the maximum fading rate being recorded at 1500 hours, and a broad minimum between midnight and 0900 hours. The median fading rate observed over two-hour periods covering the five months of record is shown in Fig. 13. The fading rate at 1500 hours is a factor of 1.9 greater than that obtained at 0300 hours. The number of observations involved in the determination of each of these points varied from a high of 192 to a low of 87.

Results of the five 2-hour periods comprising the minimum were combined and the density distribution of fading rate plotted in Fig. 14. Similarly, the four 2-hour periods, which included the highest fading rates, were

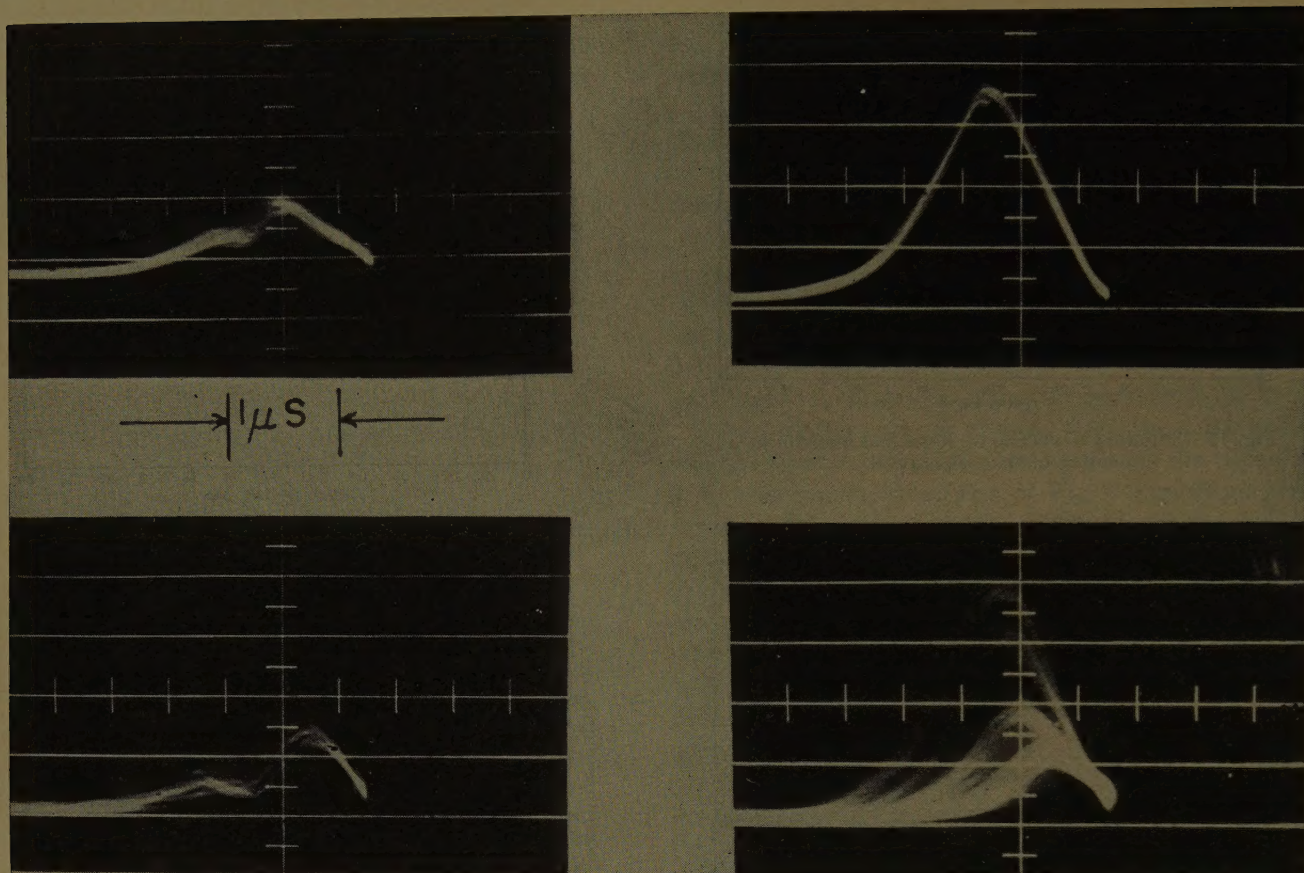


Fig. 15—Sample photographs of received pulse. (Upper right—undistorted pulse; lower right—multiple exposure during fade). Time runs from right to left.

combined and are shown on the same figure. For the period 0000–1000 hours, Fig. 14 shows the maximum probability of the fading rate lying in the range 0.4 to 1.0 cps. Almost 50 per cent of the observations were in this range. The density distribution curve for the period 1200–2000 hours has a maximum in the range 1.0 to 1.6 cps, but is much less sharply peaked.

It is appropriate to mention again that these fading-rate data are derived from observations made with a horizontal array of two 4-foot paraboloids. In another paper, in course of preparation, it will be shown that the fading rate depends upon antenna size. The fading rate decreases with increasing antenna size, although presumably only when the size exceeds some critical value. This critical value is itself a variable, but it is believed that for the particular antenna configuration used here this critical size is exceeded for the majority of the observations in the period 1200–2000 hours. The fading rates for a smaller antenna would be increased by a factor of the order of 25 per cent. If this argument is correct the diurnal variation would be even more pronounced for smaller antennas.

VIII. PULSE DISTORTION

The transmitter output consisted of 1- μ sec pulses at a repetition frequency of 600 pulses per second. The received pulses were observed routinely on an oscilloscope operated at a sweep speed of 2 cm per microsecond. A

few photographs of the pulse display were taken, both with a single-shot camera and with a movie camera operated at 8 frames per second.

Fig. 15 shows some sample photographs. (Time increases from right to left.) The sweep was triggered by the pulse and then the pulse was displayed after a $\frac{1}{4}$ - μ sec delay. The upper right-hand photograph is assumed to be undistorted by the transmission medium. It has the shape expected after transmission of a 1- μ sec pulse through a 2 mc-wide receiver. The two photographs on the left are typical of the distorted pulse. All photographs of distorted pulses show what would appear to be a low amplitude second pulse on the trailing edge of the main pulse. From visual observations of the oscilloscope it was possible to see on occasion the appearance of this second pulse on the leading edge of the pulse. It then traveled quickly forward across the pulse and dwelt momentarily in the position shown in the photographs.

The presence of a distorted pulse was relatively rare—less than 5 per cent of the photographs showed any pulse distortion—but when distortion did occur it was always during the low-signal portion of the fading period. The photograph in the lower right of Fig. 15 shows a multiple exposure on the same frame during one fade of the signal. In this case the undistorted shape of the pulse is maintained during the fade. This is the more common situation.

IX. METEOROLOGICAL CONSIDERATIONS

No systematic attempt at meteorological correlations was attempted. Aside from the obvious seasonal correlation there was the equally obvious, and often repeated correlation between the flow of hot warm air from the south and high-signal levels, and the flow of cold dry air from the north and low-signal levels. Attempts to correlate the signal characteristics with frontal passages as deduced from surface temperature and humidity, and from upper air winds—these were the only available Meteorological Service data—were unsuccessful except in the very obvious cases mentioned above. Qualitatively, the passage of fronts across the propagation path results in a disturbed signal. Wide excursions (5 to 15 db) of the short-term median level occur within the space of five or ten minutes. This is in marked contrast to the usual stability of the signal as indicated in Section VI-A, where 1 to 2 db is the indicated variation over a 10-minute period. Associated with the signal-level changes are changes in fading rate—usually there is a noticeable increase in the rate, but not invariably.

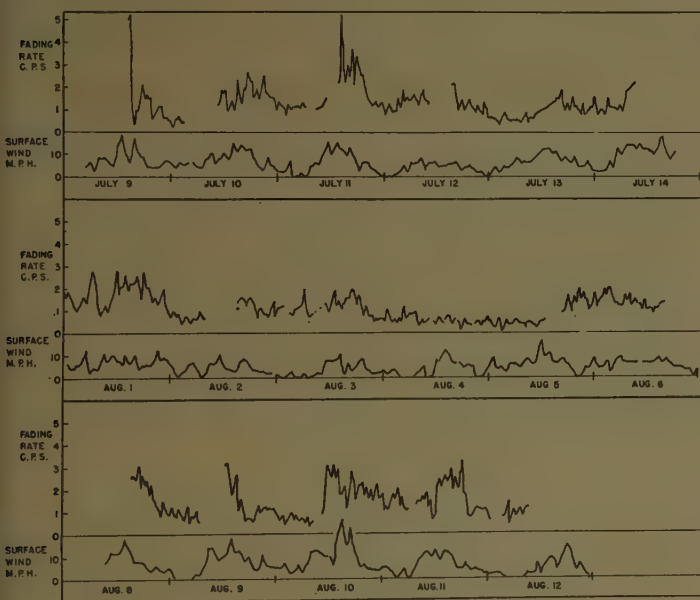


Fig. 16—Fading rate and surface wind near midpoint of path plotted on the same scale.

The diurnal variation of fading rate has been described in Section VII, and another aspect of this variation is shown in Fig. 16. In this figure the observed fading rate is plotted vs time, and immediately below and to the same time scale is shown the surface wind as measured at Stirling, Ontario, which is situated very near the midpoint of the path. It may be noted that the first and third periods in Fig. 16 show the commonly observed diurnal variation of surface wind. The fading-rate records for these periods show quite clearly the same form of diurnal variation. No correlation calculations have been performed on these data, but it is quite clear that a correlation coefficient, close to one,

would be obtained, when a time advance of about two hours is applied to the fading-rate record. The middle period shows very little indication of any regular diurnal variation in wind, and there is a corresponding lack in the fading-rate record. Upper air wind measurements are taken three times a day by the Canadian Meteorological Service at Trenton, Ontario, about 40 miles from the midpoint of the path. The data are insufficient for a proper analysis, but there is no obvious correlation between the wind speed at 5000 feet (the approximate height of the intersection of the earth tangents from transmitter and receiver) and the fading rate.

X. DISCUSSION

The signal level recorded on this 2720-mc, 215-mile transmission path does not depart appreciably from those reported by others for the same frequency and distance range. Bullington,¹ and Gerks,² for example, give values between 70 db and 80 db below free space for microwave frequencies at this distance. This is to be compared with the yearly median of 79 db below free space recorded here. The seasonal variation of 14 db observed is in general agreement with those reported elsewhere, although Chisholm, *et al.*³ have reported variations greater than 20 db.

There is little or no evidence of a diurnal variation of signal level on the Ottawa-Toronto path, and there is no reason to believe that superrefraction had any significant role to play in the transmission.

The results of signal amplitude distributions show what appears to be significant departures from the Rayleigh distribution expected from scattering theory. An appreciable fraction of the 30-second distributions has fading ranges less than the 13.4 db of the Rayleigh distribution. The sample is small and, although the ten days on which these records were taken were scattered over a period of nine months, the meteorological conditions may not be representative. On the other hand, the 10-minute distributions show fading ranges both greater and less than Rayleigh. This has also been reported by Bullington, Inkster, and Durkee.⁴ It should of course be possible to explain the 10-minute distributions in terms of the 30-second distributions, and their time variation. The existence of fading ranges less than 13.4 db is common to both sampling periods and is, in this sense, understandable. There are no 30-second distributions with fading ranges greater than 13.4 db, and hence their presence among the 10-minute distributions must be explained in terms of the time variation of short-

¹ K. Bullington, "Characteristics of beyond-the-horizon radio transmission," *Proc. IRE*, vol. 43, pp. 1175-1180; October, 1955.

² I. H. Gerks, "Factors affecting spacing of radio terminals in a UHF link," *Proc. IRE*, vol. 43, pp. 1290-1297; October, 1955.

³ J. H. Chisholm, P. A. Portmann, J. T. deBettencourt, and J. F. Roche, "Investigations of angular scattering and multipath properties of tropospheric propagation of short radio waves beyond the horizon," *Proc. IRE*, vol. 43, pp. 1317-1335; October, 1955.

⁴ K. Bullington, W. J. Inkster, and A. L. Durkee, "Results of propagation tests at 505 mc and 4090 mc on beyond the horizon paths," *Proc. IRE*, vol. 43, pp. 1306-1316; October, 1955.

term median signal. A change in 30-second median signal of 1 or 2 db within a 10-minute period has been reported in Section VI-A. This is sufficient to explain small increases in the 10-minute fading range. Here again the small sample of 30-second medians is restrictive. It is possible that considerably greater variations in this median occur on occasion. Aircraft reflections also provide another source of change of signal level which would lead to fading ranges greater than 13.4 db. It was not possible to eliminate from the automatic totalizer operation the cases where these reflections were present. They were eliminated from the Brush records, which yielded the 30-second medians.

The observation of fading ranges less than 13.4 db on both the 30-second and 10-minute records suggests the presence of a steady component of signal. The existence of a diurnal variation in fading range is indicated by the data of Section V-B. The nature of this diurnal variation is not such as to permit identification of this steady signal with a superrefracted signal. Further, the 30-second observations yielding fading ranges of the order of 9 to 11 db were daytime observations. It would appear that some mechanism such as layer reflection is necessary to explain these data.

The time variation of the 30-second median may be used to determine to what extent the propagation process is stationary in a statistical sense. The sample is small and the deviations forming the sample are large, but the data do provide some measure of the time variability of the median signal. If the standard deviation of the ensemble of 30-second medians is 0.4 db, as suggested, then an appreciable percentage of the power spectrum of fading is contained in the frequencies of the order of 1/30 cps and slower.

The study of the time variation of the hourly median has shown an important difference in the time correla-

tion of these medians between different months of the year. Correlation between hourly medians exists for only about 12 hours during July and August, but for about 48 hours during December and January. This latter period would be of the order of the average duration of an air mass over the propagation path. Some correlation between hourly medians exists as long as the transmission is through the same air mass. The absence of this effect during July and August must be because there is no significant difference, propagationwise, between air masses during July and August. A different factor is evident in the October data where no plateau is reached with time separations as great as ten days. These curves point up the problem of correlating signals with meteorological measurements. There will be rare instances which are masked by these statistics, but, in general, there is little hope during July and August of improving on the statement that tomorrow's signal will be the same as today's and last week's. Attempts at meteorological correlations should presumably start with some transition month, such as October. In July and August changes in signal level are completed within 12 hours and the meteorological changes must be relatively minor and small-scale compared to October where the time element is extended to at least ten days.

The fading rate has been shown to have a diurnal variation and to be correlated with surface wind at mid-point of the path. On any scattering theory basis there should not be any direct relationship between surface wind and fading rate. The surface wind is, in part, a measure of the hydrostatic instability of the atmosphere, and thus a measure of higher turbulent velocities aloft. The 2-hour lag of the fading rate maximum behind the wind maximum presumably is due to the delay in transferring the turbulent energy from ground level to 5000 feet.

Preliminary Results of 400-MC Radar Investigations of Auroral Echoes at College, Alaska*

R. L. LEADABRAND†, L. DOLPHIN†, AND A. M. PETERSON†

Summary—Results of radar investigations of auroral ionization at a frequency of 398 mc are described. The radar detected auroral echoes at College, Alaska (near Fairbanks), even when the line of sight from the transmitter does not intersect the earth's magnetic field lines at perfect perpendicular incidence. The auroral echoes were observed with off-perpendicular intersection angles as great as 10° . The requirement for near-perpendicular intersection of the radar beam with the earth's magnetic field is therefore met.

The auroral echoes at 398 mc were seen frequently. Occasionally they were very strong; those of highest amplitude were as much as 27 db above the receiver noise level. The echoes were detected over a relatively large echoing region corresponding to bearings within $\pm 45^\circ$ of geomagnetic north, and elevation angles of 0° – 17° .

Two types of auroral echoes were observed—discrete and diffuse. The discrete echoes corresponded roughly to reflections from visual auroral forms seen at night. The diffuse echoes corresponded to reflections from a large echoing region that apparently existed most often during daylight hours. Estimates of the wavelength, λ , dependence of auroral echo power, although quite crude, are deduced as λ^{10} for the radar site at College, Alaska, and λ^8 for sites where perpendicular reflection can be obtained.

INTRODUCTION

THIS REPORT was written to describe the preliminary results of radar investigations of auroral ionization at a frequency of 400 mc at College, Alaska (geomagnetic latitude 65° north).

Studies of radar reflection from auroral ionization have been numerous for frequencies in the HF and VHF ranges.¹⁻⁷ None of the studies referenced has been extended into the UHF range. Also, none of the referenced studies has allowed the precise determination of those characteristics of auroral ionization that are essential to

an understanding of the mechanism of auroral reflection. Those characteristics that must be known for a more complete understanding of auroral reflection are the wavelength dependence of the reflection mechanism, aspect sensitivity, amplitude fluctuations, and Doppler shifts. It is for the purpose of determining these characteristics at UHF that Stanford Research Institute undertook the investigation of auroral reflection at frequencies of 200 and 400 mc. At this writing, only preliminary results at 400 mc are available.

Other similar UHF studies have been in progress at the Defence Research Board,⁸ Ottawa, Canada, and at Lincoln Laboratory,⁹ Massachusetts Institute of Technology. The results of these other studies will differ from the SRI results because of the different locations of the auroral radar equipments. The SRI radar, located at College, Alaska, is 100 km south of the maximum of the auroral zone, and visual auroras are seen frequently in all directions from the radar.

EQUIPMENT

The characteristics of the radar used to detect the auroral reflections are listed in Table I.

TABLE I
SRI 400-MC RADAR CHARACTERISTICS

Peak power	60 kw
Average power	20 kw (maximum)
Antenna gain	36 db (61-foot diameter, steerable, parabolic reflector)
Antenna beamwidth	3° between half-power points, E and H planes
Frequency	398 mc
Receiver noise figure	6.5 db
Receiver bandwidth	0.3–15 kc
Minimum detectable signal	10^{-16} watts
Minimum detectable radar cross section at 500 km	0.03 meter squared
Typical operating conditions	
Pulse width	400–900 μ s
Pulse repetition frequency	75–150

The following types of displays were available:

- 1) A-scope.
- 2) B-scope (range-azimuth) with amplitude intensity modulation.
- 3) Range-elevation with amplitude intensity modulation.

* Manuscript received by the PGAP, April 17, 1958; revised manuscript received, January 2, 1959. The work described in this paper was made possible by an SRI contract with U. S. Air Force Rome Air Dev. Center. The experiments described were conducted at the Geophysical Institute, University of Alaska.

† Stanford Research Institute, Menlo Park, Calif.

¹ L. Harang and B. Landmark, "Radio echoes observed during aurorae and geomagnetic storms using 35- and 74-mc/s waves simultaneously," *J. Atmos. Terrest. Phys.*, vol. 4, pp. 332–338; 1954.

² P. A. Forsyth, "Radio measurements and auroral electron densities," *J. Geophys. Res.*, vol. 58, pp. 53–66; 1953.

³ K. Bowles, "Some Recent Experiments with VHF Radio Echoes from Aurora and Their Possible Significance in the Theory of Magnetic Storms and Auroras," Ph.D. dissertation, School of Elec. Eng., Cornell University, Ithaca, N. Y.; June 1, 1955.

⁴ R. Dyce, "Communication Aspects of VHF Auroral Reflections," Ph.D. dissertation, School of Elec. Eng., Cornell University, Ithaca, N. Y.; June 1, 1955.

⁵ G. Hellgren and J. Meos, "Localization of aurorae with 10-m high-power radar technique using a rotating antenna," *Tellus*, vol. 3, pp. 249–261; 1952.

⁶ R. L. Leadabrand, "Radio Echoes from Auroral Ionization Detected at Relatively Low Geomagnetic Latitudes," *Tech. Rep. 98*, DA-04-200-ORD-181, Radio Propagation Lab., Stanford Univ., Stanford, Calif.; December, 1955.

⁷ K. Bullough and T. R. Kaiser, "Radio reflections from aurorae," *J. Atmos. Terrest. Phys.*, vol. 5, pp. 189–200; September, 1954.

⁸ S. J. Fricker, R. P. Ingalls, M. L. Stone, and S. C. Wang, "UHF auroral observations," *J. Geophys. Res.*, vol. 62, pp. 527–546; December, 1957.

⁹ Comments on previous paper by Canadian Defence Research Board, Ottawa, Ont., Can.

GEOMETRY OF RADAR SITE

The location of the radar at College, Alaska, was such that the auroral zone maximum was only 100 km to the magnetic north of College. This location made it impossible for a line of sight from the radar to intersect the earth's magnetic field lines at right angles within the *E* layer. Calculations of the off-perpendicular contours, based on a dipole magnetic field, were made for heights of 80, 90, 100, 110, 120, 130, 140, and 150 km and are shown in Figs. 1-8. It may be seen that the closest-to-perpendicular intersection that is possible for a height of 100 km is 1.6° . For lesser heights of reflection, the off-perpendicular angle may be less (at 80 km, as small as 0.1°). At greater heights, the off-perpendicular angles are larger (the minimum off-perpendicular angle possible for a height of 150 km is 4.8°).

RESULTS

In general, two types of auroral echoes were seen with this radar—termed “discrete” and “diffuse” by the authors for reasons mentioned later in this report. The “discrete” echoes corresponded to reflection from visual auroral displays seen within $\pm 95^\circ$ of general magnetic north during the hours of darkness. The “diffuse” auroral echoes were seen when no visual auroras were detectable due to daylight. In general, the “diffuse” echo corresponded to reflections from a much larger echoing region than was commonly seen visually in the aurora. In the following detailed description of the results, the words “discrete” and “diffuse” are used to describe the two different types of echoes observed.

Range

The range of the auroral echoes depends upon the elevation angle of the antenna. The ranges varied between 1100 km and 400 km. A range histogram is shown in Fig. 9. When the antenna was pointed at low elevation angles near the horizon, the echoes were at the greatest range; when pointed at high elevation angles (up to 17°) the echoes were at the shortest range. The echoes were found most often at ranges between 500 and 900 km. This phenomenon is discussed in the section on geometry of reflection.

Depth of Range

The discrete echoes are 100 km deep in range using a transmitter pulse width of 400 μ sec. The diffuse echoes are at times spread as much as 200-300 km in range. An A-scope display of a single discrete echo is shown in Fig. 10 and a display of a double echo in Fig. 11. Both types of auroral echoes occurred frequently. In general, the discrete echoes are found at antenna bearings, elevation angles and ranges corresponding to reflections from a single homogeneous auroral arc. The diffuse auroral echoes were found at all ranges (400-1100 km) depending on the elevation angle of the antenna and the height of auroral ionization.

Bearings

The bearings of the auroral echoes were found to vary from as much as 50° west to 50° east of geomagnetic north. Plots showing the locations of auroral reflectors for two particular nights are shown in Figs. 12 and 13. At times, diffuse auroral echoes were detected at all antenna bearing angles between these limits. See, for example, the shaded area in Fig. 14. In no case were auroral echoes detected when looking at bearings outside these limits, even though visual auroras were seen frequently in these directions.

Elevation Angles

Auroral echoes were detected at elevation angles between 0° and 17° . The majority of the echoes were detected at elevation angles around 5° . At this elevation the intersection angle between a transmitted ray and the earth's magnetic field lines was nearest 90° .

Strength

The strength of the auroral echoes was found to vary within wide limits. The maximum strength of any echo detected was 27 db above the receiver noise level for a discrete echo. The majority of the echoes, however, were weaker. In general, the diffuse echoes were weaker than the discrete echoes.

Times of Occurrence

The auroral echoes were detected most frequently during the evening hours (approximately 1900-2300 AST) and during the early morning hours (0500-0800 AST). Auroral echoes have also been seen as late as 1100 in the morning and as early as 1400 in the afternoon. During the period of operation (March, April, and May, 1957) the discrete echoes were observed during the times of darkness and, hence, were seen very seldom during May. The diffuse echoes were, however, seen throughout this period during daylight hours.

Duration of the Echoes

In general, the discrete auroral echoes detected were short-lived. That is, any particular echo lasted only a few minutes. The diffuse echoes, on the other hand, sometimes persisted for as long as several hours with relatively little change in the echo pattern.

DISCUSSION OF RESULTS

Height of Reflection

The height of reflection was determined by making use of the 3° antenna beamwidth in elevation (3° between half-power points). By measuring the range and the elevation angle at which the echoes occurred, it was possible to calculate the effective height of the auroral reflector. Figs. 15 and 16 are histograms which indicate the height of auroral echoes for two nights, March 24 and 26, 1957, respectively. Typical range-elevation angle displays of discrete echoes are shown in Figs.

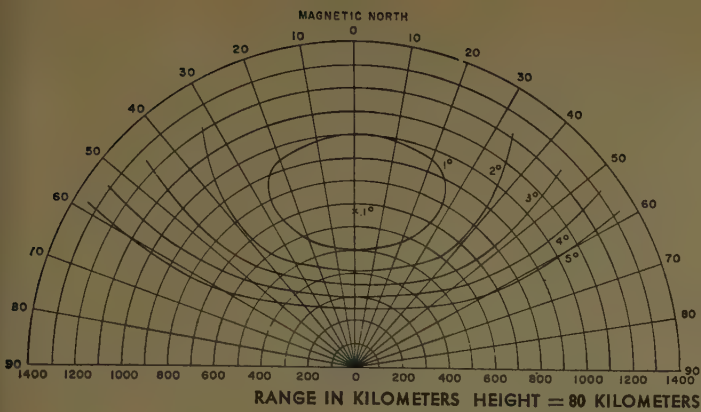


Fig. 1—Contours of off-perpendicular intersection angles for 80-km reflection height.

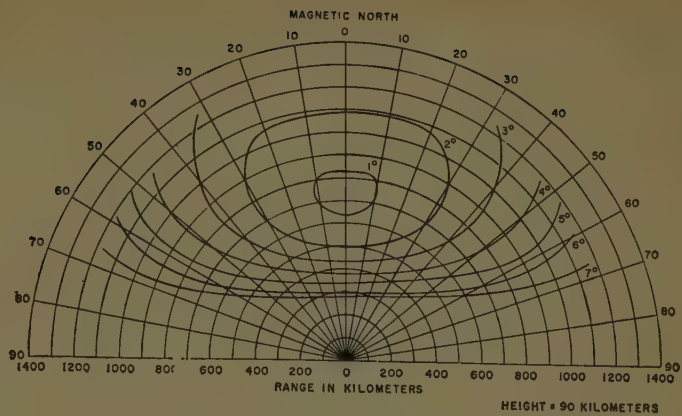


Fig. 2—Contours of off-perpendicular intersection angles for 90-km reflection height.

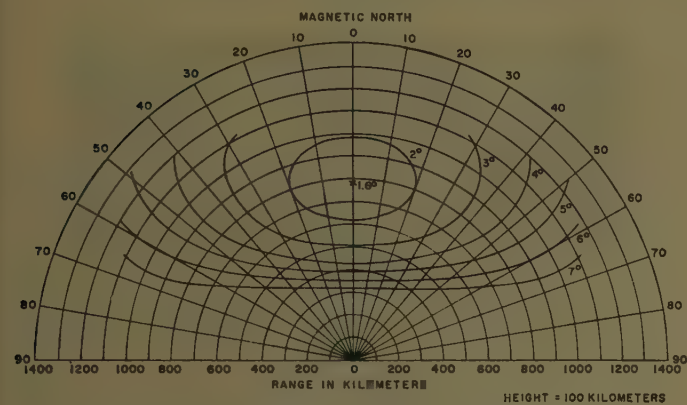


Fig. 3—Contours of off-perpendicular intersection angles for 100-km reflection height.

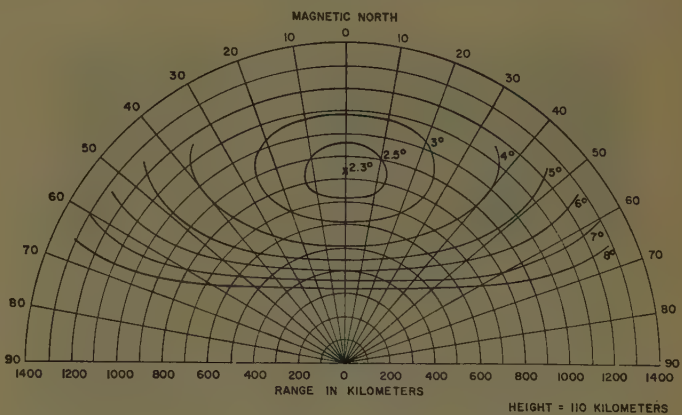


Fig. 4—Contours of off-perpendicular intersection angles for 110-km reflection height.

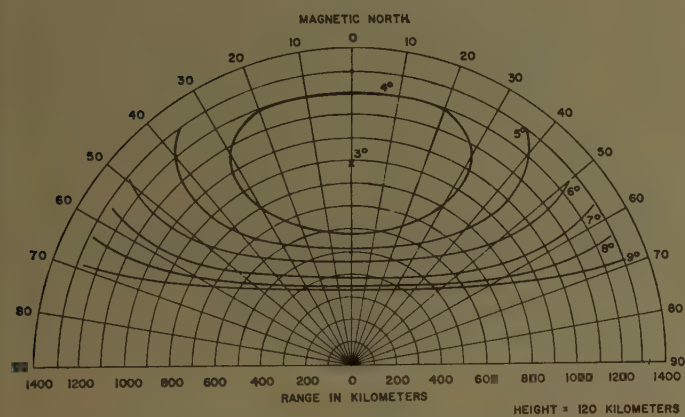


Fig. 5—Contours of off-perpendicular intersection angles for 120-km reflection height.

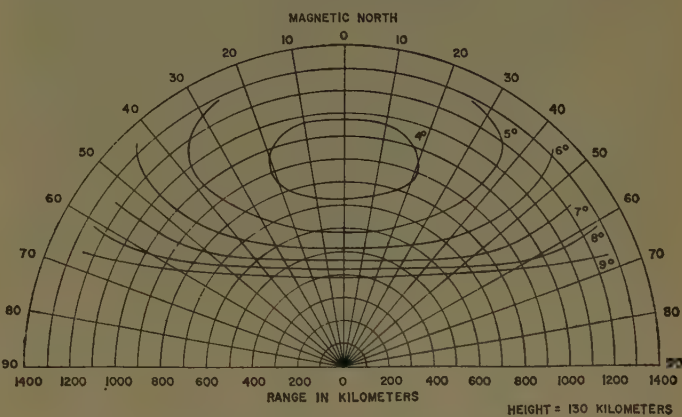


Fig. 6—Contours of off-perpendicular intersection angles for 130-km reflection height.

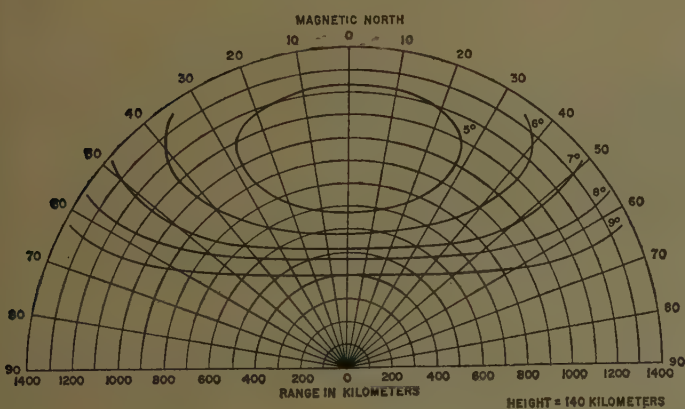


Fig. 7—Contours of off-perpendicular intersection angles for 140-km reflection height.

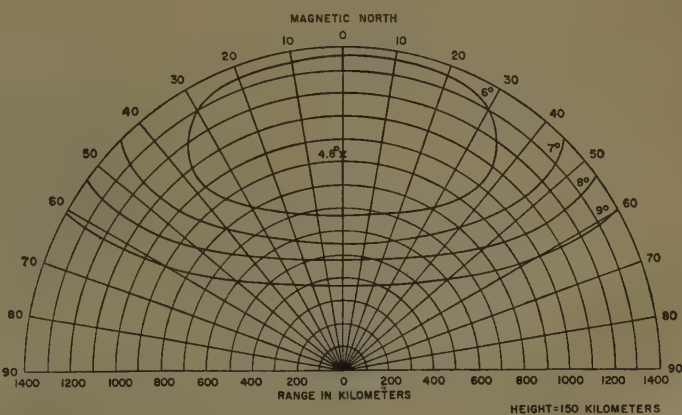


Fig. 8—Contours of off-perpendicular intersection angles for 150-km reflection height.

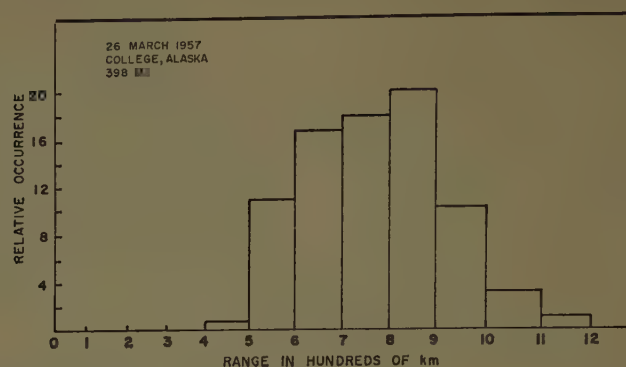


Fig. 9—Relative occurrence of auroral echoes as a function of range.

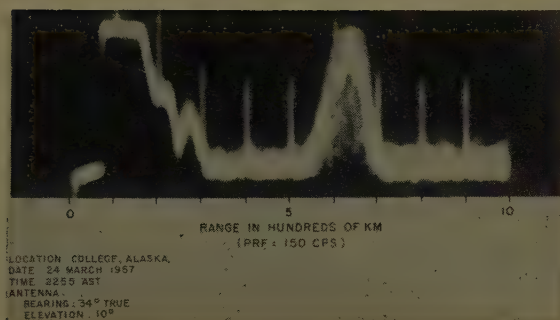


Fig. 10—A-scope display of an auroral echo.

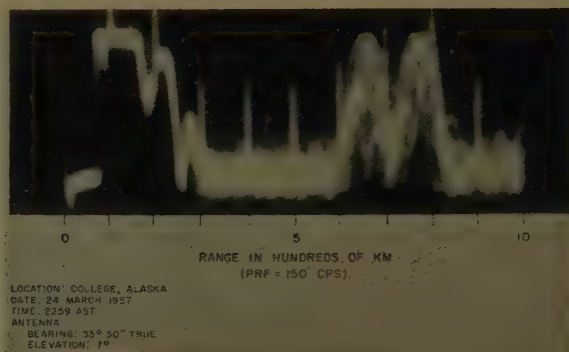


Fig. 11—A-scope display of a double auroral echo.

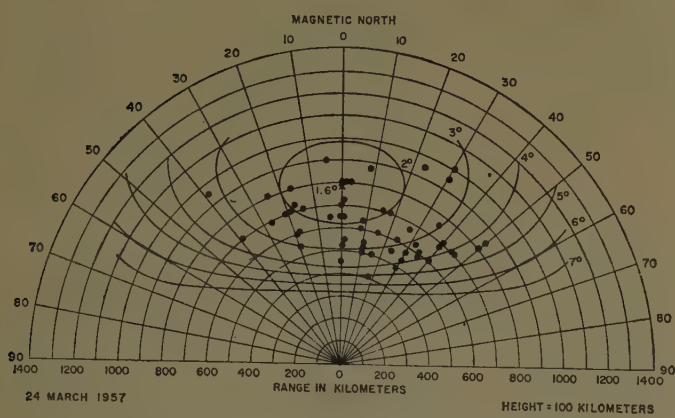


Fig. 12—Position in azimuth and range of auroral reflection centers on March 24, 1957.

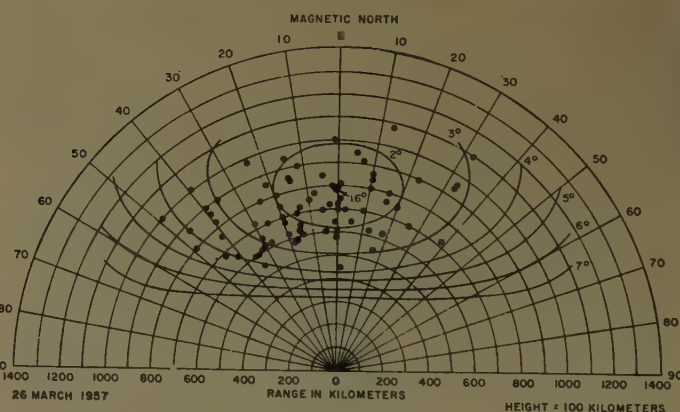


Fig. 13—Position in azimuth and range of auroral reflection centers on March 26, 1957.

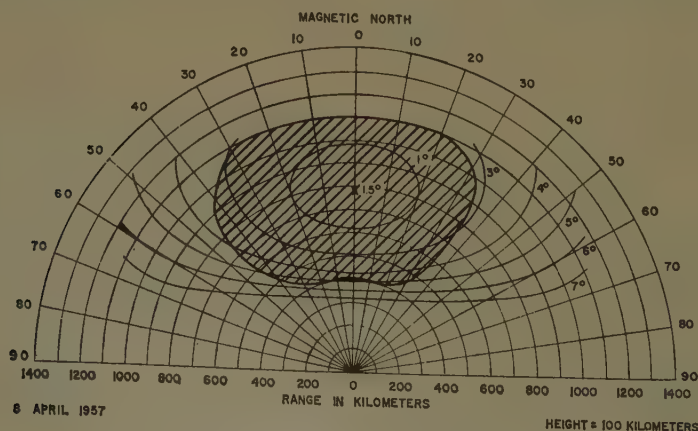


Fig. 14—Area from which diffuse auroral echoes were detected on April 8, 1957.

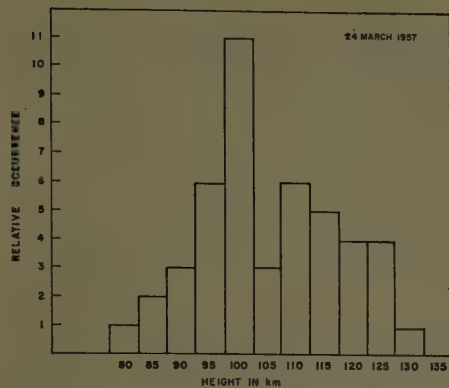


Fig. 15—Relative occurrence of auroral echoes as a function of height of reflection on March 24, 1957.

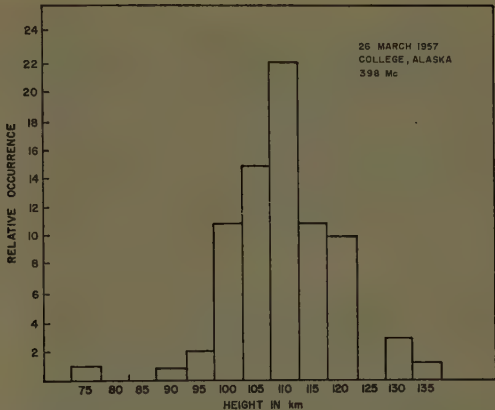


Fig. 16—Relative occurrence of auroral echoes as a function of height of reflection on March 26, 1957.

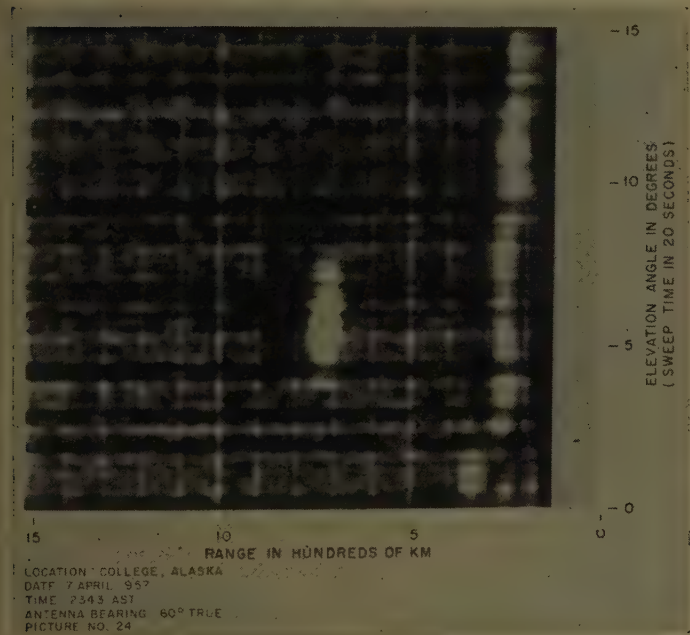


Fig. 17—Range-elevation angle display of an auroral reflection at 398 mc.

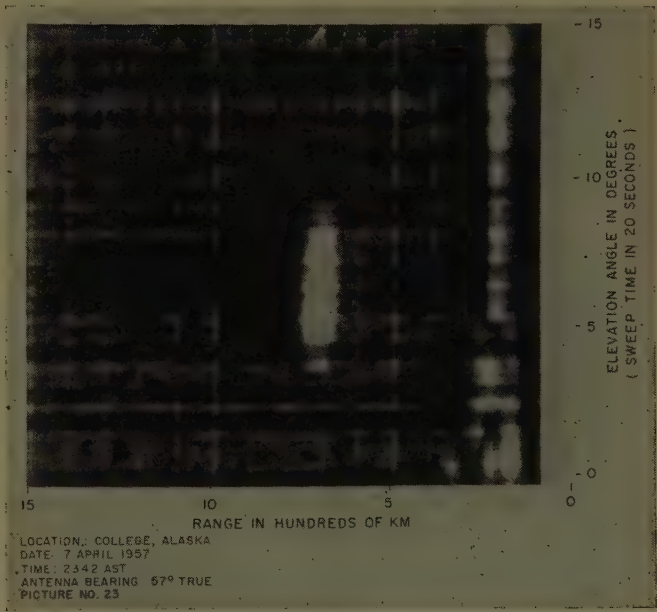


Fig. 18—Range-elevation angle display of an auroral echo at 398 mc.

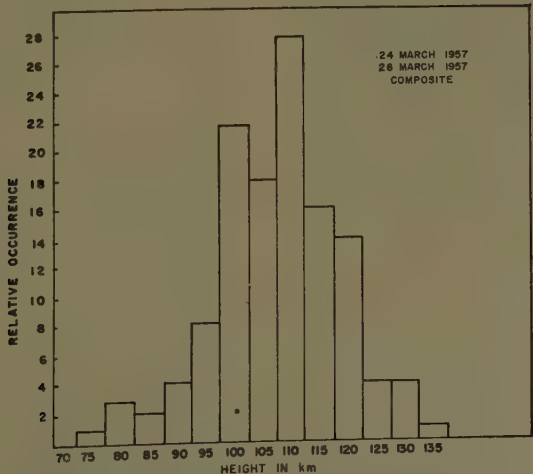


Fig. 19—Relative occurrence of auroral echoes as a function of height of reflection for March 24 and 26, 1957.

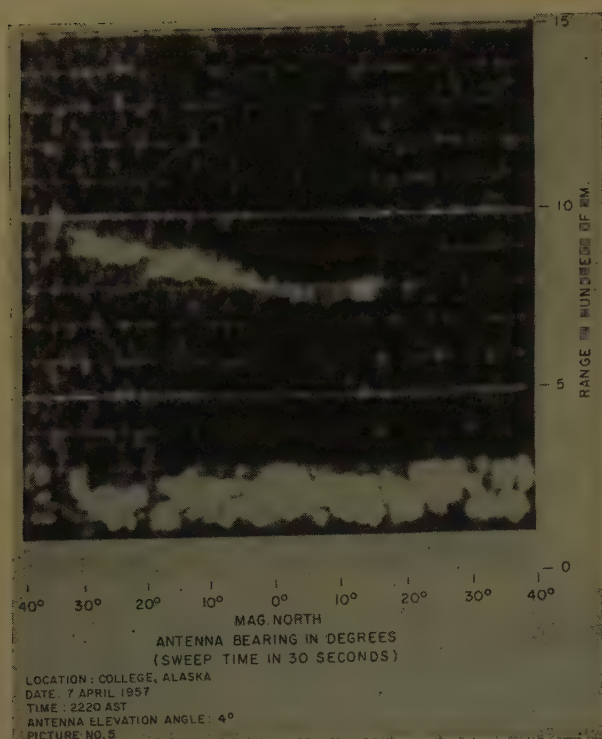


Fig. 20—Range-azimuth angle display of an auroral echo at 398 mc.

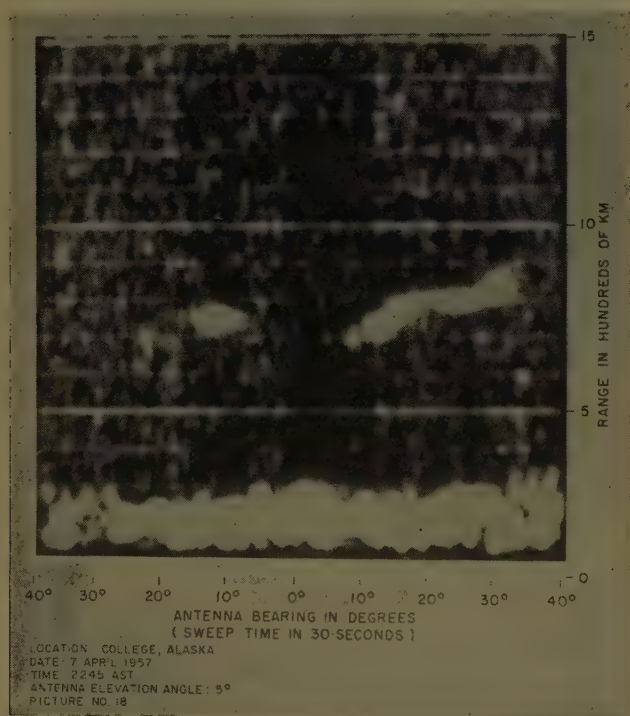


Fig. 22—Range-azimuth angle display of an auroral echo at 398 mc.

17 and 18. The auroral echoes were seen with heights of reflection as low as 75 km and as high as 135 km. On one occasion, an echo was detected at a 2° elevation angle and 600-km range, which corresponded to a height of reflection of 50 km. It is felt that tropospheric bending could not explain this apparent low-height reflection. It can be seen in the histogram of Fig. 19 (a composite of the observations on March 24 and

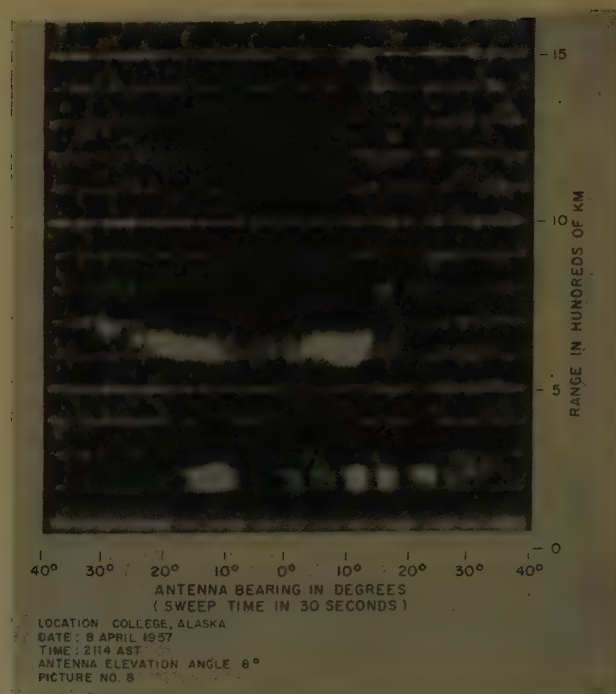


Fig. 21—Range-azimuth angle display of an auroral echo at 398 mc.

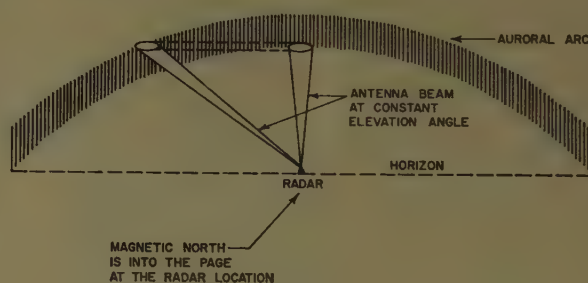


Fig. 23—Geometry of reflection from an auroral arc.

26), however, that the majority of the reflection heights fall in the region of 100–110 km. Refraction was not taken into account in the preparation of this histogram. Range was read from the leading edge of the echo pulse and elevation angle was obtained for the elevation giving the strongest echo. These factors were used to compute height and all calculated heights were divided into 5-km groupings for plotting purposes.

Location in Space of Auroral Ionization

Discrete Echoes: The discrete type of auroral echo in most cases corresponds to reflections from an auroral arc that lies along a geomagnetic latitude line. By varying the antenna elevation angle as one varies the antenna bearing, it is possible to obtain reflections from an auroral arc extending from horizon to horizon over a bearing-angle separation spread of approximately 60°. However, if the antenna elevation is kept constant and only the bearing of the antenna is changed, it is possible to trace out an auroral arc on the radar indicator over a limited bearing angle, as shown in Figs. 20–22. In this case, the auroral echo detected in the direction of magnetic north corresponds to reflections from the lower

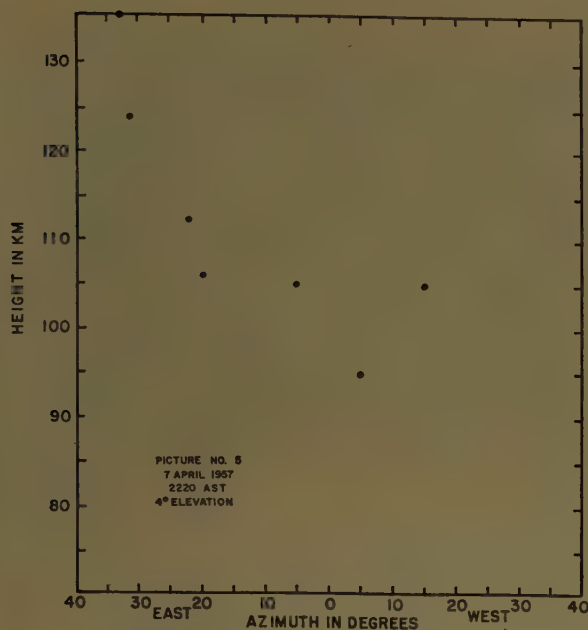


Fig. 24—Height of reflection as a function of azimuth angle for the auroral echo shown in Fig. 20.

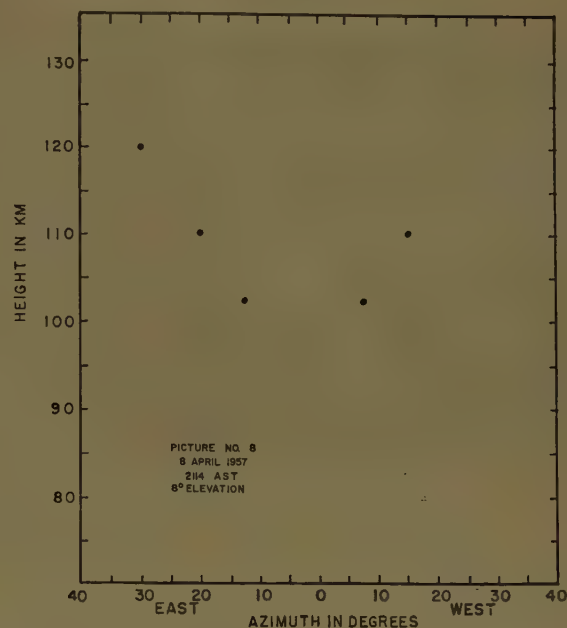


Fig. 25—Height of reflection as a function of azimuth angle for the auroral echo shown in Fig. 21.

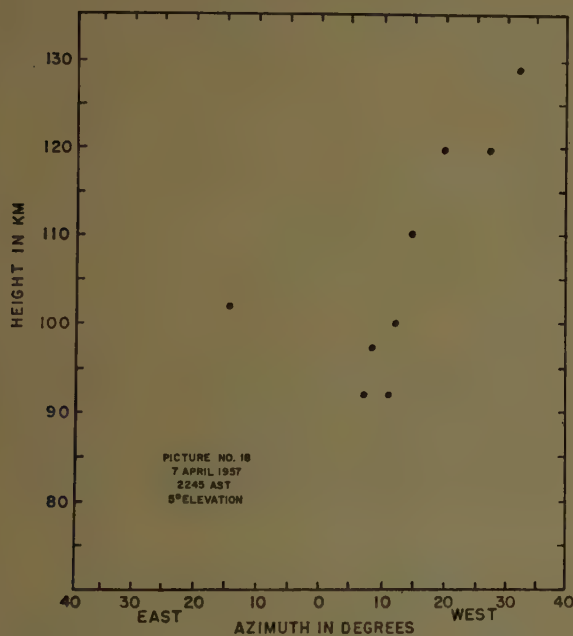


Fig. 26—Height of reflection as a function of azimuth angle for the auroral echo shown in Fig. 22.

edge of an auroral arc, with echoes at bearing angles away from magnetic north coming from a higher position on an auroral arc, as shown in Fig. 23. The range-azimuth displays shown in Figs. 20–22 are examples of this characteristic.

Several azimuth sweeps at appropriate elevation angles can measure the vertical extent of auroral ionization. By scaling the range and elevation angle of the antenna from these scans, it is possible to obtain the height of the auroral reflection as a function of azimuth angle. Figs. 24–26 are plots of the height of reflection for the range-azimuth presentations in Figs. 20–22, re-

spectively. Refraction corrections have been ignored. These plots describe the variation of reflection height with bearing angle mentioned above and define the vertical extent of the auroral ionization.

Diffuse Echoes: Diffuse auroral echoes may be detected over wide ranges of bearing angles, elevation angles, and ranges. On one occasion they were detected within the following limits:

45° west to 35° east of magnetic north
0° to 17° elevation
400–1100 km range.

This corresponds roughly to the area shown in Fig. 14. Another interesting feature of the diffuse auroral echo is illustrated in Figs. 27 and 28, which show a series of range-elevation angle scans with the antenna at various bearing angles. As seen in Figs. 27 and 28, the diffuse auroral echoes vary within wide limits of range, corresponding to wide ranges of elevation angle. Calculating the height of the reflector as a function of range, it was found that reflection did not occur at constant heights. Instead, as shown in Figs. 29 and 30, the height of reflection was at approximately 80–90 km for the longer-range echoes and at 120–130 km for the shorter-range echoes. Fig. 31 illustrates this effect. In addition, it is interesting that by calculating the height of the trailing edge of the echo for all ranges, Figs. 32 and 33, the trailing edge of the echoes corresponds to constant reflection height. The cause of this is not completely understood, but is thought to be an effect of the particular reflection mechanism.

Off-Perpendicular Reflection Angles

Comparing observations with the off-perpendicular contours shown in Figs. 1–8, it may be seen that those

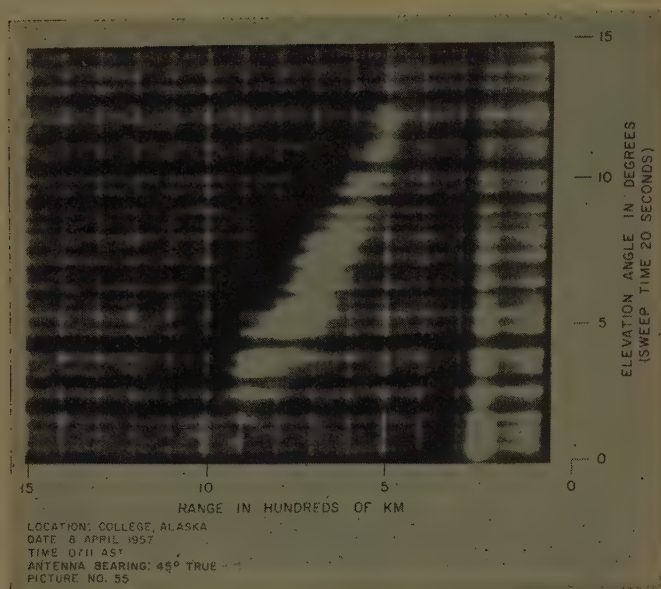


Fig. 27—Range-elevation angle display of a diffuse type of auroral echo at 398 mc.

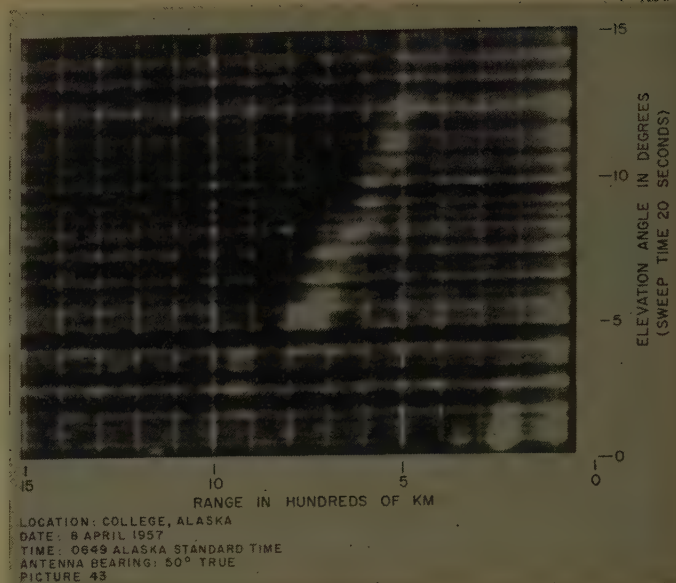


Fig. 28—Range-elevation angle display of a diffuse type of auroral echo at 398 mc.

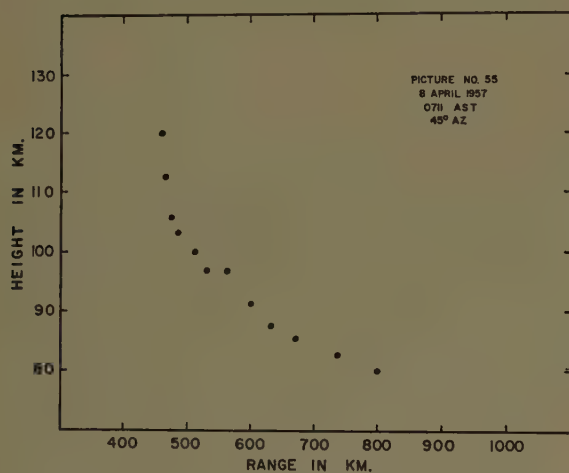


Fig. 29—Height of reflection as a function of range for the auroral echo shown in Fig. 27.

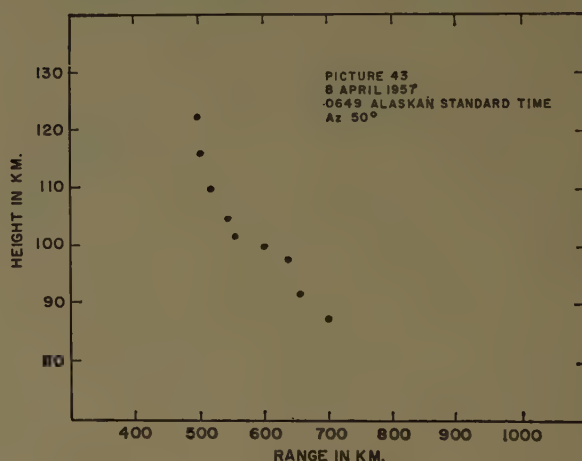


Fig. 30—Height of reflection as a function of range for the auroral echo shown in Fig. 28.

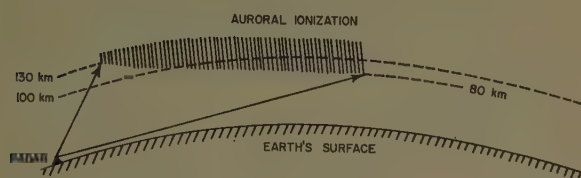


Fig. 31—Geometry of reflection for a diffuse type of auroral echo.

auroral echoes occurring at greater heights also occur at greater off-perpendicular angles, and those auroral echoes occurring at lower heights in general occur at more nearly perpendicular reflection angles.

For the diffuse auroral echoes shown in Figs. 27 and 28, which change the height of the reflection with elevation angle, the off-perpendicular reflection angle is much greater at the higher elevation angles than it is at the lower elevation angles, as shown in the plots of Figs. 34 and 35.

Reflection Mechanisms

The reflection mechanism of auroral echoes is not completely understood, although numerous papers on the subject have been written.⁵⁻⁷ In general, the echoes are seen in the direction of magnetic north, where near-perpendicular reflection from ionization aligned with the earth's magnetic field line occurs. Thus, one would suspect that the reflection mechanism is similar to that proposed by many others—near-specular reflection from small cylindrical columns or elongated blobs which have a relatively high length-to-diameter ratio and which are in alignment with the earth's magnetic field. A search for echoes in other bearings and elevation angles supported this theory. At times considerable aurora was visible to the magnetic south from Fairbanks and at those times the antenna was pointed at the proper bearing and elevation angle to illuminate the auroras with radio energy. However, no auroral echoes were seen. At

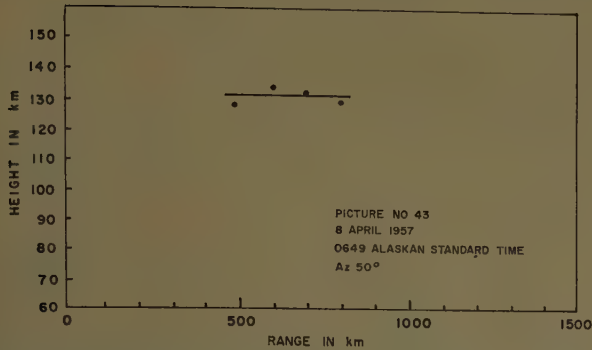


Fig. 32—Height of trailing reflection as a function of range for the auroral echo shown in Fig. 27.

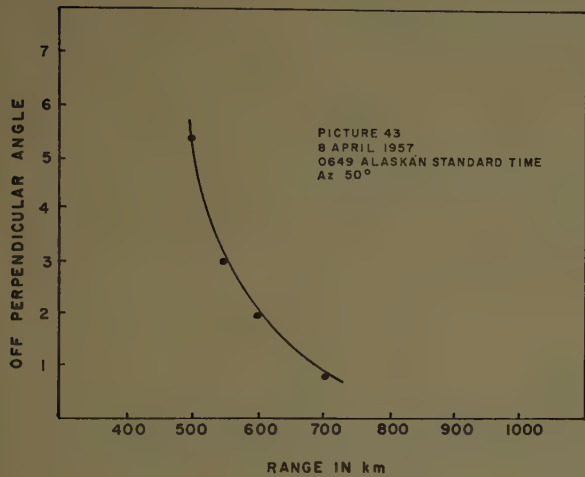


Fig. 34—Off-perpendicular intersection angle as a function of range for the auroral echo shown in Fig. 27.

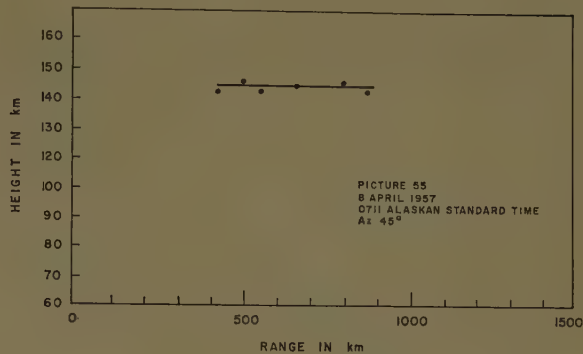


Fig. 33—Height of trailing edge reflection as a function of range for the auroral echo shown in Fig. 28.

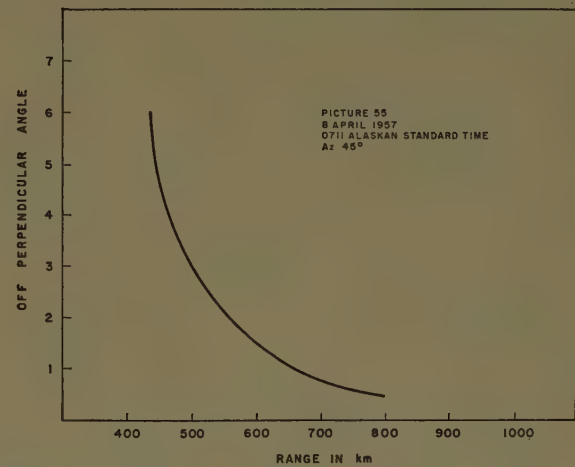


Fig. 35—Off-perpendicular intersection angle as a function of range for the auroral echo shown in Fig. 28.

times when brilliant coronas were visible overhead, the antenna was pointed at these brilliant patches and again no auroral echoes were seen as would be expected from the column reflection theory. The theory that long cylindrical columns provide the reflection mechanism of the aurora seems to fit in general; however, there are several specific cases in which it does not appear to fit too well—namely, the case of the diffuse auroral echoes which appear to change reflection height with a change in the intersection angle between the transmitted ray and the earth's magnetic field line. For such echoes, present theories of auroral scattering do not hold.¹⁰

In order to estimate the wavelength dependence of auroral echoes at College, the 106-mc results obtained in 1955 by Bowles³ are used together with the 400-mc SRI results. The maximum detected auroral echo power seen by Bowles was 10⁻⁹ watts. The transmitter peak power was 100 kw and the antenna gain was 21 db. Comparing these characteristics and results with the 398-mc radar characteristics and the maximum auroral echo power detected of 5×10⁻¹⁴ watts, the following comparison may be made:

	106 mc	398 mc	db difference
Transmitter power	100 kw	50 kw	- 3 db
Antenna gain (one way)	21 db	36 db	+15 db
Maximum detected auroral echo power	10 ⁻⁹ watts	5×10 ⁻¹⁴ watts	+43

Thus, in going from a frequency of 100 mc to a frequency of 400 mc at College, over 55 db are lost due to the wavelength dependence of the reflection mechanism and the aspect sensitivity. This leads to the following crude wavelength dependence in the radar equation for the College site:

$$P_R \propto P_T \lambda^{11}$$

There are, however, many questionable factors in establishing wavelength dependence on the results of only these two experiments. For example:

- 1) Did the aurora seen at 100 mc have the same intensity as the aurora seen at 400 mc several years later?
- 2) Did the aurora at 100 mc fill the entire beam of the antenna (20° by 25°) as it most likely did at 400 mc (3°)? (The preceding comparison assumed that it did fill the beam at both frequencies.) Unless these

¹⁰ H. G. Booker, C. W. Gartlein, and B. Nichols, "An Interpretation of Radio Reflections from the Aurora," School of Elec. Eng. Cornell University, Ithaca, N. Y., Tech. Rep. 14; August 27, 1953. See also *J. Geophys. Res.*, vol. 60, pp. 1-22; March, 1955.

¹¹ R. K. Moore, "Theory of radio scattering from the aurora," IRE TRANS. ON ANTENNAS AND PROPAGATION, vol. AP-3, pp. 217-230; August, 1952.

experiments are repeated with both equipments operating simultaneously with antennas of equal beamwidths, the answers to these questions will be difficult to obtain.

Further evidence for the λ^{10} proportion for auroral echo power can be obtained by using the 210-mc College¹² results, which were negative; that is, a search for echoes was made but none were seen. The characteristics of the College 210-mc auroral radar are:

Transmitter peak power, 50 kw
Pulse length, 50 μ s
PRF, 120 cps
Antenna gain, 22 db
Receiver noise figure, 10 db
Receiver bandwidth, 20 kc
Minimum detectable power, 2×10^{-16} watts.

By comparing the results and equipment at 400 mc with those at 210 mc, using the auroral radar equation ($P_R \propto P_T \lambda^{10}$) it is found that the maximum auroral echo power which may be detected is only 8 db above the 210-mc radar receiver noise level. Thus, it is not unreasonable to suspect that auroral echo observations at 210 mc were never made during a time of auroral activity sufficient to produce echoes. Therefore, it is interpreted that the 210-mc negative results roughly support the λ^{10} dependence previously derived.

In order to determine the degree of aspect sensitivity of the auroral echoes, the following comparison between the Canadian results⁸ and the SRI results was made. The Canadians have detected auroral echoes at 488 mc using 10 kw of power and two 28-foot dishes, one for receiving and one for transmitting. The maximum echo detected was 50 db above KTB (noise figure, 5 db). Normalizing the equipment factors, it is found that the Canadians received echoes 30–35 db in excess of the SRI auroral echoes detected at College, Alaska. This gives a rough measure of the aspect sensitivity of the auroral echoes, since the location of the Canadian installation permits the possibility of detecting auroral echoes when the transmitter ray intersects the earth's magnetic field lines at perpendicular incidence for a height of 100 km.

If it is assumed that the aspect sensitivity is not extremely important for measurements at 100 mc—that is, signals are not appreciably weaker than if obtained at perpendicular reflection—then wavelength dependence law may be obtained for the reflection mechanism alone as follows:

$$P_R \propto P_T \lambda^5.$$

FURTHER RESEARCH

Additional characteristics of the auroral echoes which should be studied using the 398-mc radar are:

- 1) Accurate diurnal variation;
- 2) Percentage of time of occurrence;
- 3) Fading rate of the auroral echoes;
- 4) Doppler frequency of the auroral echoes;
- 5) Polarization (the polarization used for all of the above measurements was horizontal, receiving and transmitting).

The data thus far gathered at 398 mc suggest that auroral echoes should be detected at even higher frequencies in the Fairbanks area. By going to a frequency of 800 mc, a 6-db increase in the two-way antenna gain can be obtained if it is assumed that the aurora fills the antenna beam. Also, since the echoes are found to have strength as great as 27 db above the noise level, using the modified radar equation having λ^{10} variation the maximum detected auroral echo would be 3 db above receiver noise level. Thus, a search for auroral echoes at 800 mc using transmitter powers of the order of 50-kw peak and 10-kw average should yield marginal but positive results. However, if no auroral echoes are detected at 800 mc, the negative results would further support a λ^{10} , or greater, relationship.

CONCLUSIONS

Auroral echoes using a high sensitivity radar are seen at a frequency as high as 398 mc at Fairbanks, Alaska. The geometry of reflection is such that in no case (except possibly for very low reflection heights) does perpendicular reflection from columns aligned with the earth's magnetic field exist. The echo strength is as great as 27 db above the receiver noise level and the echoes seen over wide ranges of bearings and elevation angles (within $\pm 50^\circ$ of magnetic north and 0° – 17° elevation angle). The echoes are detected at off-perpendicular reflection angles from the earth's magnetic field line at angles as great as 10° . The echoes are seen quite frequently; they were detected, at some time, during nearly all hours of the day for the period that these tests were made.

Two distinctly different types of auroral echoes are observed, discrete and diffuse. The discrete echoes correspond to reflection from visual auroral forms seen during the night. The diffuse echoes are seen during daylight hours when visual auroras cannot be seen.

Based on previous 100-mc results obtained at College, it has been possible to estimate very crudely a λ^{10} power law dependence for auroral reflections at College. Utilizing the recent 488-mc Canadian auroral echo results,⁸ a λ^5 wavelength dependence of the auroral reflection mechanism alone is established.

ACKNOWLEDGMENT

The author wishes to acknowledge the cooperation and assistance of the University of Alaska, where these experiments were conducted, as well as the help of the many staff members of the Engineering Division of Stanford Research Institute, Stanford, Calif.

¹² C. G. Little, *et al.* "Radio Propagation in the Arctic," Geophys. Inst., College, Alaska, Final Rep., Contract AFCRC AF 19(604)-1089.

Correlation Function and Power Spectra of Radio Links Affected by Random Dielectric Noise*

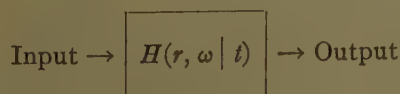
DIMITRI S. BUGNOLO†

Summary—The correlation function and corresponding power spectrum of an electromagnetic wave affected by random dielectric noise is related to the power spectrum of the source by an extension of the notions of time-variable linear networks. It will be shown that in general, the power spectrum of the received signal can be regarded as the output of a network characterized by a time-variable transfer function. The results are applied to a long line of sight radio link and used to predict the error in the received signal in a mean squared sense. This will be used to show that the rate of a source is bounded such that there exists a maximum rate R given a bandwidth δ and scattering parameters of the atmosphere.

INTRODUCTION

RECENT papers dealing with the propagation of electromagnetic waves in a region containing dielectric noise have been restricted to the special case of a monochromatic source. This paper is concerned with an extension to the more general case when the source can be considered a stationary random process. The general analysis will also consider the problem of a nonstationary dielectric noise. Since the environment surrounding the physical system leading to the generation of a dielectric noise is essentially time variable, it follows that the assumption of a stationary dielectric noise is open to question.

The notions of time-variable linear systems will be applied to the propagation problems under consideration. This has some intuitive appeal since the results can be put into a form readily understood by workers in the parallel fields of communication and information theory. For example, it will be shown that the received signal over a long line-of-sight or scatter-propagation link can be regarded as the output of a time variable linear network characterized by a suitable transfer function or, in general, by a suitable transfer tensor.



The results of this analysis could be used to study any of the following general class of problems.

- 1) Correlation function of the received signal for the case of a nonstationary or stationary dielectric noise.

- 2) Power spectral density of the received signal given the power spectral density of the source for the case of a stationary dielectric noise.

As an example this paper will conclude with a simplified analysis of the band-limited long line-of-sight problem. Since models available for the dielectric noise assume a stationary process, this example will be so restricted.

GENERAL THEORY

Consider an unbounded region containing a source and observer located at r' and r respectively (see Fig. 1).

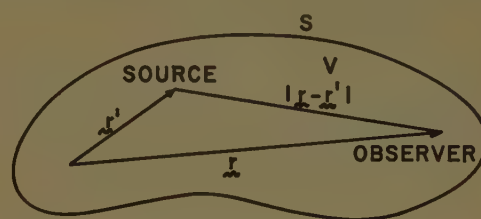


Fig. 1.

The vector wave equation for the electric field intensity is the usual

$$\nabla \times \nabla \times \mathbf{E} + \mu \epsilon \ddot{\mathbf{E}} = -2\mu \dot{\epsilon} \dot{\mathbf{E}} - \mu \ddot{\epsilon} \mathbf{E} - \mu \dot{\mathbf{J}}, \quad (1)$$

where the dot stands for partial differentiation with respect to time. If the carrier frequency of the source is very large compared to the largest frequency component in the dielectric noise, (1) can be approximated by

$$\nabla \times \nabla \times \mathbf{E} + \mu \epsilon \ddot{\mathbf{E}} = -\mu \dot{\mathbf{J}}. \quad (2)$$

Since the space variation of the dielectric is bounded such that

$$|\nabla \epsilon| \lambda / \epsilon \ll 1,$$

(2) can be further approximated by the usual wave equation,

$$\nabla^2 \mathbf{E}(r, t) - \mu \epsilon(r, t) \ddot{\mathbf{E}} = \mu \dot{\mathbf{J}}. \quad (3)$$

In order to eliminate the excessive formalism of a general analysis this paper will be restricted to a solution of the scalar wave equation.¹ This, of course, assumes that cross coupling between field components is negligible; this also neglects any shift of the plane of polarization during propagation. It is the hope of the author that the simplicity will make up for the lack of generality.

¹ The solution of the vector wave equation is considered in the Appendix.

* Manuscript received by the PGAP, June 9, 1958; revised manuscript received, November 3, 1958. This research was supported in whole or in part by the U. S. Air Force under contract number 49(638)-350 monitored by the Air Force Office of Sci. Res. Air Res. Dev. Command.

† Dept. of Elec. Eng., Columbia University, New York, N. Y.

Consider the geometry of Fig. 2. Let the region of dielectric noise be restricted to the far field of the source. The received signal as seen by the observer will be a sum of the direct and "scattered" fields,

$$\phi_R(\mathbf{r}, t) = \phi_0(\mathbf{r}, t) + \phi_s(\mathbf{r}, t) \quad (4)$$

where $\phi_s(\mathbf{r}, t)$ is a solution of

$$\nabla^2 \phi_s(\mathbf{r}, t) - \mu \epsilon(\mathbf{r}, t) \ddot{\phi}_s(\mathbf{r}, t) = 0. \quad (5)$$

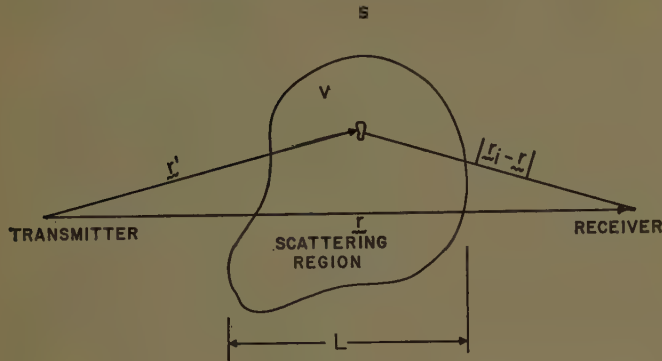


Fig. 2.

Let $\epsilon(\mathbf{r}, t) = \epsilon_0 + \Delta\epsilon(\mathbf{r}, t)$, where ϵ_0 is the ensemble average of the random variable $\epsilon(\mathbf{r}, t)$ at a time t^2 . Substituting into (5), we have

$$\nabla^2 \phi_s - \epsilon_0 \mu \ddot{\phi}_s = \mu \Delta\epsilon(\mathbf{r}, t) \ddot{\phi}_s. \quad (6)$$

In the first Born Approximation for the scattered field, it is customary to replace the field component of the source by the unperturbed incident field, $\phi_0(\mathbf{r}, t)$. Hence,

$$\nabla^2 \phi_s - \epsilon_0 \mu \ddot{\phi}_s = \mu \Delta\epsilon(\mathbf{r}, t) \ddot{\phi}_0. \quad (7)$$

Let us assume that the Fourier transform of ϕ_s exists; then

$$\phi_s(\mathbf{r}, w) = \frac{1}{2\pi} \int_{-\infty}^{\infty} \phi_s(\mathbf{r}, t) e^{jw t} dt \quad (8)$$

with the inverse

$$\phi_s(\mathbf{r}, t) = \int_{-\infty}^{\infty} \phi_s(\mathbf{r}, w) e^{-jw t} dw. \quad (9)$$

Taking the Fourier transform of (7), we have

$$\nabla^2 \phi_s(\mathbf{r}, w) - F\{\epsilon_0(t) \mu \ddot{\phi}_s\} = F\{\mu \Delta\epsilon(\mathbf{r}, t) \ddot{\phi}_0\}. \quad (10)$$

The right-hand side of this result can be reduced by defining

$$\Delta\epsilon(\mathbf{r}, t) = \int_{-\infty}^{\infty} \Delta\epsilon(\mathbf{r}, w') e^{-jw' t} dw'.$$

Substituting and rearranging terms, we have

$$F\{\mu \Delta\epsilon(\mathbf{r}, t) \ddot{\phi}_0\} = \frac{\mu}{2\pi} \int_{-\infty}^{\infty} dw' \Delta\epsilon(\mathbf{r}, w') \int_{-\infty}^{\infty} dt \ddot{\phi}_0 e^{j(w-w')t}. \quad (11)$$

² Since the dielectric noise is not stationary, the mean value will in general be a function of time.

Since the modified Fourier transform of the source can be defined by

$$\phi_0(\mathbf{r}, w - w') = \int_{-\infty}^{\infty} \phi_0(\mathbf{r}, t) e^{j(w-w')t} dt,$$

it follows that (11) reduces to

$$F\{\} = -\mu \int_{-\infty}^{\infty} (w - w')^2 \Delta\epsilon(\mathbf{r}, w') \phi_0(\mathbf{r}, w - w') dw'. \quad (12)$$

Solving the inhomogeneous wave (10) for the first Born Approximation, we have for the scattered field

$$\begin{aligned} \phi_s(\mathbf{r}, w) &= \frac{\mu}{8\pi} \int \frac{e^{jkR}}{R} dv' \\ &\cdot \int_{-\infty}^{\infty} (w - w')^2 \Delta\epsilon(\mathbf{r}', w') \phi_0(\mathbf{r}', w - w') dw' \\ R &= |\mathbf{r} - \mathbf{r}'|; \quad k = w^2 \mu \epsilon_0(t). \end{aligned} \quad (13)$$

It should be noted that the wave number k is a slowly varying function of time. This results from the fact that the mean value of the random process changes with time and the approximation,

$$F\{\epsilon_0(t) \mu \ddot{\phi}_s\} \cong -w^2 \mu \epsilon_0(t) \phi_s(\mathbf{r}, w). \quad (14)$$

This result could be used to predict the power spectral density of the received signal by first constructing the correlation function using (13). Such a procedure is rigorous but unfortunately rather lengthy. Rather than proceed in this fashion it is useful to further simplify the Fourier transform of the total source given by (12). By so doing it will be possible to apply many of the results useful in the analysis of linear time-variable networks.^{3,4,5}

As a first approximation for the Fourier transform given by (12) consider

$$F\{\} \cong \frac{\mu}{2\pi} \Delta\epsilon(\mathbf{r}, t) \int_{-\infty}^{\infty} \ddot{\phi}_0(\mathbf{r}, t) e^{jw t} dt \quad (15)$$

or

$$F(\mathbf{r}, w | t) = -w^2 \mu \epsilon(\mathbf{r}, t) \phi_0(\mathbf{r}, w). \quad (16)$$

The modified transform is now *time dependent*. This approximation is reasonable since the major contribution of the integration in w' is in the vicinity of $w' = 0$. The modified wave (10) is now approximately

$$\begin{aligned} \nabla^2 \phi_s(\mathbf{r}, w | t) + w^2 \mu \epsilon_0(t) \phi_s(\mathbf{r}, w | t) \\ = -w^2 \mu \Delta\epsilon(\mathbf{r}, t) \phi_0(\mathbf{r}, w). \end{aligned} \quad (17)$$

The notation has been changed to stress the time dependence of the solution ϕ_s .

³ L. A. Zadeh, "Correlation function and power spectra in variable networks," *PROC. IRE*, vol. 38; November, 1950.

⁴ L. A. Zadeh, "Circuit analysis of linear varying-parameter networks," *J. Appl. Phys.*, vol. 21, pp. 1171-1177; November, 1950.

⁵ J. Landing and R. Batten, "Random Processes in Automatic Control," McGraw-Hill Book Co., Inc., New York, N. Y., ch. 5; 1956.

The first Born Approximation for the scattered field reduces to

$$\phi_s(\mathbf{r}, w | t) = \frac{\mu w^2}{4\pi} \int_{V'} \Delta\epsilon(\mathbf{r}, t) \phi_0(\mathbf{r}, w) \frac{e^{ikR}}{R} dv'. \quad (18)$$

The inverse of (18) is now an approximate result for the time-dependent signal.

$$\phi_s(\mathbf{r}, t) = \int_{-\infty}^{\infty} \phi_s(\mathbf{r}, w | t) e^{i\omega t} dw. \quad (19)$$

The exact character of the unscattered field $\phi_0(\mathbf{r}', w)$ will depend on the Fourier components of the source, the transmitting antenna and the size and distance of the scattering region V . For simplicity, in the following it will be assumed that ϕ_0 in the scattering volume is essentially plane. The results that follow could be easily extended to include a more general case. Let

$$\phi_0(\mathbf{r}', t) = \int_{-\infty}^{\infty} \phi_0(w) e^{-j(\omega t - \mathbf{k} \cdot \mathbf{r}')} dw. \quad (20)$$

Substituting into (18) we have

$$\phi_s(\mathbf{r}, w | t) = \frac{\mu w^2}{4\pi} \phi_0(w) \int_{V'} \Delta\epsilon(\mathbf{r}', t) e^{i\mathbf{k} \cdot \mathbf{r}'} \frac{e^{ikR}}{R} dv'.$$

From this it is evident that the scattered signal can be regarded as the output of the time-dependent linear system characterized by the transfer function

$$H(w | t) \equiv \frac{w^2 \mu}{4\pi} \int_{V'} \Delta\epsilon(\mathbf{r}', t) \frac{e^{ikR}}{R} e^{i\mathbf{k} \cdot \mathbf{r}'} dv' \quad (21)$$

$$\phi_0(\mathbf{r}, t) \rightarrow \boxed{H(w, t)} \rightarrow \phi_s(\mathbf{r}, t)$$

where

$$\phi_s(\mathbf{r}, t) = \int_{-\infty}^{\infty} H(w | t) \phi_0(w) e^{-j\omega t} dw. \quad (22)$$

Theorem I

The scattered component of the received signal can be regarded as the output of a time-variable linear network characterized by the time-dependent transfer function $H(w/t)$.

CORRELATION FUNCTION OF THE RECEIVED SIGNAL

The received signal is given as the sum of the unscattered and scattered field.⁶

$$\phi_2(\mathbf{r}, t) = \phi_0(\mathbf{r}, t) + \phi_s(\mathbf{r}, t).$$

Consider the correlation function of the received signal.

⁶ Or the scattered signal alone in the case of beyond-the-horizon scatter-propagation links.

This is defined as

$$\overline{\phi(\mathbf{r}, t_1) \phi(\mathbf{r}, t_2)} = \overline{\{\phi_0(\mathbf{r}, t_1) + \phi_s(\mathbf{r}, t_1)\} \{\phi_0(\mathbf{r}, t_2) + \phi_s(\mathbf{r}, t_2)\}}.$$

Since the random variable $\Delta\epsilon(\mathbf{r}, t)$ has zero mean by definition, it follows that

$$\overline{\phi(\mathbf{r}, t_1) \phi(\mathbf{r}, t_2)} = \overline{\phi_0(\mathbf{r}, t_1) \phi_0(\mathbf{r}, t_2)} + \overline{\phi_s(\mathbf{r}, t_1) \phi_s(\mathbf{r}, t_2)}. \quad (23)$$

$\phi_0(\mathbf{r}, t_1) \phi_0(\mathbf{r}, t_2)$ is just the correlation function of the input. The correlation function of the scattered component is given by repeated use of (22).

$$\overline{\phi_s(\mathbf{r}, t_1) \phi_s(\mathbf{r}, t_2)} = \int_{-\infty}^{\infty} dw \int_{-\infty}^{\infty} dw' \overline{H(w | t_1) H(w' | t_2)} \overline{\phi_0(w) \phi_0(w')} e^{-j\omega t_1} e^{-j\omega' t_2}.$$

Since the input is assumed to be a stationary random process, it follows that

$$\overline{\phi_0(w) \phi_0(w')} = S(w) \delta(w + w')$$

where $S(w)$ is the power spectral density of the source. Consequently

$$\overline{\phi_s(\mathbf{r}, t_1) \phi_s(\mathbf{r}, t_2)} = \int_{-\infty}^{\infty} \overline{H(-w | t_1) H(w | t_2)} S(w) e^{-j\omega(t_2 - t_1)} dw. \quad (24)$$

The correlation function of the received signal is then given by

$$\Psi_R(\mathbf{r}, t_2 - t_1) = \Psi_0(\mathbf{r}, \tau) + \overline{\phi_s(\mathbf{r}, t_1) \phi_s(\mathbf{r}, t_2)}. \quad (25)$$

The power spectral density of the received signal which follows directly is

$$S(\mathbf{r}, w) = \frac{1}{2\pi} \int_{-\infty}^{\infty} \Psi_R(\mathbf{r}, t_2 - t_1) e^{j\omega(t_2 - t_1)} d(t_2 - t_1). \quad (26)$$

FIDELITY OF THE RECEIVED SIGNAL

One useful measure of signal distortion resulting from scattering is the fidelity of the received signal in a mean-squared sense. This is defined as^{7,8}

$$v^2 \equiv \overline{\{\phi_0(\mathbf{r}, t) - \phi_R(\mathbf{r}, t)\}^2}.$$

Since $\phi_R = \phi_0 + \phi_s$, it follows that

$$v^2 = \overline{\phi_s(\mathbf{r}, t)^2}.$$

Using (24) it follows that the mean-squared error of the received signal is given by

$$v^2 = \int_{-\infty}^{\infty} \overline{H(-w | t_1) H(w | t_1)} S(w) dw. \quad (27)$$

⁷ Claude E. Shannon, "The Mathematical Theory of Communication," University of Illinois Press, Urbana, Ill., p. 76; 1949.

⁸ Note that the fidelity may be time dependent when the random dielectric noise is not stationary. This definition of fidelity is not useful in the study of beyond-the-horizon scatter propagation since $\phi_0 = 0$.

FIDELITY OF A BAND-LIMITED LONG LINE-OF-SIGHT RADIO LINK

As an illustrative example of the result it is of interest to consider the special case of a band-limited long line-of-sight radio link. The result can be used as a measure of system reliability as a function of bandwidth.

We might expect the fidelity of a system to increase with increasing bandwidth. This in effect would place an upper bound on useful bandwidth given a bound on fidelity as determined by permissible receiver error and the power of the source. Consider the geometry of Fig. 3.

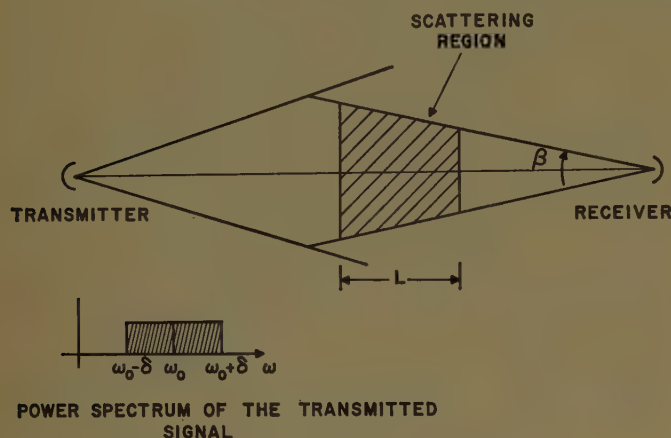


Fig. 3.

Substituting for $H(w, t)$ in (27) from (24),

$$v^2 = \frac{\mu^2}{16\pi^2 R_0^2 R^2} \int_{-\infty}^{\infty} S(w) w^4 dw \int dv_1' \int dv_2' \cdot \overline{\Delta\epsilon(\mathbf{r}_1', t_1) \Delta\epsilon(\mathbf{r}_2', t_1)} \epsilon^{iK \cdot (\mathbf{r}_2' - \mathbf{r}_1')} \quad (28)$$

$$K = (k_0 - k_s),$$

where the far field approximation has been used.

$$\frac{\epsilon^{ikR}}{R} \cong \frac{\epsilon^{ik_s r}}{r} \epsilon^{-ik_s \cdot r'}.$$

In order to apply some of the proposed forms for the correlation function of the dielectric noise, it is convenient to assume an isotropic turbulence. This results in the usual cross-section approximation and (28) reduces to

$$v = \frac{1}{R_0^2 R^2} \int_{-\infty}^{\infty} S(w) dw \int_{v'} \frac{\sigma(K)}{r'^2} dv'. \quad (29)$$

For the geometry of Fig. 3, the exponential space-correlation function for the dielectric noise given by⁹

$$\overline{\Delta\epsilon(\mathbf{r}_1, t) \Delta\epsilon(\mathbf{r}_2, t)} = \overline{\Delta\epsilon^2} \epsilon^{-|r_{12}|/l_0}$$

⁹ A. D. Wheelon and R. B. Muchmore, "Line of sight propagation phenomena—I Ray treatment," "Line of sight propagation phenomena—II Scattered components," A. D. Wheelon, "Near field corrections to line of sight propagation," *Proc. IRE*, vol. 43, pp. 1437-1466; October, 1955.

results in a fidelity of¹⁰

$$v^2 = \frac{l_0}{\pi} \frac{\overline{\Delta\epsilon^2}}{\epsilon_0^2} L \left(\frac{w_0}{c} \right)^2 \delta, \quad (30)$$

where

w_0 —carrier frequency; $w_0 \gg \delta$

2δ —bandwidth.

The Gaussian correlation function given by⁹

$$\overline{\Delta\epsilon(\mathbf{r}, t) \Delta\epsilon(\mathbf{r}_2, t)} = \overline{\Delta\epsilon^2} \epsilon^{-r_{12}^2/l_0}$$

results in a fidelity of

$$v^2 = \frac{l_0}{2\sqrt{\pi}} \frac{\overline{\Delta\epsilon^2}}{\epsilon_0} L \left(\frac{w_0}{c} \right)^2 \delta. \quad (31)$$

The above assumes that the receiving antenna beam-width

$$\beta > 10 \left(\frac{c}{w_0 l_0} \right),$$

a condition met in most experimental efforts. It should be noted that the two results differ by a small constant.

$$\frac{\overline{v^2} \text{ Gaussian}}{\overline{v^2} \text{ Exponential}} = 1.13.$$

MAXIMUM POSSIBLE RATE OF THE SOURCE

Since the fidelity of the received signal is a function of bandwidth, we would expect the rate of a source to be somehow limited by the fidelity, bandwidth, and source power. Shannon⁷ has shown that the rate of a white noise source of average power Q and bandwidth W relative to a root-mean-square measure of fidelity is

$$R = W \log \frac{Q}{N} \quad (32)$$

where N = maximum permissible mean-squared error.

The fidelity of a band-limited long line-of-sight link as given by (30) or (31) assume a source of average power,

$$Q = \int_0^\infty S(w) dw = 2\delta.$$

Substituting for N and W in (32), we have for the exponential correlation function,

$$R = 2\delta \log_2 \left\{ \frac{2\pi}{l_0} \frac{\epsilon_0^2}{\overline{\Delta\epsilon^2}} \left(\frac{c}{w_0} \right)^2 L^{-1} \right\} \text{ bits/second.} \quad (33)$$

For the Gaussian correlation function we have

$$R = 2\delta \log_2 \left\{ \frac{4\sqrt{\pi}}{l_0} \frac{\epsilon_0^2}{\overline{\Delta\epsilon^2}} \left(\frac{c}{w_0} \right)^2 L^{-1} \right\} \text{ bits/second.} \quad (34)$$

¹⁰ This assumes that the size L of the scattering volume V is then a mean free path. D. S. Bugnolo, "Fidelity of a Communication System Affected by Atmospheric Turbulence," *Tech. Rep. T-2/c*, Columbia University, New York, N. Y.; October, 1958.

As a particular example consider the case where

$$\begin{aligned} l_0 &= 10 \text{ m}; & w_0 &= 2 \times 10^8. \\ L &= 10^5 \text{ m}; \\ \frac{\Delta \epsilon^2}{\epsilon_0^2} &= 10^{-10} \end{aligned}$$

$$R \cong 21 \text{ bits/second/cycle.}$$

It should be noted that the Rate is *independent* of the source power! This result will of course be modified by the presence of noise.

To further illustrate this example consider a teletype channel. Since each symbol contains 5 bits of information, it follows that rate of the source could be at the most 4.2 symbols per second, for each cycle of bandwidth. This is an upper bound that could not be reached in practice since the conditions used by Shannon to derive (32) are not really satisfied in practice.

It is also of interest to note that if a television source is assumed to have ten possible transitions from white to black, then the rate of the source is approximately 5 bits/second/cycle of bandwidth. This implies that the capacity of a television channel over a long line-of-sight path of about 100 miles is more likely to be limited by noise than dielectric turbulence. It would appear that this condition is met in practice.

APPENDIX

The general analysis developed in this paper for the special case of a scalar wave equation can be extended to the general-vector wave equation for the electric field intensity. When the Fourier transformations are approximated in a manner similar to (14) and (15), the vector wave equation for the E , (2) reduces to

$$\begin{aligned} \nabla \times \nabla \times E_s(r, w | t) + w^2 \mu \epsilon_0(t) E_s \\ = -w^2 \mu \Delta \epsilon(r, t) E_0(r, w). \end{aligned} \quad (35)$$

It should be stressed that the Fourier transform is time dependent.

If the incident field is assumed plane in the scattering region, then the first Born Approximation for the scattered E is

$$E_s(r, w | t) = \mu w^2 \int_{v'} \Delta \epsilon(r', t) \epsilon^{jk \cdot r'} G(r, r', w) \cdot E_0(w) dv' \quad (36)$$

where

$$E_0(r', t) = \int_{-\infty}^{\infty} E_0(w) \epsilon^{-j(wt - k \cdot r')} dw.$$

The inverse transformation yields the time response.

$$E_s(r, t) = \int_{-\infty}^{\infty} E_s(r, w | t) \epsilon^{-jw t} dw. \quad (37)$$

Let the transfer tensor $H(r, w | t)$ be defined by

$$H(r, w | t) \equiv \frac{\mu w^2}{4\pi} \int_{v'} \Delta \epsilon(r', t) \epsilon^{jk \cdot r'} G(r, r', w) dv'. \quad (38)$$

It then follows that

$$E_s(r, w | t) = H(r, w | t) \cdot E_0(w).$$

From this it is evident that the scattered signal can be regarded as the output of a time-variable linear system characterized by the transfer tensor $H(r, w | t)$.

$$E_0(r, t) \rightarrow \boxed{H(r, w | t)} \rightarrow E_s(r, t)$$

where

$$E_s(r, t) = \int_{-\infty}^{\infty} H(r, w | t) \cdot E_0(w) \epsilon^{-jw t} dw. \quad (39)$$

The correlation function of the scattered component of the electric field intensity must in general contain auto as well as cross-correlation components. By following a procedure similar to that for the scalar wave equation, it is possible to show that

$$\begin{aligned} \overline{E_i(r, t_1) E_m(r, t_2)} \\ = \sum_{p, n} \int_{-\infty}^{\infty} H_{ip}(w | t_1) H_{mn}(-w | t_2) S_{pn}(w) \epsilon^{-jw(t_2 - t_1)} dw \end{aligned} \quad (40)$$

where $S_{pn}(w)$ is the auto or cross-power spectral density of the incident electric field intensity. The Green's function suitable for the above result is the usual¹¹

$$G(r, r', w) \cong \left(I - \frac{\nabla \nabla'}{k^2} \right) \frac{\epsilon^{-jk|r-r'|}}{4\pi|r-r'|} \quad (41)$$

where I is the unit dyadic. Using the above Green's function, the Fernel approximation for the correlation of the scattered component of the electric field intensity can be shown to be

$$\begin{aligned} \overline{E_i(r, t_1) E_m(r, t_2)} &= \frac{\mu^2}{16\pi^2} \sum_{p, n} \int_{-\infty}^{\infty} dw S_{pn}(w) \epsilon^{-jw(t_2 - t_1)} \\ &\cdot w^4 \int dv_1' \int dv_2' (\delta_{ip} - h_i h_p) (\delta_{mn} - k_m k_n) \\ &\quad \overline{\Delta \epsilon(r_1', t_1) \Delta \epsilon(r_2', t_2) \epsilon^{jK \cdot (r_2' - r_1')}}. \end{aligned} \quad (42)$$

For the special case of a stationary dielectric noise, the above result can be simplified by taking $t_2 = t_1 + \tau$.

¹¹ S. Stein, "Some observations on scattering by turbulent inhomogeneities," IRE TRANS. ON ANTENNAS AND PROPAGATION, vol. AP-6, pp. 299-300; July, 1958.

Aperture-to-Medium Coupling on Line-of-Sight Paths: Fresnel Scattering*

E. LEVIN†, R. B. MUCHMORE‡, AND A. D. WHEELON‡

Summary—An electromagnetic signal propagated through a medium of randomly varying dielectric exhibits random-phase fluctuations. The phase of the total signal is the average of all rays which strike the reflector and is therefore smoothed by a receiver-reflector combination of finite aperture. This paper presents a theoretical analysis and numerical results for this phase-smoothing for small phase perturbations. The receiver is assumed to be a circular parabolic reflector with a collecting feed at the focus. The propagation is described by Fresnel scattering and the one dimensional ray theoretical expressions employed. Closed form results are obtained for three separate space correlation models of the random dielectric medium. These results are valid so long as the scattering parameter $L\lambda_0^{-2}$ is small.

INTRODUCTION

THE stochastic variations of an electromagnetic signal caused by propagation through a medium of randomly varying dielectric have been studied in several recent papers.¹⁻⁵ An infinitesimal receiver was assumed in these studies, so that only the electromagnetic field at a point was computed. Actual experiments, however, employ receiver-reflector combinations of finite aperture, for which it is necessary to consider medium-to-receiver coupling.⁶ This effect is most important for large apertures, and is of considerable interest in the estimation of resolution for large radio telescopes.

We consider a plane-wave incident on a semi-infinite dielectric medium with a receiver located at a depth L below the upper boundary. The analysis is directly applicable to the scintillation of radio stars imposed by the troposphere, but is also similar to the "radio relay link" problem in which a transmitter and receiver are both immersed in an infinite turbulent medium a distance L apart. The radio star problem discussed here is decidedly easier to analyze. This paper presents a theoretical analysis of the phase variations induced in a receiver by the essential coupling between the propagation medium and the receiver.

* Manuscript received by the PGAP, July 10, 1958; revised manuscript received December 9, 1958.

† Rand Corp., Santa Monica, Calif.

‡ Space Tech. Labs., Inc., Los Angeles, Calif.

¹ R. B. Muchmore and A. D. Wheelon, "Line-of-sight propagation phenomena—I. Ray treatment," *PROC. IRE*, vol. 43, pp. 1437-1449; October, 1955.

² A. D. Wheelon and R. B. Muchmore, "Line-of-sight propagation phenomena—II. Scattered components," *PROC. IRE*, vol. 43, pp. 1450-1458; October, 1955.

³ B. M. Fannin, "Line-of-sight wave propagation in a randomly inhomogeneous medium," *IRE TRANS. ON ANTENNAS AND PROPAGATION*, vol. AP-4, pp. 661-665; October, 1956.

⁴ D. Mintzer, "Wave propagation in a randomly inhomogeneous medium, I," *J. Acous. Soc. Am.*, vol. 25, p. 922; September, 1953.

⁵ A. D. Wheelon, "Near-field corrections to line-of-sight propagation," *PROC. IRE*, vol. 43, pp. 1459-1466; October, 1955.

⁶ C. M. Angulo and J. P. Ruina, "Antenna resolution as limited by atmospheric turbulence," presented at URSI, May, 1957.

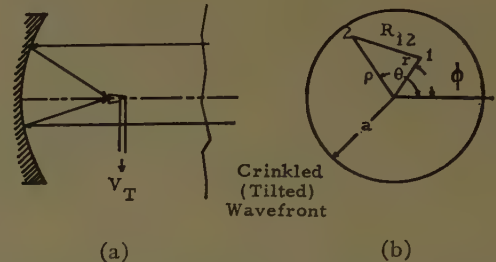


Fig. 1—(a) Receiver-reflector feed arrangement. (b) Geometry and co-ordinate system of reflector.

The receiver is assumed to be a circular parabolic reflector with a collecting feed at the focus, as shown in Fig. 1. This is the configuration most often used in experiments and also leads to significant analytical simplifications. Other reflectors can be treated by extensions of our method. Closed-form expressions for the phase-smoothing effect due to the finite aperture are derived for three stochastic models of the dielectric medium.

FRESNEL SCATTERING IN THE MEDIUM

The random atmosphere is characterized by a time and space varying dielectric constant:

$$\epsilon(\vec{r}, t) = \epsilon_0 + \Delta\epsilon(\vec{r}, t) \quad (1)$$

where ϵ_0 is the free space value, and $\Delta\epsilon$ is a small stochastic fluctuation. The fluctuations give rise to both phase and amplitude variations of the received signal. It is usually assumed that the dielectric fluctuations form a zero mean random process in space and time. For a stationary and homogeneous process, the space correlation is given by

$$\langle \Delta\epsilon(\vec{r}, t) \Delta\epsilon(\vec{r} + \vec{R}, t) \rangle = \langle \Delta\epsilon^2 \rangle C(\vec{R}/l_0). \quad (2)$$

The irregularities are very weak since the root mean square dielectric fluctuation at a point, $[\langle \Delta\epsilon^2 \rangle]^{1/2}$, is measured experimentally as about $10^{-6}\epsilon_0$. This paper assumes that the irregularities are isotropic, and the space correlation function therefore depends only on the magnitude of the separation distance $|\vec{R}|$. The correlation function $C(\vec{R}/l_0)$ is the critical assumption for propagation studies. Three analytical models are used in the discussion which follows:

1) Exponential:

$$C(R/l_0) = e^{-R/l_0}$$

2) Bessel:

$$= \frac{R}{l_0} K_1\left(\frac{R}{l_0}\right)$$

TABLE I
MEAN SQUARE PHASE AND PHASE CORRELATION BETWEEN PARALLEL RAYS FOR THREE TURBULENCE MODELS

$C(R/l_0)$	e^{-R/l_0}	$\frac{R}{l_0} K_1\left(\frac{R}{l_0}\right)$	e^{-R^2/l_0^2}
$\langle \alpha^2 \rangle$	$2\pi^2 \langle \Delta \epsilon^2 \rangle \frac{Ll_0}{\lambda^2}$	$\pi^2 \langle \Delta \epsilon^2 \rangle \frac{Ll_0}{\lambda^2}$	$\pi^{5/2} \langle \Delta \epsilon^2 \rangle \frac{Ll_0}{\lambda^2}$
$Q(D/l_0) = \frac{\langle \alpha(x)\alpha(x+D) \rangle}{\langle \alpha^2 \rangle}$	$\frac{D}{l_0} K_1\left(\frac{D}{l_0}\right)$	$\left[1 + \frac{D}{l_0}\right] e^{-D/l_0}$	e^{-D^2/l_0^2}

3) Gaussian:

$$= e^{-R^2/l_0^2}. \quad (3)$$

The correlation falls to about $1/e$ in a distance $R=l_0$ in each case. l_0 is called the scale of turbulence and is measured as several hundred feet in the troposphere.

The equation for electromagnetic propagation through a random medium characterized by (1) is

$$\{\nabla^2 + k^2[\epsilon_0 + \Delta\epsilon(\mathbf{r}, t)]\} \vec{E}(\mathbf{r}, t) = 0. \quad (4)$$

The problem is to solve this partial differential equation for a random fluctuation $\Delta\epsilon$, so as to exhibit the phase and amplitude variations induced in the electric field E . This is a purely mathematical problem which has not been solved exactly and approximate methods must be used.

We assume that the induced signal variations are very small compared with the mean (unperturbed) amplitude and phase. Within this restriction, however, there are two distinct scattering regimes: Fresnel and Fraunhofer. They are distinguished by the magnitude of the "scattering parameter,"

$$\eta = \frac{L\lambda}{l_0^2}, \quad (5)$$

where L is the length of the propagation path and λ the wavelength of the radiation. If this parameter is less than unity, the radiation propagates as though through a sequence of random laminae "cored" from the spherical blobs. This is called Fresnel scattering and is described by the geometrical optics approximation. When the scattering parameter η is greater than unity, one must recognize the three dimensional nature of the scattering and the projection of energy into the receiver by off-axis blobs. This is called Fraunhofer scattering and is described by the Born (iterative) approximation to the wave (4), which contains the Fresnel results as a special case.

This study works exclusively with the Fresnel approximation. The energy which falls on the receiver is thus propagated along nearly parallel rays and a WKB solution of the one dimensional form of the wave (4) is equivalent to the geometrical optics result. The phase variation induced along a ray path (x) by the refractive changes of the wave's phase speed becomes,

$$\alpha = \frac{\pi}{\lambda} \int_0^L dx \Delta\epsilon(x, t). \quad (6)$$

The mean square phase and phase correlation between adjacent *parallel* rays for our three models are summarized in Table I.¹ These results are derived by the methods of Muchmore and Wheelon.¹

The Fresnel approximation also implies amplitude fluctuations for the incoming wave. Physically, these amplitude changes are due to the random bunching and separation of the energy-bearing rays which are caused in turn by random refractive bending. Such effects are of minor importance unless the scattering parameter (5) is greater than one. The ratio of the instantaneous amplitude variance δE to the mean amplitude E_0 is^{7,8}

$$\frac{\delta E}{E_0} = -\frac{\lambda}{4\pi} \int_0^L dx \nabla_n^2 \alpha(x, y, z). \quad (7)$$

The second derivatives here suggest that amplitude variations are very sensitive to the shape of the correlation function $C(R)$ near the origin. Of the three models considered, only the Gaussian correlations predict a finite mean square amplitude variation (see Appendix I). The result for $L \gg l_0$ is

$$\left\langle \left| \frac{\delta E}{E_0} \right|^2 \right\rangle = \langle \Delta \epsilon^2 \rangle L^3 / l_0^3. \quad (8)$$

If this result is compared with the mean square phase expressions in Table I, one finds that

$$\left\langle \left| \frac{\delta E}{E_0} \right|^2 \right\rangle = \frac{1}{\pi^{5/2}} \langle \alpha^2 \rangle \eta^2 \ll \langle \alpha^2 \rangle. \quad (9)$$

Percentile amplitude variations are thus much smaller than the mean square phase in the Fresnel region,¹⁰ and will be neglected.

⁷ V. A. Krasil'nikov, "The effect of variations of the coefficient of refraction in the atmosphere upon the propagation of ultrashort radio waves," *Izv. Ak. Nauk U.S.S.R.*, vol. 13, pp. 33-57; 1949.

⁸ P. G. Bergman, "Propagation of radiation in a medium with random inhomogeneities," *Phys. Rev.*, vol. 70, pp. 486-492; October, 1946. A closely related development is presented.

⁹ ∇_n^2 is the Laplacian taken normal to the ray path x :

$$\nabla_n^2 = \frac{\partial^2}{\partial y^2} + \frac{\partial^2}{\partial z^2}.$$

¹⁰ They are equal in the Fraunhofer region.

PHASE SMOOTHING

We have noted that the Fresnel approximation describes energy propagated along nearly parallel rays. The rays have slightly different phase shifts imposed on them, however, since each has traversed a different (somewhat uncorrelated) *sequence* of blobs. This lack of phase correlation over the wave front causes the phase front to be randomly "crinkled" or tilted as shown in Fig. 1. The wavefront is described as tilted or "crinkled" depending on whether the scale of phase coherence is greater or less than the reflector radius ($l_0 \lesseqgtr a$) respectively. When this energy is focused to the receiver feed, there is a gross addition of the phase shifts of all rays which strike the reflector. The total phase shift α_T induced on the receiver voltage is an average over the aperture of these individual variations.

$$\alpha_T = \frac{1}{A} \iint_A d\sigma \alpha(\sigma). \quad (10)$$

This expression may also be established by using the reciprocity between the aperture illumination function $G(\sigma)$ and the complex field which falls on the reflector element $d\sigma$.

$$G(\sigma) = [E_0 + \delta E(\sigma)] e^{i[\mu(\sigma) + \alpha(\sigma)]}. \quad (11)$$

If the receiver uses a circular paraboloid with the feed at the focus, the phase delay between any plane normal to the x axis and the feed is a constant.

$$\mu(\sigma) = \frac{2\pi}{\lambda} 2 \text{ (focal distance)} = \text{constant.}$$

The amplitude illumination function E_0 is also assumed constant and the total field induced in the feed is given by a summation over the aperture in a geometric optics approximation. (The validity of this approximation is discussed by Silver.¹¹ It should be quite good for $a \gg \lambda$.)

$$\begin{aligned} E_T e^{i(\mu + \alpha_T)} &= \frac{1}{A} \iint_A d\sigma G(\sigma) \\ &= E_0 e^{i\mu} \frac{1}{A} \iint_A d\sigma \int \left[1 + \frac{\delta E(\sigma)}{E_0} \right] e^{i\alpha(\sigma)}. \end{aligned} \quad (12)$$

Since the phase variation must be much less than one radian for our original approximations to hold, the total phase (10) may be identified immediately by expanding both the exponentials to first order and taking the imaginary part of both sides.

The mean square total phase shift is computed by squaring (10) and inserting the parallel ray phase correlation results from Table I.

$$\begin{aligned} \langle \alpha_T^2 \rangle &= \frac{1}{A^2} \iint_A d\sigma_1 \iint_A d\sigma_2 \langle \alpha(\sigma_1) \alpha(\sigma_2) \rangle \\ &= \frac{\langle \alpha^2 \rangle}{A^2} \iint_A d\sigma_1 \iint_A d\sigma_2 Q(R_{12}/l_0). \end{aligned}$$

The area integrals over the circular reflector are conveniently expressed in terms of the polar coordinates shown in Fig. 1.

$$\langle \alpha_T^2 \rangle = \frac{\langle \alpha^2 \rangle}{\pi^2 a^4} \int_0^a dr r \int_0^{2\pi} d\phi \int_0^a d\rho \rho \int_0^{2\pi} d\theta Q \left(\frac{[r^2 + \rho^2 - 2r\rho \cos(\phi - \theta)]^{1/2}}{l_0} \right). \quad (13)$$

It was found that the complicated integral (13) could be evaluated exactly for each of the three models in Table I.

It is convenient to describe the extent of phase smoothing in terms of the ratio of the total mean square measured with a finite aperture to that which would be measured with a point receiver. Letting $r = ax$ and $\rho = ay$ in (13), one finds that

$$\frac{\langle \alpha_T^2 \rangle}{\langle \alpha^2 \rangle} = F \left(\frac{a}{l_0} \right) = \frac{1}{\pi^2} \int_0^1 dx x \int_0^1 dy y \int_0^{2\pi} d\phi \int_0^{2\pi} d\theta Q \left(\frac{a}{l_0} [x^2 + y^2 - 2xy \cos(\phi - \theta)]^{1/2} \right), \quad (14)$$

which depends only on the ratio of the dish radius to the scale length of the irregularities. The analytical results given below are derived in Appendix II.

1) Exponential Model:

$$F(t) = \frac{8K_1(t)I_2(t)}{t} \quad (15)$$

2) Bessel Model:

$$F(t) = \frac{1}{t^2} \left\{ \frac{16t}{\pi} + 6 + 24[I_0(2t) - L_0(2t)] - 2 \frac{(15 + 4t^2)}{t} [I_1(2t) - L_1(2t)] \right\} \quad (16)$$

3) Gaussian Model:

$$F(t) = \frac{1}{t^2} - \frac{e^{-2t^2}}{t^2} [I_0(2t^2) + I_1(2t^2)]. \quad (17)$$

$I_\mu(z)$ and $K_\mu(z)$ are modified Bessel functions of the first and second kind respectively, and $L_\mu(z)$ is the modified Struve function.

The results in Fig. 2 show that there is very little phase smoothing unless the dish radius is larger than the scale length of the turbulent irregularities ($a/l_0 > 1$). The effect of small scale irregularities is therefore smoothed by large apertures since they average over

¹¹ S. Silver, "Microwave Antenna Theory and Design," McGraw-Hill Book Co., Inc., New York, N. Y., 1949.

many such blobs.¹² The differences between these curves are probably not significant, since l_0 itself is experimentally uncertain to within a factor of two. If one turbulence model is to be favored, it should probably be the Bessel model which is derivable from the physical theory of mixing-in-gradient.^{13,14}

If the scattering parameter η in (5) is greater than one, amplitude fluctuations δE affect the phase smoothing process through (12). The phase variations also cause detuning of the reflector-feed combination, which induces amplitude fluctuations in the total signal by changing the receiver gain randomly. This problem is intrinsically more complicated, both in the propagation and signal statistical descriptions, and will be discussed in a later communication.

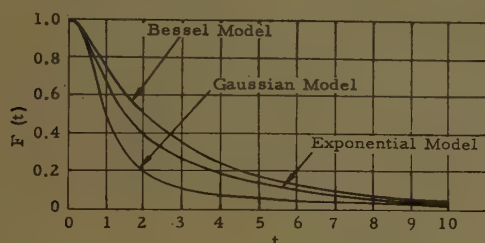


Fig. 2—Relative phase smoothing for a) Exponential model, b) Bessel model, and c) Gaussian model.

APPENDIX I

It has been shown by Krasil'nikov⁷ that (in our notation) the mean square fractional variation in amplitude is given by

$$\left\langle \left| \frac{\delta E}{E} \right|^2 \right\rangle = \frac{1}{8} \int_0^L dx \int_0^L dx' (L-x)(L-x') \left[\frac{\partial^4 C(R/l_0)}{\partial v^4} - \frac{\partial^4 C(R/l_0)}{\partial v^2 \partial^2 w} \right] \quad (18)$$

where u, v, w are the components of \vec{R} , i.e.,

$$\begin{aligned} u &= x - x' \\ v &= y - y' \\ w &= z - z' \\ R^2 &= u^2 + v^2 + w^2. \end{aligned} \quad (19)$$

A quick examination of the models presented in Table I for $C(R/l_0)$ shows that at the origin only the Gaussian model possesses the necessary derivatives. Thus, only this model will yield a finite value in (18) above. This

¹² A. D. Wheelon, "Relation of radio measurements to the spectrum of tropospheric dielectric fluctuations," *J. Appl. Phys.*, vol. 28, pp. 684-693; June, 1957. Actual smoothing may be somewhat less than is indicated by (14) and Fig. 2 because most antennas in practice will have tapered illumination to at least some degree.

¹³ A. D. Wheelon, "Spectrum of turbulent fluctuations produced by convective mixing of gradients," *Phys. Rev.*, vol. 105, pp. 1706-1710; March 15, 1957.

¹⁴ F. Villars and V. F. Weisskopf, "On the scattering of radio waves by turbulent fluctuations of the atmosphere," *PROC. IRE*, vol. 43, pp. 1232-1239; October, 1955.

does not mean that the other models are not useful in predicting phase effects; the deficiency in the model in the vicinity of the origin appears in an insignificant way in the phase results.

APPENDIX II

It is of some interest to note briefly how the exact integration of expression (14) was performed, since the method is applicable to other models which may come into favor. In (14) let $(\theta - \phi) = \psi$ and recognize the symmetry in xy to obtain

$$F(t) = \frac{8}{\pi} \int_0^1 x dx \int_0^x y dy \int_0^\pi d\psi Q \{ t \sqrt{x^2 + y^2 - 2xy \cos \psi} \}. \quad (20)$$

Let $y = \rho x$, and then transform the last two integrals (ρ, ψ) into rectangular coordinates (z, v) .

$$F(t) = \frac{8}{\pi} \int_0^1 x^3 dx \int_{-1}^1 dz \int_0^{\sqrt{1-z^2}} dv Q \{ tx \sqrt{(1-z)^2 + v^2} \}. \quad (21)$$

Now set $v = (1-z)w$ and reverse the order of integration in the (w, z) plane.

$$F(t) = \frac{8}{\pi} \int_0^1 x^3 dx \int_0^\infty dw \int_{w^2-1/w^2+1}^1 dz (1-z) Q \{ tx(1-z)\sqrt{1+w^2} \}. \quad (22)$$

Substituting $m = x(1-z)\sqrt{1+w^2}$ and $w = \tan \theta$, we find

$$F(t) = \frac{8}{\pi} \int_0^1 x dx \int_0^{\pi/2} d\theta \int_0^{2x \cos \theta} m dm Q \{ tm \}. \quad (23)$$

Transform (x, θ) into rectangular coordinates (s, p)

$$F(t) = \frac{8}{\pi} \int_0^1 \sqrt{1-s^2} ds \int_0^{2s} m dm Q \{ tm \}. \quad (24)$$

It is possible to reduce this to a single integral by a further change of order, but the final steps are easier to perform starting from (24).

Case I. Exponential Model: $Q \{ tm \} = tm K_1(tm)$

Since $K_0' = -K_1$

$$\begin{aligned} F(t) &= -\frac{8t}{\pi} \frac{d}{dt} \int_0^1 \sqrt{1-s^2} ds \int_0^{2s} m dm K_0(tm) \\ &= \frac{8t}{\pi} \frac{d}{dt} \frac{1}{t^2} \int_0^1 \sqrt{1-s^2} ds [2ts K_1(2ts) - 1] \\ &= \frac{4}{t^2} - \frac{8t}{\pi} \frac{d}{dt} \frac{1}{t} \frac{d}{dt} \int_0^{\pi/2} \sin^2 \theta K_0(2t \cos \theta) d\theta \\ &= \frac{4}{t^2} - 2t \frac{d}{dt} \frac{1}{t} \frac{d}{dt} [I_0(t) K_0(t) + I_1(t) K_1(t)]^{15} \end{aligned}$$

¹⁵ G. N. Watson, "A Treatise on the Theory of Bessel Functions," Cambridge University Press, Cambridge, Eng., 2nd ed., p. 441; 1952.

or finally,

$$F(t) = \frac{8K_1(t)I_2(t)}{t}.$$

Case II. Bessel Model: $Q\{tm\} = (1+tm)e^{-tm}$

$$\begin{aligned} F(t) &= -\frac{8}{\pi} \left[1 - t \frac{d}{dt} \right] \frac{d}{dt} \int_0^1 \sqrt{1-s^2} ds \int_0^{2s} e^{-tm} dm, \\ &= -\frac{8}{\pi} \left[1 - t \frac{d}{dt} \right] \frac{d}{dt} \int_0^{\pi/2} \sin^2 \theta d\theta \left[\frac{1}{t} - \frac{e^{-t \cos \theta}}{t} \right], \\ &= -\frac{8}{\pi} \left[1 - t \frac{d}{dt} \right] \frac{d}{dt} \left\{ \frac{\pi}{4t} - \frac{\pi}{4t^2} [I_1(2t) - L_1(2t)] \right\}^{16} \end{aligned}$$

or finally,

¹⁶ *Ibid.*, p. 425.

$$F(t) = \frac{1}{t^2} \left\{ \frac{16t}{\pi} + 6 + 24[I_0(2t) - L_0(2t)] - \frac{30 + 8t^2}{t} [I_1(2t) - L_1(2t)] \right\}.$$

Case III. Gaussian Model: $Q\{tm\} = e^{-t^2 m^2}$

$$\begin{aligned} F(t) &= \frac{8}{\pi} \int_0^1 \sqrt{1-s^2} ds \int_0^{2s} m dm e^{-t^2 m^2}, \\ &= \frac{1}{t^2} - \frac{4}{\pi t^2} \int_0^{\pi/2} \cos^2 \theta e^{-4t^2 \sin^2 \theta} d\theta, \\ &= \frac{1}{t^2} - \frac{e^{-2t^2}}{\pi t^2} \int_0^\pi (1 + \cos \phi) e^{-2t^2 \cos \phi} d\phi, \end{aligned}$$

and finally,

$$F(t) = \frac{1}{t^2} - \frac{e^{-2t^2}}{t^2} [I_0(2t^2) + I_1(2t^2)].$$

The Inverse Scattering Problem in Geometrical Optics and the Design of Reflectors*

JOSEPH B. KELLER†

Summary—The inverse scattering problem considered here is that of finding the shape of a reflector which produces a prescribed scattered wave. The scattered wave is characterized by its angular pattern, which determines the differential scattering cross section of the reflector. The problem is solved by means of explicit formulas for cylindrical and for rotationally symmetric objects. Plane, cylindrical, and spherical incident waves are considered. The general three dimensional object is also treated. The method of geometrical optics is used throughout.

INTRODUCTION

WHEN radiation of any type is incident upon an object, some of the radiation is scattered in all directions by the object. The direct problem of the theory of scattering is that of determining the intensity of the radiation scattered in each direction when the properties of the incident radiation as well as those of the object are known. The inverse scattering problem is that of determining the properties of the scattering object when the incident radiation and the intensity of the radiation scattered in each direction are known. This latter problem has been studied extensively in

atomic and nuclear physics by the methods of quantum mechanics and, to some extent by classical mechanics. [1] The classical mechanical solution is also applicable to the scattering of light (or other radiation obeying the laws of geometrical optics) by a region in which the index of refraction varies in any continuous spherically symmetric manner. We now propose to consider the inverse problem in geometrical optics when the scatterer is an opaque object, such as a piece of metal, with a definite boundary. We will call an object of this type a reflector or mirror.

In the two dimensional case, which we treat first, the scattered wave is cylindrical. Its intensity in the direction θ is denoted by $\sigma(\theta)$. When the incident radiation is a plane wave of unit amplitude, $\sigma(\theta)$ is called the differential scattering cross section of the reflector. We then find that the shape of the reflector is completely determined if $\sigma(\theta)$ and the reflection coefficient of the reflector are given. However the reflector may be placed so that either its concave or convex side is exposed to the incident radiation. When the incident radiation is a cylindrical wave, a one parameter family of different reflectors is found. In both cases, formulas for the shape of the reflector are obtained in terms of $\sigma(\theta)$. Similar results are obtained for reflectors which are surfaces of revolution in three dimensions, when the incident radia-

* Manuscript received by the PGAP, April 29, 1958. The research reported in this document has been sponsored by the Air Force Cambridge Research Center, Air Res. and Dev. Command, under Contract No. AF19(604)1717.

† Inst. of Math. Sciences, New York Univ., New York, N. Y.

tion is either a plane wave incident along the axis of revolution or a spherical wave from a point source on this axis.

In the general three dimensional case, the differential scattering cross section $\sigma(\theta, \phi)$ and the reflection coefficient of the surface do not determine the shape of the reflector at all. However, if the differential scattering cross section is known for two plane waves incident from opposite directions, and if the reflection coefficient is also known, then the reflector is uniquely determined, provided that it is convex. But in this case, it has not been possible to determine the shape explicitly. Instead, a nonlinear partial differential equation must be solved to find the shape.

Our investigation was pursued not only because of its intrinsic interest, but also because the results may be of use in the design of optical systems containing reflectors. This, as well as most design problems, may profitably be viewed as an inverse problem. For purposes of comparison, we have also included some well-known results on the direct problem.

S. N. Karp has also treated certain inverse scattering problems for reflectors without restriction to the realm in which geometrical optics is valid.

FORMULATION AND SOLUTION

In geometrical optics, light propagates along rays which, in a homogeneous medium, are straight lines. Therefore, by conservation of energy, in a non-absorbing medium, the flux of energy is the same through every cross section of each tube of rays. This flux is proportional to the light intensity I multiplied by the cross sectional area of the tube. In a cylindrical wave, a tube of angular width $d\theta$ has a cross section of length $rd\theta$ so energy conservation yields $Ird\theta = \sigma d\theta$ where σ is constant along the tube. Thus $I = \sigma(\theta)/r$. Here σ is written as $\sigma(\theta)$ since it may vary from one tube to another. Now suppose the cylindrical wave is produced by reflection from a reflector of an incident plane wave of unit intensity propagating from the left parallel to the x -axis. (See Fig. 1.) Suppose the ray at height y is reflected in the direction θ , and that at height $y+dy$, is reflected in the direction $\theta+d\theta$. Let the energy reflection coefficient be R . Then of the incident energy between the two rays, which is proportional to dy , the fraction Rdy is reflected into the tube between the rays in the directions θ and $\theta+d\theta$. Thus by the conservation of energy

$$Rdy = \pm \sigma(\theta)d\theta. \quad (1)$$

The sign in (1) must be chosen the same as that of $dy/d\theta$.

The reflection coefficient R may not be a constant, but may be a function of the angle of incidence. This angle is just $\theta/2$ since the normal to the reflector at each point bisects the angle between the incident and reflected rays at this point. Thus in (1), $R = R(\theta/2)$. If y and x are coordinates of a point on the reflector surface, then the slope of the normal also leads to

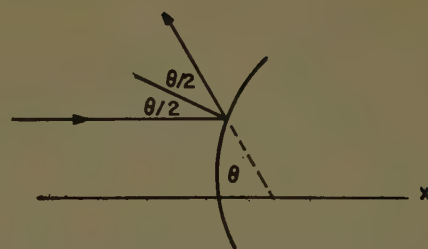


Fig. 1—Incident and reflected rays both making the angle $\theta/2$ with the normal to the reflector. The reflected ray makes the angle θ with the negative x -axis, along which the incident rays are incident. If the reflector is a surface of revolution, the figure represents a cross section containing the axis of revolution.

$$\frac{dy}{dx} = \cot \frac{\theta}{2}. \quad (2)$$

Eqs. (1) and (2) enable us to solve the inverse problem of finding the reflector shape in terms of $\sigma(\theta)$ and $R(\theta/2)$. For integrating (1) yields

$$y = y_0 \pm \int_0^\theta \frac{\sigma(\theta)}{R(\theta/2)} d\theta. \quad (3)$$

Elimination of dy from (1) and (2) and integration of the result also gives

$$x = x_0 \pm \int_0^\theta \frac{\sigma(\theta) \tan \frac{\theta}{2}}{R(\theta/2)} d\theta. \quad (4)$$

Eqs. (3) and (4) are parametric equations for the reflector and thus provide the solution of the inverse problem. The integration constants x_0 and y_0 determine the location of the reflector. The sign, which must be the same in both equations, determines whether the reflector is convex (+) or concave (−) toward the incident wave. In the concave case, the specified $\sigma(\theta)$ is obtained only for a limited range of θ due to blocking of the reflected rays by the reflector itself.

As an example of the use of (3) and (4), let us suppose that

$$\sigma(\theta) = \frac{b}{2} R\left(\frac{\theta}{2}\right) \cos \frac{\theta}{2}. \quad (5)$$

Here b is a constant. Now (3) and (4) yield

$$x = x_0 \pm b \left[1 - \cos \frac{\theta}{2} \right], \quad (6)$$

$$y = y_0 \pm b \sin \frac{\theta}{2}. \quad (7)$$

These are the equations of a circle of radius b centered at $x_0 \pm b, y_0$. (See Fig. 2)

As a second example, let a be a constant and suppose that

$$\sigma(\theta) = \frac{aR}{2}. \quad (8)$$

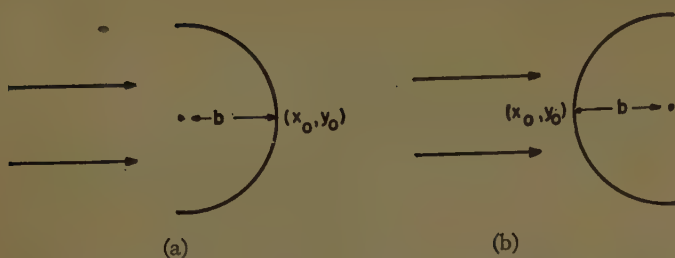


Fig. 2—A semicircular reflector of radius b which is either concave (a) or convex (b) to the incident wave. In both cases the differential scattering cross section is the same, being given by (5).

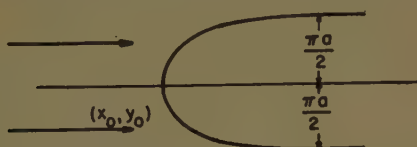


Fig. 3—An isotropic scatterer given by (9) and (10) with the upper sign. If the reflection coefficient R is constant, this reflector has the constant differential cross section $\sigma = aR/2$. Its width is asymptotically πa .

If R is constant, then σ is independent of θ and the corresponding reflector is an isotropic scatterer. From (3) and (4), its equations are

$$x = x_0 \mp a \log \cos \frac{\theta}{2}, \quad (9)$$

$$y = y_0 \pm \frac{a\theta}{2}. \quad (10)$$

In Fig. 3, this reflector is drawn, using (9) and (10) with the upper sign.

Eq. (1) can also be used to solve the direct problem of scattering. If $b(\theta/2)$ denotes the radius of curvature of the reflector at the point where its normal points in the direction $\theta/2$, then simple geometry shows that

$$\frac{dy}{d\theta} = \frac{1}{2} b(\theta/2) \cos \frac{\theta}{2}. \quad (11)$$

When (11) is used in (1), the result is

$$\sigma(\theta) = \frac{1}{2} R \left(\frac{\theta}{2} \right) b \left(\frac{\theta}{2} \right) \cos \frac{\theta}{2}. \quad (12)$$

This is the solution of the direct problem. It can be used in solving the inverse problem, but the method used above is simpler.

OTHER CASES

By exactly the same methods as those used above, we have also considered the direct and inverse problems for three other cases. These are the two dimensional case with an incident field due to a line source and the three dimensional case of a reflecting surface of revolution with a plane wave incident along the axis of revolution or with a point source located on this axis. The notation in the plane wave case is the same as in Fig. 1 except that r is used instead of y and z instead of x . For the line and point source cases, the notation is explained in Fig. 4. In these cases, ϕ denotes the angle of incidence

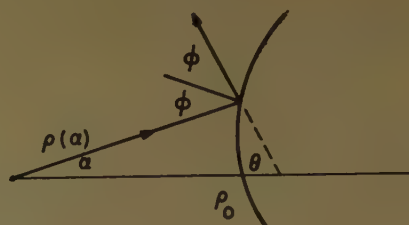


Fig. 4—An incident ray making the angle α with the x or z axis and the angle ϕ with the normal to the reflector. The reflected ray also makes the angle ϕ with the normal and the angle θ with the axis. The distance from the source to the reflector is $\rho(\alpha)$, and $\rho(0)$ is also denoted by ρ_0 .

and of reflection and α denotes the angle between the incident ray and the axis. These angles are related to θ by

$$\theta = 2\phi - \alpha. \quad (13)$$

The intensity on each incident ray is denoted by $I(\alpha)$, and the equation of the reflector is written as $\rho = \rho(\alpha)$ where the source is the origin. The results are given in Table I.

As an example, let us consider the two-dimensional case in which the field comes from a line source. Suppose that σ , I , and R are constants and $\theta_0 = 0$. Then, from the table we have

$$\pm \sigma \theta = IR\alpha, \quad (14)$$

$$\rho = \rho_0 \left[\cos \left\{ \left(1 \pm \frac{IR}{\sigma} \right) \frac{\alpha}{2} \right\} \right]^{-2(1 \pm (IR/\sigma))^{-1}}. \quad (15)$$

Eq. (15) is the polar equation of the reflector. If the positive sign is taken and if $IR = \sigma$, then it is the equation of a plane at distance ρ_0 from the source.

In the three dimensional case with rotational symmetry and a plane wave incident along the axis, let us seek a reflector for which σ and R are constants. From the table, we find for its equation

$$r^2 = \frac{4\sigma}{R} \sin^2 \frac{\theta}{2}, \quad (16)$$

$$z = z_0 \pm 2\sqrt{\sigma/R} \left(1 - \cos \frac{\theta}{2} \right). \quad (17)$$

This is the equation of a sphere of radius $2\sqrt{\sigma/R}$ centered at $r=0$, $z=z_0 \pm 2\sqrt{\sigma/R}$. Thus, we find the well-known result that the sphere is an isotropic scatterer—in fact, in this case, the only one.

THE GENERAL CASE

Suppose the reflector is an arbitrary smooth convex closed surface in three dimensional space. Let $\sigma(\theta, \phi)$ denote its differential scattering cross section in the direction θ, ϕ due to a plane wave of unit intensity incident from the left along the x -axis. Let $P(\theta, \phi)$ be the point on the reflector from which a ray is reflected in the θ, ϕ direction. Then the normal at $P(\theta, \phi)$ must point in the direction $\theta/2, \phi$ and the angle of incidence at P must be $\theta/2$. These facts follow from the law of reflection. Now

TABLE I

Results for Inverse Scattering Two Dimensions, Line Source	
	$\pm \sigma(\theta) d\theta = R(\phi) I(\alpha) d\alpha$ $\rho^{-1} \frac{d\rho}{d\alpha} = \tan \frac{\alpha + \theta}{2}$
If $R = \text{constant}$	$\pm \int_{\theta_0}^{\theta} \sigma(\theta) d\theta = R \int_0^{\alpha} I(\alpha) d\alpha$ $\log \rho/\rho_0 = \int_0^{\alpha} \tan \frac{\alpha + \theta(\alpha)}{2} d\alpha$
Rotational Symmetry, Plane Wave	
	$\sigma(\theta) \sin \theta d\theta = R \left(\frac{\theta}{2} \right) r dr$ $\frac{dr}{dz} = \pm \cot \frac{\theta}{2}$
If $R = \text{constant}$	$r^2 = \frac{2}{R} \int_0^{\theta} \sigma(\theta) \sin \theta d\theta$ $z = z_0 + \frac{1}{R} \int_0^{\theta} \frac{\sigma(\theta)}{r(\theta)} \sin \theta \tan \frac{\theta}{2} d\theta$
Rotational Symmetry, Point Source	
	$\pm \sigma(\theta) \sin \theta d\theta = R(\phi) I(\alpha) \sin \alpha d\alpha$ $\rho^{-1} \frac{d\rho}{d\alpha} = \tan \frac{\alpha + \theta(\alpha)}{2}$
If $R = \text{constant}$	$\pm \int_{\theta_0}^{\theta} \sigma(\theta) \sin \theta d\theta = R \int_0^{\alpha} I(\alpha) \sin \alpha d\alpha$ $\log \rho/\rho_0 = \int_0^{\alpha} \tan \frac{\alpha + \theta(\alpha)}{2} d\alpha$
Results for Direct Scattering Two Dimensions, Line Source	
	$\sigma(\theta) = R(\phi) I(\alpha) \left[\frac{2\rho(\alpha)}{b(\alpha) \cos \phi} + 1 \right]^{-1}$
Rotational Symmetry, Plane Wave	
	$\sigma(\theta) = \frac{r(\theta/2)}{2 \sin \theta} R(\theta/2) b(\theta/2) \cos \theta/2$
Rotational Symmetry, Point Source	
	$\sigma(\theta) = \frac{\sin \alpha}{2 \sin \theta} R(\phi) I(\alpha) \left[\frac{2\rho(\alpha)}{b(\alpha) \cos \phi} + 1 \right]^{-1}$

It is well known that the differential scattering cross section in the direction of any reflected ray is equal to $R/4G$ where G is the Gaussian curvature at the point of reflection. Therefore, we have

$$\sigma(\theta, \phi) = \frac{R \left(\frac{\theta}{2} \right)}{4G \left(\frac{\theta}{2}, \phi \right)} \quad (18)$$

Let us make use of (18) to analyze the inverse problem. We see that when σ and R are known for all values of their arguments, the Gaussian curvature G is determined over the hemisphere $0 \leq \theta < \pi/2$ of the unit sphere. This unit sphere, each point of which corresponds to the direction of the normal at one point on the reflector surface, is called the spherical image of that surface. The problem of determining a surface when its Gaussian curvature is given on the entire surface of the spherical image is known as Minkowski's problem [3]. It has one and only one solution for any sufficiently smooth positive function $G(\theta, \phi)$ which satisfies the condition

$$\int G^{-1}(\theta, \phi) \vec{n}(\theta, \phi) d\Omega = 0. \quad (19)$$

Here $\vec{n}(\theta, \phi)$ is the unit normal at the point θ, ϕ ; $d\Omega$ is the element of area of the unit sphere, and the integration extends over the whole sphere. Thus for any arbitrary [subject to (19)] smooth continuation over the rest of the sphere of the function G given on half the sphere by (18), there is exactly one reflector. The reflector shape is determined by the solution of an elliptic partial differential equation involving G . Therefore, we may conclude that the shape of all parts of the reflector are effected by the arbitrary continuation of G . Consequently, the data provided by (18) do not suffice to determine the shape of the reflector nor any part of it. The inverse problem has too large a family of solutions.

Suppose, however, that two functions $\sigma_+(\theta, \phi)$ and $\sigma_-(\theta, \phi)$ are given, corresponding to two different incident waves coming from opposite directions. If R is also known, then (18) determines G over the whole sphere. If this G satisfies (19)—as it must if it actually corresponds to a surface—then the inverse problem has a unique solution. The calculation of this solution, in the general case, requires the solution of an elliptic partial differential equation. In the cases treated in the previous sections, this equation could be reduced to an ordinary differential equation. This explains why explicit solutions could be obtained in those cases.

REFERENCES

- [1] J. B. Keller, I. Kay, and J. Shmoys, "Determination of the potential from scattering data," *Phys. Rev.*, vol. 102, pp. 557-559; April, 1956. The procedure of Keller, Kay, and Shmoys requires the determination of $\theta(b)$ from $\sigma(\theta)$, which is possible if and only if at most one trajectory is scattered in each direction. Then $V(r)$ is found from $\theta(b)$ provided that $[1 - E^{-1}V(r)]r^2$ is a monotone increasing function of r for $r \geq r_{\min}(E)$. Monotonicity is required to permit the change of integration variable from u in (3) to w in (5). It also ensures that there are no bounded orbits in the region $r \geq r_{\min}(E)$, while without monotonicity there are such orbits. Thus $\theta(b)$ at energy E determines $V(r)$ for $r \geq r_{\min}(E)$ provided that there are no bound states at energy E in the region $r \geq r_{\min}(E)$. If there is such a bound state, this method does not work, and it seems that it can be modified to show that $V(r)$ is then not uniquely determined by $\theta(b)$.
- [2] S. Silver, ed., "Microwave Antenna Theory and Design," Rad. Lab. Series No. 12, McGraw-Hill Book Co., Inc., New York, N. Y., pp. 497-500; 1949. In this reference, it is not made clear that the constant K is actually the reflection coefficient R .
- [3] L. Nirenberg, "The Weyl and Minkowski problems in differential geometry on the large," *Comm. Pure and Appl. Math.*, vol. 6, pp. 337-394; August, 1953.

On Scattering by Large Conducting Bodies*

ROGER F. HARRINGTON†

Summary—Two sets of sources, equivalent in the sense that they produce the same field as does an illuminated conductor, are discussed. Both representations are suggestive of approximation. Crude approximations are made, yielding what are called "the physical optics solution," and the "image induction solution." It is shown that these two solutions are reciprocal to each other. This means that, given a source and an observer, the solution by one method is equal to the solution by the other method with the source and observer interchanged. Both solutions are amenable to further refinement if more accurate solutions are desired.

INTRODUCTION

THIS paper is concerned primarily with two approximate solutions to problems of electromagnetic wave scattering by large conducting obstacles. One of these, the physical optics solution, has received considerable attention in the literature.¹ The other, stemming from an application of the induction theorem,² appears to have been overlooked. These two solutions are of the same order of approximation, and are in a sense complementary to each other.

Let us consider first the exact equivalences from which our approximations originate. Fig. 1(a) represents a conducting body illuminated by an electromagnetic source. Let the total field \mathbf{E} , \mathbf{H} be expressed as the sum of an incident field \mathbf{E}^i , \mathbf{H}^i , equal to that of the source with the conductor absent, plus a scattered field \mathbf{E}^s , \mathbf{H}^s , produced by the currents on the conductor. If the conductor is perfect, these are surface currents given by

$$\mathbf{J} = \mathbf{n} \times \mathbf{H} \quad (1)$$

as illustrated by Fig. 1(b). Schelkunoff's induction theorem applied to a perfectly conducting body states that the magnetic surface currents

$$\mathbf{K} = \mathbf{n} \times \mathbf{E}^i \quad (2)$$

with the conductor retained, also produce the scattered field \mathbf{E}^s , \mathbf{H}^s . This is illustrated by Fig. 1(c). We say that the two source systems of Figs. 1(b) and 1(c) are equivalent in the region external to the obstacle boundary, for they produce the same field in this region. We shall call Fig. 1(b) the *physical equivalent*, and Fig. 1(c) the *induction equivalent*.

A short discussion of these two equivalences is in order. In the physical equivalent, we have the unknown current of (1) radiating into unbounded free space, producing a field \mathbf{E}^s , \mathbf{H}^s external to S and a field $-\mathbf{E}^i$, $-\mathbf{H}^i$

internal to S . We can immediately construct the potential integral solution

$$\nabla \times \iint_S \mathbf{J} \frac{e^{-jkr}}{4\pi r} ds = \begin{cases} \mathbf{H}^s & \text{external to } S. \\ -\mathbf{H}^i & \text{internal to } S. \end{cases} \quad (3)$$

If we knew the current, we could determine the scattered field. An exact determination of \mathbf{J} requires the solution to the original boundary-value problem, Fig. 1(a). In the induction equivalent, we have the known currents of (2) radiating in the presence of the conductor. Let $[\Gamma]$ be the tensor of proportionality between an element of current on the conductor and the \mathbf{H} field it produces, that is,

$$d\mathbf{H} = [\Gamma]d\mathbf{K}. \quad (4)$$

The total scattered field is then simply an integration over the partial fields, or

$$\mathbf{H}^s = \iint_S [\Gamma] \mathbf{K} ds. \quad (5)$$

If we knew $[\Gamma]$, we could determine the scattered field. The exact determination of $[\Gamma]$ requires the solution to a boundary-value problem of the same (or greater) complexity as the original boundary-value problem, Fig. 1(a).

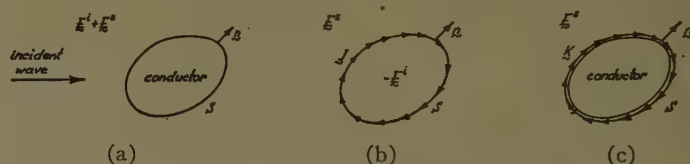


Fig. 1—(a) Original problem, (b) physical equivalent, (c) induction equivalent.

APPROXIMATIONS

Our solutions so far are exact. If the exact solution is desired, the equivalent problems of Figs. 1(b) and 1(c) represent no advantage over the original problem of Fig. 1(a). The value of the equivalent problems lies in the approximations that they suggest. We shall in this paper discuss only the crudest type of approximations.

The *physical optics solution* involves the following approximation for \mathbf{J} in Fig. 1(b) and in the corresponding (3). For a large obstacle having large (with respect to wavelength) radius of convex curvature, the illuminated portion of the conductor is similar to a large plane reflector. The tangential components of magnetic intensity at an infinitely conducting ground plane are exactly twice those from the same source in unbounded space (recall image theory). Using this knowledge, we approximate (1) by

$$\mathbf{J} = 2\mathbf{n} \times \mathbf{H}^i \quad (6)$$

* Manuscript received by the PGAP, June 16, 1958.

† Dept. of Elec. Engrg., Syracuse University, Syracuse, N. Y.

¹ J. R. Mentzer, "Scattering and Diffraction of Radio Waves," Pergamon Press, New York, N. Y.; 1955.

² S. A. Schelkunoff, "Electromagnetic Waves," D. Van Nostrand Co., New York, N. Y., p. 158; 1943.

over the illuminated portion of S . In other words, (3) reduces to

$$\mathbf{H}^s = \nabla \times \iint_{S'} \frac{e^{-ikr}}{2\pi r} ds \times \mathbf{H}^i \quad (7)$$

where S' is the illuminated portion of S . Further refinements in approximating J can be made if desired.

The corresponding approximation in the induction equivalent problem, Fig. 1(c), leads to what we shall call the *image induction solution*. Again we assume large obstacles of small convex curvature to approximate a plane reflector. The field of each element of \mathbf{K} on S is then approximated by the field of a magnetic dipole adjacent to an infinite ground plane. According to image theory, this field is the same as that from a magnetic dipole of twice the moment radiating into unbounded free space. This applies only in front of the ground plane, the field being zero behind the ground plane. Thus, in the image induction solution, we take the field of each element of \mathbf{K} to be that of $2\mathbf{K}$ in free space if \mathbf{K} is seen from the observation point, and zero when not seen. In other words, we approximate (5) by

$$\mathbf{H}^s = \frac{1}{j\omega\mu} \nabla \times \nabla \times \iint_{S''} \frac{e^{-ikr}}{2\pi r} ds \times \mathbf{E}^i \quad (8)$$

where S'' is the portion of S seen from the observation point. Further refinements in approximating $[\Gamma]$ can be made if desired.

A pictorial representation of the above approximate solutions is given in Fig. 2. The general problem is represented by Fig. 2(a). It consists of a source producing the incident field, a conducting obstacle producing the scattered field, and an observer representing the point at which the field is to be evaluated. In the physical optics solution, Fig. 2(b), the currents of (6) exist only over S' (illuminated by the source) and radiate into unbounded free space. In the image induction solution, Fig. 2(c), the net effect of our approximations is that double the currents of (2) exist over S'' (seen by the observer) and radiate into unbounded free space.

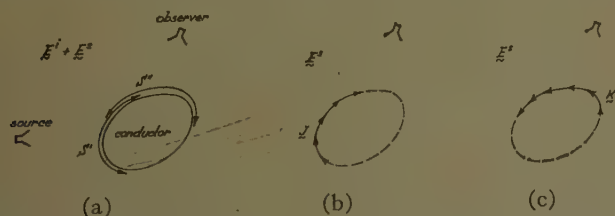


Fig. 2—(a) Original problem, (b) physical optics approximation, (c) image induction approximation.

RECIPROCITY

An exact solution to the scattering problem satisfies the reciprocity theorem.³ The approximate solutions (physical optics and image induction) do not, in general,

³ V. H. Rumsey, "The Reaction Concept in Electromagnetic Theory," *Phys. Rev.*, vol. 94, p. 1483; June 15, 1954.

satisfy the reciprocity theorem. There is, however, an interesting reciprocity relationship existing between the physical optics and image induction solutions.

A general statement of reciprocity in terms of electric and magnetic sources is

$$\int (\mathbf{E}_1 \cdot d\mathbf{J}_2 - \mathbf{H}_1 \cdot d\mathbf{K}_2) = \int (\mathbf{E}_2 \cdot d\mathbf{J}_1 - \mathbf{H}_2 \cdot d\mathbf{K}_1) \quad (9)$$

where \mathbf{E}_i , \mathbf{H}_i is the field of \mathbf{J}_i , \mathbf{K}_i . In the problem of Fig. 2(a), visualize a set of terminals (1) at the source and a set of terminals (2) at the receiver. If unit electric currents are impressed across both these terminals, (9) reduces to

$$V_{12} = V_{21}, \text{ or } V_{12}^i + V_{12}^s = V_{21}^i + V_{21}^s \quad (10)$$

where V_{ij} represents the voltage at terminals i due to the unit current at terminals j . The superscripts i and s refer to incident and scattered components. Since $V_{12}^i = V_{21}^i$ by reciprocity, the second equation of (10) reduces to

$$V_{12}^s = V_{21}^s \quad (11)$$

Thus, in the exact solution, the scattered field received remains unchanged when source and observer are interchanged. Eq. (11) does *not* apply when the physical optics method is used to evaluate both V 's, or when the image induction method is used to evaluate both V 's.

Now suppose that we evaluate V_{21}^s by the physical optics method, and V_{12}^s by the image induction method. By (9), applied to the problem of Fig. 2(b), we have

$$\begin{aligned} (V_{21}^s)_{\text{phys. opt.}} &= \iint_S \mathbf{E}_2^i \cdot \mathbf{J}_1 ds \\ &= 2 \iint_{S'} \mathbf{E}_2^i \cdot \mathbf{n} \times \mathbf{H}_1^i ds \end{aligned} \quad (12)$$

where the last equality makes use of (6). The problem to be evaluated by the image induction method is reciprocal to that of Fig. 2(c); that is, source and observer are interchanged and \mathbf{K} exists over S' . We then have by (9)

$$\begin{aligned} (V_{12}^s)_{\text{im. ind.}} &= - \iint_S \mathbf{H}_1 \cdot \mathbf{K}_2 ds \\ &= - 2 \iint_{S'} \mathbf{H}_1^i \cdot \mathbf{n} \times \mathbf{E}_2^i ds \end{aligned} \quad (13)$$

where the last equality stems from (8). A comparison of (12) and (13) shows that

$$(V_{12}^s)_{\text{im. ind.}} = (V_{21}^s)_{\text{phys. opt.}} \quad (14)$$

Thus, an evaluation of the scattered field by the physical optics method is equivalent to an evaluation of the scattered field of the reciprocal problem by the image induction method, and vice versa. If we are interested only in back scattering (radar echoes), the two methods give exactly the same answer. In this case, the source and observer coincide and the reciprocal problem is the same as the original problem.

The equivalence of back scattering for the two methods, and the reciprocity relationship of differential scattering, can be illustrated pictorially. In Fig. 3(a) we represent an element of the scatterer and an incident plane wave. The current element of the physical optics solution corresponding to this element of scatterer is shown in Fig. 3(b). The current element of the image induction solution, with its image taken into account, is shown in Fig. 3(c). Let the fields be normalized so that η (intrinsic impedance) is unity, and $E^i = H^i$. Then the magnitudes of K and J are in the ratio $\sin \theta$. But the radiation pattern of K is different from that of J , as shown in Figs. 3(b) and 3(c). The field radiated back from J is $\sin \theta$ times its maximum radiated field, while that from K is equal to its maximum. These two effects just compensate one another, so that J and K radiate equal fields in the back direction. For an incident plane wave of polarization orthogonal to that of Fig. 3(a), the magnitudes, directions, and patterns of J and K are essentially reversed, giving no net change in the results. The picture for differential scattering is a little more complicated, but can be constructed by similar reasoning. If the incident field is not a plane wave, and if the observer is not distant from the scatterer, a simple picture of the type of Fig. 3 would not be possible. We must then rely upon the mathematics to assure us of the reciprocity relationship of (14).

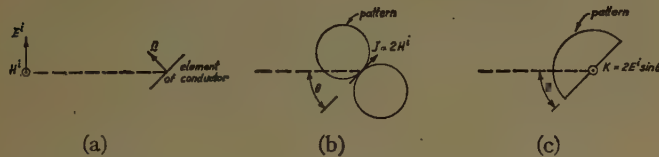


Fig. 3—(a) Incident field and element of scatterer, (b) current element of physical optics method, (c) current element of image induction method.

AN EXAMPLE

To illustrate the concepts of this paper, let us consider an example for which the exact, physical optics, and image induction solutions can readily be obtained. In particular, take the case of a semi-infinite ground plane illuminated by a plane wave, as illustrated by Fig. 4(a). Let the incident wave be specified by

$$H_y^i = e^{jk(x \sin \theta_0 + z \cos \theta_0)}. \quad (15)$$

The exact solution for the distant scattered field can be obtained by the Wiener-Hopf method,⁴ and is

$$H_y^s \xrightarrow[kp \rightarrow \infty]{} C(kp) \frac{2 \sin(\theta_0/2) \sin(\theta/2)}{\cos \theta_0 + \cos \theta} \quad (16)$$

where

$$C(kp) = \frac{e^{-ikp}}{\sqrt{2j\pi kp}}. \quad (17)$$

⁴ E. T. Copson, "On an integral equation arising in the theory of diffraction," *Quart. J. of Math.*, Oxford Series, vol. 17, pp. 19-26; January, 1946.

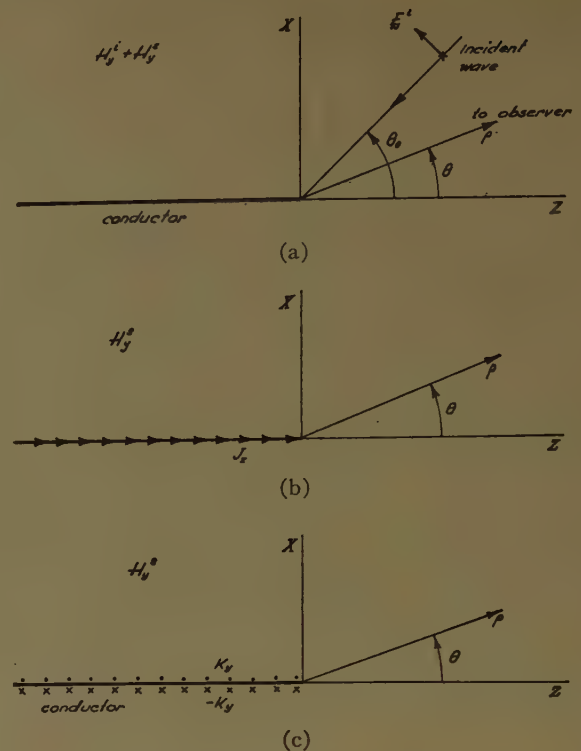


Fig. 4—(a) Plane wave incident upon a conducting half-plane, (b) physical equivalent, (c) induction equivalent.

The physical equivalent for the scattered field is shown in Fig. 4(b). Using the physical optics approximation for J_z , we find

$$(H_y^s)_{\text{phys. opt.}} \xrightarrow[kp \rightarrow \infty]{} C(kp) \frac{\sin \theta}{\cos \theta_0 + \cos \theta}. \quad (18)$$

The induction equivalent for the scattered field is shown in Fig. 4(c). Imaging K_y whenever it can be seen by the observer, we have for the image induction method

$$(H_y^s)_{\text{im. ind.}} \xrightarrow[kp \rightarrow \infty]{} C(kp) \frac{\sin \theta_0}{\cos \theta_0 + \cos \theta}. \quad (19)$$

Eqs. (18) and (19) were obtained by the usual vector potential method.

For the above example, note that, a) The exact solution obeys reciprocity; b) the physical optics solution and the image induction solution do not individually obey reciprocity; c) the physical optics solution and the image induction solution are reciprocal to each other; d) the physical optics solution and the image induction solution give the same back-scattered field. It should be expected that both the physical optics method and the image induction method converge to the exact solution for a large smooth obstacle. They do not for the half-plane example of Fig. 4 because of the sharp edge at $z=0$. Note that they do, however, approach the exact back scattering as $\theta = \theta_0 \rightarrow 90^\circ$. This is to be expected, for at this aspect all J_z in Fig. 4(b) and all K_y in Fig. 4(c) radiate in phase, masking the contributions from elements near the sharp edge.

CONCLUSIONS

Two equivalent sources for the field scattered by a conducting obstacle have been discussed. These can be summarized as follows: a) The physical equivalent, which results in a known formula for the scattered field in terms of unknown currents; b) the induction equivalent, which results in an unknown formula for the scattered field in terms of known currents. Both representations are suggestive of approximation. In the first, we can approximate the currents. The crudest approximation, (6), yields the physical optics solution. In the second, we can approximate the field of the currents. The crudest approximation, that of using image theory,

yields the image induction solution. Further refinements of approximation can be made in either solution. The theory can be extended to imperfect conductors or to dielectrics, but it becomes more difficult to formulate valid approximations.

If one is interested only in the crude approximations of physical optics and image induction, then there is no need to solve a given problem by both methods. They must always give the same back scattering and reciprocal differential scattering. However, as further approximations are made, this reciprocity relationship no longer applies. One should then use whichever method results in the best approximation for an allowable degree of complexity.

Asymmetrical Trough Waveguide Antennas*

W. ROTMAN† AND A. A. OLINER‡

Summary—Line source radiators of the leaky wave type may be constructed readily with trough waveguide, which consists of a rectangular trough containing a symmetrically located center fin. Two types of such radiators are investigated: a continuously asymmetrical form suitable for near endfire radiation, and a periodically asymmetrical design permitting radiation through broadside. The propagation characteristics of the leaky wave on the continuously asymmetrical structure are determined theoretically by means of a transverse resonance procedure, and comparison is made with measured values. The influence of finite center fin thickness is also accounted for. Designs and radiation patterns are presented for a typical antenna of each type.

I. INTRODUCTION

SINCE the properties of a microwave linear antenna array are strongly influenced by the transmission line on which the radiators are located, the transmission line is a logical starting point for building new types of line sources. The trough waveguide, shown in Fig. 1, has several interesting characteristics. This symmetrical structure is mechanically open on one side, yet is a nonradiating transmission line. It combines the mechanical simplicity of a strip transmission line with the frequency characteristics of a waveguide. It can be coupled smoothly to a coaxial line. Its bandwidth for single-mode propagation is greater than that for rectangular waveguide by a factor of about $3/2$. These advantages, in addition to simple means of obtaining con-

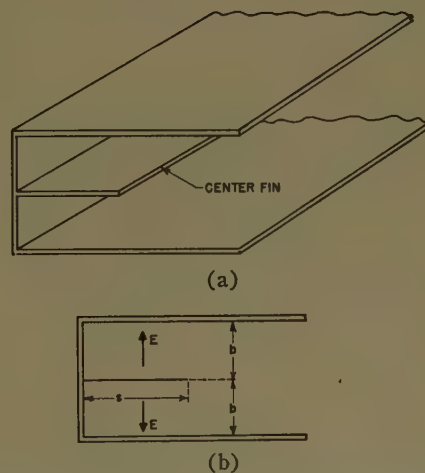


Fig. 1—Symmetrical trough waveguide, (a) full view, (b) cross-section view for zero-thickness center fin.

trolled radiation by a controlled asymmetry in the trough structure, have stimulated interest in trough-guide antennas.¹

The present paper describes two types of troughguide antennas for fixed beam systems. One of these antennas is based on a continuously asymmetrical trough waveguide, while the other is a periodically asymmetrical array. Design procedures are presented for both types of antennas together with experimental results, which include the radiation patterns of typical structures. This

* Manuscript received by the PGAP, June 30, 1958.

† Air Force Cambridge Res. Center, H. G. Hanscom Field, Bedford, Mass.

‡ Microwave Res. Inst., Polytech. Inst. Brooklyn, Brooklyn, N. Y.

¹ W. Rotman and N. Karas, "Some new microwave antenna designs based on the trough waveguide," 1956 IRE CONVENTION RECORD, pt. 1, pp. 230-235.

design discussion is presented in Section VI. The sections preceding it are devoted to theoretical material and to direct experimental checks on the theory. Section II reviews the theory for the cutoff wavelength of symmetrical trough waveguide, which is a nonradiating line. Section III presents a theoretical analysis of the propagation and radiation characteristics of continuously asymmetrical trough waveguide, while in Section IV these theoretical results are compared with measured values. In Section V the effect of finite center fin thickness on both the symmetrical and asymmetrical trough waveguides is considered, and comparison with measurement is presented for the symmetrical case. The measured results in both Sections IV and V show good agreement with the corresponding theoretical values.

When the trough waveguide is made asymmetrical in a continuous fashion, the bound mode of the guide is changed into a leaky wave and radiation is produced all along the length of the guide. This leaky wave is similar in character to that produced in rectangular waveguide by a continuous slit, say, in one of the narrow walls. The wave can be described by a complex propagation constant which is determined, in Section III, by means of a transverse resonance procedure. The resulting transverse resonance relation, which is a complex transcendental equation, is solved by a perturbation technique to obtain expressions for the attenuation and phase constants in simple and practical form.

Since the continuously asymmetrical trough waveguide is a continuous line source antenna, its radiation is restricted primarily to the near endfire direction. By introducing the asymmetry in a periodic fashion which includes a phase reversal between successive asymmetrical elements, this limitation is overcome and beams at any angle can be obtained. A practical means for accomplishing this is discussed in Section VI. It is also shown that the method described permits operation even through broadside without pattern or impedance deterioration.

II. SYMMETRICAL TROUGH WAVEGUIDE: THEORY

The geometry of symmetrical trough waveguide is shown in Fig. 1. By virtue of the symmetry, it is a nonradiating structure. It is derived from symmetrical strip transmission line by placing a short-circuiting plate at the midplane of the latter.^{2,3} For this reason, the dominant mode in trough waveguide is identical with the first higher mode in the strip transmission line.

In view of the relation between strip transmission line and trough waveguide, the cutoff wavelength for the dominant mode in trough guide is obtained directly from that for the first higher mode in strip transmission line upon appropriate change in notation. One then finds

that for zero-thickness center strips the cutoff wavelength λ_{co} is given by the transcendental relation⁴

$$\frac{\lambda_{co}}{4b} = \frac{s}{b} + \frac{2}{\pi} \ln 2 + \frac{\lambda_{co}}{2\pi b} S_1\left(\frac{4b}{\lambda_{co}}; 0, 0\right) - \frac{\lambda_{co}}{\pi b} S_1\left(\frac{2b}{\lambda_{co}}; 0, 0\right), \quad (1)$$

where S_1 is the rapidly convergent arcsine sum

$$S_1(x; 0, 0) = \sum_{n=1}^{\infty} \left(\sin^{-1} \frac{x}{n} - \frac{x}{n} \right). \quad (2)$$

Dimensions b and s are indicated in Fig. 1; the subscript o on the cutoff wavelength signifies the nonradiating case. Eq. (1) is arranged as shown because the arcsine sum contributions are not major, although significant; in employing (1) for computational purposes one should solve for s/b for values of b/λ_{co} . The variation of $\lambda_{co}/2b$ with s/b is presented as the solid line of Fig. 2.

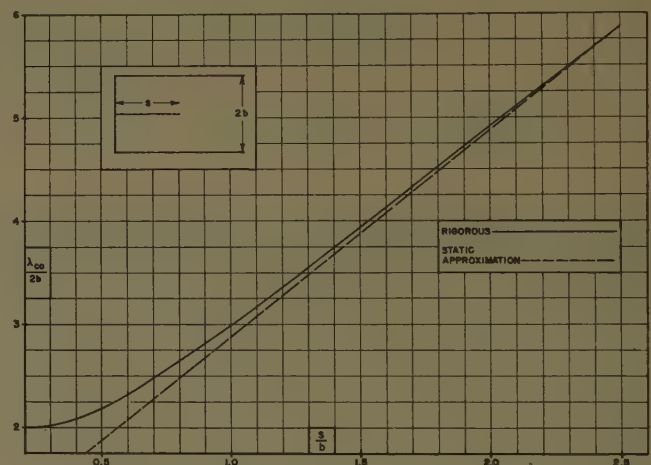


Fig. 2—Cutoff wavelength of dominant mode in symmetrical trough waveguide.

When the arcsine sums are neglected, the dashed line of Fig. 1 is obtained. The latter is useful as an approximate formula, particularly in the range of s/b large. The error in the use of the approximate form is less than 3 per cent for $s/b > 1$.

Eq. (1) is valid for center strips of zero thickness. An approximate procedure for determining the effect on λ_{co} of finite center strip thickness is presented in Section V.

III. LEAKY WAVES ON ASYMMETRICAL TROUGH WAVEGUIDE: THEORY

A. Description of Structure

One method of producing an asymmetry which is continuous along the length of the trough waveguide is to make the two halves of the guide of different widths, as

² Airborne Instruments Lab., Advertisement on Trough Waveguide, *Proc. IRE*, vol. 44, p. 2A; August, 1956.

³ H. S. Keen, "Scientific Report on Study of Strip Transmission Lines," Airborne Instruments Lab., Rep. No. 2830-2 on AFRCR Contract No. AF19(604)-708; December 1, 1955.

⁴ A. A. Oliner, "Theoretical developments in symmetrical strip transmission line," *Proc. Symp. on Modern Advances in Microwave Techniques*, Polytech. Inst. Brooklyn, pp. 387-390; November, 1954.

shown in Fig. 3. Such asymmetry produces a leaky wave, resulting in a beam radiated at some angle determined by the wavelength and the geometry.

The leaky wave obtained from this guide is similar in nature to those produced by rectangular waveguides containing, for example, a continuous slit or a series of holes in one of the narrow walls.⁵ The wave is characterized by a complex propagation constant down the guide, wherein the attenuation constant is a measure of the power radiated per unit length along the guide. The angle of maximum radiation is then given approximately, when the attenuation constant α is small, by

$$\sin \theta \cong \lambda / \lambda_0, \quad (3)$$

where θ is the angle between the emerging beam and the normal to the guide axis, and λ and λ_0 are the free space and guide wavelengths, respectively.

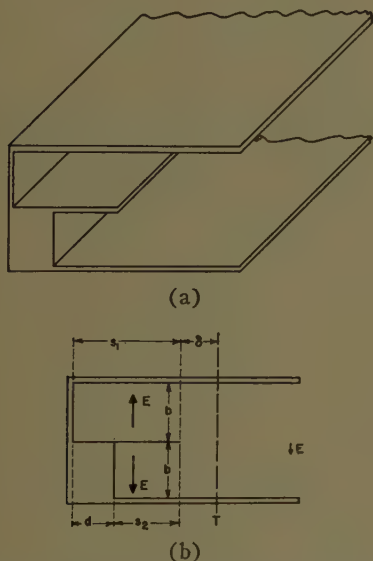


Fig. 3—Continuously asymmetrical trough waveguide, (a) full view, (b) cross-section view for zero-thickness center fin.

B. The Transverse Resonance Relation for Leaky Waves

Following the procedure employed for leaky rectangular waveguides,⁵ the complex propagation constant characterizing the leaky wave is obtained by using the transverse resonance method together with a perturbation technique. Fortunately, the transverse equivalent network required in the transverse resonance procedure is directly available⁶ for this geometry. The network is shown in Fig. 4; it is seen to parallel the geometry of Fig. 3, and to consist of two lengths of line, each short-circuited at one end and connected as shown at the other end. The lengths L_1 and L_2 are different from the physical lengths s_1 and s_2 because of the fringing capacity at

the bifurcation edge; they are related by

$$\begin{aligned} L_1 &= s_1 + \delta \\ L_2 &= s_2 + \delta, \end{aligned} \quad (4)$$

where δ is the shift to reference plane T (see Fig. 3) and is given by Marcuvitz,⁷ upon suitable change of notation, as

$$\delta = \frac{2b}{\pi} \ln 2 + \frac{1}{\kappa} S_1\left(\frac{2\kappa b}{\pi}; 0, 0\right) - \frac{2}{\kappa} S_1\left(\frac{\kappa b}{\pi}; 0, 0\right), \quad (5)$$

where S_1 is defined by (2). The cutoff wavelength is equal to $2\pi/\kappa$.

The possible values of the transverse wavenumber κ are determined from the resonances of the transverse network of Fig. 4. The resonance equation, found by equating to zero the sum of the impedances looking both to the right and to the left at reference plane T , is

$$\tan \kappa L_1 + \tan \kappa L_2 = 2j, \quad (6)$$

where L_1 and L_2 are given by (4) and (5). Although (6) is a rigorous relation, when the center strip is of zero thickness and when the parallel plates of spacing $2b$ extend to infinity, it is a complex transcendental equation whose exact solution is far from simple to obtain. We may also note from (5) that the lengths L_1 and L_2 are functions of κ , although this dependence is far from dominant.

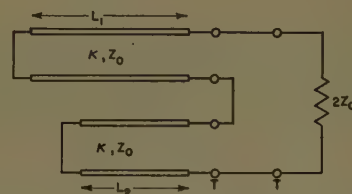


Fig. 4—Transverse equivalent network for asymmetrical trough waveguide.

C. Perturbation Solution for the Lowest Leaky Wave⁸

For practical reasons, one is usually interested in a leaky wave with slow leakage; it is easier under these conditions to taper the leaky guide in order to obtain the desired aperture distribution. It is therefore appropriate to solve the resonance relation (6) approximately by perturbing about the symmetrical, and therefore non-radiating, case. Recognizing from Fig. 3 that

$$L_2 = L_1 - d, \quad (7)$$

⁷ *Ibid.*, p. 353, (2a).

⁸ The transverse resonance relation (6) can also be solved by separating it into two equations whose simultaneous solution gives the real and imaginary parts of the complex propagation constant in the transverse plane. This method has been used by one of the authors to obtain an alternate solution for the asymmetrical trough waveguide. Numerical results computed from both the perturbation and non-perturbation methods are in substantial agreement, although somewhat closer agreement with measurement is found for the perturbation method. For the alternate analysis, together with additional experimental information, see W. Rotman and S. J. Naumann, "The Design of Trough Waveguide Antennas," AFRC Rep. TR-58-154; June, 1958.

⁵ L. O. Goldstone and A. A. Oliner, "Leaky Wave Antennas I: Rectangular Waveguides," accepted for publication in TRANS. IRE, vol. AP-7.

⁶ N. Marcuvitz, "Waveguide Handbook," Rad. Lab. Ser., vol. 10, McGraw-Hill Book Co., New York, N. Y., 1951; pp. 353-355.

(6) can be rewritten as

$$\tan \kappa L_1 + \tan \kappa(L_1 - d) = 2j. \quad (8)$$

Slow leakage occurs when $d \ll L_1$; under these conditions the complex κ value which is the solution of (8) is only slightly different from the unperturbed value κ_o , which is real and is

$$\kappa_o = \frac{\pi}{2L_1}, \quad (9)$$

where L_1 is given by (4) and (5). κ_o is also a solution of (1), since $\kappa_o = 2\pi/\lambda_{co}$ in the symmetrical case. These results for κ_o are, of course, identical; for simplicity, the solid curve of Fig. 2 is recommended when numerical values of κ_o are desired.

Writing

$$\kappa = \kappa_o + \Delta\kappa = \frac{\pi}{2L_1} + \Delta\kappa, \quad (10)$$

and substituting into (8), one finds

$$\tan \left[\frac{\pi}{2} + L_1 \Delta\kappa \right] + \tan \left[\frac{\pi}{2} + L_1 \Delta\kappa - \frac{\pi d}{2L_1} - d\Delta\kappa \right] = 2j, \quad (11)$$

or

$$\cot(L_1 \Delta\kappa) + \cot \left[L_2 \Delta\kappa - \frac{\pi d}{2L_1} \right] = -2j, \quad (12)$$

on use of (7). The perturbation approximation is employed at this step; since $L_1 \Delta\kappa$, $L_2 \Delta\kappa$, and d/L_1 are all assumed to be small quantities, (12) may be written as

$$\frac{1}{L_1 \Delta\kappa} + \frac{1}{L_2 \Delta\kappa - (\pi d/2L_1)} = -2j. \quad (13)$$

Eq. (13) yields the following for $\Delta\kappa$:

$$(\Delta\kappa)^2 (2jL_1 L_2) + (\Delta\kappa) [L_1 + L_2 - j\pi d] - \frac{\pi d}{2L_1} = 0. \quad (14)$$

The solution of (14) is

$$\Delta\kappa = \frac{-[L_1 + L_2 - j\pi d] \pm (L_1 + L_2) \sqrt{1 - \left(\frac{\pi d}{L_1 + L_2} \right)^2 - 2j \frac{\pi d^2}{(L_1 + L_2)^2}}}{4jL_1 L_2}, \quad (15)$$

upon rearrangement of the square root term. If one approximates the square root term, since $d/L_1 \ll 1$, and chooses the positive sign in (15) to keep $\Delta\kappa$ small, one finds

$$\Delta\kappa = \frac{\pi d}{4L_1 L_2} \left[\left(1 - \frac{d}{L_1 + L_2} \right) + j \frac{\pi}{2} \left(\frac{d}{L_1 + L_2} \right) \right]. \quad (16)$$

The complex propagation constant k_z in the longitudinal direction is related to the transverse wavenumber κ by

$$k_z = \beta - j\alpha = \sqrt{k^2 - \kappa^2}. \quad (17)$$

By employing (10) and the approximations appropriate to the perturbation procedure, (17) can be simplified so as to relate α and β to the real and imaginary components of (16). Defining

$$\beta_o = k_{zo} = \sqrt{k^2 - \kappa_o^2} \quad (18)$$

and substituting (10) into (17), one finds

$$k_z = \beta_o \left[1 - \frac{\kappa \Delta\kappa}{\beta_o^2} \right], \quad (19)$$

when terms of the order of $(\Delta\kappa)^2$ are neglected. Eq. (19) may be rewritten in the form

$$\beta = \beta_o - \frac{\kappa_o}{\beta_o} \operatorname{Re}(\Delta\kappa) \quad (20)$$

$$\alpha = \frac{\kappa_o}{\beta_o} \operatorname{Im}(\Delta\kappa). \quad (21)$$

Since $\kappa_o = 2\pi/\lambda_{co}$ and $\beta_o = 2\pi/\lambda_{go}$, where λ_{co} and λ_{go} are the cutoff wavelength and guide wavelength of the symmetrical, and therefore nonradiating, trough waveguide, (20) and (21) can be rephrased as

$$\frac{\lambda}{\lambda_g} = \frac{\lambda}{\lambda_{go}} - \frac{\lambda}{2\pi} \frac{\lambda_{go}}{\lambda_{co}} \operatorname{Re}(\Delta\kappa) \quad (22)$$

$$\alpha = \frac{\lambda_{go}}{\lambda_{co}} \operatorname{Im}(\Delta\kappa), \quad (23)$$

with

$$\operatorname{Re}(\Delta\kappa) = \frac{\pi d}{4L_1 L_2} \left[1 - \frac{d}{L_1 + L_2} \right] \quad (24)$$

$$\operatorname{Im}(\Delta\kappa) = \frac{(\pi d)^2}{8L_1 L_2 (L_1 + L_2)}. \quad (25)$$

IV. ASYMMETRICAL TROUGH WAVEGUIDE: COMPARISON WITH MEASUREMENT

Measurements of the values of α and of λ/λ_g for several asymmetrical trough waveguides are compared in

Figs. 5 and 6 with theoretical values which are computed by means of (22) to (25). Values of λ/λ_g and of α in decibels are plotted as a function of the step thickness d (see Fig. 3) for three different values of center strip width s_1 . The theoretical values are plotted as a solid line, while the measured results are indicated as individual points. It is seen that the agreement is reasonably good. The approximate theory described here is not expected to be valid for values of d/s_1 greater than about 0.5.

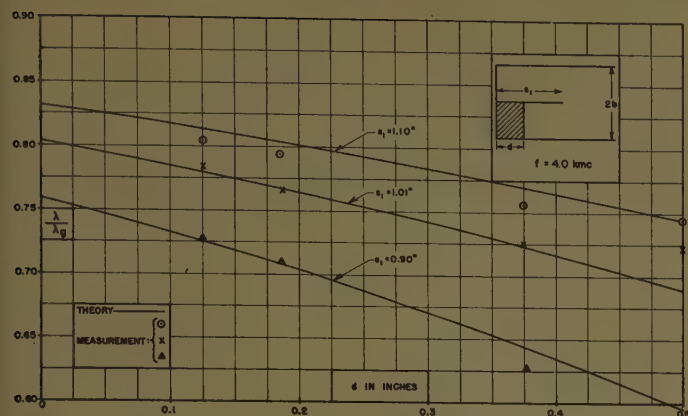


Fig. 5—Guide wavelength in asymmetrical trough waveguide.

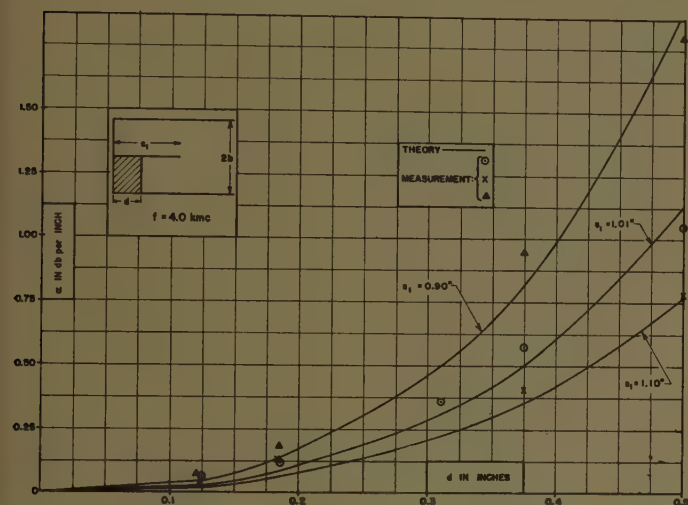


Fig. 6—Attenuation constant in asymmetrical trough waveguide.

The theoretical values are computed using the following procedure. First, the propagation characteristics of the symmetrical, or unperturbed, trough waveguide are obtained by taking $s = s_1$. From a knowledge of the geometry of the guide, the λ_{co} value is found from the curve of Fig. 2; the value of λ_{co} is then readily determined. For the perturbation calculation for the case of the asymmetrical trough guide one then computes L_1 from

$$L_1 = s_1 + \frac{2b}{\pi} \ln 2, \quad (26)$$

and L_2 using (7). It is unnecessary in this perturbation calculation to use the more accurate expressions (4) and (5) for L_1 ; their use makes only a tiny numerical difference anyway. With L_1 and L_2 known, the real and imaginary parts of $\Delta\kappa$ are found via (24) and (25), and the final desired values of λ/λ_0 and α from (22) and (23).

V. EFFECT OF FINITE THICKNESS OF CENTER FIN: THEORY

All of the equations above are valid when the center fin is of zero thickness. In practice, however, the center fin will possess some finite thickness and the values of

guide wavelength and attenuation constant will be somewhat different accordingly. The approximate effect of such fin thickness can be accounted for in a simple manner. This treatment is applied first to the symmetrical trough guide.

A. Symmetrical Trough Waveguide⁹

The symmetrical trough waveguide with a finite thickness center fin is shown in Fig. 7. When the center fin is of zero thickness, as in Fig. 1, the cutoff wavelength λ_{co} , which is given by (1), is different from $4s$ because of the fringing susceptance at the edge of the fin. This fringing susceptance is seen from (1) to consist of a static term, $(2/\pi) \ln 2$, plus frequency dependent terms in the form of arcsine sums. However, one notes from Fig. 2 that the value of λ_{co} computed using the total fringing susceptance, represented by the solid curve, differs only slightly from the value obtained by using the static contribution only, denoted by the dashed line. It is therefore seen that the static contribution is the dominant one by far.

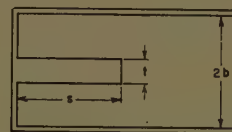


Fig. 7—Symmetrical trough waveguide with finite thickness center fin.

When the center fin is of finite thickness, a rigorous expression for the corresponding fringing susceptance is, unfortunately, not available as in the zero-thickness case. The static contribution to this susceptance, however, is given in the literature.¹⁰ If we then assume that the static contribution remains dominant, and that the frequency dependent contribution, which is not very significant, does not change with thickness, we have available a simple approximate means of treating the thick center fin case.

The results given by Thomson¹⁰ may be employed directly as a correction term which permits (1) to apply also to thick center fins. If we denote by

$$(\lambda_{co})_{t=0}$$

the value of λ_{co} for the zero-thickness case, and by

$$(\lambda_{co})_t$$

the value when the center fin is of finite thickness t , then we may write

$$\frac{(\lambda_{co})_t}{4b} = \frac{(\lambda_{co})_{t=0}}{4b} + \Delta, \quad (27)$$

⁹ K. S. Packard, of the Airborne Instruments Laboratory, has independently obtained a correction to the cutoff wavelength for symmetrical trough waveguide which is similar to that discussed here but is derived in a different manner. His work is as yet unpublished.

¹⁰ J. J. Thomson, "Recent Researches in Electricity and Magnetism," Clarendon Press, Oxford, Eng., p. 221; 1893.

where

$$\Delta = \frac{2}{\pi} \ln \left[\frac{2 - t/2b}{2(1 - t/2b)} \right] - \frac{t}{2\pi b} \ln \left[\frac{\frac{t}{2b} \left(2 - \frac{t}{2b} \right)}{\left(1 - \frac{t}{2b} \right)^2} \right],$$

and where $(\lambda_{co})_{t=0}$ is obtainable from (1).

When the fin thickness t is small, (27) reduces to

$$\frac{(\lambda_{co})_t}{4b} = \frac{(\lambda_{co})_{t=0}}{4b} + \frac{t}{2\pi b} \left[1 - \ln \frac{t}{b} \right]. \quad (28)$$

The correction term in (28) agrees with Δ in (27) to within 1 per cent for $t/2b \leq 0.05$, and to within 3 per cent for $t/2b \leq 0.10$. The percentage error in $(\lambda_{co})_t$ due to the use of (28) rather than (27) is much less, of course, and depends on the value of s/b .

A plot of the correction terms Δ of (27) as a function of $t/2b$ is given in Fig. 8. It is seen that the cutoff wavelength increases with t for low values of $t/2b$, but then decreases as the thickness increases further. In the limit as $t \rightarrow 2b$, Δ approaches the value

$$\left[-\frac{2}{\pi} \ln 2 \right],$$

exactly cancelling the corresponding term appearing in (1). The correction term in (28) is also presented in Fig. 8 as a dashed line. It is seen that the two curves agree well for small thickness, up to $t/2b = 0.10$ or so.

A comparison between theoretical values for $(\lambda_{co})_t$, computed from (27) with measured values, is presented in Fig. 9. The agreement is seen to be very good.

The effect on β_o or λ_{go} of a small change in center fin thickness can be estimated readily. Let the change in λ_{co} due to this thickness be written as

$$(\lambda_{co})_t = (\lambda_{co})_{t=0}(1 + \delta), \quad (29)$$

where

$$\delta = \frac{4b\Delta}{(\lambda_{co})_{t=0}}, \quad (30)$$

and Δ is defined by (27). We therefore have

$$(k_{co})_t = \frac{2\pi}{(\lambda_{co})_t} = (k_{co})_{t=0}(1 - \delta), \quad (31)$$

when $\delta \ll 1$. Since

$$(\beta_o)_t = \sqrt{k^2 - (k_{co})_t^2},$$

we find, upon substitution of (31),

$$(\beta_o)_t \cong (\beta_o)_{t=0} \left[1 + \delta \left(\frac{k_{co}}{\beta_o} \right)_{t=0}^2 \right], \quad (32)$$

or

$$(\lambda_{go})_t \cong (\lambda_{go})_{t=0} \left[1 - \delta \left(\frac{\lambda_{go}}{\lambda_{co}} \right)_{t=0}^2 \right]. \quad (33)$$

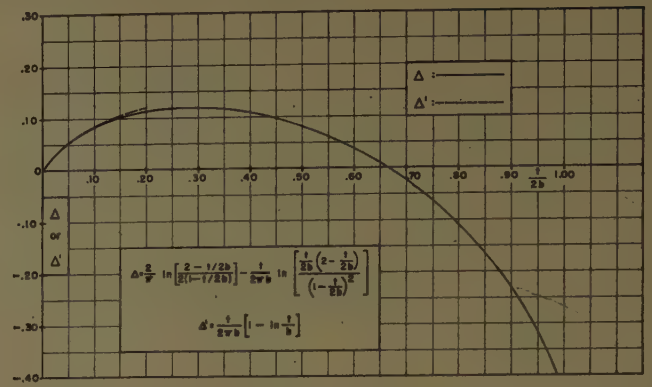


Fig. 8—Thickness correction for cutoff wavelength of symmetrical trough waveguide.

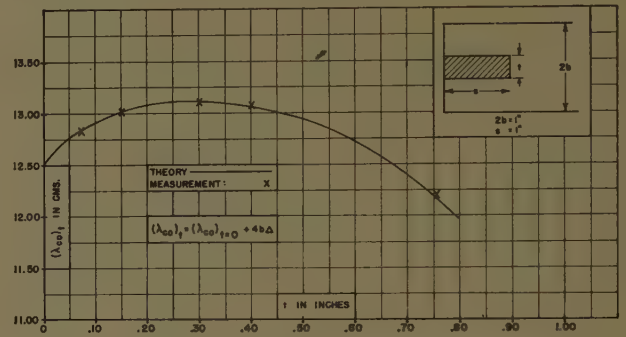


Fig. 9—Cutoff wavelength $(\lambda_{co})_t$ vs fin thickness t for symmetrical trough waveguide.

We therefore see that small center fin thickness will increase the cutoff wavelength but will decrease the guide wavelength. We also note that the effect of thickness is more pronounced when the mode is nearer to cut-off.

B. Asymmetrical Trough Waveguide

The calculations associated with the perturbation procedure are affected in two places by the finite thickness of the center fin. First, since the perturbation procedure begins from the symmetrical case just treated, the values of λ_{co} and λ_{go} in (22) and (23) must now be replaced by $(\lambda_{co})_t$ and $(\lambda_{go})_t$, where $(\lambda_{co})_t$ is given by (27) or by the combined use of Figs. 2 and 8, and where $(\lambda_{go})_t$ is found from

$$(\lambda_{go})_t = \frac{\lambda}{\sqrt{1 - [\lambda/(\lambda_{co})_{t=0}]^2}}. \quad (34)$$

Second, the calculation of L_1 is affected. Eq. (26) for L_1 must now be replaced by

$$L_1 = s_1 + \frac{2b}{\pi} \ln 2 + b\Delta, \quad (35)$$

with Δ given by (27) or Fig. 8. L_2 is still found from (7).

The effect of small thickness on α and λ/λ_g can be estimated by using (29) and (33) to examine (22) to (25). Noting that $(L_1)_{t=0}$ can be written as $(\lambda_{co})_{t=0}/4$, we readily obtain the following approximate relations in terms of δ , which is defined in (30) and is $\ll 1$:

$$(\alpha)_t \approx (\alpha)_{t=0} \frac{\left[1 - \delta \left(\frac{\lambda_{go}}{\lambda_{co}}\right)^2\right]}{[1 + \delta]^4} \quad (36)$$

$$\left(\frac{\lambda}{\lambda_g}\right)_t \approx \left(\frac{\lambda}{\lambda_{go}}\right)_{t=0} \left[1 + \delta \left(\frac{\lambda_{go}}{\lambda_{co}}\right)^2\right] - \left[\frac{\lambda}{2\pi} \frac{\lambda_{go}}{\lambda_{co}} \operatorname{Re}(\Delta\kappa)\right]_{t=0} \frac{\left[1 - \delta \left(\frac{\lambda_{go}}{\lambda_{co}}\right)^2\right]}{[1 + \delta]^3} \quad (37)$$

At midband operation, $\lambda_{go} \approx 2\lambda_{co}$; under these conditions (36) and (37) reduce to

$$(\alpha)_t \approx (\alpha)_{t=0} [1 - 8\delta] \quad (38)$$

$$\left(\frac{\lambda}{\lambda_g}\right)_t \approx \left(\frac{\lambda}{\lambda_{go}}\right)_{t=0} [1 + 4\delta] - \left[\frac{\lambda}{2\pi} \frac{\lambda_{go}}{\lambda_{co}} \operatorname{Re}(\Delta\kappa)\right]_{t=0} [1 - 7\delta] \quad (39)$$

From these relations it is seen that the effect of small thickness is to decrease α but to increase λ/λ_g .

VI. DESIGN OF TROUGH WAVEGUIDE ANTENNAS

A. Continuously Asymmetrical Radiator

A narrow-beam troughguide antenna was constructed as an illustrative example. Its parameters include the following theoretical values:

Design frequency: $f_o = 4$ kmc
 Guide wavelength ratio; $\lambda_o/\lambda_g = 0.738$
 Angle of emerging beam: $\theta = 47.5^\circ$ [from (3)]
 Percentage of input power radiated: 90 per cent
 Length of array: $L = 24$ inches
 Troughguide width: $2b = 1$ inch
 Amplitude distribution:

$$A = 0.2 + 0.8 \cos \frac{\pi}{2} \frac{z}{L}$$

Side lobe level: 22 db down from peak.

The attenuation constant necessary to give the desired amplitude distribution is computed from¹¹

$$2\alpha(z) = \frac{A^2}{\int_0^L A^2 dz + \frac{P(L)}{P(0) - P(L)} \int_0^L A^2 dz} \quad (40)$$

nepers
unit length

where

$$\frac{P(L)}{P(0)} = \frac{1}{10}$$

¹¹ J. N. Hines, V. H. Rumsey, and C. H. Walter, "Traveling wave slot antennas," *PROC. IRE*, vol. 41, pp. 1624-1631; November, 1953.

The measured data of Figs. 5 and 6 were used to compute the dimensions of the trough waveguide, which varies in cross section along its length.

Radiation patterns of this antenna were measured over the frequency range from 3.4 to 5.0 kmc. A typical pattern at the design frequency of 4 kmc is shown in Fig. 10. Patterns at other frequencies were equally good except at frequencies below 3.6 kmc. This degradation at low frequencies may be caused by cutoff effects in the troughguide.

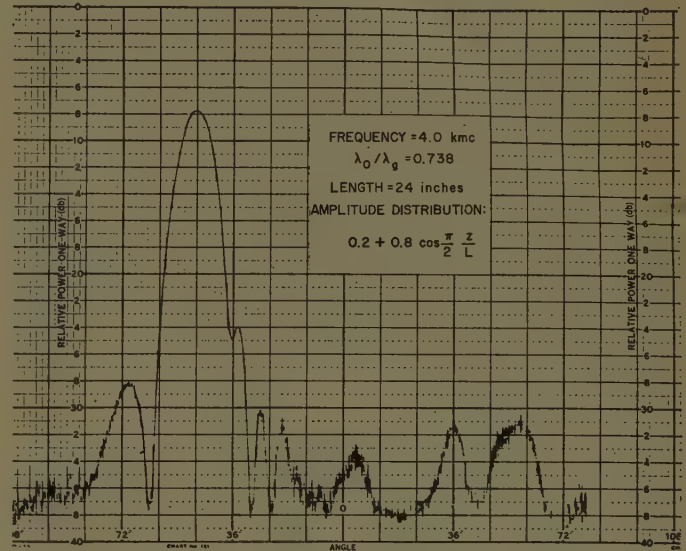


Fig. 10—Radiation pattern of a continuously asymmetrical trough waveguide antenna.

The 4-kmc radiation pattern exhibits the characteristics predicted from theory. For example, the peak of the beam is at the theoretical value of about 48° . Also, the side lobe level is everywhere lower than 20 db below the peak (with the exception of a small shoulder at 16 db). The half-power beamwidth is about 11° ; this is compatible with the size of the aperture.

The input VSWR to this array (measured in a uniform section of troughguide) is below 1.3 over the entire frequency range from 3.4–5.0 kmc. These characteristics indicate the broad-band nature of the asymmetrical trough waveguide.

B. Periodically Asymmetrical Radiator

The limitation of the troughguide antenna with continuous asymmetry is that the radiation patterns are limited primarily to those with peaks in the near end-fire direction. This restriction may be overcome if phase reversal is introduced by varying the asymmetrical base periodically between alternate sides of the center fin, as shown in Fig. 11, in which the troughguide is shown placed on its end. When the center-to-center spacing between successive asymmetrical sections (base blocks) is one-half the guide wavelength, a broadside beam results. In the construction of the array, each base block was also made one-half guide-wavelength long. In gen-

eral, the principal maximum of the radiated beam occurs at the angle:

$$\sin \theta = \frac{\lambda_o}{\lambda_g} - \frac{\lambda_o}{2a}, \quad (41)$$

where a is the center-to-center spacing between successive blocks. If the beam is restricted to near broad-side conditions and if the guide wavelength is less than twice the free space wavelength, no other principal maxima appear.

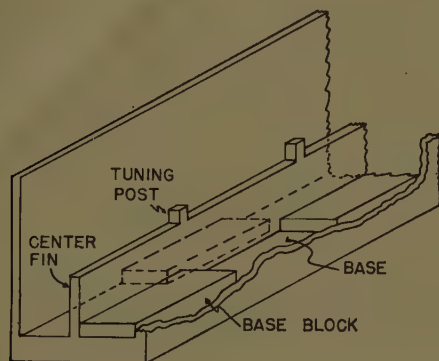


Fig. 11—Periodically asymmetrical trough waveguide.

The periodically asymmetrical troughguide antenna differs fundamentally from the usual linear array with respect to its impedance-frequency characteristics. Linear arrays of discrete resonant elements, such as series or shunt slots in a waveguide, can be classified into two types: resonant and nonresonant.

Characteristics of the resonant (standing wave) array are a half-wave spacing between elements and an input impedance match when the beam is normal to the array. If the frequency is changed so that the beam is not normal, the antenna becomes badly mismatched and the pattern deteriorates.

For nonresonant (traveling wave) arrays of resonant elements the situation is reversed. Here the element spacing cannot be a half-wavelength nor can the beam radiate in the direction normal to the array without impedance and pattern deterioration. As a consequence, for any type of end-fed linear array built of resonant elements, the beam cannot be swung through the normal by changing the frequency. This restriction limits the bandwidth of the antenna and also its scanning capabilities.

Some of these restrictions may be removed by the use of nonresonant radiators, such as the inclined-displaced slot in a waveguide,¹² which can be adjusted to transform a terminating match at its output into a match at its input at a given frequency. In other words, the overall impedance behavior of such an array at the chosen frequency is similar to that of a lossy transmission line.

At other frequencies, the reflections from the individual compensated slots do not add up in phase. A traveling wave array built of such nonresonant elements therefore does not have the limitation on scanning capabilities which is inherent with resonant elements. Unfortunately, little experimental data has been obtained for these slots since the capacitive irises or probes, required as part of the matching adjustment, complicate the array.

An array of periodically asymmetrical base blocks in a trough waveguide can also be designed to possess the impedance characteristics of a lossy transmission line at a given frequency. The detailed mechanism of operation differs from that of the inclined-displaced slots, however, and permits a more broad-band performance. The beam from a traveling wave array of these blocks has good scanning capabilities, and does not deteriorate as it scans through the direction normal to the guide. These line sources exhibit very large bandwidth compared to arrays with resonant elements.

The periodically asymmetrical block radiators are not inherently matched, however, since a small reflection occurs at each interface between blocks in the troughguide. Experimentally, these reflections act like shunt negative susceptances in a plane close to that of the interface and therefore may be compensated by capacitive tuning posts placed on the center fin. This compensation is required only at the frequency for which the blocks are a half guide wavelength long since the reflections do not add up in phase at other frequencies.

A linear troughguide array with a periodically asymmetrical base can be designed from a lossy transmission line viewpoint similar to that for the continuously asymmetrical troughguide. That is, phase and attenuation constants may be specified for each section of the line even though the line is not continuous. Furthermore, the relation between the amplitude distribution and the attenuation constant is still given by (40). The only basic difference is that the direction of the peak of the beam is determined by (41) rather than by (3).

The dimensions of the periodically asymmetrical trough waveguide are shown in Fig. 12 as a function of attenuation constant for a constant phase velocity ratio, $\lambda_o/\lambda_g = 0.738$. These dimensions cannot be easily computed, but may be readily measured. For a given cross section, the guide wavelengths for both the continuous and periodic cases are almost identical, while the attenuation constant is somewhat less for the periodic structure than for the continuous structure. These results are reasonable since the transmission line characteristics of either type of array, at a moderate distance from an interface, are similar. Near each interface, however, the periodic type behaves like a symmetrical structure and radiates less, thereby contributing to a lower average attenuation rate.

The height and position of the capacitive posts which are required to compensate a given block size are given

¹² W. H. Watson, "Waveguide transmission and antenna systems," Oxford University Press, New York, N. Y., Secs. 6.6, 6.8, pp. 93-102; 1947.

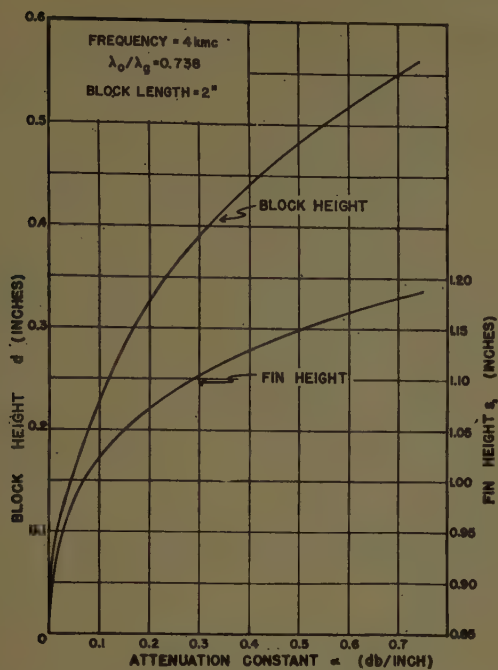


Fig. 12—Dimensions of a periodically asymmetrical trough waveguide vs attenuation constant.

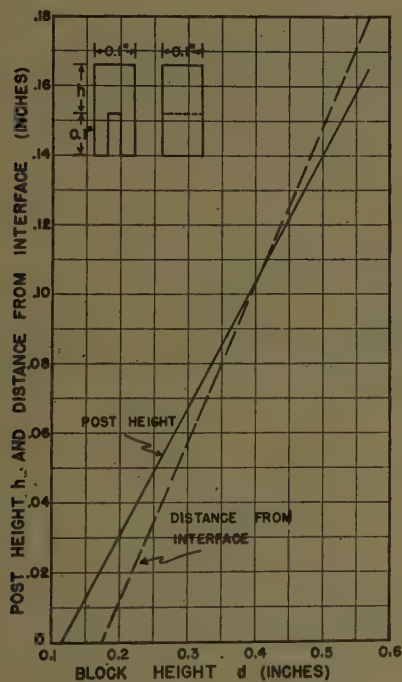


Fig. 13—Post height h vs block height d for periodically asymmetrical trough waveguide.

in Fig. 13. For small block heights no compensating posts are required since their uncompensated reflections are very small. For larger blocks the posts are situated at the interfaces, while for the largest blocks the posts are moved back from the interfaces by a small fraction of a wavelength. This shift in position indicates that the block interface cannot be represented as a purely shunt susceptance, but that its equivalent circuit has a small series component.

The location and dimensions of the posts were determined experimentally from input VSWR measurements

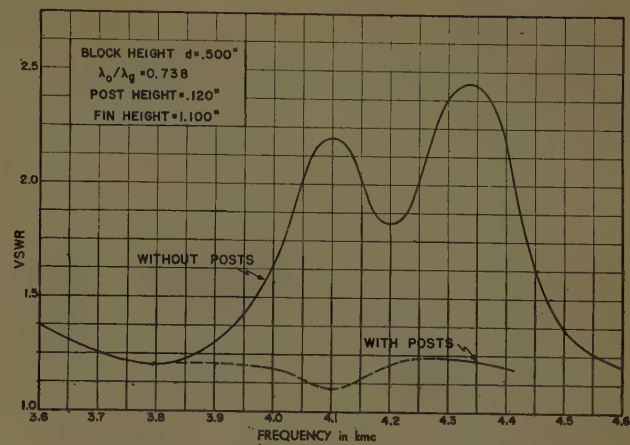


Fig. 14—Effect of matching posts on input VSWR of periodically asymmetrical trough waveguide.

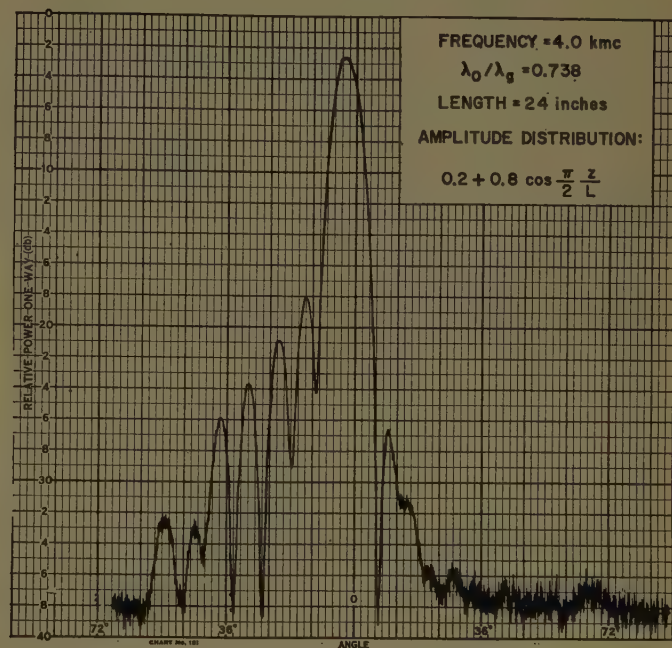


Fig. 15—Radiation pattern of a periodically asymmetrical trough waveguide array.

of ten identical blocks, each a half guide wavelength long at the design frequency. The VSWR was measured with and without the matching posts in place and with the troughguide terminated in a matched load. The parameters and location of the posts were varied until the best possible match (averaged over a band of frequencies near the resonant value) was obtained. Fig. 14 indicates the behavior of the input VSWR with and without posts for a block with a height of one-half inch.

A narrow-beam, periodic, troughguide array was constructed as a model. Its design is similar to that of the continuously asymmetrical array, except that the beam emerges broadside rather than at an angle. Its parameters include the following theoretical values:

- Design frequency: $f_0 = 4$ kmc
- Guide wavelength ratio: $\lambda_0/\lambda_g = 0.738$
- Angle of emerging beam: $\theta = 0^\circ$
- Percentage of input power radiated: 90 per cent

Length of array: 24 inches
 Length of individual blocks: $a = 2$ inches
 Troughguide width: $2b = 1$ inch
 Amplitude distribution:

$$A = 0.2 + 0.8 \cos \frac{\pi}{2} \frac{z}{L}$$

Side lobe level: 22 db down from peak.

The theoretical values of amplitude and attenuation constant at discrete points along the array are identical with those for the continuously asymmetrical case. The corresponding troughguide dimensions, such as block, fin, and post heights, are obtained from Figs. 12 and 13.

Radiation patterns of this array, terminated in a matched load, were measured over the frequency range from 3.4 to 5.0 kmc. A typical pattern at the design frequency of 4 kmc is shown in Fig. 15. The input VSWR of the array is below 1.4 over the entire frequency range of 3.4–5.0 kmc. The 16-db sidelobe level is higher than the predicted value, probably due to phase deviations caused by errors in the data of Fig. 12. This pattern and impedance behavior confirm our prediction that no resonant effects are present in the array.

VII. CONCLUSIONS

The trough waveguide is a relatively new form of transmission line which is easily adapted to the design

of new types of fixed-beam linear antenna arrays. The radiation from such arrays may be controlled by varying the degree of asymmetry of the structure. For beams near the end-fire direction this asymmetry can be made continuous while for broadside beams the asymmetry should be of a periodic type to introduce phase reversal. The theory of these structures is well understood and can be used to predict their performance.

These radiators are superior, in many instances, to similar types constructed in standard waveguides. In particular, they may be easily adapted to parallel plate systems since the side walls of the trough waveguide may be extended indefinitely. Also, they have excellent bandwidth, are simple and compact mechanically, and have good radiation properties.

Several other types of trough waveguide radiators, in addition to those reported here, have also been investigated. These include both resonant and nonresonant discrete radiators, and a traveling wave array of horizontal rods. Their characteristics are similar, but not superior, to those models which have been described.

ACKNOWLEDGMENT

The authors wish to thank Miss S. J. Naumann of the AFCRC, and A. Hessel of the Microwave Research Institute, Polytechnic Institute of Brooklyn, for their help in the experimental phase of this study.

A Contribution to the Theory of Cylindrical Antennas—Radiation Between Parallel Plates*

L. LEWIN†

Summary—A solution of the wave equation is obtained corresponding to an outgoing cylindrical wave between two parallel ground planes, and satisfying the boundary conditions appropriate to a center-fed, full height antenna at the origin. Expressions for the antenna current and impedance are obtained from a small radius approximation to these; formulas are obtained for comparison with those from usual antenna theory. Attention is directed to the expansion parameter and gap capacitance.

I. INTRODUCTION

SINCE the complete formulation by Hallén¹ of the equation to be satisfied by the currents in a radiating antenna, many attempts have been made to

solve either the exact equation, or various approximations to it. Since a suitable solution in closed form apparently is not obtainable, various expansions have been investigated,² including Fourier expansions and expansions in powers of a quantity Ω (related to the antenna wave-impedance), and known as the expansion parameter. Since Ω involves the logarithm of a nominally small quantity, this expansion is suitable if Ω^{-1} is small enough; but in practical cases Ω^{-1} is not all that small and since (within reason) a constant term can be absorbed in the logarithm, there is really no unique choice of expansion parameter, and the absorption of such a constant alters the form taken by the expansion. This arbitrariness is really linked to the rather vague notion

* Manuscript received by the PGAP, June 30, 1958; revised manuscript received December 30, 1958.

† Standard Telecommunication Labs., Progress Way, Enfield, Eng.

¹ E. Hallén, "Über die elektrischen Schwingungen in drahtförmigen Leitern," Uppsala University Arsskrift, Sweden, No. 1; 1930.

² A full account of various expansions used in the theory is given in S. A. Schelkunoff, "Advanced Antenna Theory," Chapman and Hall Ltd., London, Eng., ch. 5; 1952.

of the antenna wave impedance, which in the present case is not an accurately defined concept at all; and the various forms which have from time to time been proposed for this quantity reflect the possible choices of expansion parameter. At the other extreme, a naïve application of transmission line theory leads through various approximations and *ad hoc* arguments to expressions which link up with the more rigorous theory. The paradox of Van der Pol's calculation of the radiation from a sinusoidal current distribution, in itself wattless, is well known. It is desirable to be able to exhibit in a straightforward way these simpler approximations from the theory.

A further complication, which has been rigorously investigated for the case of an ellipsoidal antenna as an approximation to a cylindrical one, is the effect of the gap in the antenna, which must exist at the feed point if the antenna is to be excited by a generator. If this gap is reduced to zero, an infinite capacitance appears which shorts out the generator and makes the calculation valueless.³ It is desirable to be able to separate out this "gap capacitance" as a separate term, so that the gap can be taken to be zero in the rest of the calculation. In practice, of course, the antenna is fed by a feeder, and the gap corresponds to the antenna end of the feeder. However, in order not to complicate the problem by the awkward geometrical problem caused by the introduction of a real feeder, an idealized case is taken, but this idealization must not be pushed so far as to short out the gap completely. The actual effect of a transition at the feed has been treated in detail by King⁴ who shows how the impedance is modified from the ideal case by the proximity effects of the antenna and feeder. We shall not be concerned with this aspect here, though a simple formula for the gap capacity will appear in the course of the calculation.

In a recent investigation⁵ of the impedance of a probe in a rectangular waveguide, an expression was found in variational form for the probe impedance; but in fact this special form was not really required since the mode expansion used gave the complete and explicit solution. In retrospect it was apparent that the solution contained a special case of the antenna problem, namely, that of a full height antenna radiating into a rectangular waveguide and that for this configuration the antenna problem had, *pari passu*, been solved.

The solution is given here for the simpler case of radiation into the cylindrical region between two parallel ground planes. The total height is taken, for simplicity, to be less than a wavelength, so that only one propagating mode exists, but this limitation is not essential and the results can be used with very little alteration in the general case. The antenna is center-fed and full height,

shorted at the ends to the ground planes. An arbitrary terminating impedance, as in the case of the waveguide probe, can be included but is not treated here. Tai⁶ has shown how the kernel for a current filament can be used to obtain, for an antenna in free space, an expression for the antenna impedance which, for a certain assumed form of current distribution, is identical to that calculated from the rigorous kernel using surface currents of the same form on the antenna cylinder. In the probe investigation⁵ divergencies arose from the use of a fictitious current filament rather than the actual probe current, and were removed by an *ad hoc* argument of an approximate nature. If Tai's assumed current form had been used, a finite result would have been obtained, from which it appears that Tai's conclusions are specific to his assumed form of current. This is sinusoidal in $|z|$ and therefore implies a δ -function excitation. As shown by King,³ and also here, an infinite shorting capacitance is associated with such a feed, but no such term appears in Tai's results. Schelkunoff⁷ has shown that a rigorous solution of the integral equation with the filament kernel is impossible, and this is reflected in the divergence occurring in the probe analysis. It therefore appears that for an accurate solution, the actual surface currents must be used, and these are treated in the present analysis.

All surfaces are presumed to be of infinite conductance.

II. THE SOLUTION OF THE WAVE EQUATION

Fig. 1 shows a cylindrical region with coordinates r, θ, z bounded by parallel plates at $z = \pm \frac{1}{2}b$. At the origin is a cylindrical antenna of radius a with a gap at the center of (small) height δ .

Throughout the gap we suppose a generator to supply a constant driving field in the z direction. If the voltage across the gap is V , then at $r=a$ we have

$$E_z = -V/\delta \text{ for } -\frac{1}{2}\delta < z < \frac{1}{2}\delta, \text{ and zero elsewhere.} \quad (1)$$

For $r > a$ we need a solution representing uniform outgoing or attenuated waves with $E_r = 0$ at $z = \pm \frac{1}{2}b$. The radiating field involves the Hankel function $H_0^{(2)}(kr)$ but the superscript⁽²⁾ is to be understood and will be omitted henceforth. The attenuated waves involve the modified Bessel Function K . In view of the angular symmetry only E_z , E_r , and H_θ components of the wave will be excited.

The general solution satisfying the above conditions for $r > a$ is

$$E_z = A_0 H_0(kr)/H_0(ka) + 2 \sum_{n=1}^{\infty} A_n K_0(\Gamma_n r) \cos(2n\pi z/b)/K_0(\Gamma_n a) \quad (2)$$

³ R. King, "Gap problem in antenna theory," *J. Appl. Phys.*, vol. 26, pp. 317-321; March, 1955.

⁴ R. King, "Antennas and open wire lines," *J. Appl. Phys.*, vol. 20, pp. 832-850; September, 1949.

⁵ L. Lewin, "A Contribution to the Theory of Probes in Waveguides," IEE Mono. No. 259R; October, 1957.

⁶ C. T. Tai, "A new interpretation of the integral equation formulation of cylindrical antennas," *IRE TRANS. ON ANTENNAS AND PROPAGATION*, vol. AP-3, pp. 125-127; July, 1955.

⁷ Schelkunoff, *op. cit.*, p. 149.

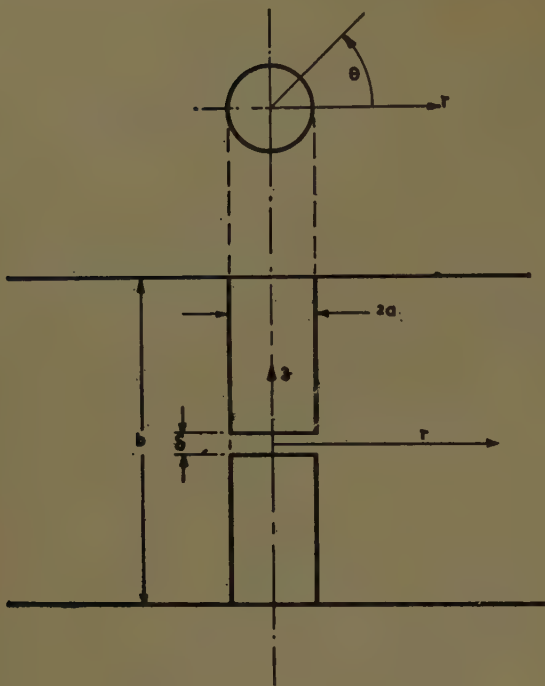


Fig. 1—Center-fed cylindrical antenna between parallel earth plates.

where

$$\Gamma_n = \sqrt{(2n\pi/b)^2 - k^2} \approx 2n\pi/b$$

when n is large. In order to determine the A_n we put $r=a$ and use Fourier analysis in conjunction with (1),

$$A_n = \frac{1}{b} \int_{-1/2\delta}^{1/2\delta} -\frac{V}{\delta} \cos(2n\pi z/b) dz \\ = -\frac{V}{b} \frac{\sin(n\pi\delta/b)}{(n\pi\delta/b)} \quad (3)$$

Since

$$H_\theta = \frac{jk}{300r} \int r E_z dr \text{ and } i_z = \frac{10}{4\pi} (2\pi r H_\theta)_{r=a}$$

we get, for the total current,

$$i_z = \frac{-jVa}{60b} \left\{ \frac{H_1(ka)}{H_0(ka)} - 2 \sum_1^\infty \frac{k}{\Gamma_n} \frac{K_1(\Gamma_n a)}{K_0(\Gamma_n a)} \frac{\sin(n\pi\delta/b)}{(n\pi\delta/b)} \cos(2n\pi z/b) \right\} \quad (4)$$

The admittance is obtained by putting $z = \frac{1}{2}\delta$ and dividing by V .

$$Y = \frac{-ja}{60b} \left\{ \frac{H_1(ka)}{H_0(ka)} - 2 \sum_1^\infty \frac{k}{\Gamma_n} \frac{K_1(\Gamma_n a)}{K_0(\Gamma_n a)} \frac{\sin(2n\pi\delta/b)}{(2n\pi\delta/b)} \right\} \quad (5)$$

III. APPROXIMATIONS FOR THE INPUT ADMITTANCE

A) The usual approximation of antenna theory is that the radius of the wire is small. We can take $H_0(ka) \approx 1 - j(2/\pi) \log(\beta ka)$ where $\log \beta = \gamma - \log 2 \approx -.1159$, and $H_1(ka) \approx 2j/(\pi ka)$. For the K functions we have $K_1(x)$

$\approx 1/x$ and $K_0(x) \approx -\log(\beta x)$ when x is small, but $K_1(x)/K_0(x) \rightarrow 1$ when x is large. Since $\Gamma_n a = 1$ when $n \approx b/2\pi a$, it is apparent that the approximation, valid near the origin, can only be used for the early terms of the series. However, in the limit of vanishing radius more and more terms become included in this region, and we shall investigate first the quantity Y_a obtained by making this approximation throughout,

$$Y_a = \frac{-ja}{60b} \left\{ \frac{2j/(\pi ka)}{1 - j(2/\pi) \log(\beta ka)} + 2 \sum_1^\infty \frac{k}{a\Gamma_n^2} \frac{1}{\log(\beta a\Gamma_n)} \frac{\sin(2n\pi\delta/b)}{(2n\pi\delta/b)} \right\} \quad (6)$$

This series converges when δ is zero, and by ignoring the variation of the factor containing δ , which approaches 1 in the limit, there is deduced the simpler form

$$Y_a = \frac{1}{30kb} \left\{ \frac{1}{\pi - 2j \log(\beta ka)} - j \sum_1^\infty \frac{k^2}{(2n\pi/b)^2 - k^2} \frac{1}{\log(\beta a\Gamma_n)} \right\} \quad (7)$$

The series in (7) is not directly summable on account of the term involving $\log(\beta a\Gamma_n)$. Now $\Gamma_n \approx k(n\lambda/b)$ and as a very crude approximation, bearing in mind that a slowly varying logarithmic function is involved, the factor $(n\lambda/b)$ could be ignored. The effect of doing this is to produce from (7) a series which is readily summable and which can be recognized as a quasi-static contribution to the admittance; the remainder then forms a radiative correction.

Now we have for the sum of a general series

$$\sum_1^\infty \frac{\cos n\theta}{n^2 - A^2} = \frac{1}{2A^2} \left\{ 1 - \frac{\pi A}{\sin \pi A} \cos[A(\pi - |\theta|)] \right\} \quad 0 < \theta < 2\pi. \quad (8)$$

With the particular case $\theta=0$, $A=b/\lambda$ we get

$$\sum_1^\infty \frac{k^2}{(2n\pi/b)^2 - k^2} = \left(\frac{b}{\lambda}\right)^2 \sum_1^\infty \frac{1}{n^2 - (b/\lambda)^2} = \frac{1}{2} \left[1 - \frac{\pi b}{\lambda} \cot(\pi b/\lambda) \right] \quad (9)$$

Multiplying this by $j/\log(\beta ka)$ and adding and subtracting within the brackets in (7), we get

$$Y_a = Y_{qs} + Y_{rad} \quad (10)$$

where

$$Y_{qs} = \frac{1}{j120 \tan(\frac{1}{2}kb) \log(1/\beta ka)} \quad (11)$$

is the quasi-static inductive susceptance to be expected from simple line theory for a shorted line pair of length $\frac{1}{2}b$ and wave impedance $Z_0 = 120 \log(1/\beta ka)$.

Y_{rad} is the radiation admittance given by the remaining terms of the series.

$$Y_{\text{rad}} = \frac{1}{30kb} \left\{ \frac{1}{\pi - 2j \log(\beta ka)} + \frac{1}{2j \log(\beta ka)} - j \sum_1^{\infty} \frac{k^2}{\Gamma_n^2} \left[\frac{1}{\log(\beta a \Gamma_n)} - \frac{1}{\log(\beta ka)} \right] \right\}. \quad (12)$$

This can be put in the form

$$Y_{\text{rad}} = \frac{1}{30kb \log^2(\beta ka)} \left\{ -j \frac{1}{2} \pi \log(\beta ka) \left[\pi - 2j \log(\beta ka) \right] + j \sum_1^{\infty} \frac{k^2}{\Gamma_n^2} \log(\Gamma_n/k) \frac{\log(\beta ka)}{\log(\beta \Gamma_n a)} \right\}. \quad (13)$$

The term in brackets remains finite as a goes to zero giving, to this order of approximation, *i.e.*, for thin antennas

$$Y_{\text{rad}} \approx \frac{1}{30kb \cdot \log^2(\beta ka)} \cdot \left\{ \pi/4 + j \sum_1^{\infty} \frac{k^2}{\Gamma_n^2} \log(\Gamma_n/k) \right\}. \quad (14)$$

If this be combined with (11) and the result inverted to give the impedance, we get

$$Z \approx j120 \log(1/\beta ka) \tan(\frac{1}{2}kb) + 60\pi \frac{\tan^2(\frac{1}{2}kb)}{\frac{1}{2}kb} + j240 \frac{\tan^2(\frac{1}{2}kb)}{\frac{1}{2}kb} \sum_1^{\infty} \frac{k^2}{\Gamma_n^2} \log(\Gamma_n/k), \quad (15)$$

(not valid when $\tan(\frac{1}{2}kb)$ is large).

The first term, as already stated, is the quasi-static expression for the antenna reactance, while the second and third terms give, respectively, the radiation resistance and reactance of this particular antenna configuration.

If we make the substitution $\log(\Gamma_n/k) \approx \log n + \log(\lambda/b)$, valid for large n , then the term involving $\log(\lambda/b)$ can be summed, giving

$$j120 \log\left(\frac{\lambda}{b}\right) \left[\frac{\tan^2(\frac{1}{2}kb)}{\frac{1}{2}kb} - \tan(\frac{1}{2}kb) \right].$$

It may be appropriate to absorb the second term of this expression with the quasi-static reactance, giving a modified wave impedance $Z'_0 = 120 \log(b/2\pi\beta a)$. This shows how it is possible for either the antenna length or the wavelength to appear in the logarithm, and mirrors the vagueness of the concept of wave impedance applied to this case. At the same time it is apparent from what has already been shown, that the expansion in going from (13) to (14) is with respect to a logarithmic term with argument (βka) .

Analytically, the above expressions are still valid when $b > \lambda$, the only difference being that the earlier terms involving $\log \Gamma_n$ introduce resistive components

corresponding to coupling into higher order modes. The formulas are therefore usable for large b . Now the usual antenna expansion parameter involves $\log(b/a)$, though Gray⁸ observed that a better agreement between Hallén's formula and both mode theory and experiment could be obtained by using $\log(b/a) - \gamma - \log(\pi b/\lambda) + \text{Ci}(\pi b/\lambda) = \log(\beta ka) + \text{Ci}(\pi b/\lambda)$. When b is large the second term approaches zero and we are left with $\log(\beta ka)$. Thus the expansion parameter which appears naturally in the present calculations is the same as Gray's limiting form for large b/λ , thus giving support to Gray's form. But when b/λ is small it cannot be overlooked that the present analysis, involving an infinite series of positive images, tends to make the physical arrangement rather far removed from that of a small antenna, and the conclusion may not hold. However, for small b/λ Gray's additional term $\text{Ci}(\pi b/\lambda)$ is no longer negligible, and it seems likely that his combination is a good one for an antenna of any length, in free space.

A possible exception to the above conclusions appears when b/λ is such that one of the Γ_n is near zero, *i.e.*, $b \approx n\lambda$. When such is the case Y , from (5), is dominated by the term

$$\frac{-j}{30kb \log(\beta \Gamma_n a)} \cdot \frac{1}{(n^2 \lambda^2 / b^2) - 1} \approx \frac{2j}{-120 \log(\beta \Gamma_n a) kb(n\lambda/b - 1)}. \quad (16)$$

Now the admittance of a shorted line pair of length $\frac{1}{2}b$ is $1/jZ_0 \tan(\frac{1}{2}kb)$ and when b is near $n\lambda$ this approximately equals $2j/[Z_0 kb(n\lambda/b - 1)]$. On comparison with (16) we see that in this case the value to take for the wave impedance is $120 \log(1/\beta \Gamma_n a)$, and this becomes infinite as $\Gamma_n \rightarrow 0$. Its reciprocal therefore seems to be a suitable expansion parameter in the immediate region of interest. However, it is not clear why the wave impedance should be large in this region, and to what extent this conclusion is tied to the particular configuration under study. As regards the latter point we note that an equivalent structure, obtained by a consideration of the images in the plates, would be an infinite antenna with a sinusoidal current distribution fed at intervals of b . The mutual influence from any particular section to a point on the antenna is in phase with that from a neighboring section, since the current changes sign from section to section, but a further 180° -phase change is introduced in the propagation path. Thus all the current loops add in phase, and if their influence had a $1/R$ dependence, then a logarithmic infinity would indeed be expected. Unfortunately for this argument, however, the influence comes from the E_z component of the field, and this varies as $1/R^2$ from a distant point on the antenna. Accordingly it would appear that the distant images are *not* responsible for the infinite Z_0 , and that

⁸ M. C. Gray, "A modification of Hallén's solution of the antenna problem," *J. Appl. Phys.*, vol. 15, pp. 61-65; January, 1944.

its occurrence must be a local phenomenon, *i.e.*, it is not tied to the particular configuration under study. The reason for its anomalous value is not, however, understood; the essential feature seems to be the appearance of a current standing-wave loop at the feed point, suggesting that already for a half-wave antenna in free space some such similar phenomenon might be present. It would show itself, presumably, as a large gradient of the reactance vs frequency curve in the immediate neighborhood of the zero reactance point. From (16) an infinite gradient can be expected at tuning, but because of the logarithmic dependence the region of large gradient would be very restricted and could be easily overlooked.

Although no such phenomenon has apparently been reported in the literature, the measured values obtained by King⁴ for the reactance of a half-wave antenna near resonance may be of some interest. If the experimental points of his Fig. 24(b) for the reactance are plotted on a linear scale, as shown in Fig. 2, the curve through these points appears to exhibit a kink as it goes through zero.

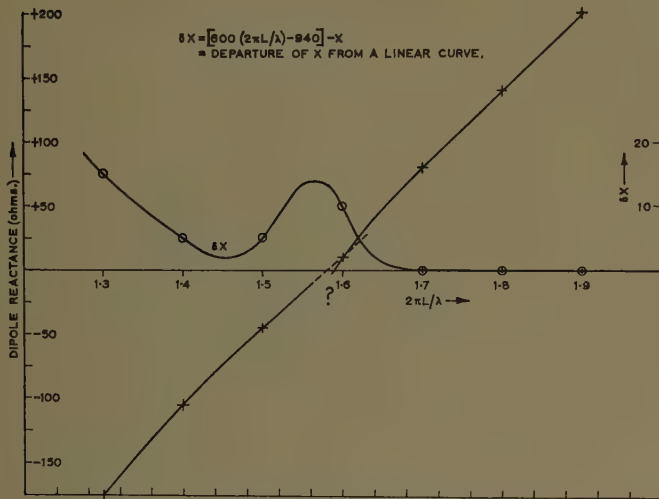


Fig. 2—Dipole reactance showing a possible kink in the curve at resonance.

The points are too far apart for this conclusion to be definite, and of course small experimental errors could easily either swamp or artificially cause such an effect. Nevertheless the possibility of an anomaly in the reactance near tuning would appear to warrant a more detailed investigation.⁹

B) As was explained in Section III-A, the approximations for the K functions are only valid near the origin, and for a finite radius the terms for $n > b/2\pi a$ approach the limiting form

⁹ In a recent discussion with Professor King he pointed out that a similar kink appears at resonance in the effective length and some other properties of half-wave receiving antennas. It is possible, therefore, that the two phenomena are closely related.

$$\frac{k}{\Gamma_n} \frac{\sin(2n\pi\delta/b)}{(2n\pi\delta/b)} \approx \frac{b}{\lambda} \frac{\sin(2n\pi\delta/b)}{(2n^2\pi\delta/b)}.$$

If we put $\delta=0$ the limiting form for this term is $b/\lambda n$ giving rise, on summation, to a logarithmic infinity. This is just the gap capacitance which shorts out the generator: its effects may not be neglected and it must be separated out before δ can be put equal to zero. To do this we add and subtract, within the brackets of (5) the series

$$2 \sum_1^{\infty} \frac{b}{\lambda} \frac{\sin(2n\pi\delta/b)}{(2n^2\pi\delta/b)}$$

giving

$$Y = \frac{ja}{30\lambda} \sum_1^{\infty} \frac{\sin(2n\pi\delta/b)}{(2n^2\pi\delta/b)} - \frac{ja}{60b} \left\{ \frac{H_1(ka)}{H_0(ka)} - 2 \sum_1^{\infty} \left[\frac{k}{\Gamma_n} \frac{K_1(\Gamma_n a)}{K_0(\Gamma_n a)} - \frac{b}{\lambda n} \right] \frac{\sin(2n\pi\delta/b)}{(2n\pi\delta/b)} \right\}. \quad (17)$$

The first term we denote by Y_c' and it sums to

$$Y_c' = \frac{-ja}{30\lambda} \cdot \frac{1}{\theta} \int_0^{\theta} \log(2 \sin \frac{1}{2}\phi) d\phi \quad \text{where } \theta = 2\pi\delta/b.$$

For small values of θ we can replace $2 \sin(\frac{1}{2}\phi)$ by ϕ , giving on integration

$$Y_c' \approx \frac{ja}{30\lambda} \log(eb/2\pi\delta). \quad (18)$$

After the separation out of the term Y_c' , δ can be taken zero in the rest of the expressions. From (17) we get

$$Y \approx Y_c' - \frac{ja}{60b} \left\{ \frac{H_1(ka)}{H_0(ka)} - 2 \sum_1^{\infty} \left[\frac{k}{\Gamma_n} \frac{K_1(\Gamma_n a)}{K_0(\Gamma_n a)} - \frac{b}{\lambda n} \right] \right\}. \quad (19)$$

The dominant part of the term in brackets is given by Y_a of (7) when a is small, but there seems to be no way of summing (19) directly. Suppose we wish to replace the summation in brackets in (19) by Y_a from (7) or some of the later equations. These equations sum from $n=1$ to ∞ although only the sum from $n=1$ to $N \approx b/2\pi a$ is really relevant; the terms for higher n are cancelled by the term $b/\lambda n$, though these terms contribute little to Y_a . On the other hand the term $b/\lambda n$ must also be summed from 1 to N , and since

$$\sum_1^N 1/n \approx \gamma + \log N,$$

this summation gives rise to an additional component

$$\frac{-ja}{30\lambda} \log\left(\frac{\beta b}{\pi a}\right)$$

to be added to Y_a . It seems that this term really belongs with the expression for Y_e' (18) which becomes modified to

$$Y_e = \frac{ja}{30\lambda} \log \left(\frac{ae}{2\delta\beta} \right). \quad (20)$$

If this be equated to $j\omega C$, the susceptance of a gap capacity C , then

$$C = \frac{1}{9.10^{11}} \frac{a}{2\pi} \log \left(\frac{ae}{2\delta\beta} \right). \quad (21)$$

This capacity is caused by the fringe field round the edge of the gap and is proportional to the antenna perimeter. The *interior* of the antenna has not been considered in this calculation: if there are end caps closing the cylinders, a further capacity must be added for a parallel plate condenser of plate area πa^2 and separation δ

$$C_{\text{plate}} = \frac{1}{9.10^{11}} \frac{a^2}{4\delta}. \quad (22)$$

On the other hand, if the cylinders were hollow there would be a contribution to the fringe field from the inside of the cylinders and the result of (21) would be doubled.

This aspect can be amplified from a consideration of a ribbon gap between two infinite co-planar plates. If z is the coordinate in the plane of the plates, perpendicular to the gap of width δ , then the charge distribution is given by

$$dQ = dz / \sqrt{z^2 - \delta^2/4}.$$

The charge per unit length to a distance $\frac{1}{2}D$ is therefore

$$Q = \int_{1/2\delta}^{1/2D} dz / \sqrt{z^2 - \delta^2/4} \approx \log (2D/\delta) \text{ if } D \gg \delta.$$

The potential between the plates is given by

$$\phi = 4 \int_{1/2\delta}^{\infty} \log \left| \frac{z+z'}{z-z'} \right| \frac{dz}{\sqrt{z^2 - \delta^2/4}}$$

where z' is the coordinate of a point in the plate. It is readily verified that this expression is independent of z' if $z' \geq \frac{1}{2}\delta$, and by taking $z' = \frac{1}{2}\delta$ its value is found to be $2\pi^2$. Hence the capacity per unit length of gap to a distance $\frac{1}{2}D$ is $(1/2\pi^2) \log (2D/\delta)$. If now such a pair of strips be wrapped round to make two aligned cylinders of radius a , then to a first order the capacity is given by multiplying the above expression by the perimeter $2\pi a$. For large values of D/δ (very small gaps) this capacity is double that given by (21), as anticipated.

From the form of (21) it is seen that the fringe field stretches out from the gap a distance of the order of the stub radius, which seems a physically reasonable behavior for the effect of the gap.

IV. APPROXIMATION FOR THE CURRENT

Except at $z=0$ the series in (4) is convergent for $\delta=0$ and in general, it will not be necessary to consider further the effects of the gap. However, it can be noted that the term $\cos (2n\pi z/b) \sin (n\pi\delta/b)/(n\pi\delta/b)$ can be written in the form

$$\frac{1}{\delta} \int_{z-1/2\delta}^{z+1/2\delta} \cos (2n\pi z'/b) dz',$$

i.e. it is the mean over a distance δ . Hence the full expression can always be recovered by an integration over δ . Accordingly we take

$$i_z \approx \frac{-jVa}{60b} \left\{ \frac{H_1(ka)}{H_0(ka)} - 2 \sum_1^{\infty} \frac{k}{\Gamma_n} \frac{K_1(\Gamma_n a)}{K_0(\Gamma_n a)} \cos (2n\pi z/b) \right\}. \quad (23)$$

This series is not summable in closed terms. However, for small a we can make the same type of approximations as in Section III-A, obtaining

$$i_z \approx \frac{V}{30kb} \left\{ \frac{1}{\pi - 2j \log (\beta ka)} - j \sum_1^{\infty} \frac{k^2}{(2n\pi/b)^2 - k^2} \frac{\cos (2n\pi z/b)}{\log (\beta a \Gamma_n)} \right\}. \quad (24)$$

This series is still not summable because of the term in $\log (\beta a \Gamma_n)$, which can be written $\log (\beta ka) + \log (\Gamma_n/k)$. If a is small enough for the first of these two terms to predominate then (8) may be used to obtain the quasi-static approximation

$$i_{qs} = \frac{jV}{120 \log (\beta ka)} \frac{\cos (k \frac{1}{2}b - |z|)}{\sin (\frac{1}{2}kb)}. \quad (25)$$

The nature of the departure of the current from a pure sinusoidal form can now be seen by comparing (25) and (23). If in the latter we take ka small in the Hankel functions, but not elsewhere, we get

$$i_z \approx i_{qs} + \frac{jV}{60kb} \left\{ \frac{1}{\log (\beta ka) + j\pi/2} - \frac{1}{\log (\beta ka)} + 2 \sum_1^{\infty} \frac{k^2}{\Gamma_n^2} \cdot \cos (2n\pi z/b) \left[\frac{\Gamma_n a K_1(\Gamma_n a)}{K_0(\Gamma_n a)} + \frac{1}{\log (\beta ka)} \right] \right\}. \quad (26)$$

The early terms of the infinite series are small because the K functions approximately cancel the logarithm, and the later terms are small because of the factor $1/\Gamma_n^2$. It is from this circumstance that the fair approximation given by the quasi-static current derives.

Part of the correction to the quasi-static current is given by the terms

$$\frac{1}{\log (\beta ka) + j\pi/2} - \frac{1}{\log (\beta ka)}.$$

For large values of $\log(\beta ka)$ this approximately equals

$$\frac{-j\pi/2}{\log^2(\beta ka)},$$

and it is apparent that this is the first term in an expansion of inverse powers of $\log(\beta ka)$.

It does not seem possible to express (26) in a more compact form.

V. CONCLUSIONS

Although the present paper does not throw any light on the solution in closed form of the free-space antenna equation, it does provide some information on the various approximations and expansions in use. The divergence difficulty met with in the waveguide probe investigation, which was avoided here through consideration of the actual surface currents rather than a filamentary fictitious current, strongly suggests that more attention be paid to this particular point, since a similar approximation is commonly made in antenna theory.⁷ In particular, Tai's analysis⁶ is relevant only to a particular form of approximation and is of no guidance in more rigorous formulations for which, among other things, the gap capacitance must appear if a δ -function type feed is assumed. With regard to expansion parameters, there seems to be some support for the structure put forward by Gray, though an anomalous increase in the wave impedance is predicted for antennas with a current antinode at the feed point. This aspect warrants further investigation.

LIST OF SYMBOLS

- a = antenna radius (cms)
- A_n = expansion coefficient
- b = plate separation (cms)
- C = gap capacitance (farad)
- E_r, E_z = electric field components (v/cm)
- $H_{0,1}$ = Hankel function $H_{0,1}^{(2)}$
- H_θ = magnetic field component (oersteds)
- i_z = antenna current (amps)
- i_{qs} = quasi-static component of antenna current
- $k = 2\pi/\lambda$
- $K_{0,1}$ = modified Bessel function
- n = summation integer
- N = integer nearest to $b/2\pi a$
- r, θ, z = cylindrical coordinates
- Y = antenna admittance (mhos)
- Y_a = small-radius approximation to Y
- Y_c, Y_c' = capacity-gap component of Y
- Y_{qs} = quasi-static component of Y
- Y_{rad} = radiative component of Y
- V = driving potential (volts)
- Z = antenna impedance (ohms)
- Z_0, Z_0' = antenna wave impedance
- β = a constant given by $\log \beta = \gamma - \log 2 = -0.1159$
- γ = Euler's constant, $= 0.5772$
- $\Gamma_n = \sqrt{(2n\pi/b)^2 - k^2}$
- δ = antenna gap (cm)
- λ = free-space wavelength (cm)
- ω = angular frequency
- Ω = a quantity related to the expansion parameter of antenna theory.

Radiation from Ring Sources in the Presence of a Semi-Infinite Cone*

LEOPOLD B. FELSEN†

Summary—A rigorous formulation for ring source Green's functions for a semi-infinite cone, carried out in terms of images in an infinitely extended angular transmission line, is evaluated asymptotically in the short-wave length range to yield geometric-optical, diffracted, and transition effects. Both scalar problems with Neumann or Dirichlet type boundary conditions, and electromagnetic problems appropriate to a perfectly conducting cone, are treated. The results are applied to calculate approximately the radiation pattern for a prescribed magnetic current distribution on the cone surface which can be taken to represent the excitation due to certain leaky wave type antenna arrays.

* Manuscript received by the PGAP, July 28, 1958; revised manuscript received, December 8, 1958. This work was sponsored by the University of Michigan, Ann Arbor, in connection with subcontract No. 3 under Contract AF-33(038)-28634.

† Microwave Res. Inst., Polytechnic Inst. of Brooklyn, Brooklyn, N. Y.

I. INTRODUCTION

IN a previous study of the radiation from scalar and vector point sources in the presence of a semi-infinite cone, it has been shown that an analysis in terms of a continuous spectrum of waves propagating in the latitudinal (θ) direction in a spherical coordinate system is suitable for an asymptotic field evaluation in the quasi-optic range (wave number $k \rightarrow \infty$).^{1,2} The quasi-optic effects are expected to comprise geometric-

¹ L. B. Felsen, "Plane wave scattering by small-angle cones," IRE TRANS. ON ANTENNAS AND PROPAGATION, vol. AP-5, pp. 121-129; January, 1957.

² L. B. Felsen, "Asymptotic expansion of the diffracted wave for a semi-infinite cone," IRE TRANS. ON ANTENNAS AND PROPAGATION, vol. AP-5, pp. 401-404; October, 1957.

optical (primary and reflected) contributions, a diffracted wave due to the cone tip, creeping waves around the cone body and transition phenomena at the boundaries of the domains of existence of the various wave types.^{3,4} The angular transmission analysis carried out previously has led to a direct formulation of the primary and diffracted field contributions in those restricted regions of space where the total field is describable in terms of these effects alone. This paper deals with an extension of the angular transmission approach to permit a quasi-optic asymptotic field evaluation everywhere. Although the discussion here is limited to problems which are essentially two-dimensional, it is felt that the techniques employed can also be applied, with suitable modifications, to the more difficult general three-dimensional case.

To be considered are excitations of the cone by a ring source with variation $\cos m\phi$ or $\sin m\phi$, $m = 0, 1, 2, \dots$, as shown in Fig. 1. Since the ϕ -variation of the field everywhere is identical with that due to the source, the problem is essentially two-dimensional in r and θ . A consequence of this special excitation is the absence of a creeping wave contribution to the quasi-optic field. The previously obtained quasi-optic formulations comprising the primary and diffracted fields are then valid in the angular domain $0 \leq \theta < (2\theta_0 - \pi - \theta')$ (see Fig. 1), where θ_0 is the exterior cone angle and $(r' \sin \theta')$ the radius of the ring source. To extend their range of validity into the region $\theta_0 \geq \theta > 2\theta_0 - \pi - \theta'$ requires the additional separation of the diffracted wave and the waves reflected from the cone body according to the laws of geometrical optics. This separation of geometric-optical and diffraction effects in a rigorous angular transmission analysis is required not only in the cone problem but as well as in the wedge,⁵ cylinder,⁶⁻⁸ and sphere problems. In the latter two, the creeping waves are descriptive of the diffraction effects.

The isolation of a geometric-optical contribution in a particular configuration can be carried out on purely mathematical grounds by subtracting certain divergent parts from the integrands arising in a contour integral formulation for the effects due to the scatterer. As applied by Fok and Franz to the cylinder and sphere,^{7,8} this procedure is based solely on a formal mathematical motivation for the desired breakup. The separation can, however, be carried out systematically in what appears to be the simplest and most direct manner by consider-

ing not the actual problem with its restricted angular region ($0 \leq \theta \leq \theta_0$ for the cone, $0 \leq \theta \leq \pi$ for the sphere, $0 \leq \phi \leq 2\pi$ for the cylinder with axis along the z coordinate, $0 \leq \phi \leq \alpha$ for the wedge), but an artificial problem in which the angular variable is generalized to extend over an infinite domain ($-\infty < \theta < \infty$ for the cone and sphere, $-\infty < \phi < \infty$ for the wedge and cylinder). (This concept was exploited for the cylinder problem by Friedlander⁶ and Wu.⁹) The boundary conditions at the angular end points of the physical region are then restored by a superposition of an infinite set of image sources. The advantage of this formulation will be found to be that each source in the infinitely extended angular domain contributes precisely a single geometric-optical wave which can be observed only within an angular interval of $\pm\pi$ from the source location. The application of these concepts to the cone problem, and their network interpretation, is discussed in Section IIB. It should be pointed out that the problem involving a single source in an infinitely extended angular region is of interest by itself for the study of absorbing surfaces since it can be interpreted to represent the response in the presence of a structure which absorbs perfectly all "angularly propagating" waves. A well-known example of such an obstacle in cylindrical geometry is Sommerfeld's black screen:¹⁰ its counterpart in spherical geometry would be a "black cone."

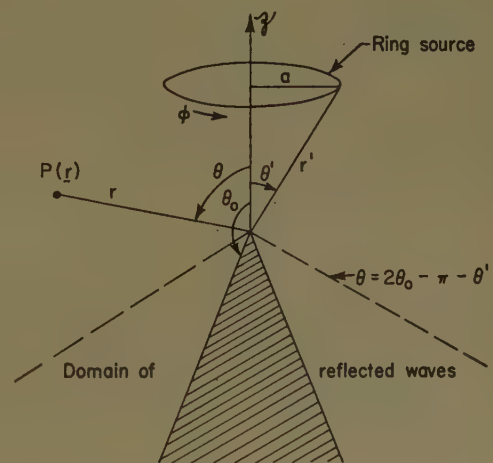


Fig. 1—Ring-source excited cone.

After a brief review of previously obtained results and their application to scalar ring-source excited cone problems, Section II of this paper deals with the image formulation alluded to above. An asymptotic evaluation in the quasi-optic range is then carried out to yield the first order geometric-optical, diffracted wave and transition contributions for all θ and θ' in the range $0 \leq (\theta, \theta') \leq \theta_0$. The analogous techniques for the electro-

³ J. B. Keller, R. M. Lewis, and B. D. Seckler, "Asymptotic solutions of some diffraction problems," *Comm. Pure Appl. Math.*, vol. 9, pp. 207-265; May, 1956.

⁴ J. B. Keller, "Back-scattering from a finite cone," paper presented at URSI meeting, Washington, D. C.; April, 1958.

⁵ M. J. Kontorovitch and N. H. Lebedev, *J. Phys., U.S.S.R.*, vol. 1, pp. 229-241; 1939.

⁶ F. G. Friedlander, "Diffraction of Pulses by a Circular Cylinder," *Inst. Math. Sci.*, New York University, New York, N. Y., No. EM-64; April, 1954.

⁷ V. A. Fok, "Diffraction of Radio Waves Around the Earth's Surface" (M. D. Friedman trans.), Academy of Sciences, Moscow, U.S.S.R., p. 9; 1946.

⁸ W. Franz, "Über die Greenschen Funktionen des Zylinders und der Kugel," *Z. Naturforsch.*, vol. 9a, pp. 705-716; 1954.

⁹ T. T. Wu, "High-Frequency Scattering," Cruft Lab., Harvard University, Cambridge, Mass., Tech. Rep. No. 232; May, 1956.

¹⁰ A. Sommerfeld, "Die differential- und integral Gleichungen der Mechanik und Physik," P. Frank and R. v. Mises, editors, Vieweg and Son, Braunschweig, Ger., ch. 20; 1935.

magnetic problems arising from ring source excitations of radial or azimuthal magnetic currents, and first order asymptotic evaluations, are summarized in Section III. Sample calculations are carried out for the radiation from a special magnetic current distribution on the cone surface representative of certain leaky wave antenna arrays.

substitution into (2) of the various expressions for \mathcal{G}' , previously given,¹ leads directly to the following alternative representations for \mathcal{G}'

$$\mathcal{G}'(\mathbf{r}; \mathbf{r}', \theta') = \frac{Ar' \sin \theta'}{r} \left\{ \frac{\cos m\phi}{\sin m\phi} \right\} G'(\varrho, \varrho'), \quad \varrho = (r, \theta), \quad (4)$$

where, in terms of the notation employed previously,

$$G'(\varrho, \varrho') = \frac{i}{2kr'} \csc^2 \left(\frac{\theta_0}{2} \right) j_0(kr_{<}) h_0^{(1)}(kr_{>}) \delta_{m0} - \frac{i\pi}{2kr'} \sum_q (2q+1) \frac{\Gamma(q+m+1)(d/d\theta_0)P_q^{-m}(-\cos \theta_0)P_q^{-m}(\cos \theta)P_q^{-m}(\cos \theta')}{\Gamma(q-m+1) \sin(q-m)\pi (\partial^2/\partial q \partial \theta_0)P_q^{-m}(\cos \theta_0)} \cdot j_q(kr_{<}) h_q^{(1)}(kr_{>}) \quad (4a)$$

$$= \frac{1}{2} \sqrt{\frac{r}{r'}} \oint_{C_1+C_2} \xi J_\xi(kr_{<}) H_\xi^{(1)}(kr_{>}) G_{\theta'}'(\theta, \theta'; m^2; \xi^2 - \frac{1}{4}) d\xi \quad (4b)$$

$$= G^0(\varrho, \varrho') + G_s'(\varrho, \varrho') \quad (4c)$$

$$G_s'(\varrho, \varrho') = \frac{1}{4} \sqrt{\frac{r}{r'}} \int_{C_1'+C_2'} \xi H_\xi^{(1)}(kr) H_\xi^{(1)}(kr') G_{\theta_s'}'(\theta, \theta'; m^2; \xi^2 - \frac{1}{4}) d\xi, \quad \theta + \theta' < 2\theta_0 - \pi. \quad (4d)$$

II. ALTERNATIVE GREEN'S FUNCTION FORMULATIONS (SCALAR PROBLEMS)

A. Direct Alternative Representations

In a previous paper,¹ alternative representations were given for the three-dimensional Neumann type Green's function $\mathcal{G}'(\mathbf{r}, \mathbf{r}')$ satisfying the inhomogeneous wave equation

$$(\nabla^2 + k^2)\mathcal{G}'(\mathbf{r}, \mathbf{r}') = -\delta(\mathbf{r} - \mathbf{r}') \quad (1)$$

with the boundary condition

$$\frac{\partial \mathcal{G}'}{\partial \theta} = 0 \text{ at } \theta = \theta_0, \quad (1a)$$

and a finiteness and radiation condition at $r \rightarrow 0$ and $r \rightarrow \infty$, respectively; k is the free space wavenumber, \mathbf{r} the vector coordinate to the point (r, θ, ϕ) , and $\delta(\mathbf{r} - \mathbf{r}')$ the delta function defined in the usual manner as

$$\delta(\mathbf{r} - \mathbf{r}') = 0, \quad \mathbf{r} \neq \mathbf{r}';$$

$$\int_{\tau} \delta(\mathbf{r} - \mathbf{r}') d\tau = 1, \quad \mathbf{r}' \text{ in volume } \tau. \quad (1b)$$

A time dependence $\exp(-i\omega t)$ is implied throughout. The Green's function $\mathcal{G}'(\mathbf{r}; \mathbf{r}', \theta')$ for a source distributed around a circle of radius a as in Fig. 1 with an angular variation $A(\phi)$ is obtained from an integration of \mathcal{G}' as

$$\mathcal{G}'(\mathbf{r}; \mathbf{r}', \theta') = a \int_0^{2\pi} A(\phi') \mathcal{G}'(\mathbf{r}, \mathbf{r}') d\phi', \quad a = r' \sin \theta'. \quad (2)$$

If the source function is sinusoidal, i.e.,

$$A(\phi) = A \begin{Bmatrix} \cos m\phi \\ \sin m\phi \end{Bmatrix}, \quad m=0, 1, 2, \dots, \quad A = \text{constant}, \quad (3)$$

In (4a), $\delta_{00}=1$, $\delta_{m0}=0$, $m \neq 0$. The summation extends over all positive zeros $\nu=q$ of the function $(d/d\theta_0)P_q^{-m}(\cos \theta_0)$,

$$\frac{d}{d\theta_0} P_q^{-m}(\cos \theta_0) = 0, \quad q > 0 \quad (m, \theta_0 \text{ prescribed}), \quad (5a)$$

where $P_q^{-m}(x)$ is the associated Legendre function of degree q , order $(-m)$ and argument x . The spherical Bessel functions are related to the cylindrical Bessel functions via

$$z_\nu(y) = \sqrt{\frac{\pi y}{2}} Z_{\nu+1/2}(y) \quad (5b)$$

with z_ν and Z_ν representing, respectively, j_ν , $h_\nu^{(1)}$ and J_ν , $H_\nu^{(1)}$. Moreover, the notation

$$r_{<} = \begin{matrix} r, & r < r' \\ r', & r > r' \end{matrix} \quad r_{>} = \begin{matrix} r, & r > r' \\ r', & r < r' \end{matrix}, \quad (5c)$$

has been employed. The integral representations in (4b) and (4d) are defined over the contours C_1 , C_2 about the positive real axis and C_1' , C_2' along the imaginary axis in the complex ξ -plane as shown in Fig. 2. The Neumann type angular characteristic Green's function $G_{\theta'}'$ is represented as the sum of the "free-space" contribution G_{θ}^0 appropriate to an angular domain $0 \leq \theta \leq \pi$ and a "correction term" $G_{\theta_s'}'$ accounting for the presence of the cone at $\theta = \theta_0$.¹¹

¹¹ For the Dirichlet Green's function \mathcal{G} satisfying (1) with $\mathcal{G}=0$ at $\theta=\theta_0$, all the considerations in this section apply as well if one substitutes G_θ for $G_{\theta'}'$, where G_θ is given as in (6) except that the operator $(d/d\theta_0)$ is replaced by unity.

$$G_{\theta'} = G_{\theta}^0 + G_{\theta s'}, \quad (6)$$

$$G_{\theta}^0 \left(\theta, \theta'; m^2; \xi^2 - \frac{1}{4} \right) = -\frac{\pi}{2} \frac{\Gamma(\nu + m + 1)}{\Gamma(\nu - m + 1) \sin(\nu - m)\pi} P_{\nu}^{-m}(\cos \theta_<) P_{\nu}^{-m}(-\cos \theta_>), \quad \nu = \xi - \frac{1}{2}, \quad (6a)$$

$$G_{\theta s'} \left(\theta, \theta'; m^2; \xi^2 - \frac{1}{4} \right) = \frac{\pi}{2} \frac{\Gamma(\nu + m + 1)}{\Gamma(\nu - m + 1) \sin(\nu - m)\pi} \frac{(d/d\theta_0) P_{\nu}^{-m}(-\cos \theta_0)}{(d/d\theta_0) P_{\nu}^{-m}(\cos \theta_0)} P_{\nu}^{-m}(\cos \theta) P_{\nu}^{-m}(\cos \theta'). \quad (6b)$$

Since $G_{\theta'} = G_{\theta}^0$ when the cone is absent, the integral in (4b) containing the G_{θ}^0 portion of $G_{\theta'}$ represents the free-space result $G^0(\theta, \theta')$. The integral in (4b) containing the $G_{\theta s'}$ portion of $G_{\theta'}$ expresses the scattered contribution $G_{s'}(\theta, \theta')$ due to the cone; its representation as in (4d) is discussed below. Since $G_{\theta'}$ and $J_k H_k^{(1)}$ in (4b) have no singularities in the finite parts of the first and fourth quadrants of the complex ξ -plane, the contours C_1 and C_2 in (4b) can be deformed into the contours $(C_1' + C_1'')$ and $(C_2' + C_2'')$, respectively, as shown in Fig. 2, with the radius of the quarter circles $C_{1,2}''$ approaching infinity.

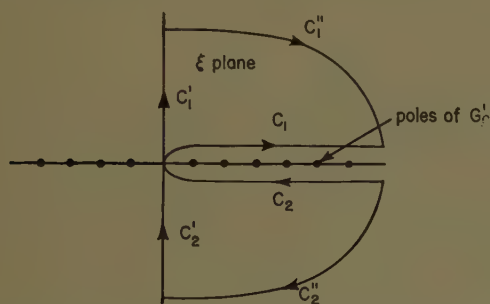


Fig. 2—Contours of integration and singularities in complex ξ -plane.

The series representation in (4a) results from an analysis of the problem in terms of radially propagating waves and converges for all values $\theta \neq \theta'$. (See Appendix I for the behavior of the summand as $q \rightarrow \infty$.) However, it is convenient for numerical computation only when kr or kr' is not too large ($r \neq r'$) since the magnitude of the terms in the series does not decrease until q is larger than kr (when $r < r'$) or kr' (when $r' < r$). Use of the series representation requires a knowledge of the values of q as defined in (5a), and the ability to evaluate the various functions in the summand at those values.

When kr and kr' are both large, the direct summation of the series in (4a) becomes impractical. In this range, which will concern us throughout the remainder of this paper, the diffraction phenomenon is expected to be characterized approximately by quasi-optic effects including geometric-optical, transition and diffracted contributions. A representation as in (4b) and (4c) is especially desirable in this respect since the free-space field and the scattered fields emerge distinctly, a separation not exhibited directly in (4a). In particular, if the observation point moves to infinity, the free-space ring source Green's function \hat{G}_f can be expressed in closed form by carrying out the integration in (2) for the three-dimensional free-spaced Green's function

$$\hat{G}_f(r, r') = \frac{e^{ik|r-r'|}}{4\pi|r-r'|} \sim \frac{e^{ikr}}{4\pi r} \cdot e^{-ikr'[\cos \theta \cos \theta' + \sin \theta \sin \theta' \cos(\phi - \phi')]}, \quad r \rightarrow \infty, \quad (7)$$

to yield:

$$\hat{G}_f(r; r', \theta') = \frac{Ar' \sin \theta'}{r} \begin{Bmatrix} \cos m\phi \\ \sin m\phi \end{Bmatrix} G_0(\theta, \theta'), \quad r \rightarrow \infty, \quad (8a)$$

$$G_0(\theta, \theta') = \frac{1}{2} e^{i(kr - m\pi/2)} e^{-ikr' \cos \theta \cos \theta'} \cdot J_m(kr' \sin \theta \sin \theta'). \quad (8b)$$

The scattered contribution $G_{s'}(\theta, \theta')$ due to the cone as expressed in (4d) for the restricted range $(\theta + \theta') < (2\theta_0 - \pi)$ is the result of an analysis of the diffraction problem in terms of a continuous spectrum of waves propagating in the angular (θ) direction and is particularly suitable for an evaluation in the quasi-optic range. If $r \rightarrow \infty$ and $kr' \rightarrow \infty$ with $r' \ll r$, $G_{s'}$ can be expressed uniformly in θ and θ' in terms of an asymptotic expansion in inverse powers of kr' as follows:²

$$G_{s'}(\theta, \theta') \sim \frac{i}{2\pi} \frac{e^{ik(r+r')}}{kr'} \sum_{n=0}^{\infty} \frac{A_n(\theta, \theta')}{(-2ikr')^n}, \quad kr' \rightarrow \infty, (\theta + \theta') < (2\theta_0 - \pi), \quad (9)$$

where

$$A_0(\theta, \theta') = 2 \int_0^{\infty} x \sinh x\pi G_{\theta s'}(\theta, \theta'; m^2; -x^2 - \frac{1}{4}) dx, \quad (9a)$$

and¹²

$$A_n(\theta, \theta') = -\frac{1}{n} \left[\frac{1}{\sin \theta} \frac{d}{d\theta} \sin \theta \frac{d}{d\theta} - \frac{m^2}{\sin^2 \theta} + n(n-1) \right] A_{n-1}(\theta, \theta'), \quad n = 1, 2, \dots \quad (9b)$$

It is noted that the evaluation of A_0 in (9a) does not require the knowledge of the zeros of the Legendre functions as in (5a); moreover the integrand in (9a) is exponentially damped for large x so that numerical evaluation procedures or approximate analytical techniques can be employed to advantage.

$G_{s'}$ as given in (9) can be interpreted as representing the scattering due to the tip singularity of the cone as

¹² R. B. Barrar and A. F. Kay, "A series development of a solution of the wave equation in powers of $\frac{1}{r}$," paper presented at URSI meeting, Washington, D. C., May, 1954. See also Keller, *et al.*, example 8, *op. cit.*

evidenced by the phase $(r+r')$ of the exponential, which is equal to the path length from the point r' to the point r via the cone tip, and by the magnitude dependence on $(1/kr')$. In fact, the integral (9a) exists only when $\theta < 2\theta_0 - \pi - \theta'$ (see Appendix I for behavior of $G_{\theta\theta'}$ as $x \rightarrow \infty$), *i.e.*, in that region of space which excludes the waves reflected from the cone body according to geometrical optics (Fig. 1). It is evident that this condition is violated for the radiation problem where the source is situated on the cone surface ($\theta' = \theta_0$). The failure of the representation in (4c) and (4d) in the domain $\theta > 2\theta_0 - \pi - \theta'$ is due to the inability to represent a geometric-optical field contribution directly in terms of angularly propagating waves. We must therefore seek a formulation which exhibits separately not only the incident field as in (4c) but all geometric-optically reflected waves. Before proceeding to such a formulation, it is desirable to state the conditions under which a θ -transmission representation applies. These conditions have been utilized in the transition from (4b) involving the contours $C_{1,2}$ or, alternatively, $(C_{1,2}' + C_{1,2}'')$ in the complex ξ -plane to (4d) involving the contours $C_{1,2}'$ only.

The following result is basic in the analysis: If a field contribution is represented by the integrals

$$I = \int_{C_1' + C_1''} \xi J_\xi(kr_<) H_\xi^{(1)}(kr_>) f(\xi) d\xi + \int_{C_2' + C_2''} \xi J_\xi(kr_<) H_\xi^{(1)}(kr_>) f(-\xi) d\xi \quad (10)$$

where the contours are shown in Fig. 2, and if

$$f \sim B(\xi) e^{-|\text{Im } \xi| \alpha} \quad \text{as } |\xi| \rightarrow \infty, \quad \alpha > \pi \quad (10a)$$

where $B(\xi)$ is of algebraic growth, then for $r \rightarrow \infty$, $kr' \rightarrow \infty$, $r' \ll r$, I possesses an asymptotic expansion as follows:

$$I \sim \frac{2i}{\pi k \sqrt{rr'}} e^{ik(r+r')} \sum_{n=0}^{\infty} \frac{I_n}{(-2ikr')^n}, \quad (11)$$

with

$$I_n = \int_0^\infty x \sinh x \pi f(ix) (ix, n) dx, \quad (11a)$$

$$(ix, n) = \frac{(-1)^n}{n!} (x^2 + \frac{1}{4})(x^2 + \frac{1}{4} + 2) \dots (x^2 + \frac{1}{4} + n(n-1)); \quad (ix, 0) \equiv 1. \quad (11b)$$

To prove (11), one observes that $J_\xi H_\xi^{(1)}$ behaves at worst like $\exp(|\text{Im } \xi| \pi)$ as $|\xi| \rightarrow \infty$ along a semi-circle in the right half ξ -plane, $-\pi/2 \leq \arg \xi \leq \pi/2$ [see (51)]. In view of (10a) the contribution from the quarter circles C_1'' and C_2'' vanishes. The change of variable $\xi \rightarrow -\xi$ permits the integral along C_2' to be combined with that along C_1' . Since

$$J_\xi(y) = \frac{1}{2} [H_\xi^{(1)}(y) + H_\xi^{(2)}(y)] \quad (12a)$$

and

$$H_{-\xi}^{(1)/(2)}(y) = e^{\pm i\pi} H_\xi^{(1)/(2)}(y), \quad (12b)$$

one obtains the alternative representation for I , *i.e.*,

$$I = -i \int_0^\infty \xi f(\xi) e^{i\pi\xi} \sin \pi\xi H_\xi^{(1)}(kr) H_\xi^{(1)}(kr') d\xi. \quad (13)$$

Eq. (11) follows directly upon letting $\xi = ix$ and substituting the asymptotic expansion for the Hankel functions as previously.² The imaginary ξ -axis is the pertinent contour for the θ -transmission formulation. From the form of the resulting asymptotic expansion, it is evident that the associated field contribution represents only a tip diffraction effect. If $\alpha < \pi$ in (10a), the integrals over paths C_1'' and C_2'' do not vanish and (10) also contains a geometric-optical contribution. Since $G_{\theta\theta'}$ is an even function of ξ and satisfies the conditions on f in (10) with $\alpha = 2\theta_0 - \theta - \theta'$, one is led directly from (4b) via (4d) to (9). The recursive relation between A_n and A_{n-1} in (9b) is a consequence of the differential equation satisfied by $G_{\theta\theta'}$.^{2,12}

B. Image Representation

To separate the geometric-optical from the diffraction effects, it is desirable to characterize the geometric-optical contributions in their simplest form. If the diffraction process is considered to be describable in terms of angularly propagating waves, these waves will experience repeated reflection from the surfaces $\theta = 0$ and $\theta = \theta_0$ terminating the angular region. In a uniform region with identical cross sections along the transmission coordinate, each wave reflected from the terminations with reflection coefficients Γ_0 and Γ_b as in Fig. 3(a) can be represented as arising from a suitably chosen image source located outside the physical domain in an infinitely extended transmission system [Fig. 3(b)].

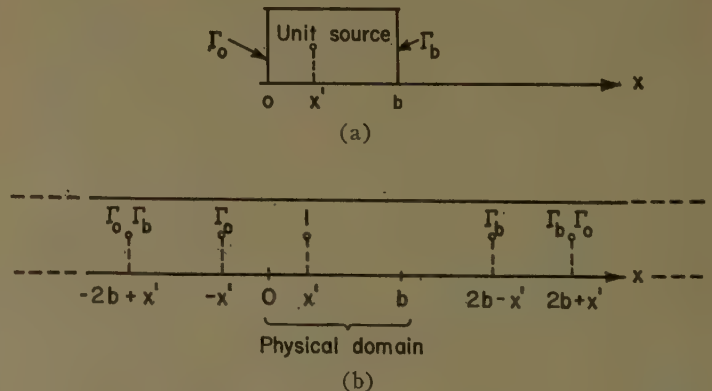


Fig. 3—Image representation of Green's function in a uniform region: (a) physical configuration, (b) equivalent image problem.

Since the transmission coordinate is a straight line, all images contribute a geometric-optical field in the region $0 < x < b$ and no diffraction occurs. If the transmission coordinate is *curved* as in the present problem, the concept of an infinitely extended transmission region re-

quires the generalization of the angular coordinate from a periodic to an infinite domain. Mathematically, this can be accomplished by introducing an infinitely sheeted Riemann surface;^{6,9,10} from a network viewpoint, one thinks of the angular transmission region as extending to infinity so that a particular angularly propagating wave experiences no reflection. If images are introduced to restore the actual boundary conditions at $\theta=0$ and $\theta=\theta_0$, it is found that not all images contribute a geometric-optical field in the range $0<\theta<\theta_0$. In fact, the geometric-optical field due to a typical image source is observable only within an angular distance of $\pm\pi$ from the source location so that the number of contributing

from which one notes that $P_{\xi m}^{(1)/(2)}$ represent (asymptotically for large ξ) waves traveling in the $\pm\theta$ directions. Upon substituting (14) into (6), making use of the relations of Appendix I, expanding the denominator into a power series.

$$\frac{1}{1+q_{\xi m}'} = \sum_{n=0}^{\infty} (-q_{\xi m}')^n, \quad q_{\xi m}' = \frac{(d/d\theta_0)P_{\xi m}^{(1)}(\theta_0)}{(d/d\theta_0)P_{\xi m}^{(2)}(\theta_0)} \equiv -e^{i(2\xi\theta_0 - m\pi - \pi/2)}f_{\xi m}', \quad (16)$$

and combining terms, one obtains the following representation for G_{θ}' ;

$$G_{\theta}'\left(\theta, \theta'; m^2; \xi^2 - \frac{1}{4}\right) = \left[\frac{\Gamma(\xi + m + 1/2)\Gamma(\xi - m + 1/2)}{\xi\Gamma^2(\xi)} \right] \frac{1}{\sqrt{\sin\theta \sin\theta'}} \{ \}, \quad \text{Im } \xi > 0, \quad (17)$$

$$\begin{aligned} \{ \} &= G_{\theta}^{\infty}(\theta, \theta')R_{\xi m}^{(2)}(\theta_{<})R_{\xi m}^{(1)}(\theta_{>}) + \sum_{n=1}^{\infty} \Gamma_0^{n-1}\Gamma_{\theta_0}'^n G_{\theta}^{\infty}(\theta, 2n\theta_0 - \theta')f_{\xi m}'^n R_{\xi m}^{(2)}(\theta)R_{\xi m}^{(2)}(\theta') \\ &+ \sum_{n=1}^{\infty} \Gamma_0^n \Gamma_{\theta_0}'^n f_{\xi m}'^n [G_{\theta}^{\infty}(\theta, -2n\theta_0 + \theta')R_{\xi m}^{(1)}(\theta)R_{\xi m}^{(2)}(\theta') + G_{\theta}^{\infty}(\theta, 2n\theta_0 + \theta')R_{\xi m}^{(2)}(\theta)R_{\xi m}^{(1)}(\theta')] \\ &+ \sum_{n=0}^{\infty} \Gamma_0^{n+1}\Gamma_{\theta_0}'^n f_{\xi m}'^n G_{\theta}^{\infty}(\theta, -2n\theta_0 - \theta')R_{\xi m}^{(1)}(\theta)R_{\xi m}^{(1)}(\theta'), \end{aligned} \quad (17a)$$

images is precisely equal to the number of possible geometric-optical reflections in the actual problem. All of the images do, however, contribute to the diffraction field which results as a consequence of the curved transmission coordinate. The above remarks will now be made quantitative.

The transmission properties of an angularly propagating mode are given by the angular characteristic Green's function G_{θ}' in (6). To effect a traveling wave description as indicated above, it is desirable to represent the standing wave functions $P_{\xi-1/2}^{-m}$ in terms of traveling wave functions $P_{\xi m}^{(1)/(2)}$ defined as follows:¹³

$$P_{\xi-1/2}^{-m}(\cos\theta) = \frac{1}{2}[P_{\xi m}^{(1)}(\theta) + P_{\xi m}^{(2)}(\theta)], \quad (14)$$

where

$$P_{\xi m}^{(1)/(2)}(\theta) = \left(\frac{2}{\pi \sin\theta} \right)^{1/2} \frac{\Gamma(\xi - m + \frac{1}{2})}{\Gamma(\xi + 1)} \cdot e^{\pm i[\xi\theta - m\pi/2 - \pi/4]} R_{\xi m}^{(1)/(2)}(\theta), \quad (14a)$$

$$R_{\xi m}^{(1)/(2)}(\theta) = (1 - e^{\pm i2\theta})^{1/2-m} \cdot F(1/2 - m, \xi - m + 1/2; \xi + 1; e^{\pm i2\theta}). \quad (14b)$$

$F(a, b; c; z)$ in (14b) is the hypergeometric function. Some properties of the traveling wave functions are given in Appendix I. Of special interest is the asymptotic behavior

$$R_{\xi m}^{(1)/(2)}(\theta) \sim 1, \quad |\xi| \rightarrow \infty, \quad \sin\theta \neq 0, \quad (15)$$

¹³ Although $m=0, 1, 2, \dots$ for the present discussion, (14) is also valid for arbitrary m .

where

$$G_{\theta}^{\infty}(\theta, \theta') = \frac{e^{i\xi|\theta-\theta'|}}{-2i\xi}, \quad (17b)$$

and

$$\Gamma_0 = e^{-i(m+1/2)\pi}, \quad \Gamma_{\theta_0}' = 1. \quad (17c)$$

$R_{\xi m}^{(1)/(2)}$ and $f_{\xi m}'$ have no singularities along the imaginary ξ -axis (see Appendix I) and behave for large $|\xi|$ as shown in (18). Convergence of the series expansion (16) requires $\text{Im } \xi > 0$, so that the representation (17) is valid along the contour $(C_1' + C_1'')$ in Fig. 2. Since G_{θ}' is an even function of ξ , an alternative formulation is obtained by replacing ξ in (17) by $(-\xi)$; the resulting expression is valid along the contour $(C_2' + C_2'')$. (Actually, only the behavior along $C_{1,2}''$ need concern us here.)

Eq. (17a) has been expressed in a manner which highlights the asymptotic behavior in the limit $|\xi| \rightarrow \infty$ since

$$R_{\xi m}^{(1),(2)}, f_{\xi m}', \quad [] \sim 1 + O\left(\frac{1}{\xi}\right), \quad |\xi| \rightarrow \infty; \quad \sin\theta, \sin\theta', \sin\theta_0 \neq 0, \quad (18)$$

where $[]$ denotes the terms inside the square brackets on the right-hand side of (17). It is evident that the resulting asymptotic representation of (17a) can be interpreted in terms of images on an infinitely extended θ -transmission line as in Fig. 3, with the x -coordinate replaced by θ ; the response due to a unit source located at θ' is given in (17b). Γ_0 and Γ_{θ_0}' are the reflection coefficients at $\theta=0$ and $\theta=\theta_0$, respectively. The perfectly re-

flecting boundary at $\theta = \theta_0$ gives rise to the Neumann type reflection coefficient $\Gamma_{\theta_0}' = +1$, while the reflection coefficient associated with the boundary $\theta = 0$ is seen to be equal to $\exp(-im\pi - i\pi/2)$. A directly analogous representation can be found for the Dirichlet characteristic Green's function G_θ which vanishes at $\theta = \theta_0$. In this instance, the differential operator $(d/d\theta_0)$ in (16) is replaced by unity, leading to a reflection coefficient $\Gamma_{\theta_0} = -1$.

Since the vanishing of the contributions from the contours $C_{1,2}''$ in Fig. 2 is governed by the behavior of G_θ' as $|\xi| \rightarrow \infty$, it suffices to focus attention on this asymptotic range. Each image term in (17) behaves like $(\pm 1/\xi) \exp[\pm i\xi|\theta - \varphi|]$, $|\xi| \rightarrow \infty$, $\text{Im } \xi \geq 0$, where φ is the location of the image source in the infinite angular transmission line; when substituted into (4b) (taken over the contours $C_{1,2}' + C_{1,2}''$) it leads to a field contribution as in (10) which can alternatively be expressed as in (11) provided that $|\theta - \varphi| > \pi$. Thus, all image sources located outside an angular interval $\pm\pi$ with respect to the observation angle θ contribute only to the diffracted wave. If the cone angle $\theta_0 > \pi/2$, then for any value $0 \leq (\theta, \theta') \leq \theta_0$ all the image sources fall into this category except those at $\varphi = -\theta', 2\theta_0 \pm \theta', -2\theta_0 + \theta'$. Let us represent G_θ' in (6) as

$$G_\theta' = (G_\theta' - \bar{G}_\theta') + \bar{G}_\theta', \quad (19)$$

where for $\theta_0 > \pi/2$, \bar{G}_θ' is the sum of those terms in (17) representing sources at $\varphi = \pm\theta', 2\theta_0 \pm \theta', -2\theta_0 + \theta'$. Since $f(\xi) = (G_\theta' - \bar{G}_\theta')$ satisfies the conditions in (10), the integral has an asymptotic expansion as in (11) and contributes only to the diffracted wave. Thus, we may write

$$I = \int_{C'} \xi J_\xi(kr_<) \bar{H}_\xi^{(1)}(kr_>) G_\theta' d\xi = I_1 + I_2,$$

$$C' = C_1' + C_1'' + C_2' + C_2'', \quad (20)$$

$$I_1 = \int_{C'} \xi J_\xi(kr_<) \bar{H}_\xi^{(1)}(kr_>) \bar{G}_\theta' d\xi, \quad (20a)$$

$$I_2 \sim \frac{2i}{\pi k \sqrt{rr'}} e^{ik(r+r')} \sum_{n=0}^{\infty} \frac{(I_2)_n}{(-2ikr')^n},$$

$$r \rightarrow \infty, kr' \rightarrow \infty, r' \ll r, \quad (20b)$$

where $(I_2)_n$ is given by (11a) with $f = (G_\theta' - \bar{G}_\theta')$, uniformly in θ, θ' for $0 \leq \theta \leq \theta_0, 0 \leq \theta' \leq \theta_0$. Eqs. (20) constitute the desired reformulation in which all geometric-optical effects are contained in I_1 . However, I_1 also contributes to the diffracted field.

C. First-Order Asymptotic Evaluation

When $\theta + \theta' < 2\theta_0 - \pi$, the contribution to I_1 from the image sources located at $\varphi = 2\theta_0 \pm \theta', -2\theta_0 + \theta'$ can be expressed as in I_2 so that \bar{G}_θ' comprises only the two terms corresponding to $\varphi = \pm\theta'$. The representation (20) so obtained is alternative to that in (8) and (9) [see also (4b)–(4d)], in which the geometric-optical result is ex-

pressed exactly in closed form. For other ranges in θ, θ' , I_1 must be evaluated directly to exhibit the separation of geometric-optical and diffraction effects. For the sake of simplicity, this evaluation will be carried out only to $O(1/\sqrt{kr'})$. We begin by writing \bar{G}_θ' in (20a) as follows:

$$\bar{G}_\theta' = \bar{G}_\theta'^{\infty} + (\bar{G}_\theta' - \bar{G}_\theta'^{\infty}), \quad (21)$$

where $\bar{G}_\theta'^{\infty}$ represents the asymptotic form of \bar{G}_θ' as $|\xi| \rightarrow \infty$ [see (17) and (18)]:

$$\bar{G}_\theta'^{\infty} = \frac{1}{\sqrt{\sin \theta \sin \theta'}} \{ G_\theta^{\infty}(\theta, \theta') + \Gamma_0 G_\theta^{\infty}(\theta, -\theta') \\ + \Gamma_{\theta_0}' G_\theta^{\infty}(\theta, 2\theta_0 - \theta') \\ + \Gamma_0 \Gamma_{\theta_0}' [G_\theta^{\infty}(\theta, 2\theta_0 + \theta') + G_\theta^{\infty}(\theta, -2\theta_0 + \theta')] \}, \quad (21a)$$

$$G_\theta^{\infty}(\theta, \theta') = \frac{e^{\pm i\xi|\theta - \theta'|}}{\mp 2i\xi}, \quad \text{Im } \xi \geq 0. \quad (21b)$$

It has been assumed that $\sin \theta, \sin \theta' \neq 0$, and $(\pi/2) < \theta_0 < \pi$. Since the contribution to I_1 from the second term in (21) is $O(1/\sqrt{kr'})$ and affects only the diffracted wave (see Appendix II), the geometric-optical effects ($O(1)$ in kr') will be contained correctly to the lowest order in $\bar{G}_\theta'^{\infty}$. The complete solution also contains geometric-optical terms of $O(1/kr')$ as seen from an asymptotic expansion of (8b). The contribution from a typical term in (21a) to the integral in (20a) (to be denoted by \bar{I}) is obtained readily by substituting for $H_\xi^{(1)}$ its asymptotic form as $r \rightarrow \infty$, for $J_\xi(kr')$ the Sommerfeld integral representation

$$J_\xi(kr') = \frac{1}{2\pi} \int_W e^{ikr' \cos \psi} e^{i\xi(\psi - \pi/2)} d\psi, \quad (22)$$

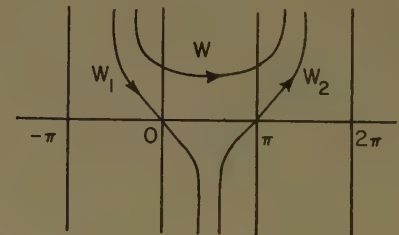


Fig. 4—Contours of integration in ψ -plane.

with the path W shown in Fig. 4, deforming the contour C' into $(C_1 + C_2)$ (see Fig. 2), performing a permissible interchange of the ξ and ψ integrations ($\text{Im } \psi > 0$ on W), and evaluating the ξ -integral

$$\bar{I} = \int_{C'} \xi J_\xi(kr_<) \bar{H}_\xi^{(1)}(kr_>) G_\theta^{\infty}(\theta, \varphi) d\xi \quad (23a)$$

$$= -\frac{1}{4\pi} \sqrt{\frac{2}{\pi kr}} e^{i(kr - \pi/4)} \int_W d\psi e^{ikr' \cos \psi} \\ \cdot \left[\frac{1}{\psi - \pi + |\theta - \varphi|} + \frac{1}{\psi - \pi - |\theta - \varphi|} \right],$$

$$r \rightarrow \infty. \quad (23b)$$

The contour W can now be continued analytically into the contour $W_1 + W_2$ in Fig. 4. If W_2 is chosen symmetrically with respect to $\psi = \pi$, there is no contribution to the integral over this path since the integrand is an odd function of $(\psi - \pi)$. If $|\theta - \varphi| < \pi$, a pole of the integrand is located at $\psi_p = \pi - |\theta - \varphi|$ on the real axis between $\psi = 0$ and $\psi = \pi$ and must be taken into account in the contour deformation. The remaining integral over the path W_1 can now be evaluated asymptotically as $kr' \rightarrow \infty$ for all values of ψ_p including $\psi_p \approx 0$, i.e., when the pole lies near the saddle point $\psi = 0$. The steepest descent path through $\psi = 0$ has the form of W_1 .¹⁴ One then obtains the following result to $O(1/\sqrt{kr'})$ valid for all $|\theta - \varphi|$:

$$\begin{aligned} \bar{I} \sim & \sqrt{\frac{1}{2\pi kr'}} e^{i(kr + \pi/4)} \left\{ e^{-ikr'} \cos(\theta - \varphi) \eta(\pi - |\theta - \varphi|) \right. \\ & - \frac{e^{i(kr' + \pi/4)}}{\sqrt{2\pi kr'}} \left(\frac{1}{\pi - |\theta - \varphi|} + \frac{1}{\pi + |\theta - \varphi|} \right) \\ & \left. - T(r', |\theta - \varphi|) \right\}, \end{aligned} \quad (24)$$

where

$$T(r', \alpha) = \frac{e^{ikr'}}{2} \operatorname{sgn}(\pi - \alpha) \left[F(w) - \frac{e^{i\pi/4}}{w\sqrt{2\pi}} \right], \quad (24a)$$

$$w = \sqrt{kr'} \left| \cos \frac{\alpha}{2} \right|, \quad F(w) = \frac{2}{\sqrt{\pi}} e^{-i2w^2} \int_{[1-i]w}^{\infty} e^{-y^2} dy, \quad (24b)$$

$$\begin{aligned} F(w) & \sim \frac{e^{i\pi/4}}{w\sqrt{2\pi}}, & w \rightarrow \infty, \\ & \sim 1 - \frac{4}{\sqrt{\pi}} e^{-i\pi/4} w, & w \rightarrow 0, \end{aligned} \quad (24c)$$

$$\eta(\pi - \alpha) = \begin{cases} 1, & \alpha < \pi \\ 0, & \alpha > \pi \end{cases}; \quad \operatorname{sgn}(\pi - \alpha) = \pm 1, \quad \alpha \leq \pi. \quad (24d)$$

The first and second terms inside the braces in (24) represent, respectively, the geometric-optical and diffracted contributions, while the third term T accounts for the transition effects through the geometric-optical boundary $|\theta - \varphi| = \pi$. It is noted that the singularity in the diffracted wave at $w = 0$ is compensated for by that in T . The extent of the transition domain, i.e., the range of w for which T is appreciable, can be assessed from Fig. 5, which shows a plot of the Fresnel integral function $F(w)$ and its asymptotic form in (24c). It is noted that the functional form of the diffracted wave as a function of θ, θ' in (24), contributed by a typical domain, since the same comment applies to the diffracted wave contribution from I_2 in (20b) and to that arising from I_1 in (20a), when one inserts into the integrand the second term in (21) (see Appendix II), the total diffracted wave function obeys this property to $O(1/\sqrt{kr'})$. It is highly suggestive that the diffracted

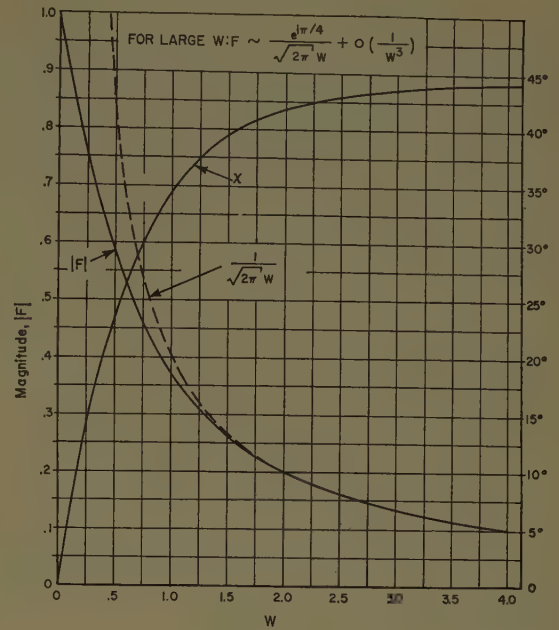


Fig. 5—Plot of $F = |F| e^{i\varphi} = \frac{2}{\sqrt{\pi}} e^{-i2w^2} \int_{(1-i)w}^{\infty} e^{-x^2} dx$.

wave contribution behaves in this manner to any order in $(1/kr')$.³

Upon collecting the various contributions to G' in (4b) arising from the utilization of the image formulation as in (19), (20), and (21), one obtains a representation for G' alternative to that in (4c) valid for all θ and θ' . Since the diffracted wave contribution to I has been shown to have the same functional form for all values of θ and θ' (to $O(1/\sqrt{kr'})$), one can evaluate G_s' from the integral representation for A_0 in (9a) subject to the restriction $(\theta + \theta') < (2\theta_0 - \pi)$, and then employ the function $A_0(\theta, \theta')$ for all values of θ and θ' . Thus, one is led to the following asymptotic result to $O(1/kr')$ for $r \rightarrow \infty$, $kr' \gg 1$, when $\theta, \theta' \neq 0$ and $\theta_0 > \pi/2$:

$$G'(\theta, \theta') \sim G_{\text{opt}}'(\theta, \theta') + G_s'(\theta, \theta'), \quad (25)$$

$$\begin{aligned} G_{\text{opt}}' &= \frac{e^{i(kr + \pi/4)}}{2\sqrt{2\pi kr'} \sin \theta \sin \theta'} \left\{ B(r', |\theta - \theta'|) \right. \\ &+ \Gamma_0 B(r', \theta + \theta') + \Gamma_{\theta_0}' B(r', 2\theta_0 - \theta - \theta') \\ &\left. + \Gamma_0 \Gamma_{\theta_0}' [B(r', 2\theta_0 + \theta' - \theta) + B(r', 2\theta_0 + \theta - \theta')] \right\}, \end{aligned} \quad (25a)$$

$$G_s' = \frac{i}{2\pi} \frac{e^{ik(r+r')}}{kr'} A_0(\theta, \theta'), \quad (25b)$$

with

$$B(r', \alpha) = e^{-ikr'} \cos \alpha \eta(\pi - \alpha) - T(r', \alpha), \quad (25c)$$

$$\Gamma_{\theta_0}' = 1, \quad \Gamma_0 = e^{-i(m+1/2)\pi}. \quad (25d)$$

For $(\theta + \theta') < (2\theta_0 - \pi)$, the geometric-optical contribution is given exactly in (8b). As a check on the approximate result above, one notes that an asymptotic evaluation of (8b) for $kr' \sin \theta \sin \theta' \rightarrow \infty$ agrees with that in (25). The singularities in $B(r', \alpha)$ as $\alpha \rightarrow \pi$ in the various terms in (25a) compensate for those in $A_0(\theta, \theta')$ on the

¹⁴ B. L. Van der Waerden, "On the method of saddle points," *Appl. Sci. Res.*, vol. B2, pp. 191-217; 1951.

geometric-optical boundaries so that the result is finite for all $\theta, \theta' \neq 0$. It is to be emphasized that the diffracted wave function $A_0(\theta, \theta')$, if evaluated exactly from (9a) applies for all values of θ and θ' , including $\theta, \theta' \rightarrow 0$.

To obtain the geometric-optical result for $\theta \rightarrow 0$, we make use of the known exact expression in (8b) which contains the contributions to I_1 from the sources located at $\varphi = \pm\theta'$. \bar{G}_θ' is given for $\theta \rightarrow 0$ exactly by [see (17)]:

$$\bar{G}_\theta' = \frac{[]}{\sqrt{\sin \theta \sin \theta'}} D, \quad (26)$$

$$D = R_{\xi m}^{(1)}(\theta') [G_\theta^\infty(\theta, \theta') R_{\xi m}^{(2)}(\theta) + \Gamma_0 G_\theta^\infty(\theta, -\theta') R_{\xi m}^{(1)}(\theta)] + R_{\xi m}^{(2)}(\theta') f_{\xi m}' [G_\theta^\infty(\theta, 2\theta_0 - \theta') R_{\xi m}^{(2)}(\theta) + \Gamma_0 G_\theta^\infty(\theta, -2\theta_0 + \theta') R_{\xi m}^{(1)}(\theta)] \Gamma_{\theta_0}', \quad (26a)$$

where $[]$ denotes the terms inside the square brackets on the right-hand side of (17). If $\sin \theta', \sin \theta_0 \neq 0$, we may again approximate

$$R_{\xi m}^{(1),(2)}(\theta'), f_{\xi m}', [] \approx 1, \quad (27)$$

since the geometric-optical effects can be shown to arise from the vicinity of saddle points located in the large ξ range of the integrand in (20a), through which the path of integration can be deformed. It is now evident that, to within the constant factor Γ_{θ_0}' , the only difference between the first and second terms in (26a) is the replacement of θ' by $(2\theta_0 - \theta')$. The geometric-optical contribution to I_1 from the first term in (26a) is known, however, to be that in (8b). Thus, the entire geometric-optical result arising from (26a) is given to a first order by

$$G_{opt}' = \frac{1}{2} e^{i(kr - m\pi/2)} \left\{ e^{-ikr' \cos \theta \cos \theta'} J_m(kr' \sin \theta \sin \theta') + \Gamma_{\theta_0}' \sqrt{\frac{\sin(2\theta_0 - \theta')}{\sin \theta'}} e^{-ikr' \cos \theta \cos(2\theta_0 - \theta')} \cdot J_m[kr' \sin \theta \sin(2\theta_0 - \theta')] \eta[\pi - (2\theta_0 - \theta')] \right\}, \quad \theta \rightarrow 0. \quad (28)$$

The diffracted wave contribution is still given by (25b). As θ increases away from zero, (28) goes over into (25a) upon use of the asymptotic formula for the Bessel functions. Directly analogous considerations apply, of course, if $\theta' \rightarrow 0$ and $\theta \neq 0$; the appropriate formula for this case is obtained by changing $\theta \leftrightarrow \theta'$ in (28).

If both θ and θ' approach zero, the geometric-optical contribution is given by the first term on the right-hand side of (28), except when $\theta_0 \rightarrow \pi/2$, in which case θ and θ' lie in a transition region. The transition formulas for the special case of back-scattering along the cone axis ($\theta = \theta' = 0$) have been presented previously.¹⁵

¹⁵ L. B. Felsen, "Back-scattering from wide-angle and narrow-angle cones," *J. Appl. Phys.*, vol. 26, pp. 138-151; February, 1955. See also "Back-scattering from a semi-infinite cone," Microwave Res. Inst., Polytechnic Inst. of Brooklyn, Brooklyn, N. Y., Electrophysics Group Memo. No. 43; July, 1958.

D. Remarks Concerning $A_0(\theta, \theta')$

An exact expression for the diffracted wave amplitude $A_0(\theta, \theta')$ is given in (9a). In particular, for $m=0$,

$$A_0(\theta, \theta') = \pi \int_0^\infty x \tanh \pi x \cdot \frac{K_x^1(-\cos \theta_0)}{K_x^1(\cos \theta_0)} K_x(\cos \theta) K_x(\cos \theta') dx, \quad m=0, \quad (29)$$

where $K_x^m(\cos \theta) \equiv P_{-1/2+ix}^m(\cos \theta)$, and it is assumed for the evaluation of the integral that $\theta + \theta' < 2\theta_0 - \pi$. Although it appears difficult to evaluate the integral in closed form in terms of known functions, numerical and approximation methods can be employed advantageously since the integrand is a positive real function of x and decays exponentially for large x . Such calculations have not been carried out as yet for all ranges of θ, θ' and θ_0 . However, for small cone angles ($\theta_0 \approx \pi$), an approximate evaluation to $O[(\pi - \theta_0)^2]$ yields,²

$$A_0(\theta, \theta') \approx \left(\frac{\pi - \theta_0}{2} \right)^2 2\pi \frac{1 + \cos \theta \cos \theta'}{(\cos \theta + \cos \theta')^3}, \quad \theta_0 \approx \pi. \quad (30)$$

For $m > 0$, the result is $O[(\pi - \theta_0)^2]$, i.e., very small. Eq. (30) should be a good approximation for $\theta_0 > 160^\circ$, outside the geometric-optical transition regions. The transition function T as in (24a) does not account for the singularity in the approximate formula for A_0 in (30) as $(\theta + \theta') \rightarrow \pi$, since in the derivation of T it was assumed that $\sin \theta_0 \approx 0$.

Since the ring-source excited cone has no shadow region, there exists a geometric-optical field contribution at every point in space. Consequently, the diffracted field, being of higher order in $(1/kr')$, is of relatively minor importance except near geometric-optical transition regions where its magnitude can be appreciable. Near these regions, characterized by $|\theta - \varphi| \approx \pi$, the predominant behavior of the diffracted wave is contained in (24); as $|\theta - \varphi| \rightarrow \pi$, the singularity in the diffracted wave amplitude is compensated for by the transition function T . Upon regrouping the terms in (24), it is noted that the transition and diffracted wave behavior as $|\theta - \varphi| \rightarrow \pi$ is adequately described by the function

$$\bar{T}(r', \alpha) = \frac{e^{ikr'}}{2} \operatorname{sgn}(\pi - \alpha) F(w), \quad w = \sqrt{kr'} \left| \cos \frac{\alpha}{2} \right|, \quad (31)$$

which, for $w \geq 4$ (see Fig. 5 and (24c)) yields the main diffracted wave contribution. Thus, for an evaluation accounting properly for the geometric-optical and transition phenomena and only approximately for the less important diffraction effects, G_s' in (25) may be neglected provided that in (25c), $T(r', \alpha)$ is replaced by $\bar{T}(r', \alpha)$.

III. ELECTROMAGNETIC RING SOURCE PROBLEMS

The electromagnetic problems of radiation from ring sources comprised of radial or azimuthal electric or magnetic currents in the presence of a perfectly con-

ducting semi-infinite cone can be reduced to equivalent scalar problems,^{1,16} which resemble those discussed in Section II, and which can be analyzed by directly analogous techniques. As an illustration, we treat the radiation from radial or azimuthal magnetic current distributions situated on the cone surface.

A. Radial Magnetic Currents

Consider a narrow annular slot on the cone surface as in Fig. 6 excited with a prescribed electric field

$$\mathbf{E}(\mathbf{r}') = \phi_0 E(r'), \quad E(r') = \begin{cases} \cos m\phi' \\ \sin m\phi' \end{cases} E(r'), \quad 0 \leq \phi' \leq 2\pi, \quad (32)$$

where ϕ_0 is a unit vector in the ϕ -direction. This electric field excitation is equivalently represented by the radial magnetic current distribution $\mathbf{M}(\mathbf{r}') = \mathbf{n} \times \mathbf{E}(\mathbf{r}') = r_0 E(r')$ flowing on the perfectly conducting cone, with $\mathbf{n} \equiv \theta_0$ and r_0 representing unit vectors in the θ and r directions, respectively. Since the vector electric field at \mathbf{r} due to a radially directed magnetic dipole located at \mathbf{r}' can be represented in terms of the Neumann type Green's function \mathcal{G}' as

$$\mathbf{r}' E(\mathbf{r}, \mathbf{r}') = -\nabla \times [\mathbf{r}_0 \mathcal{G}'(\mathbf{r}, \mathbf{r}') \mathbf{M}(\mathbf{r}')], \quad (33)$$

one obtains for the ring source distribution in (32),

$$\hat{E}_\theta(\mathbf{r}, \mathbf{r}') = -\frac{1}{r' \sin \theta} \frac{\partial}{\partial \phi} \hat{\mathcal{G}}'(\mathbf{r}; \mathbf{r}', \theta_0), \quad (34a)$$

$$\hat{E}_\phi(\mathbf{r}, \mathbf{r}') = \frac{1}{r'} \frac{\partial}{\partial \theta} \hat{\mathcal{G}}'(\mathbf{r}; \mathbf{r}', \theta_0), \quad \hat{E}_r \equiv 0, \quad (34b)$$

where $\hat{\mathcal{G}}'$ is given in (4).

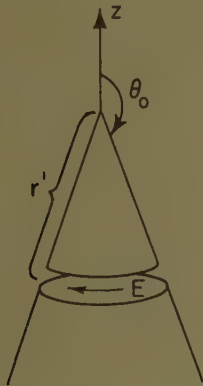


Fig. 6—Azimuthal electric field excitation.

For an approximate evaluation as $r \rightarrow \infty$, $kr' \gg 1$, one can employ for $\hat{\mathcal{G}}'$ the asymptotic formulas presented in Section II. For $\theta \approx 0$, the geometric-optical contribution from the \hat{E}_ϕ component predominates in view of the $(\partial/\partial \theta)$ operation in (34b), which results in multiplication by kr' [see (25a)]. Thus, a consistent evaluation of

\hat{E}_θ to $O(1/kr')$, including diffraction effects, requires the consideration of higher order terms in (25a). Rather than enter into this additional complication, we consider only the dominant geometric-optical effects, including the transition behavior at $\theta \approx \pi - \theta_0$ [see (31)]. It is then found that for $\theta \approx 0$,

$$r \hat{E}_\theta|_{\text{opt}} \approx \frac{m E(r') \sin \theta_0}{\sin \theta} \begin{Bmatrix} \sin m\phi \\ -\cos m\phi \end{Bmatrix} G_{\text{opt}}'(\mathbf{r}; \mathbf{r}', \theta_0), \quad (35a)$$

$$r \hat{E}_\phi|_{\text{opt}} \approx E(r') e^{i(kr - \pi/4)} \begin{Bmatrix} \cos m\phi \\ \sin m\phi \end{Bmatrix} \sqrt{\frac{kr' \sin \theta_0}{2\pi \sin \theta}} \cdot [\sin(\theta_0 - \theta) e^{-ikr' \cos(\theta_0 - \theta)} + i(-1)^m \sin(\theta_0 + \theta) \cdot e^{-ikr' \cos(\theta_0 + \theta)} \eta(\pi - \theta_0 - \theta)], \quad (35b)$$

where G_{opt}' is given in (25a) provided that $T(\mathbf{r}', \alpha)$ is replaced by $\bar{T}(\mathbf{r}', \alpha)$ in (31) near $\alpha = \theta + \theta_0 \approx \pi$. In the calculation of (35b) from the modified (25a), the θ -derivative of $\bar{T}(\mathbf{r}', \theta_0 + \theta)$ has been neglected since it is $O(1/\sqrt{kr'})$ with respect to the other terms; moreover, (35b) is continuous at $\theta_0 + \theta = \pi$ without the inclusion of \bar{T} . For $\theta \approx 0$, G_{opt}' in (35a) is taken from (28), while

$$r \hat{E}_\phi|_{\text{opt}} \approx E(r') e^{i(kr - m\pi/2)} \begin{Bmatrix} \cos m\phi \\ \sin m\phi \end{Bmatrix} (kr' \sin \theta_0) \cdot e^{-ikr' \cos \theta \cos \theta_0} [i \sin \theta \cos \theta_0 J_m(x) + \cos \theta \sin \theta_0 J_m'(x)], \quad (35c)$$

$$x = kr' \sin \theta \sin \theta_0.$$

Although the ϕ component of the geometric-optical electric field is larger by $O(kr')$ than the θ component when $\theta \approx 0$, the two components are of comparable magnitude as $\theta \rightarrow 0$. A finite field along the cone axis exists only when $m=1$, as seen from (35). The θ and ϕ components are equal in this case and yield the following electric field at $\theta=0$:

$$r \hat{E}|_{\text{opt}} = y_0 E(r') \frac{i}{2} e^{ikr} kr' \sin^2 \theta_0 e^{-ikr' \cos \theta_0}, \quad m=1, \quad (36)$$

where y_0 is a unit vector along the y -axis ($\phi = \pi/2$).

B. Azimuthal Magnetic Currents

We now consider the physical configuration in Fig. 6 excited with a radial electric aperture field distribution $r_0 E(r')$, with $E(r')$ given in (32). The corresponding magnetic current distribution $\mathbf{M} = \theta_0 \times \mathbf{E} = -\phi_0 E$ is azimuthal so that one requires in general two scalar potential functions S_1' and S_1'' to represent the radiated field. The field radiated by a ring source of azimuthal magnetic currents on the cone surface is given by^{1,16,17}

$$\hat{\mathbf{H}}(\mathbf{r}, \mathbf{r}') = \int_0^{2\pi} \mathbf{y}(\mathbf{r}, \mathbf{r}') \cdot \phi_0 E(r') d\phi' r' \sin \theta_0, \quad (37)$$

where \mathbf{y} is the dyadic magnetic Green's function, with

¹⁶ L. I. Bailin and S. Silver, "Exterior boundary value problems for spheres and cones," IRE TRANS. ON ANTENNAS AND PROPAGATION, vol. AP-4, pp. 5-16; January, 1956. See also vol. AP-5, p. 313; July, 1957.

¹⁷ L. B. Felsen, "Alternative field representations in regions bounded by spheres, cones, and planes," IRE TRANS. ON ANTENNAS AND PROPAGATION, vol. AP-5, pp. 109-119; January, 1957.

$$y(r, r') \cdot \phi_0 = \frac{i\omega\epsilon}{r'} \nabla \times \left(r_0 \frac{\partial S_1'}{\partial \theta'} \right) \Big|_{\theta'=\theta_0} + \frac{1}{i\omega\mu r' \sin \theta_0} \nabla \times \left(\nabla \times r_0 \frac{\partial^2}{\partial \phi' \partial r'} S_1'' \right) \Big|_{\theta'=\theta_0}, \quad (37a)$$

$$S_1'(r, r') = \frac{\sqrt{rr'}}{2\pi} \sum_{m=0}^{\infty} \epsilon_m \cos m(\phi - \phi') \cdot \int_{\bar{C}} \frac{d\xi}{\xi^2 - \frac{1}{4}} \xi J_\xi(kr_{<}) H_\xi^{(1)}(kr_{>}) G_\theta(\theta, \theta'; m^2; \xi^2 - \frac{1}{4}), \quad (37b)$$

$$\hat{H}_s(r, r') = \phi_0 E(r') \frac{i\omega\epsilon\pi}{8} \sin \theta' \sqrt{\frac{r'}{r}} \int_{-\infty}^{\infty} \frac{x H_{ix}^{(1)}(kr) H_{ix}^{(1)}(kr') K_x^1(\cos \theta) K_x^1(\cos \theta') K_x(-\cos \theta_0)}{(x^2 + \frac{1}{4}) \cosh \pi x K_x(\cos \theta_0)} dx, \quad (39)$$

$S_1''(r, r')$ = same as S_1' except that G_θ is replaced by G_θ' . (37c)

G_θ' is defined in (6). G_θ is obtained from G_θ' upon replacing the operator $(d/d\theta_0)$ by unity. The path \bar{C} in the ξ -plane is shown in Fig. 7 and excludes the pole at $\xi=1/2$.

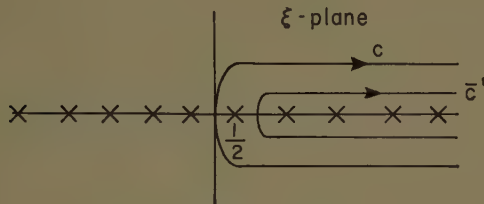


Fig. 7—Contours of integration.

For the special case of uniform field excitation, *i.e.*, $m=0$, only the S_1' term contributes since

$$\int_0^{2\pi} d\phi' \frac{\partial}{\partial \phi'} S_1''(r, r') = 0. \quad (38)$$

Thus,

$$\hat{H}(r, r') = -\phi_0 E(r') \frac{i\omega\epsilon}{2} \sin \theta_0 \sqrt{\frac{r'}{r}} \left[\frac{\partial^2}{\partial \theta \partial \theta'} I(r, r') \right]_{\theta'=\theta_0}, \quad (38a)$$

where

$$I(r, r') = \int_{\bar{C}} \frac{\xi}{\xi^2 - \frac{1}{4}} J_\xi(kr_{<}) H_\xi^{(1)}(kr_{>}) G_\theta(\theta, \theta'; 0; \xi^2 - \frac{1}{4}) d\xi. \quad (38b)$$

Since

$$\frac{\partial^2}{\partial \theta \partial \theta'} G_\theta \Big|_{\theta'=\theta_0} = \frac{-\frac{d}{d\theta} P_\nu(\cos \theta)}{\sin \theta_0 P_\nu(\cos \theta_0)}, \quad \nu + \frac{1}{2} = \xi, \quad (38c)$$

and since $(d/d\theta)P_\nu(\cos \theta) \propto \nu$ as $\nu \rightarrow 0$, the integrand in (38b), resulting upon performing the $(\partial^2/\partial \theta \partial \theta')$ operation, has no pole at $\xi=1/2$. Thus, as far as the total result in (38a) is concerned, the contour of integration

\bar{C} may be deformed directly into the path C shown in Fig. 7.

To effect an asymptotic evaluation as $r \rightarrow \infty$, $kr' \gg 1$, one may employ the image representations for G_θ' and G_θ in (17), and separate the geometric-optical from the diffracted contributions by following the technique described in the analysis of the scalar problems in Section II. An exact integral representation analogous to that in (4d) for the scattered magnetic field \hat{H}_s due to a ring source with $m=0$ situated at (r', θ') is found to be given for $\theta + \theta' < 2\theta_0 - \pi$ by

where $K_x^m = P_{-1/2+ix}^m$. The transition to an asymptotic formula as in (9) and an approximate evaluation for $\theta_0 \approx \pi$ has been discussed.^{1,2}

To obtain the geometric-optical field for $m=0$, we examine the contribution to the integral in (38b) from those sources in (17) situated at $\pm\theta'$, $\pm(2\theta_0 - \theta')$ in the infinitely extended θ -space; all other image sources contribute only to the diffracted field. For an evaluation to the lowest order in kr' (as $r \rightarrow \infty$, $kr' \gg 1$) only the large ξ behavior of the integrand is of importance so that the various image terms can be approximated by their asymptotic form as $|\xi| \rightarrow \infty$. [See (21a) with $\Gamma_{\theta_0'} = 1$ replaced by $\Gamma_{\theta_0} = -1$, since the pertinent function is \bar{G}_0 and not \bar{G}_0']. Upon performing the $(\partial^2/\partial \theta \partial \theta')$ operation and approximating $1/(\xi^2 - 1/4)$ by $1/\xi^2$, one finds that the resulting integrand is the same as would be obtained in (20a) with (21a) by letting $m=1$. Thus, the geometric-optical effects for $m=0$ in the present problem, determined to the lowest order by the large ξ behavior of the integrand, are the same as those in (25a) and (28), for $m=1$. For the behavior in the transition region $\theta \approx \pi - \theta_0$, $T(r', \alpha)$ in (25c) is replaced by $\bar{T}(r', \alpha)$ in (31). In summary, for $m=0$ in the present problem,

$$r \hat{H} \Big|_{\text{opt}} = -\phi_0 i\omega\epsilon E(r') r' \sin \theta_0 [G_{\text{opt}}(\theta; r', \theta_0)]_{m=1}. \quad (40)$$

The radiation from a narrow ring slot with uniform radial electric field excitation was computed by Bailin and Silver¹⁶ from the exact, but slowly convergent, radial transmission formulation [analogous to (4a)] for $kr' = 50\pi$, $\theta_0 = 165^\circ$. Their results have been compared by Goodrich, *et al.*,¹⁸ with the lowest order geometric-optical contribution in (40) and found to agree fairly well. Goodrich, *et al.*, computed the geometric-optical field outside the transition regions for this, as well as excitations with $\exp(im\phi')$ variation, directly by a simple physical optics calculation. Unlike the present method, the physical optics approach cannot be rigorously extended to yield information about transition and diffraction effects.

¹⁸ R. F. Goodrich, *et al.*, "Studies in Radar Cross-Sections XXII, Elementary Slot Radiators," Eng. Res. Inst., University of Michigan, Ann Arbor, Rep. No. 2472-13-T; November, 1956.

C. Sample Calculation

To illustrate the radiation pattern to be expected from a leaky wave type radial magnetic current distribution on a semi-infinite cone, we consider $E(r')$ in (32) to be given by

$$\begin{aligned} E(r') &= \cos m\phi' e^{i\xi r'}, & r_1 < r' < r_2 \\ &= 0, & r' < r_1, \quad r' > r_2. \end{aligned} \quad (41)$$

This source distribution with ξ real and less than k in magnitude represents approximately the effect of certain two-dimensional leaky wave type antenna arrays. The first-order geometric-optical field (including transition regions) is obtained from (35) upon substituting (41) and integrating over r' between the limits r_1 and r_2 . For $\theta \sim 0$, the following typical integrals must be evaluated:

$$\begin{aligned} W_1(\alpha) &= \sqrt{k} \int_{r_1}^{r_2} \frac{e^{i\alpha r'}}{\sqrt{r'}} dr' \\ &= e^{i\pi/4} \sqrt{\frac{\pi k}{\alpha}} \left[e^{i\alpha r_1} F\left(\sqrt{\frac{\alpha r_1}{2}}\right) - e^{i\alpha r_2} F\left(\sqrt{\frac{\alpha r_2}{2}}\right) \right], \end{aligned} \quad (42a)$$

$$\begin{aligned} W_2(\alpha) &= k^{3/2} \int_{r_1}^{r_2} \sqrt{r'} e^{i\alpha r'} dr' \\ &= \frac{k}{i\alpha} [\sqrt{kr_2} e^{i\alpha r_2} - \sqrt{kr_1} e^{i\alpha r_1} - \frac{1}{2} W_1(\alpha)], \end{aligned} \quad (42b)$$

where the Fresnel type integral F is defined in (24b) and plotted in Fig. 5. When $\theta \approx 0$, the integrations cannot be carried out in closed form but require the series representation for the Bessel functions and subsequent term-wise integration.¹⁹

Numerical results for the radiation patterns are presented in Figs. 8(a) and 8(b) for $kr_1=20$, $kr_2=50$, $\theta_0=165^\circ$ and $-\xi/k=0.65, 0.75, 0.85$, with $m=0, 1$. The calculations were made from the above mentioned formulas in the ranges $\theta < 4^\circ$ and $\theta > 10^\circ$. For $\theta > 4^\circ$, the series representation appropriate for small θ becomes rather unwieldy while for $\theta < 10^\circ$, the accuracy of the formulas of the type presented in (35b) is questionable. Therefore, the range $4^\circ < \theta < 10^\circ$ has been filled in by what appears to be a reasonably smooth curve.

APPENDIX I

The angular traveling wave functions are defined as follows:

$$\begin{aligned} P_{\xi\mu}^{(1)/(2)}(\theta) &= \pm i \csc(\xi - \tfrac{1}{2} - \mu)\pi [P_{\xi-1/2}^{-\mu}(-\cos\theta) \\ &\quad - e^{\pm i(\xi-1/2-\mu)\pi} P_{\xi-1/2}^{-\mu}(\cos\theta)], \end{aligned} \quad (43)$$

¹⁹ C. N. Campopiano and L. B. Felsen, "Radiation patterns of two-dimensional leaky and surface wave distributions on a semi-infinite cone," Microwave Res. Inst., Polytechnic Inst. of Brooklyn, Brooklyn, N. Y., Electrophysics Group Memo. No. 35; November, 1957.

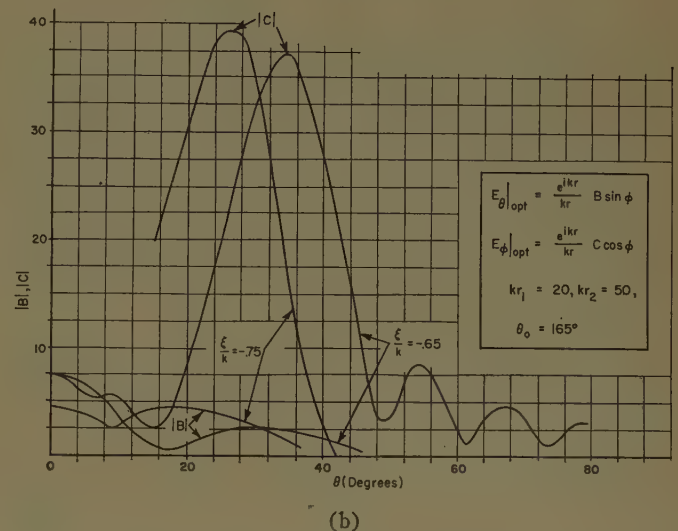
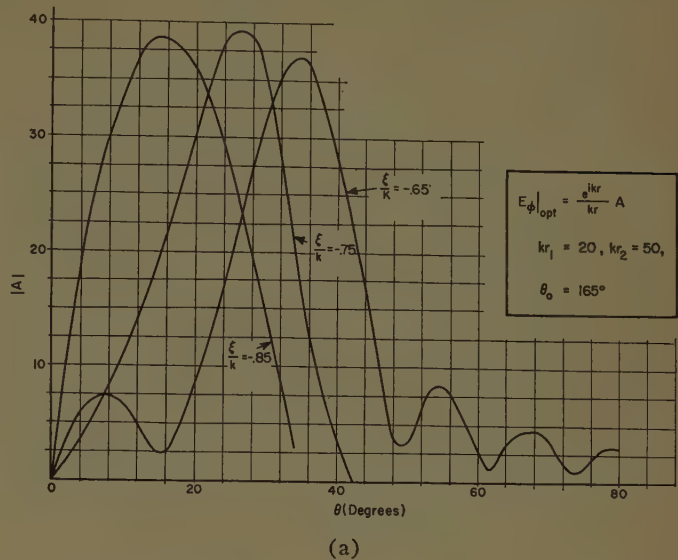


Fig. 8—Leaky wave distribution of radial magnetic currents: (a) $M(r') = r_0 e^{i\xi r'}$, (b) $M(r') = r_0 e^{i\xi r'} \cos \phi'$.

and can be represented in terms of the hypergeometric function as²⁰

$$\begin{aligned} P_{\xi\mu}^{(1)/(2)}(\theta) &= \sqrt{\frac{2}{\pi \sin \theta}} \frac{\Gamma(\xi - \mu + \tfrac{1}{2})}{\Gamma(\xi + 1)} \\ &\cdot e^{\pm i(\xi\theta - \mu\pi/2 - \pi/4)} F\left(\frac{1}{2} + \mu, \frac{1}{2} - \mu; \xi + 1; \frac{e^{\pm i\theta}}{\pm 2i \sin \theta}\right). \end{aligned} \quad (44)$$

The representation in (14a) is accomplished via the transformation²¹

$$F\left(a, b; c; \frac{z}{1-z}\right) = (1-z)^b F(b, c-a; c; z). \quad (45)$$

One notes from (43) that

$$P_{\xi\mu}^{(2)}(\pi - \theta) = e^{-i(\xi-1/2-\mu)\pi} P_{\xi\mu}^{(1)}(\theta); \quad (46)$$

²⁰ For the case $\mu=0$ in connection with the sphere problem, see Fok, op. cit., and Franz, op. cit. See also H. Bremmer, "Terrestrial Radio Waves," Elsevier Publishing Co., New York, N. Y., p. 26; 1949.

²¹ W. Magnus and F. Oberhettinger, "Special Functions of Mathematical Physics," Chelsea Publishing Co., New York, N. Y., p. 8; 1949.

moreover, the Wronskian is given by

$$P_{\xi\mu}^{(1)}(\theta) \frac{d}{d\theta} P_{\xi\mu}^{(2)}(\theta) - P_{\xi\mu}^{(2)}(\theta) \frac{d}{d\theta} P_{\xi\mu}^{(1)}(\theta) = \frac{4}{\pi i \sin \theta} \frac{\Gamma(\xi - \mu + \frac{1}{2})}{\Gamma(\xi + \mu + \frac{1}{2})}. \quad (47)$$

The large ξ behavior follows directly from (44) upon use of the asymptotic formulas

$$F(a, b; c; z) = 1 + O\left(\frac{1}{c}\right), \quad c \rightarrow \infty, \quad (48)$$

and

$$\Gamma(\xi + \alpha) \sim \sqrt{\frac{2\pi}{\xi}} \left(\frac{\xi}{e}\right)^{\xi} \xi^{\alpha} \left[1 + O\left(\frac{1}{\xi}\right)\right], \quad \xi \rightarrow \infty, \quad |\arg \xi| < \pi. \quad (48b)$$

It is noted from (44), (48a), and (14a) that $P_{\xi\mu}^{(1),(2)}(\theta)$ has no zeros or poles for values of $|\xi| \gg 1$. Since $P_{\xi-1/2}^{-\mu}(\pm \cos \theta)$ is a real function of x when $\xi = ix$, x real ($\mu > 0$), and has no zeros or poles for any finite value of x , one notes from (43) that $P_{\xi\mu}^{(1),(2)}(\theta)$ has no zeros or poles for imaginary values of ξ . Since $\Gamma(\xi + \alpha)$ has no zeros or poles for real α and imaginary ξ , it follows from the above that the functions $R_{\xi m}^{(1),(2)}$ and $f_{\xi m}'$ defined in (14a) and (16) have no singularities for imaginary values of ξ .

We also require the large order asymptotic formulas for the cylinder functions in the right half of the ξ -plane,²²

$$J_{\xi}(x) \sim \left(\frac{x}{2}\right)^{\xi} \frac{1}{\Gamma(\xi + 1)} \left[1 + O\left(\frac{1}{\xi}\right)\right], \quad |\xi| \rightarrow \infty, \quad (49a)$$

with the corresponding formula for the Hankel function obtained from

$$H_{\xi}^{(1)}(y) = \frac{-e^{-i\xi\pi} J_{\xi}(y) + J_{-\xi}(y)}{i \sin \xi\pi}. \quad (49b)$$

Thus, one finds

$$J_{\xi}(x) H_{\xi}^{(1)}(y) \sim \frac{1}{\pi i \xi} \left(\frac{x}{y}\right)^{\xi} \left[1 - \frac{e^{-i\xi\pi}}{2 \sin \xi\pi} \left(\frac{ey}{2\xi}\right)^{2\xi}\right], \quad |\xi| \rightarrow \infty, \quad |\arg \xi| < \pi. \quad (50)$$

The second term inside the brackets in (50) is negligible in the right half of the ξ -plane except when $(\arg \xi) \rightarrow \pi/2$. In that instance one has

$$|J_{\xi}(x) H_{\xi}^{(1)}(y)| \sim \frac{1}{\pi |\xi|} e^{\pi |\xi|}, \quad \xi \rightarrow i\infty. \quad (51)$$

APPENDIX II

To estimate the contribution to the integral I_1 in (20a) from the second term in (21) as $r \rightarrow \infty$, $kr' \gg 1$, consider

$$I_1' = \int_{C'} \xi J_{\xi}(kr') H_{\xi}^{(1)}(kr') G_{\theta}^{\infty}(\theta, \varphi) [F(\xi, \theta, \varphi) - 1] d\xi, \quad (52)$$

where $G_{\theta}^{\infty} F$ represents the exact form of a typical image term as given in (17), i.e., F is composed of the factors $R_{\xi m}^{(1),(2)}$, $f_{\xi m}'$, []. Let the path C' in Fig. 2 be broken up into the paths P and Q in Fig. 9 ($Q = Q_1 + Q_2 + Q'$),

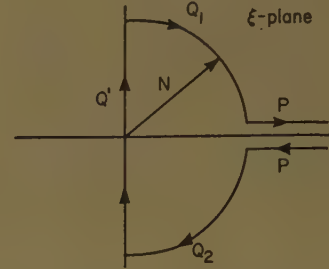


Fig. 9—Paths in complex ξ -plane.

where $N = (kr')^{1-\epsilon}$, $0 < \epsilon \ll 1/2$. This path deformation is possible since the integrand contains no singularities in the region $|\xi| > N \gg 1$. Since $(F-1) = O(1/\xi)$ as $|\xi| \rightarrow \infty$ and \bar{I} in (23a) is $O(1)$ in kr' [see (24)], the contribution to I_1' from path P is $O(1/N)$. Over the remaining contour, $\xi/kr' = 0[(kr')^{-\epsilon}]$, so that the large argument asymptotic formula for the cylinder functions can be employed to yield

$$I_1' = \frac{e^{ikr}}{\pi \sqrt{kr}} \left[\frac{e^{i(kr' - \pi/2)}}{\sqrt{kr'}} \int_Q \xi e^{-i\xi\pi} H(\xi) d\xi + \frac{e^{-ikr'}}{\sqrt{kr'}} \int_Q \xi H(\xi) d\xi \right] + O\left(\frac{1}{N}\right), \quad (53)$$

where $H = (F-1)G_{\theta}^{\infty}$. In the evaluation of the second integral in (53), we note that the contribution from paths $Q_{1,2}$ is $O(1/N)$ since $|\xi H(\xi)| \propto (1/N) \exp[-|\operatorname{Im} \xi| |\theta - \varphi|]$. Moreover, from (17),

$$H(\xi) |_{\operatorname{Im} \xi > 0} = H(-\xi) |_{\operatorname{Im} \xi < 0}, \quad (54)$$

so that the integral along the imaginary axis vanishes. Thus,

$$I_1' = \frac{-i}{\pi k \sqrt{rr'}} e^{ik(r+r')} \int_Q \xi e^{-i\xi\pi} H(\xi) d\xi + O\left(\frac{1}{N}\right), \quad |\theta - \varphi| \neq 0, \quad (55)$$

i.e., I_1' contributes only to the diffracted wave, to $O(1/\sqrt{kr'})$. Since $F(\xi, \theta, \varphi)$ is analytic along the path Q for all values of θ and φ (see Appendix I), it follows that the functional dependence of I_1' as a function of θ and φ is the same for all θ and φ .

ACKNOWLEDGMENT

The author expresses his thanks to Harold Hunter of the Radiation Laboratory of the University of Michigan, Ann Arbor, for performing the numerical calculations.

²² *Ibid.*, p. 16.

The Equiangular Spiral Antenna*

JOHN D. DYSON†

Summary—A circularly polarized antenna is described which makes possible bandwidths that a few years ago were considered to be impossible.

The design of the antenna is based upon the simple fundamental principle that if the shape of the antenna were such that it could be specified entirely by angles, its performance would be independent of wavelength. Since all such shapes extend to infinity it is necessary to specify at least one length for an antenna of finite size. The one length in this antenna, the arm length, need only be of the order of one wavelength at the lowest frequency of operation to obtain operation essentially independent of frequency, and the geometry of the antenna allows this arm length to be spiraled into a maximum diameter of one half wavelength or less. Antennas have been constructed that have an essentially constant radiation pattern and input impedance over bandwidths greater than 20 to 1.

INTRODUCTION

ONE of the serious drawbacks to any simplified solution toward providing coverage of large portions of the frequency spectrum has been the extremely limited bandwidths obtainable with both the receiving and transmitting equipment and the antennas required to successfully launch and receive electromagnetic radiation. As a result, a great deal of effort has been expended in the development of broad-band equipment. This paper is concerned with the latter portion of the problem, the development of a broad-band antenna.

The term "broad-band" has been loosely applied in the past, but has usually described antennas whose radiation and input impedance characteristics were acceptable over, at most, a frequency range of 2 or 3 to 1. The bandwidth of the radiation pattern has been the limiting factor since antennas have been developed with an input impedance that stays relatively constant with a change in frequency.

Several really broad-band antennas have been proposed in recent years—the discone by Kandoian,¹ the conical helix by Springer² and later by Chatterjee,³ the Archimedes spiral by Turner⁴ and the logarithmically periodic antenna by DuHamel and Isbell.⁵

* Manuscript received by the PGAP, June 16, 1958; revised manuscript received, December 11, 1958. This material was taken from a thesis submitted in partial fulfillment of the requirements for the Ph.D. degree in electrical engineering at the University of Illinois, 1957. A treatment in more detail is given in Tech. Rep. No. 21, Contract AF 33(616)-3220, Antenna Lab., University of Illinois, September 15, 1957. ASTIA No. AD-145019. This work was supported by the Wright Air Dev. Center under Contract No. AF 33(616)-3220.

† Antenna Lab., University of Illinois, Urbana, Ill.

¹ A. G. Kandoian, "Three new antenna types and their applications," *Proc. IRE*, vol. 34, pp. 70w-75w; February, 1946.

² P. S. Springer, "End-Loaded and Expanding Helices as Broad Band Circularly Polarized Radiators," Electronic Subdivision, USAF, Air Material Command, Wright-Patterson AFB, Tech. Rep. No. 6104; January, 1950.

³ J. S. Chatterjee, "Radiation field of a conical helix," *J. Appl. Phys.*, vol. 24, p. 550; May, 1953.

⁴ E. M. Turner, "Spiral Slot Antenna," Wright Air Dev. Center, Dayton, Ohio, Tech. Note WCLR-55-8; June, 1955.

⁵ R. H. DuHamel and D. E. Isbell, "Broadband logarithmically periodic antenna structures," 1957 IRE NATIONAL CONVENTION RECORD, pt. 1, pp. 119-128.

In the fall of 1954, Rumsey of the University of Illinois advanced the theory that an antenna constructed in the form of an equiangular spiral of infinite length would have an infinite pattern and impedance bandwidth, and proposed that the characteristics of the finite size structure be investigated. Subsequent investigation disclosed that the equiangular spiral antenna was the first antenna to exhibit, in a practical size, the characteristics associated with an infinite structure.^{6,7} Thus, it became the first of a class of antennas which may be called "frequency independent antennas."⁸ More recent work by DuHamel and Isbell has indicated that the logarithmically periodic structures which they have considered have as wide a practical bandwidth as the equiangular spiral. These structures however are linearly polarized while the spiral is a circularly polarized antenna.

This paper is concerned with some of the characteristics of, and design information for, the balanced planar equiangular spiral antenna.

DEFINITION OF THE ANTENNA

The design of the equiangular spiral antenna is based upon a simple fundamental principle. If all dimensions of a perfectly conducting antenna (immersed in lossless free space) are changed in linear proportion to a change in wavelength, the performance of the antenna is unchanged except for a change of scale in all measurements of length. Thus, as Rumsey has pointed out, it follows that if the shape of the antenna were such that it could be specified entirely by angles, its performance would be independent of frequency.

Since all such shapes extend to infinity it is necessary to specify at least one length in order to specify an antenna of finite size. This principle can be used as a basis for practical antenna design, because in some cases the antenna performance is practically independent of wavelength, provided this one length is very long compared with the wavelength of operation. An investigation of the equiangular spiral antenna has shown that for this antenna the one specified length, the arm length, need not be large compared to a wavelength, and in fact need only be comparable to one wavelength at the lowest frequency of operation to obtain performance essentially independent of frequency.

The equiangular or logarithmic spiral is a plane curve which may be defined by the equation, $\rho = ke^{a\phi}$ as in

⁶ J. D. Dyson, "The Equiangular Spiral Antenna," Fifth Symp. on the USAF Antenna Res. and Dev. Program, Robert Allerton Park, Univ. of Illinois, Monticello, Ill., October 22, 1955. (Classified)

⁷ J. D. Dyson, "The Equiangular Spiral Antenna," Univ. of Illinois, Urbana, Ill., Tech. Rep. No. 21, Contract AF 33(616)3220; September 15, 1957.

⁸ V. H. Rumsey, "Frequency independent antennas," 1957 IRE NATIONAL CONVENTION RECORD, pt. 1, pp. 114-118.

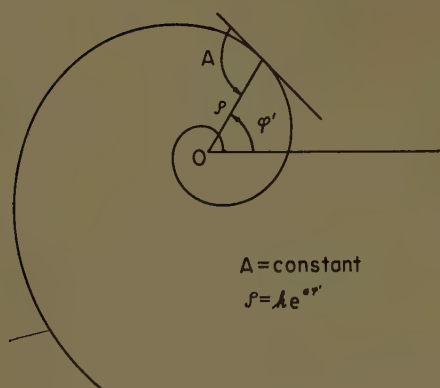


Fig. 1—The equiangular spiral.

Fig. 1; ρ and ϕ are the conventional polar coordinates and a and k are positive constants.

If the angle ϕ is increased by one full turn, the radius vector is increased by the factor $e^{2\pi a}$, hence each turn of the spiral is identical with every other turn except for a constant multiplier.

The length of the spiral may be calculated from

$$L = \int_{\rho_0}^{\rho} \left[\rho^2 \left(\frac{d\phi}{d\rho} \right)^2 + 1 \right]^{1/2} d\rho, \quad (1)$$

which reduces to

$$L = [a^{-2} + 1]^{1/2} (\rho - \rho_0). \quad (2)$$

To create an antenna from the equiangular spiral, we consider a conductor with edges defined by the two curves,

$$\rho_1 = ke^{a\phi} \quad (3)$$

and

$$\rho_2 = ke^{a(\phi-\delta)} = K\rho_1, \quad (4)$$

where

$$K = e^{-a\delta} = \frac{\rho_2}{\rho_1} < 1. \quad (5)$$

The edges of this conductor are identical curves, with one rotated through the fixed angle δ , with respect to the other. This rotation gives the arm a finite width.

A second conductor may be defined by

$$\rho_3 = ke^{a(\phi-\pi)} \quad (6)$$

and

$$\rho_4 = ke^{a(\phi-\pi-\delta)} = K\rho_3. \quad (7)$$

These two conductors constitute a balanced antenna of infinite length. To specify a finite size structure, one fixed length, the arm length, must be specified. The arm length as used here refers to the spiral length along the center line of the arm. Fig. 2 is an outline drawing of a practical antenna.

It should be noted at this point that the antenna could be completely specified by the angle, δ , which de-



Fig. 2—Outline drawing of an antenna. ($a=0.35$, $K=0.597$, $k=0.2$ inch, maximum diameter = $9 \frac{3}{16}$ inch.)

termines the arm width, the arm length, and the constants a and k , the former controlling the rate of spiral and the latter the size of the terminal region.

However, the investigation has disclosed that most of the characteristics of the antenna can be adequately specified in terms of only three variables, the arm length, the constant k and a constant K , defined in (5), which is a convenient measure of the angular width of the antenna arm, the width along the radius vector. A practical balanced antenna imposes a lower bound on K (i.e., $e^{-a\pi} < K < 1$) if the space between the arms is to remain open.

The investigation with which this paper is concerned has been confined to the balanced, planar, equiangular spiral antenna with a balanced feed. Two forms of this antenna have been used, the plane conductor antenna, i.e., metallic arms suspended in free space, and the slot antenna, which consists of spiral slots cut in a large conducting sheet. Fig. 3 shows three of the slot antennas investigated. The slot antennas are shown cut into a 14-inch square of 1/32-inch copper which was bolted into a larger ground plane.

The slot antenna is a most useful form because it makes it possible to feed the balanced structure in a completely balanced manner simply by embedding the coaxial feed cable in the ground plane, or soldering it to the ground plane, as shown in Figs. 3 and 4. This method of feed, which might be referred to as an "infinite balun," is made possible by the rapid attenuation of the near fields on the arms. It is the only form of balun presently in use which will permit the fullest use

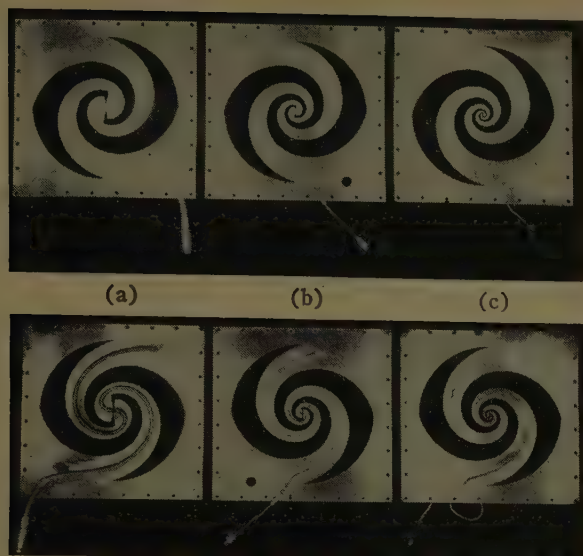


Fig. 3—One slot antenna showing modifications in terminal region to accommodate three sizes of feed cable.

of the infinite impedance and pattern bandwidths of this antenna. The only disadvantage of this type of feed is that it requires leaving sufficient ground screen between the slot arms to carry the feed cable. This imposes a requirement that the spiral be terminated at the center in a fairly large feed section, as can be seen in Fig. 3, if a large coaxial feed cable is required. As indicated later, this feed section will determine the upper frequency limit of the antenna.

If the width of the metal on which the cable is mounted approaches the diameter of the feed cable, it becomes necessary to mount a dummy cable on the opposite arm, as has been done in Figs. 3 and 4 to maintain symmetry of construction and to prevent a tilt in the radiation pattern.

THE RADIATION PATTERN

Using (3), we note that if the unit of length is chosen as a wavelength, λ , and if ρ' equals the radial coordinate measured in wavelengths,

$$\rho' = \frac{\rho}{\lambda} = \frac{e^{a\phi}}{\lambda} = e^{a(\phi - 1/a \ln \lambda)}$$

or

$$\rho' = e^{a(\phi - \phi_0)} \quad \text{where} \quad \phi_0 = \frac{1}{a} \ln \lambda. \quad (8)$$

This would indicate that the effect of changing the wavelength is equivalent to changing the angle ϕ . Thus except for a rotation, the pattern of the infinite structure would be independent of frequency. Within the necessary limitation imposed by the one fixed length, *i.e.*, the arm length, this has been found to be true for the finite size structure.

The radiation patterns of more than 40 spiral slot antennas have been investigated with the parameters a and K varying,

$$0.2 \leq a \leq 1.2 \quad \text{and} \quad 0.375 \leq K \leq 0.97.$$

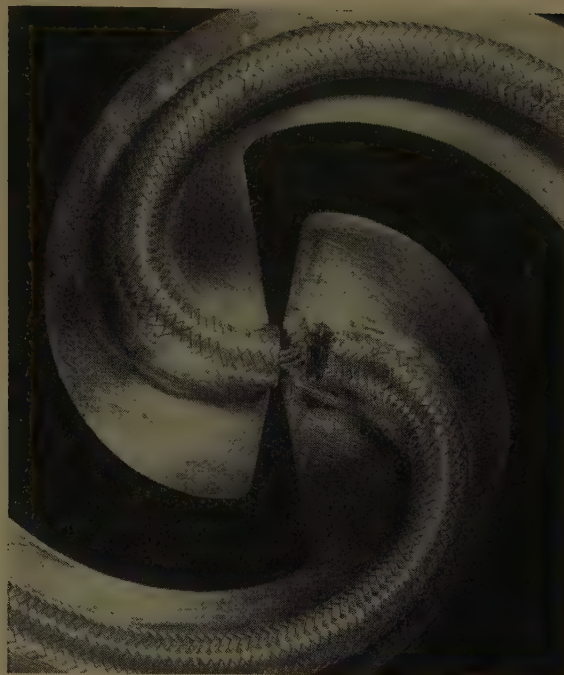


Fig. 4—Terminal region of antenna shown in Fig. 3(b).

Spirals of one-half turn up to three turns have been constructed. The antenna patterns appear to be remarkably insensitive to these variations, although there are optimum ranges of the parameters. Consistently good patterns can be obtained with spirals of only $1\frac{1}{4}$ or $1\frac{1}{2}$ turns.

The antenna radiates a broad lobe perpendicular to the plane of the antenna over a practical range of parameters. This radiation is bidirectional with equal beams radiated from the front and the back of the structure. The beam is circularly polarized on its axis, over the usable bandwidth. There is no tilt to the lobe of the symmetrical antenna.

For frequencies such that the antenna arms are very short in terms of wavelength, the radiated field is linearly polarized. As the arm length is increased (or frequency increased) the field, on the axis perpendicular to the plane of the antenna, becomes elliptically and then circularly polarized. Since there are no distinctive changes in pattern shape, this change in field polarization becomes a convenient criterion for specifying the cutoff of the pattern bandwidth.

The bandwidth, as used here, refers to that band of frequencies over which the antenna radiates a field such that the axial ratio of the polarization ellipse, recorded on the axis of the antenna, is less than 2 to 1. The radiated field will be considered circularly polarized over this bandwidth. Fig. 5 is a plot of the polarization of the radiated field of a typical antenna as a function of frequency.

In general, the relationship of the lower cutoff frequency to antenna size would be a function of the three variables, a , δ , and the length. However, it is notable that all of the measured values can be represented in terms of two parameters, the length and the angular

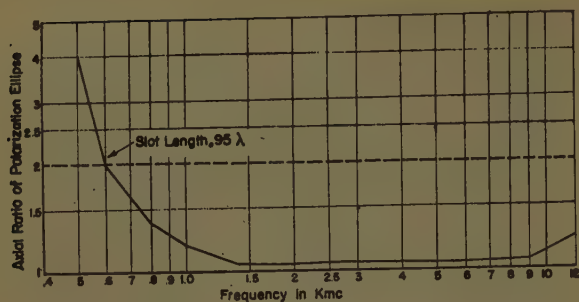


Fig. 5—Polarization, on axis, of the radiated E field of antenna shown in Fig. 3(a).

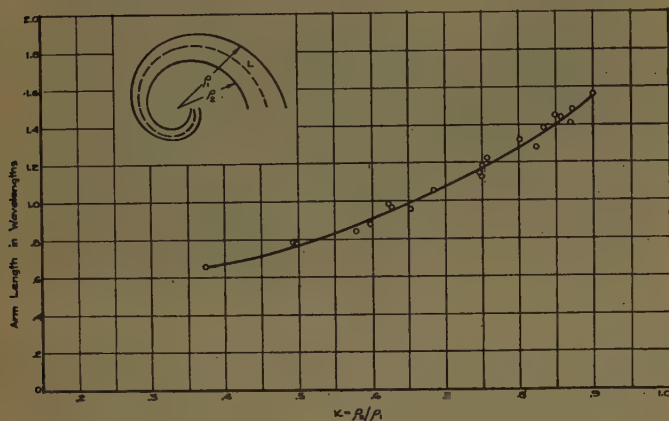


Fig. 6—Minimum slot length in wavelengths necessary to produce circularly polarized radiated field ($r \leq 2:1$ on axis; $0.2 \leq a \leq 0.45$).

width factor K as indicated in Fig. 6. Over the practical ranges of a and K tested, the bandwidth appears to be a function of antenna diameter only insofar as the diameter is a function of how tightly the required length is spiraled. This immediately suggests that the antenna be spiraled tightly (*i.e.*, a made small) if the maximum bandwidth is to be obtained for a given diameter antenna.

An examination of Fig. 2 and the fact that K is restricted to the range $e^{-a\pi} < K < 1$ indicate that a decrease in a raises the lower bound on K , in turn requiring a longer arm length. In addition, a further restriction is imposed on K if sufficient ground screen is left between the slots to carry a feed cable. Thus, depending upon the size of the feed cable, there is an optimum a and K to construct an antenna with the lowest cutoff frequency in a given diameter.

The shape of the termination of the arms has little effect upon the pattern. The arms were terminated along the radius vector, along the orthogonal curve, and along an arc of a circle whose center is at the origin of the spiral. This latter termination has the advantage that it gives the greatest effective arm length, and hence the widest bandwidth, for a given antenna diameter.

The upper cutoff of the bandwidth is a function of the fineness of construction of the spiral at the feed point. Since the spiral converges to a point, it is necessary in a practical structure to terminate the center in a small

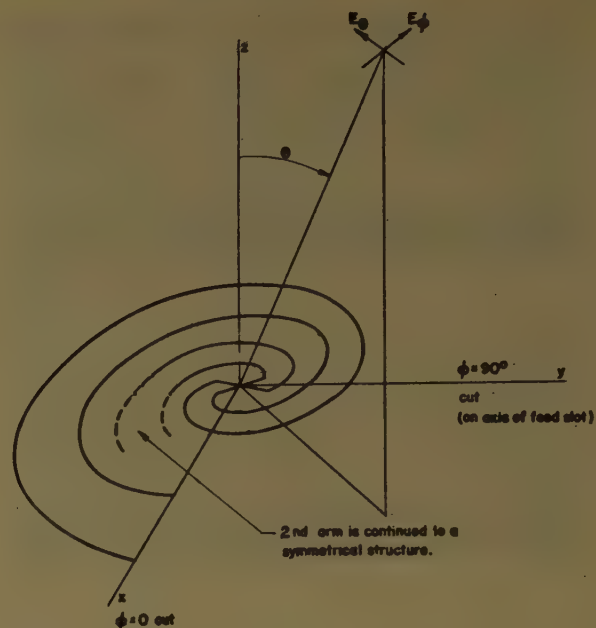


Fig. 7—Polar coordinate system for pattern measurements.

straight or tapered section. This may be noted in Figs. 2–4. At a frequency such that this straight or tapered portion becomes effectively a half-wave slot the axial ratio of the field has increased to approximately 2 to 1. The field becomes elliptically polarized for higher frequencies, so that this specifies the upper cutoff of the pattern bandwidth.

Pattern bandwidths in excess of 20 to 1 have been recorded. This was the usable limit of the pattern range at this laboratory. There is no indication that this bandwidth could not be extended indefinitely.

Since the upper and lower cutoffs are independent, the only limitation is the required diameter in which to spiral the necessary length, and the chosen size of the feed structure.

All of the radiation patterns of the slot antennas were measured on a 12-foot square ground screen pattern range. The patterns are voltage plots and the coordinate system used is indicated in Fig. 7. The spiral slot antennas were bolted into the ground screen and fed as the transmitting antenna. Four patterns were recorded at each frequency; the crossed polarization patterns were recorded at the two principal plane cuts. Polarization patterns were obtained by positioning the receiving antenna on the axis of the spiral antenna and rotating the latter structure in the ground screen.

Radiation patterns of a typical antenna over a 20 to 1 bandwidth are shown in Figs. 8 and 9. This particular antenna is shown in Fig. 3(a).

It was shown earlier that a change in wavelength of operation is equivalent merely to reorienting the antenna or shifting it through some angle around the $\theta = 0$ axis. If the radiated field were independent of ϕ this reorientation would leave the pattern unchanged. However, when viewed from different points on the $\theta = 90^\circ$ plane, the field of the practical structure may

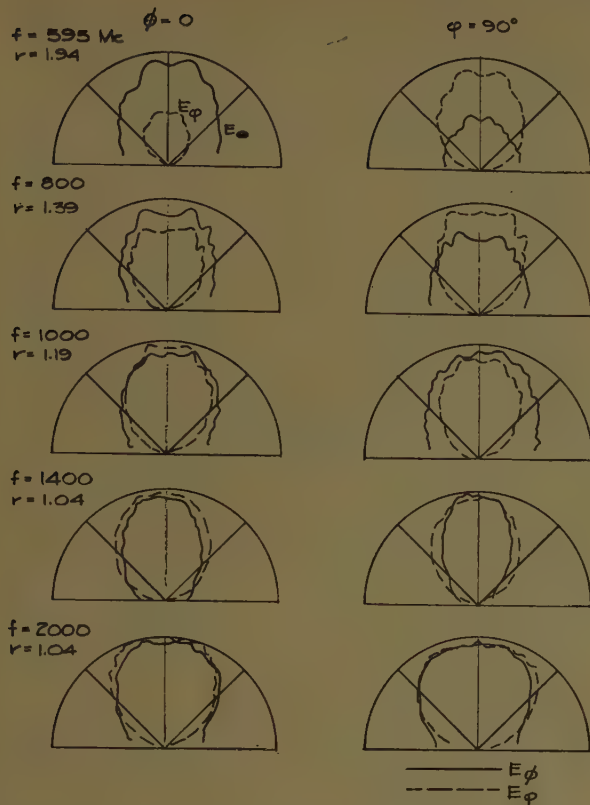


Fig. 8—Radiation patterns of antenna shown in Fig. 3(a). ($a=0.30$, $K=0.62$, $k=0.2$ inch, maximum diameter=28.4 cm, arm length=38.7 cm, r =axial ratio.)

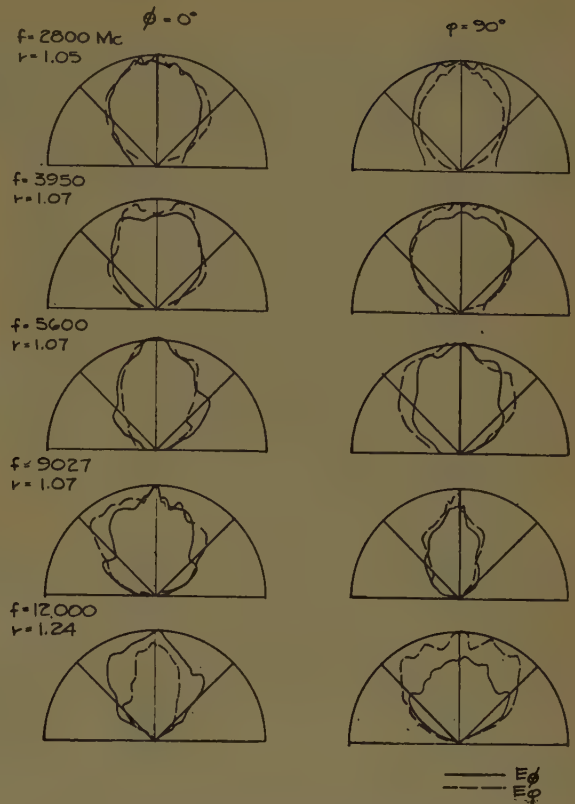


Fig. 9—Radiation patterns of antenna in Fig. 3(a).

have a beamwidth which varies 40° or more. Thus if operation is confined to a fixed frequency, an observer moving around the antenna will note a variation in the beamwidth at the half power points such as that of curve A, Fig. 10. Since the antenna is symmetrical, the variation is periodic every 180° . If the observer remains fixed with respect to the orientation of the antenna, and the frequency of operation is increased, he will observe this same variation of beamwidth. Consequently, if the frequency of operation is changed, the observer must also move around the antenna a fixed angular distance to make the pattern he sees remain unchanged. An examination of (8) indicates that this angle may be expressed as

$$\phi_0 = \frac{1}{\pi} \ln \lambda$$

or

$$\Delta\phi = \phi_1 - \phi_2 = \frac{1}{a} \ln \frac{f_1 + \Delta f}{f_1} \quad (9)$$

Since there are few distinctive pattern changes with frequency, a check of this pattern rotation may be made by a repetition of pattern beamwidth at a new frequency. Figs. 10 and 11 indicate two experimental checks on this rotation. In Fig. 10 we see that the variation in beamwidth, observed through a variation in ϕ from 0° – 210° for fixed frequency operation, is repeated

quite closely by observing at a fixed angle ϕ , and increasing the frequency from 2472 to 7505 mc. The deviation at the low end is traceable to end effect.

In Fig. 11 observe that the variation in beamwidth is held within four degrees by an antenna reorientation, when the frequency was varied from 2 to 5.18 kmc. This is to be compared with the variation of approximately 50° indicated in Fig. 10 over the same band of frequencies without reorientation.

Since the pattern of the equiangular spiral antenna rotates with frequency, a detailed study of pattern change with frequency requires a corresponding antenna rotation for every shift in frequency. In most normal operations, the antenna will be in a fixed mount, and the pattern response with respect to that fixed mount is desired. Hence the patterns in Figs. 8 and 9 are displayed as a function of frequency, without regard to any pattern rotation. This accounts for most of the apparent variation in the patterns over these frequency ranges.

A detailed study made of the near fields along the antenna arms indicated that these fields decay very rapidly (as much as 20 db in the first wavelength) and that this decay is approximately a constant function of the arm length expressed in wavelengths. This has the effect of constantly shortening the active arm length as the frequency is increased, resulting in an effective adjustment of antenna aperture size even though the physical aperture remains constant. There appears to be no tendency for the beamwidth to become narrower

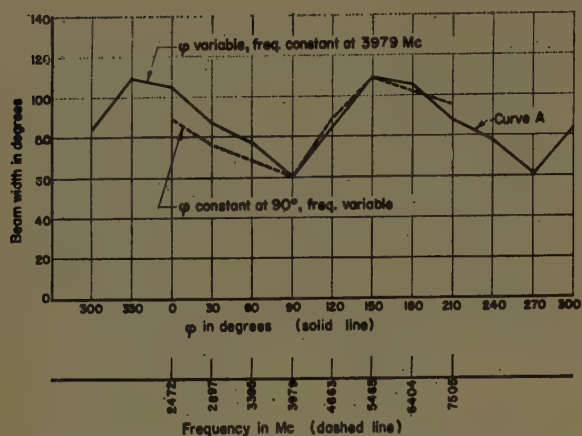


Fig. 10—Rotation of radiated field with a change in frequency. ($a=0.303$, $K=0.75$, $k=0.2$ inch, $L=33$ cm.)

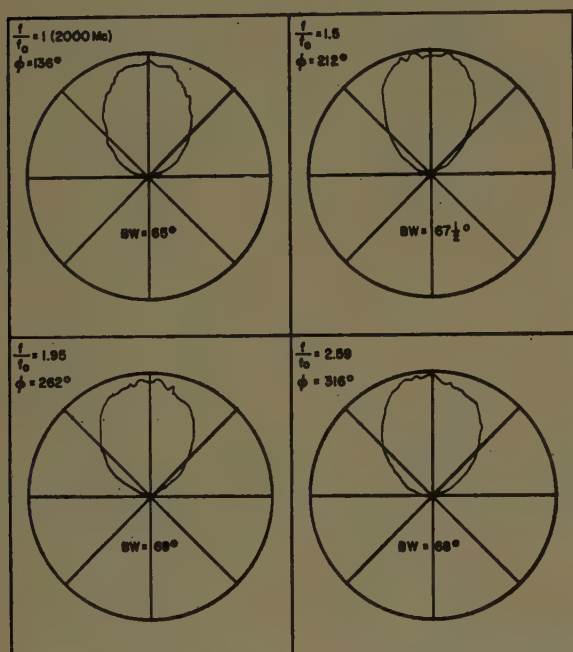


Fig. 11—Patterns obtained by simultaneous rotation of antenna and increase in frequency. ($a=0.303$, $K=0.75$, $k=0.2$ inch, $L=33$ cm) ϕ polarization.

with increased frequency and the antenna aperture expressed in wavelengths appears constant.

The average beamwidth is relatively insensitive to variations of the antenna parameters, but the tighter spiraled antennas and/or antennas with wider arms tend to have smoother and more uniform patterns which exhibit smaller variations in beamwidth.

The polarization of the radiated field, off axis, of a typical antenna is shown in Fig. 12. This particular antenna became circularly polarized on axis at 1000 mc and the bandwidth extends somewhere beyond 12,000 mc. Over more than 80 per cent of the band it is circularly polarized as much as 40° off axis.

THE INPUT IMPEDANCE

The input impedance of the planar balanced equiangular slot antenna converges rapidly as the frequency is increased. For frequencies such that the arm lengths

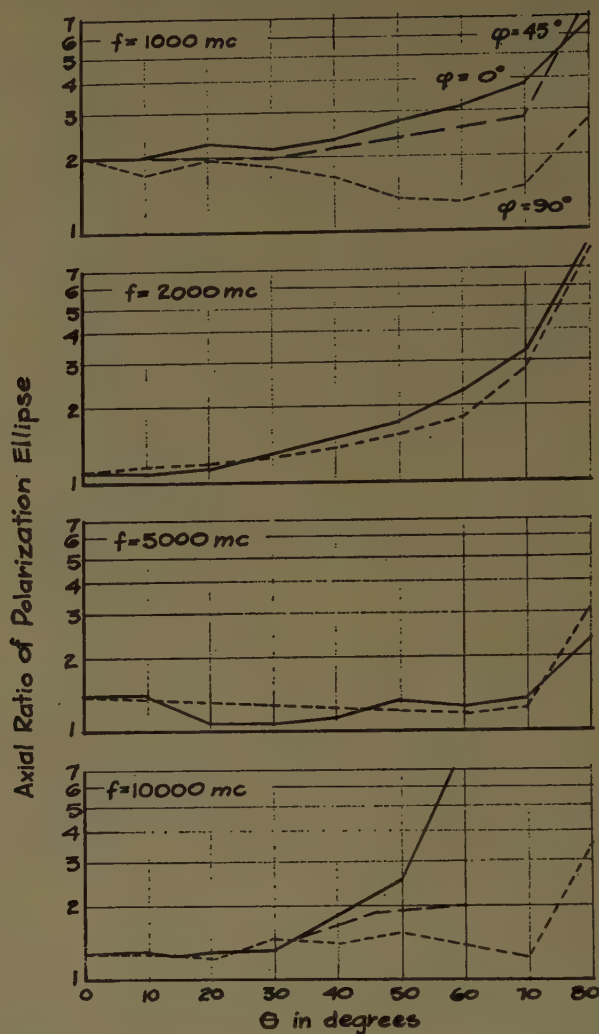


Fig. 12—Polarization of the radiated E field of a balanced planar slot antenna. ($a=0.30$, $K=0.75$, $k=0.2$ inch, $L=42.3$ cm.)

are greater than one wavelength, the impedance remains reasonably constant. The measured impedance of a typical antenna is shown in Fig. 13. This antenna was constructed of $\frac{3}{32}$ -inch copper with a 0.150-inch diameter coaxial cable (RG141/U) bonded to the ground screen between the slot arms.

The input impedance of an antenna of zero thickness would be expected to converge to its characteristic impedance with an increase in frequency. The antenna of finite thickness does not have a uniform characteristic impedance since it is a nonuniform transmission line, but the input impedance rapidly settles down to a reasonably constant value for relatively thin antennas. The measured impedance of the antennas tested is below the theoretical impedance of an infinitely thin antenna, due in part to the thickness of the metal and the presence of the feed cable. There is a relationship between the arm width and the input impedance as indicated in Fig. 14. This curve is based on the measured impedance of antennas constructed of $\frac{3}{32}$ copper, with $k=0.2$ inch, with RG141/U feed cable and without a dummy cable on the opposite arm of the ground screen. The use of a dummy cable of this size will lower the measured impedance approximately 10 per cent. The

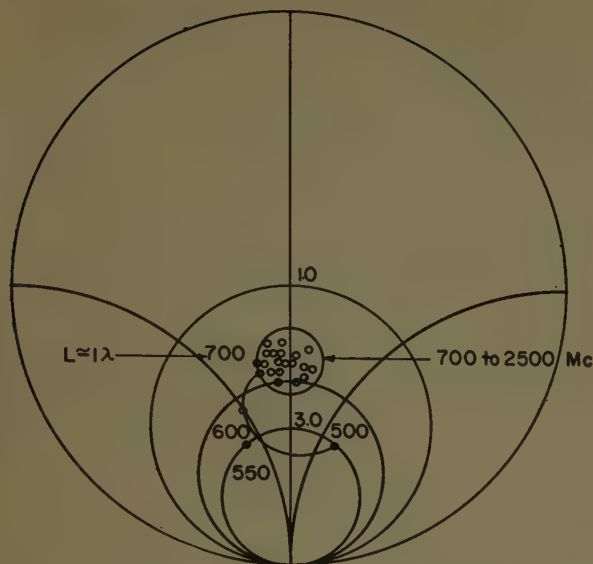


Fig. 13—Input impedance of a typical balanced slot antenna fed with RG141/U cable. ($k=.2$ inch, $a=.303$, $K=.75$, $L=42.3$ cm.)

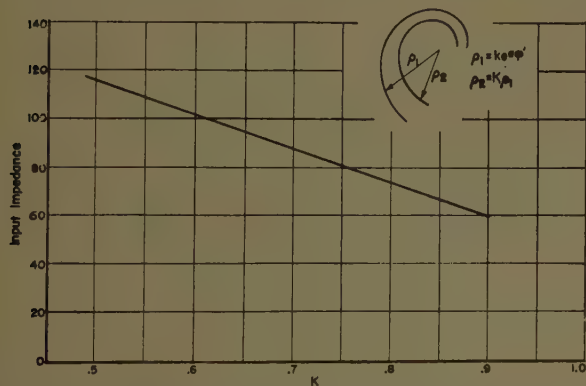


Fig. 14—Input impedance of balanced planar slot antennas (constructed of $\frac{1}{32}$ -inch copper with 0.150-inch coaxial cable bonded to screen between the slot arms). ($0.2 \leq a \leq 0.45$, $k=0.2$.)

input impedance of the antenna can be lowered still further by increasing the thickness of the metal; however, this will be at the expense of some pattern bandwidth since it will lower the upper cutoff frequency.

The measured standing wave ratio which a typical balanced slot antenna presents to a 50-ohm coaxial line is shown in Fig. 15.

The use of a miniature cable, such as "Microdot," lowers the capacitance between the arms and raises the measured impedance by approximately 20 per cent. However, an antenna fed with this cable may present considerably greater variations in the input standing wave ratio as a function of frequency due to irregularities in the miniature line after soldering it to the ground screen.

EFFICIENCY

The efficiency of the basic antenna, *i.e.*, the metal structure consisting of slots in a metal plane or metal arms in free space without dielectric material or any type of cavity backing, was measured and found to be approximately 98 per cent for antennas with an arm

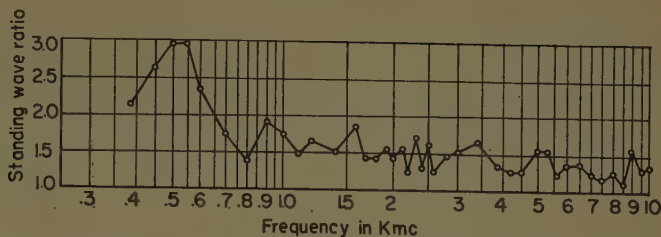


Fig. 15—Standing wave ratio which a typical balanced slot antenna presents to a 50-ohm coaxial line, ($k=0.2$ inch, $a=0.303$, $K=0.75$, arm length = 42.3 cm.)

length of one wavelength or more. For arm lengths shorter than one wavelength the efficiency decreases rapidly.

CONCLUSIONS

The planar balanced equiangular spiral antenna, in a practical size, exhibits the characteristics associated with an infinite structure. The bandwidth has been shown to be limited only by the chosen arm length and the precision of construction at the feed point. An extension of the bandwidth is a practical matter since the arm need only be of the order of one wavelength at the lowest frequency of operation.

The antenna will provide circularly polarized, single-lobe, bidirectional radiation, perpendicular to the plane of the antenna. The beamwidth varies with rotation in the plane of the antenna, and since the pattern rotates with frequency, the apparent beamwidth will vary with frequency for a fixed cut. The variation is typically approximately 40° or 50°. The more tightly wound spirals and the antennas with broader arms have somewhat more uniform patterns. The input impedance converges with increasing frequency, and for the antennas of most interest, the slot antenna is rarely mismatched more than three to one to a 50-ohm line, and is usually two to one or better over the radiation pattern bandwidth.

The structures described in this report are not miniature when compared to many present narrow-band antennas. However, the maximum diameter need only be one half wavelength. The primary advantage of the antenna is its capability of radiating circular or elliptically polarized energy with good efficiency over unlimited bandwidths that are at the discretion of the designer.

ACKNOWLEDGMENT

The author is pleased to acknowledge the advice and suggestions of V. H. Rumsey, to whom must go full credit for original concepts leading to this antenna. Appreciation is extended to R. H. DuHamel, P. E. Mayes, and R. L. Carrel for many fruitful discussions, and to W. E. Kennedy, V. P. Rash, and other members of the laboratory who assisted in the measurements.

Mention should also be made of E. M. Turner, Wright Air Development Center, whose original work on the Archimedes Spiral Antenna in 1953 and 1954 undoubtedly gave impetus to further thought in terms of spirals.

The Influence of Gain and Current Attenuation on the Design of the Rhombic Antenna*

R. P. DECKER†

Summary—With the increased use of the ionospheric scatter mode of propagation in the VHF range, the horizontal rhombic antenna is employed in many instances because of its simplicity, high performance, and low maintenance costs. Designers of these long rhombics have no doubt realized that the “maximum output” and “maximized” designs described by Harper and others do not take into account current attenuation due to radiation and cannot generally be employed when $l/\lambda > 8$ because of the requirement that the first ground factor maximum should agree closely with the free space vertical pattern maximum. This leads to the conclusion that power gain is the logical basis for design. In order to formulate an expression for power gain, a relation must be established between the radiation resistance with uniform current distribution and radiation resistance with exponential current distribution. The expression derived by Lewin is compared to that derived by Zuhrt. Gain curves are drawn using the formulas, and the “maximum output” and lobe alignment design are compared on the basis of gain with the design based on maximizing the vertical pattern function at the desired angle of radiation. It is found that only under certain conditions does the “maximum output” design have greater gain for the same leg length. The maximum gain condition is discussed together with optimum termination loss, attenuation rates, and surge impedance formulas for multiple wire rhombics.

In general, the analysis does not invalidate the design conditions previously derived, but rather increases the emphasis on the general alignment condition and gain and decreases the importance of the “maximum output” and “maximum alignment condition” which were derived on the basis of a constant input current and uniform current distribution.

INTRODUCTION

THE horizontal rhombic antenna is still extensively used in the HF and VHF regions. It has the advantages of high gain at low cost, broad-band operation from the standpoint of impedance and gain, and excellent front-to-back ratio. Disadvantages include a large amount of land required, some loss of power in the termination, and relatively high sidelobe levels with short rhombics. However, these disadvantages are not necessarily serious. The amount of land required for the same gain may be reduced considerably by vertical stacking. Only a small fraction of the input power need be wasted in the termination by using multiple wire techniques. Also, side lobe levels are always high with short rhombics, but decrease considerably as the rhombic becomes larger. Sidelobe levels in short rhombics may also be reduced by using broadside or end-fire arrays of rhombics.

Recent developments in the VHF scatter propagation field have demonstrated the importance of the antenna. Design considerations are somewhat different in the VHF from the HF range. In the HF range, the vertical

pattern is expected to follow changes in angle of signal arrival with varying frequency for long F -layer hops, or maintain efficient performance at a fixed angle with varying frequency for shorter hops. Vertical beamwidths must not be too sharp to discriminate against changes in angle of arrival. In the VHF (ionospheric scatter) range the pattern maximum should remain relatively constant with changes in frequency. Vertical pattern maximums are seldom above 7° , thus calling for relatively long high-gain rhombics with beamwidths of from 3° to 10° .

It has often been argued that the complete performance of the antenna cannot be determined because of the complexity and uncertainty of the computations. This argument is no longer valid, however, because of recent progress made in evaluation of radiation resistance with current attenuation which, except for the effects of ground, allows the gain of the antenna to be determined well within the limits of engineering accuracy.

The writer realized that present design methods are based on maximizing the free space vertical pattern function with respect to the apex angle and leg length, assuming no mutual coupling between wires. This has prompted the study of gain as a basis for design, since the true maximum gain condition and the “maximum output” condition derived on the basis of negligible coupling were suspected to be quite different.

A REVIEW OF DESIGN METHODS BASED ON MAXIMIZATION OF THE VERTICAL PATTERN FUNCTION

In the following analysis (see Fig. 1) let

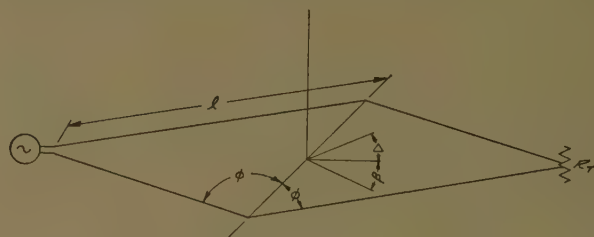


Fig. 1.

β —azimuth angle

Δ —vertical angle measured from horizon

ϕ —one half side apex angle¹

h —height of antenna above ground

a —attenuation constant ($=\alpha l$) nepers per leg length

α —attenuation constant in nepers per meter

l —rhombic leg length

λ —wave length

¹ With some authors this is called the “tilt” angle.

* Manuscript received by the PGAP, July 18, 1958; revised manuscript received, December 24, 1958.

† Collins Radio Co., Cedar Rapids, Iowa.

The above are assumed to be in the MKS system of units. The general expression for field strength over perfect ground with a given input current I_0 and an exponential current distribution² at a distance r is

$$E = \frac{240\pi I_0}{r} \frac{l}{\lambda} \cos \phi \sqrt{k_0^2 x_1^2 + a^2 (\cos^2 \beta + \sin^2 \beta \sin^2 \Delta)} \cdot \frac{\sqrt{1 + e^{-2a} - 2e^{-a} \cos k_0 x_1}}{\sqrt{k_0^2 x_1^2 + a^2}} \cdot \frac{\sqrt{1 + e^{-2a} - 2e^{-a} \cos k_0 x_2}}{\sqrt{k_0^2 x_2^2 + a^2}} \sin \left(\frac{2\pi h}{\lambda} \sin \Delta \right) \cdot 2 \sin \left(\frac{2\pi h}{\lambda} \sin \Delta \right) \quad (1)$$

is the ground factor for perfectly conducting ground with

$$k_0 x_1 = \frac{2\pi l}{\lambda} [1 - \cos \Delta \sin (\phi + \beta)]$$

$$k_0 x_2 = \frac{2\pi l}{\lambda} [1 - \cos \Delta \sin (\phi - \beta)].$$

With a uniform current distribution (1) becomes

$$E_0 = \frac{480\pi I_0}{r} \frac{l}{\lambda} \cos \phi \frac{\sin (\frac{1}{2} k_0 x_1) \sin (\frac{1}{2} k_0 x_2)}{\sqrt{\frac{1}{2} k_0 x_1} \sqrt{\frac{1}{2} k_0 x_2}} \cdot \sin \left(\frac{2\pi h}{\lambda} \sin \Delta \right). \quad (2)$$

It is to be noted that the radiated field in general is elliptically polarized except in the two principal planes, and the above expressions contain both the horizontal and vertical components. The field as given by these expressions is the square root of the time average Poynting vector.

Eq. (2) with $\beta = 0^\circ$ defines the principal plane vertical pattern function for a constant input current with a uniform current distribution (omitting the ground factor):

$$E_v = \frac{k_1 \cos \phi \sin^2 \left[\frac{\pi l}{\lambda} (1 - \cos \Delta \sin \phi) \right]}{[1 - \cos \Delta \sin \phi]}$$

$$k_1 = \frac{480 I_0}{r} \text{ for the antenna in free space.} \quad (3)$$

This is the equation normally used in the optimization of l/λ and ϕ . Now if we fix Δ and call it Δ_0' , the desired angle of vertical pattern maximum, and maximize (3) with respect to ϕ we obtain

$$\tan \left[\frac{\pi l}{\lambda} (1 - \cos \Delta_0' \sin \phi) \right] = \frac{2\pi l}{\lambda} \cos^2 \phi \cos \Delta_0' \frac{1 - \cos \Delta_0' \sin \phi}{\cos \Delta_0' - \sin \phi}. \quad (4)$$

This is generally termed the "maximized" design condition. When $\Delta_0' = 0$, we find that

$$\tan \left[\frac{\pi l}{\lambda} (1 - \sin \phi) \right] = \frac{2\pi l}{\lambda} \cos^2 \phi. \quad (5)$$

This is the "zero angle optimum" condition which should give maximum gain or output at the horizon ($\Delta = 0^\circ$).

If further we maximize (3) with respect to l/λ and solve this and (4) simultaneously, we find that

$$\sin \phi = \cos \Delta_0'$$

$$\frac{l}{\lambda} = \frac{1}{2 \sin^2 \Delta_0'}. \quad (6)$$

This is the "maximum output" condition which should give the highest gain possible for any desired angle of radiation Δ_0' for the case of uniform current distribution. The "maximum output" rhombic has the property that the main free space vertical lobe maximizes at angles less than the desired angle Δ_0' . If currents in the rhombic legs are assumed constant for a given input power with changes in l/λ and ϕ , then this condition does give the maximum possible gain at a given vertical design angle, even though the vertical pattern maximizes at a lower angle. (See Fig. 2.) Eqs. (3)–(6) were ob-

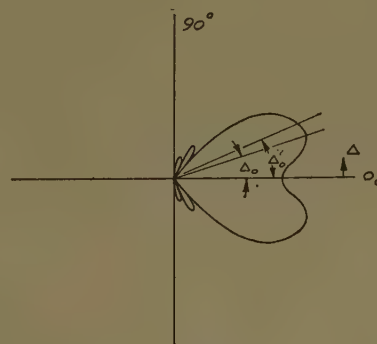


Fig. 2.

tained on the basis of a uniform current distribution, which of course is an impossibility if any power is to be radiated. The pattern functions are moderately affected by a current decrement along the rhombic wires, which is assumed to be exponential. These equations then are not strictly accurate when current attenuation is taken into account, but their accuracy is well within engineering tolerance. Eq. (3) may be maximized with respect to Δ to find the true angle of vertical pattern maximum Δ_0 .

² E. G. Hoffmann, "Der Einfluss der exponentiellen Stromverteilung auf die Strahlungseigenschaften der Rhombusantenne," *Hochfrequenztechnik u. Elektroak.*, vol. 62, pp. 15–20; July, 1943.

$$\cos \Delta_0 = \frac{\frac{l}{\lambda} - 0.371}{\frac{l}{\lambda} \sin \phi}; \quad \frac{l}{\lambda} \sin \phi \geq \frac{l}{\lambda} - 0.371. \quad (7)$$

If $l/\lambda \sin \phi \leq l/\lambda - 0.371$, then $\Delta_0 = 0^\circ$.

Now if it is desired to determine Δ_0 with exponential current attenuation, we use the general relation³

$$\cos \Delta_0 = \frac{\frac{l}{\lambda} - x}{\frac{l}{\lambda} \sin \phi} \quad (8)$$

where x is a solution of

$$\sin 2x[a^2 + 4x^2] = 2x[\cosh a - \cos^2 x]. \quad (9)$$

The quantity x is plotted as a function of a in Fig. 3. Eqs. (7) and (8) will be referred to as the general lobe alignment condition. According to (8), the vertical pattern maximum decreases in angle slightly as the attenuation constant a increases.

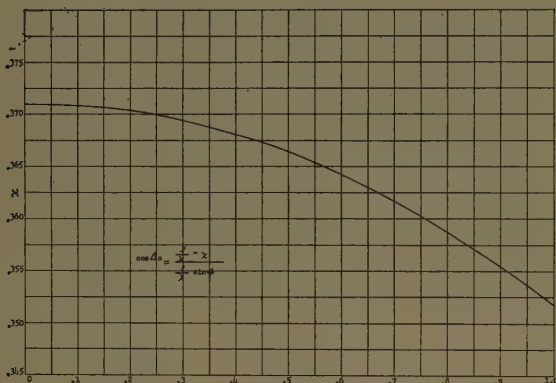


Fig. 3—Attenuation constant vs x . (After Hoffmann.)

If we let $\sin \phi = \cos \Delta_0'$ as in (6), but have the free space vertical lobe maximum coincide with the desired angle, we use (7) (uniform current case) to determine l/λ . Then we have

$$\sin \phi = \cos \Delta_0' \\ \frac{l}{\lambda} = \frac{0.371}{1 - \cos \Delta_0' \sin \phi} \quad \text{or} \quad \frac{l}{\lambda} = \frac{0.371}{\sin^2 \Delta_0'} \\ (\Delta_0' = \Delta_0). \quad (10)$$

This is termed the "maximum alignment" condition for uniform current distribution.

DETERMINATION OF POWER GAIN

The power gain of the rhombic antenna is an important quantity, particularly in scatter circuits where reliability is determined by system gain. Also, for the

purposes of this discussion, we need to compare the various design criteria on the basis of gain.

If the rhombic is properly terminated so that the back wave is minimized, then its input resistance is equal to its nominal surge impedance and terminating load Z . The expression for power gain over perfect ground (including termination losses) can then be formulated from the expression for field strength E with exponential current attenuation and antenna input power:

$$g_p = \frac{\frac{E^2}{120\pi}}{\frac{I_0^2 Z}{4\pi r^2}} \quad (11)$$

or

$$g_p = \frac{1920\pi^2 \left(\frac{l}{\lambda}\right)^2 \cos^2 \phi}{Z} \\ \frac{\left[1 + e^{-2a} - 2e^{-a} \cos \left(\frac{2\pi}{\lambda}(1 - \cos \Delta \sin \phi)\right)\right]^2}{a^2 + \left[\frac{2\pi l}{\lambda}(1 - \cos \Delta \sin \phi)\right]^2} \\ \cdot \sin^2 \left(\frac{2\pi h}{\lambda} \sin \Delta\right). \quad (12)$$

In this equation, we lack the relationship between a , Z , l/λ and ϕ . On the basis of a transmission line analogy, Lewin⁴ proposed the relation

$$a = \frac{R_0}{4Z} \quad (13)$$

where R_0 is the free space radiation resistance with uniform current distribution.

However, Zuhrt,⁵ by comparing field intensities with and without attenuation, arrives at the relation

$$e^{-a} = \frac{4Z - R_0}{4Z + R_0}. \quad (14)$$

To resolve the differences between (13) and (14) we may start with the power balance equation for the following properly terminated rhombic:

$$I_0^2 Z = I_0^2 R_r + I_0^2 Z \quad (15)$$

where

I_e = current in end termination

R_r = radiation resistance with exponential attenuation with respect to the square of the input current.

⁴ L. Lewin, "Rhombic transmitting aerial, increasing the power efficiency," *Wireless Engr.*, vol. 18, pp. 180-187; May, 1941.

⁵ H. Zuhrt, "Strahlungswiderstand und Gewinn von Rhombusantennen mit angenäherter Berücksichtigung der Strahlungsdämpfung," *Archiv der Elektrische Übertragung*, vol. 9, pp. 255-258; June, 1955.

³ Hoffmann, *op. cit.*

Since

$$I_e = I_0 e^{-2a} \quad (16)$$

we have

$$Z = R_r + e^{-4a} Z \quad (17)$$

Thus, if we can establish the relationship between R and R_0 , gain may be determined exactly with a knowledge of the antenna parameters. Lewin's (13) requires that

$$\frac{R_r}{R_0} = \frac{1 - e^{-4a}}{4a} \quad (18)$$

Zuhrt's relation requires that

$$\frac{R_r}{R_0} = \frac{(1 + e^{-2a})^2}{4} \quad (19)$$

Because of the discrepancies between (18) and (19), R_r was determined for various rhombic parameters by integration. The integrations were carried out using the IBM 650 computer and Simpson's rule, so that the probable error in R_r was estimated to be one place in the fifth decimal. R_r is found by using (1) (omitting the ground factor) to integrate the power density; and with (17) for the power balance condition we have

$$R_r = 480\pi \left(\frac{l}{\lambda} \right)^2 \cos^2 \phi I \quad (20)$$

where

$$I = \int_0^{\pi/2} \int_0^{\pi} \frac{(k_0^2 x_1 x_2 + a^2 (\cos^2 \beta + \sin^2 \beta \sin^2 \Delta))}{(k_0^2 x_1^2 + a^2)(k_0^2 x_2^2 + a^2)} \\ (1 + e^{-2a} - 2e^{-a} \cos k_0 x_1) \\ (1 + e^{-2a} - 2e^{-a} \cos k_0 x_2) \cos \Delta d\Delta d\beta.$$

R_0 is computed from the Lewin-Chaney formula:^{4,6}

$$\frac{R_0}{120} = \{ 1.1544 + 2 \ln c_1 + 2 \operatorname{Ci} b - 2 \operatorname{Ci} c \\ - \operatorname{Ci} (b + d) - \operatorname{Ci} (b - d) \\ + \cos c_1 [\operatorname{Ci} (c + c_1) + \operatorname{Ci} (c - c_1) + \operatorname{Ci} (d + d_1) \\ + \operatorname{Ci} (d - d_1) - 2 \operatorname{Ci} c_1 - 2 \operatorname{Ci} d_1] \\ + \sin c_1 [\operatorname{Si} (c + c_1) - \operatorname{Si} (c - c_1) - \operatorname{Si} (d + d_1) \\ + \operatorname{Si} (d - d_1) - 2 \operatorname{Si} c_1 + 2 \operatorname{Si} d_1] \} \quad (21)$$

where

$$b = \frac{4\pi l}{\lambda}, \quad c = \frac{4\pi l}{\lambda} \cos \phi, \quad c_1 = 4\pi \frac{l}{\lambda} \cos^2 \phi, \\ d = \frac{4\pi l}{\lambda} \sin \phi, \quad d_1 = \frac{4\pi l}{\lambda} \sin^2 \phi.$$

⁴ J. E. Chaney, "Free space radiation impedance of rhombic antenna," *J. Appl. Phys.*, vol. 24, pp. 536-540; May, 1953. See also Lewin, *op. cit.*

Table I shows the results of some of the integrations:

TABLE I R_r/R_0

a	$\frac{l}{\lambda} = 6$ $\phi = 72^\circ$ $R_0 = 647.54\Omega$	$\frac{l}{\lambda} = 18$ $\phi = 81^\circ$ $R_0 = 529.88\Omega$	$\frac{l}{\lambda} = 54$ $\phi = 84^\circ$ $R_0 = 655.45\Omega$	$\frac{1 - e^{-4a}}{4a}$ (Lewin)	$\frac{(1 + e^{-2a})^2}{4}$ (Zuhrt)
0.25	0.63265	0.63106	0.63433	0.63212	0.64523
0.40	0.49996	0.50045	0.501601	0.49881	0.52514
0.60	0.38116	0.38386	0.38291	0.37887	0.42327
0.68		0.34970		0.34343	0.39480
0.80		0.30789		0.29976	0.36114
1.0		0.25632		0.24542	0.32225

The results of the integrations indicate that Lewin's relation is within 1 per cent of R_r/R_0 for attenuation constants of 0.6 or less, and is about 2 per cent in error for $a = 0.68$. Zuhrt's expression is far less accurate, even for relatively small rates of attenuation. The inaccuracies of the Zuhrt formula could have been foreseen for high rates of attenuation since, when $R_0 = 4Z$, a must be infinite according to (14). A simple analysis shows that an error in R_r/R_0 results in a fraction of that error for g_p . On the basis of the integrated values of R_r , the average error in g_p as a result of (18) varies as follows: 0.017 per cent with $a = 0.25$, 0.12 per cent with $a = 0.4$ and 0.245 per cent with $a = 0.6$. It is concluded from this that the error incurred in g_p as a result of (13) and (18) is so small that it is of the same order of magnitude as the error due to the assumed exponential current distribution. This justifies the use of $a = R_0/4Z$ in (12). Ohmic wire losses and poor ground losses would also produce far greater errors.

It is well known that the proximity of the antenna to ground will cause the radiation resistance to undulate about the free space value approximately as $\sin x/x$ as the height of the antenna is increased.⁷ The presence of the ground will also affect the horizontally polarized component of the field differently from the vertically polarized component. While the error incurred over ground by the use of the free space formula is considered small with rhombics at practical heights, it will in most cases cause larger errors in gain than those caused by the use of Lewin's relation for attenuation constant.

A COMPARISON OF CERTAIN DESIGN CONDITIONS

On the basis of the results of the preceding section we are now in a position to determine the power gain of the rhombic antenna at beam maximum and in free space with $\beta = 0^\circ$, $\Delta = \Delta_0$:

⁷ Lewin, *op. cit.*

$g_p(\Delta=\Delta_0)$

$$= \frac{1920a\pi^2 \left(\frac{l}{\lambda}\right)^2 \cos^2 \phi [1 + e^{-2a} - 2e^{-a} \cos(2\pi x)]^2}{R_0[a^2 + 4\pi^2 x^2]} \quad (22)$$

In Fig. 4 we have a plot of this equation for a constant antenna surge impedance of 500 Ω . The solid lines are for constant apex angles, and the dashed lines for constant angle of vertical free space maximum Δ_0 . It will be noted that there are two lines for $\Delta_0 = 0^\circ$. The lower line corresponds to the lobe alignment condition $(l/\lambda) - x = l/\lambda \sin \phi$ and the upper one corresponds to the "zero angle optimum" condition given by (5). The gain curve rises until it reaches the "zero angle optimum" line and then falls due to beam splitting. The dashed curves for Δ_0 do not apply once the maximum of the gain curve for a given ϕ has been exceeded. The free space vertical maximum occurs at 0° for any point to the right of the lower $\Delta_0 - 0^\circ$ line since the derivative at $\Delta = 0^\circ$ is always zero. For a given Δ_0 , gain maximizes at leg lengths somewhat less than the "maximum output" leg length for 500 Ω rhombics.

Now for the "maximum output" condition we have

$$\frac{g_p(\Delta=\Delta_0')}{(\sin \phi = \cos \Delta_0')} = \frac{1920\pi^2 a \left(\frac{l}{\lambda}\right)^2 \cos^2 \phi [1 + e^{-a}]^4}{R_0[a^2 + \pi^2]} \quad (23)$$

For the sake of comparison with the gain of a rhombic with the same l/λ satisfying the general alignment condition, (8), we may let $a^2 \approx 0$ and in (22) $x \approx 0.371$. Eqs. (22) and (23) then become

$$g_p(\Delta=\Delta_0) \approx \frac{3487.3a \left(\frac{l}{\lambda}\right)^2 \cos^2 \phi [1 + e^{-2a} + 1.3783e^{-a}]^2}{R_0} \quad (24)$$

and

$$\frac{g_p(\Delta=\Delta_0')}{(\sin \phi = \cos \Delta_0')} \approx \frac{1920a \left(\frac{l}{\lambda}\right)^2 \cos^2 \phi [1 + e^{-a}]^4}{R_0} \quad (25)$$

The ratio of gains for the same leg length and attenuation constant is, therefore,

$$\frac{g_p(\Delta=\Delta_0)}{g_p(\Delta=\Delta_0')} = \frac{1.8163 \cos^2 \phi_1 [1 + e^{-2a} + 1.3783e^{-a}]^2 R_{0_2}}{\cos^2 \phi_2 [1 + e^{-a}]^4 R_{0_1}} \quad (26)$$

$$\frac{l}{\lambda} = \text{constant}$$

$$(a = \text{constant})$$

where the subscripts 1 and 2 refer to gain at Δ_0 and Δ_0' respectively. Now we find that the product

$$\frac{\cos^2 \phi_1 R_{0_2}}{\cos^2 \phi_2 R_{0_1}}$$

is essentially constant = .921. Also, the quantity

$$\frac{[1 + e^{-2a} + 1.3783e^{-a}]^2}{[1 + e^{-a}]^4}$$

is relatively independent of a and equal to .72.

We finally have proof that the difference in gain for the two cases is $10 \log 1.2 = 0.80$ db in favor of the general lobe alignment condition (7).

For the same antenna impedance, we have

$$\frac{g_p(\Delta=\Delta_0)}{g_p(\Delta=\Delta_0')} = 1.8163 \frac{\cos^2 \phi_1 [1 + e^{-2a_1} + 1.3783e^{-a_1}]^2}{\cos^2 \phi_2 [1 + e^{-a_2}]^4}$$

$$\frac{l}{\lambda} = \text{constant}$$

$$(Z = \text{constant}) \quad (27)$$

The conclusion in this case is that, for rhombics of the same Z and leg length, the "maximum output" rhombic has higher gain than the general lobe alignment design of approximately one db for most practical cases depending on elevation angle or leg length and Z . The difference decreases with increasing l/λ and lower surge impedance.

Although the general lobe alignment condition affords about 1 db less gain than the maximum output case for the same Z , from the practical design standpoint the advantages of the former usually outweigh those of the latter, especially for wide-band applications. The larger side apex angle of the lobe alignment case means an inherently lower-impedance antenna, and a few tenths of a db can be regained in this way. In addition, the free space vertical pattern of the maximum output design does not follow changes in the ground factor with frequency as well as the lobe alignment design. With very long rhombics also, and with sharp vertical patterns as in scatter applications, the ground factor maximum should agree closely with the free space maximum. The "maximum output" design is, therefore, seldom used.

Now for the "maximum alignment" condition (10) with equal ϕ but different l/λ , we have for the same a and angle of elevation

$$\frac{g_p(\text{max. output})}{g_p(\text{max. align.})} = \frac{\left(\frac{l}{\lambda}\right)_1^2 R_{0_2} (1 + e^{-a})^4}{\left(\frac{l}{\lambda}\right)_2^2 R_{0_1} (1 + e^{-2a} + 1.3783e^{-a})^2}$$

$$(a = \text{constant}) \cdot \frac{a^2 + (.741\pi)^2}{a^2 + \pi^2} \quad (28)$$

or

$$\left(\frac{.500}{.371}\right)^2 \cdot \left(\frac{.447}{.600}\right) \cdot .766 = 1.036 = 0.15 \text{ db.}$$

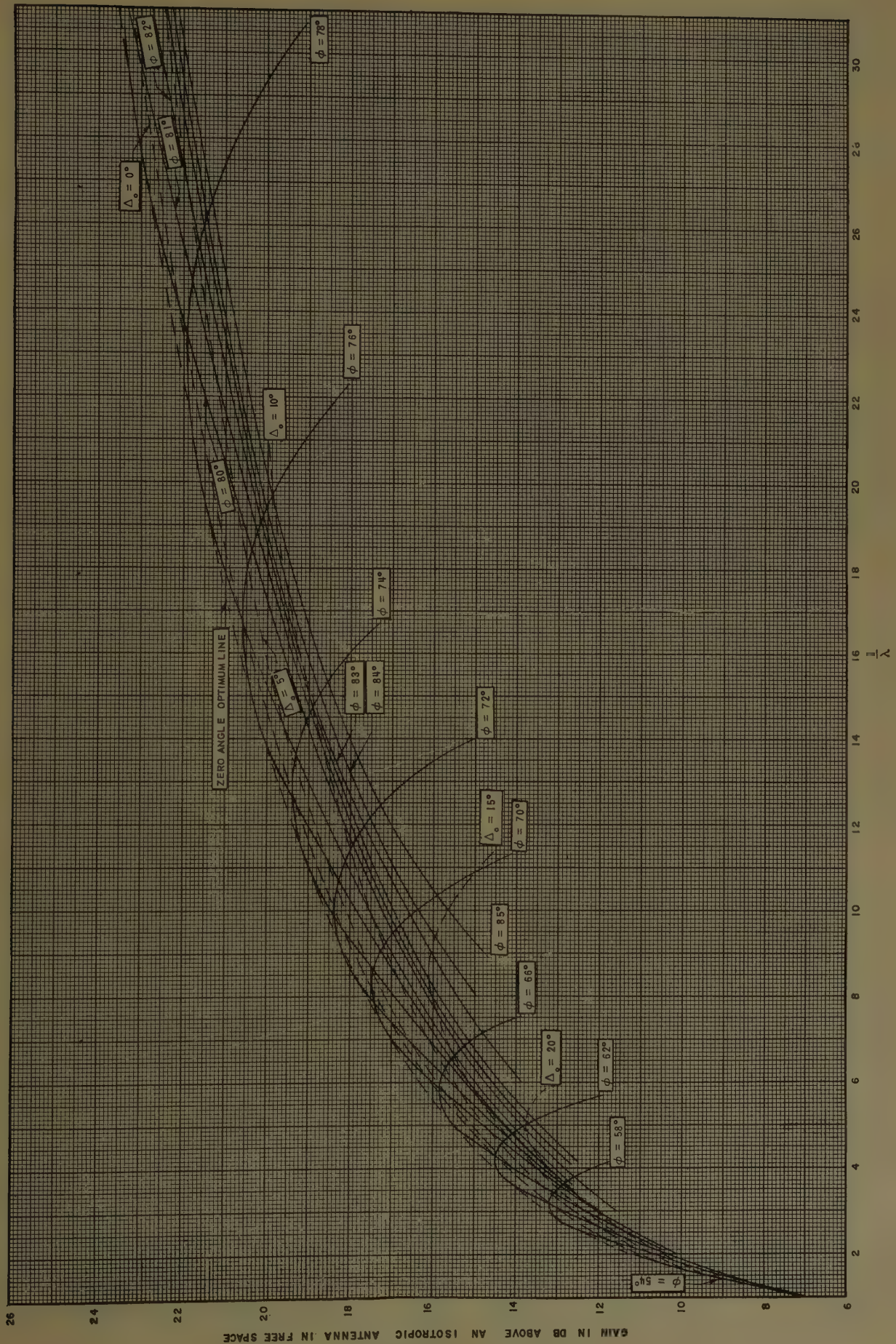


Fig. 4—Free space power gain for $Z = 500\Omega$.

With the same antenna Z :

$$\frac{g_p(\text{max. output})}{g_p(\text{max. align.})} = 1.8163 \cdot \frac{(1 + e^{-a_1})^4}{(1 + e^{-2a_1} + 1.3783e^{-a_1})}$$

$$(Z = \text{constant}) \cdot \frac{a_2^2 + (.741\pi)^2}{a_2^2 + \pi^2} \quad (29)$$

where

$$a_1 = \frac{600}{4Z}, \quad a_2 = \frac{477}{4Z}$$

The difference in gain is 1.45 db in this case.

THE TRUE MAXIMUM GAIN CONDITION AND THE OPTIMIZATION OF ATTENUATION CONSTANT AND h/l

The "maximum output" condition affords the highest gain obtainable when the vertical pattern function is maximized with a constant input current. When gain is maximized for a given vertical angle Δ_0 , however, an entirely different condition is obtained. Let the attenuation constant a be fixed. Then we have from (22)

$$g_p(\Delta=\Delta_0) = \frac{k_2 \left(\frac{l}{\lambda}\right)^2 \cos^2 \phi}{R_0} \quad (30)$$

$$(k_2 = \text{constant})$$

Now it can be shown that g_p is a maximum when

$$8 \frac{l}{\lambda} \cos^2 \phi = 1. \quad (31)$$

From (8) and with (31) we have

$$\frac{l}{\lambda} = \frac{16x - \cos^2 \Delta_0 + \cos \Delta_0 \sqrt{256x^2 - 32x + \cos^2 \Delta_0}}{16 \sin^2 \Delta_0} \quad (32)$$

Eqs. (31) and (32) are the true maximum gain condition.

We note that the maximum gain rhombic is about 23 per cent longer than the maximum output rhombic and has a value of R_0 of 174.8 Ω which is nearly independent of Δ_0 . This condition requires a very low antenna surge impedance in order to have reasonable termination losses. Such low impedances are usually obtainable only on a single frequency basis. Also, the leg lengths involved are so great that the maximum gain condition is, generally, practical only in the VHF region.

For the same attenuation constant the maximum gain rhombic affords 1.52 db more gain than the "maximum output" rhombic.

An interpretation of the differences in design conditions between those based on the pattern function (3) and those based on power gain can now be made. Consider first a constant $a = \alpha l$. By squaring (3) and holding I_0 constant we observe that if R_0 is independent of ϕ

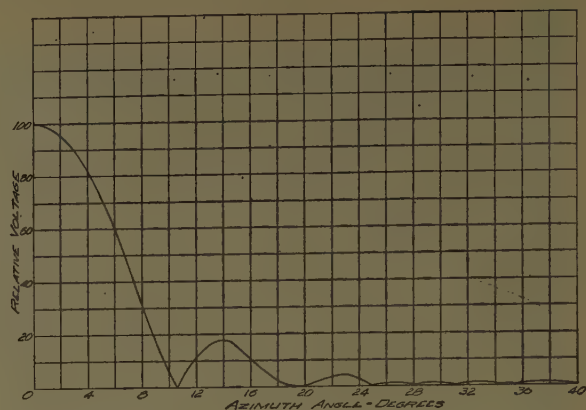


Fig. 5—Azimuth pattern of 10° maximum gain rhombic.

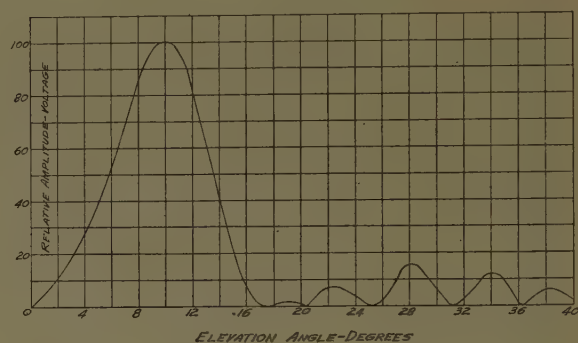


Fig. 6—Vertical pattern of 10° maximum gain rhombic over perfect ground.

or l/λ for a given Δ ; then both (3) and (12) (power gain) will give the same design conditions when they are maximized with respect to l/λ and ϕ . If ϕ is not too great with respect to l/λ for a given Δ , then R_0 is essentially constant with ϕ and l/λ . This is equivalent to saying that the radiated power is independent of ϕ for a fixed Δ . As ϕ approaches 90°, however, R_0 decreases, causing the maximum in power gain to occur at relatively large apex angles. When R_0 decreases significantly as ϕ increases, coupling between wires has increased to the point where it can no longer be neglected. With a constant surge impedance, the two design conditions will be more nearly identical, since changes in the exponential terms in (12) are second order effects even with apex angles approaching 90°. Optimization of l/λ and ϕ for a constant αl is more significant, since the termination loss or antenna efficiency is fixed while it is not in the case of constant surge impedance.

The principal plane patterns of a typical maximum gain rhombic are shown in Figs. 5 and 6. In this case $\Delta_0 = 10^\circ$, $l/\lambda = 20.362$, $\phi = 85^\circ 30'$. The azimuth pattern at $\Delta_0 = 10^\circ$ (Fig. 5) indicates a half-power beamwidth of 10.2° with a 17.8 per cent maximum sidelobe (voltage). Sidelobes beyond $\beta = 25^\circ$ are practically non-existent. The vertical pattern (Fig. 6) is shown over perfect ground with the ground factor maximizing at 10° . It also has relatively low-level sidelobes, the largest being 15 per cent.

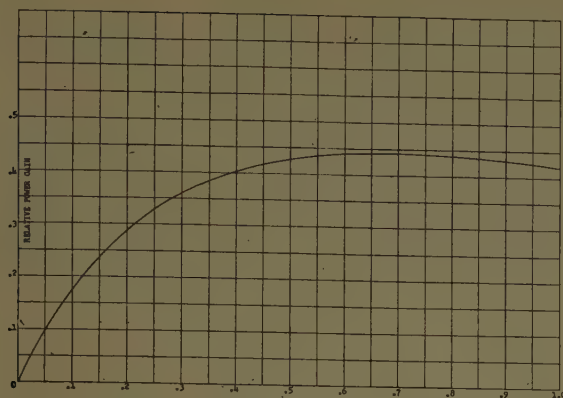


Fig. 7—Variation of power gain with attenuation constant.

We will consider next the optimum attenuation constant a . As attenuation rate increases, the ratio of maximum to average power radiated decreases as does the termination loss. This ratio is a slower varying function of a than is termination loss. Hence, there is a value of a which gives maximum power gain. Now for fixed l/λ and ϕ

$$g_p(\Delta=\Delta_0) = \frac{k_3 a [1 + e^{-2a} - 2e^{-a} \cos(2\pi x)]^2}{a^2 + 4\pi^2 x^2} \quad (33)$$

$(k_3 = \text{constant})$

$$\sin \phi = \frac{2 \frac{h}{l} \left[2x \left[\left(\frac{l}{\lambda} \right)_2^3 - \left(\frac{l}{\lambda} \right)_1^3 \right] - 3 \left(\frac{l}{\lambda} \right)_1 \left(\frac{l}{\lambda} \right)_2 \left[\left(\frac{l}{\lambda} \right)_2^2 - \left(\frac{l}{\lambda} \right)_1^2 \right] \right]}{\left(\frac{l}{\lambda} \right)_2^3 \left[16 \left(\frac{h}{l} \right)^2 \left(\frac{l}{\lambda} \right)_1^2 - 1 \right]^{3/2} - \left(\frac{l}{\lambda} \right)_1^3 \left[16 \left(\frac{h}{l} \right)^2 \left(\frac{l}{\lambda} \right)_2^2 - 1 \right]^{3/2}} \quad (36)$$

We find that gain is a maximum when $a=0.68$, which corresponds to a termination loss of 0.3 db, or 6.6 per cent of the input power. For this condition we must have $Z=0.368 R_0$. In (33) for a fixed l/λ and Δ_0, ϕ should be changed slightly to compensate for changes in a , thus affecting R_0 or k_3 . However, even if a were not precisely determined, the relative gain function (Fig. 7) is so broad near the maximum that a 10 per cent error in a would cause only a $\frac{1}{2}$ per cent error in gain. It is obvious that it will be rarely possible to obtain a surge impedance low enough so that $a=0.68$ over a wide frequency band. Lower values of a , say 0.45, may be quite practical in the VHF band, at which point power gain is degraded only a few tenths of a db from its theoretical maximum value.

In the foregoing analysis, we have seen that in the great majority of applications, the general lobe alignment condition (8) will be used. In order to cover a specified frequency band over ground, it is clear that the free space vertical pattern must follow the ground factor as closely as possible. We may determine the optimum ratio of height to leg length (h/l) as follows. Let the ground factor maximum correspond to Δ_g . Then

$$\sin \Delta_g = \frac{1}{4 \frac{h}{\lambda}} \quad \text{or} \quad \cos \Delta_g = \sqrt{1 - \frac{1}{16 \left(\frac{h}{\lambda} \right)^2}} \quad (34)$$

Also

$$\cos \Delta_0 = \frac{\frac{l}{\lambda} - x}{\frac{l}{\lambda} \sin \phi}$$

Now we want the difference between $\cos \Delta_0$ and $\cos \Delta_g$ to be a minimum over the range λ_1 to λ_2 so that on a least square basis we have

$$\frac{\partial I}{\partial l} = 0$$

where

$$I = \int_{\lambda_1}^{\lambda_2} \left[\frac{\frac{l}{\lambda} - x}{\frac{l}{\lambda} \sin \phi} - \sqrt{1 - \frac{1}{16 \left(\frac{h}{\lambda} \right)^2}} \right]^2 d\lambda \quad (35)$$

Integrating and solving for $\sin \phi$ we have

Thus the optimum h/l ratio is a function of apex angle and leg lengths at the two ends of the band.

SURGE IMPEDANCE

If the rhombic is to minimize the backward travelling wave, then the terminating resistance R_T must equal the nominal characteristic impedance Z . Also, if the rhombic is correctly terminated so that $R_T=Z$, then $R_{in}=Z$. For the single wire case, Fig. 8(a), Schelkunoff⁸ and Chaney⁹ consider the correct value for R_T to be that corresponding to the input impedance of an infinitely long V antenna:

$$R_{in} = R_T = 120 \ln \left(\frac{\lambda}{a_0} \cos \phi \right) - 292 \quad (37)$$

where a_0 =radius of wire. For frequency-independent operation, we may use conical conductors as in Fig. 8(b).¹⁰

⁸ S. A. Schelkunoff and H. T. Friis, "Antennas Theory and Practice," John Wiley and Sons, Inc., pp. 457-469; 1952.

⁹ G. G. Chaney, "Current Distribution and Driving Point Impedance for a Rhombic Antenna," U. S. Naval Postgraduate School, Tech. Rep. No. 11; March, 1954.

¹⁰ Schelkunoff, *op. cit.*

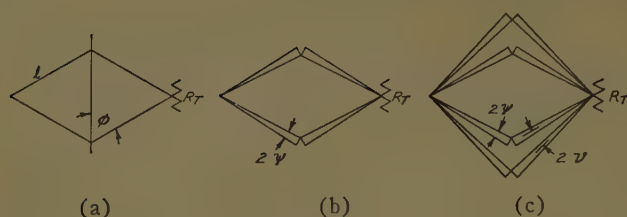


Fig. 8.

$$Z = 120 \ln \frac{2 \cos \phi}{\psi} \quad (38)$$

where ψ is one-half the apex angle in radians. In the case of two sets of conical conductors [Fig. 8(c)] we have

$$Z = 120 \ln \frac{2 \cos \phi}{\sqrt{2\psi v}} \quad (39)$$

Inasmuch as conical conductors are impractical, consider n wires equally spaced on a circle and tapered to form a cone. The expression for nominal surge impedance can be derived with the aid of Schelkunoff's nonuniform transmission line theory:¹¹

$$Z = 120 \ln \frac{2 \cos \phi}{\sqrt[n]{4\pi n \psi^{n-1} \frac{a_0}{\lambda}}} - \frac{72}{n} \quad (40)$$

Eq. (40) can be used to find the nominal surge impedance for the most common type of multiple wire configuration, namely three wires in one plane space-tapered by an angle ψ (ψ being the angle between the middle and either outside wire). A geometric mean radius is used in this case. We have

$$Z = 120 \ln \frac{.603 \cos \phi}{\sqrt[3]{\psi^2 \frac{a_0}{\lambda}}} \quad (41)$$

Eq. (40) shows that as the number of space tapered wires increases, the legs of the rhombic approach true

conical conductors and Z thus becomes less and less dependent on frequency. For $n \rightarrow \infty$, (40) approaches (38). For $n=1$, (40) reverts to (37).

The lower the surge impedance of the rhombic, the less susceptible it is to precipitation static. While single wire rhombics are commonly used for receiving, the advantages of multiple wire legs should not be overlooked. Multiple wire rhombics have shown as much as 9-db improvement in precipitation static over single wire types.

CONCLUSION

Certain general remarks can be made on the foregoing discussion. We note that the true maximum gain condition is simply a specific case of the general "lobe alignment" condition. Due to the low radiation resistance for this design, multiple wire techniques are usually required to lower the termination loss. The advantage in using gain as a design basis generally is also apparent. A good example is the design of rhombics for relatively short E and F layer hops where maximum gain is desired at a fixed elevation angle over a wide frequency band. The procedure in this case is to determine the leg length from the mean frequency and elevation angle, and then adjust ϕ in (12) to give equal free space gain at both ends of the band, taking into account changes in attenuation constant. The height is adjusted separately and in this case (36) would not apply.

The analysis has shown that any design other than the general lobe alignment case would rarely be used, especially for long rhombics. Mutual coupling cannot be neglected in the design of large maximum gain rhombics, nor can the radiated power be considered constant with changes in apex angle when the apex angle approaches that for the maximum gain condition.

ACKNOWLEDGMENT

Many thanks are due D. C. Arnold, E. W. Pappenfus, Dr. R. L. McCreary and Dr. V. W. Bolie for their encouragement and help in setting up the computing program. A special word of gratitude is due R. E. Cleary who optimized the program for the computer.

¹¹ S. A. Schelkunoff, "Electromagnetic Waves," D. Van Nostrand Co., Inc., New York, N. Y., pp. 290-292; 1943.

communications

Directivity of a Broadside Array of Isotropic Radiators*

H. E. KING†

Summary—Directivity curves, of a uniform broadside array of isotropic sources, are shown to illustrate that gain increases almost linearly with aperture size until an optimum source spacing of approximately 0.9λ is reached.

A UNIFORM linear broadside array will yield maximum gain¹ for a specified aperture, except for antennas with "supergain" characteristics. The Dolph-Tchebyscheff arrays yield less gain than a uniform array because gain or beamwidth is sacrificed to achieve low-level side lobes.

If a broadside array having maximum gain is desired, the high sidelobe levels, which are only 13 db down on the main lobe, must be accepted. To achieve the highest gain possible for a specified aperture and/or for the minimum number of elements, a knowledge of the maximum spacing possible before the gain or pattern deteriorates is necessary.

The purpose of this communication is to present curves displaying directivity characteristics of a uniform broadside array, as a function of the spacing, of N isotropic radiators.

The directivity,² relative to an isotropic radiator, of N isotropic point sources equispaced and equiphased with uniform current distribution, can be written as

$$D = \frac{1}{\frac{1}{N} + \frac{2}{N^2} \sum_{m=1}^{N-1} (N-m) \frac{\sin 2mB}{2mB}} \quad (1)$$

where

$$B = \frac{\pi d}{\lambda}$$

N = number of elements

and

d = spacing of the point sources.

Fig. 1 is a plot of the gain for N isotropic radiators versus the separation between sources in wavelengths. The spacing yielding maximum gain depends upon the number of elements. For example, for $N=2$, the spacing d for maximum gain occurs at 0.715λ , while $d=0.95 \lambda$ for $N=16$. Observe that, in general, for element spacings less than 0.9λ , the improvement in gain is chiefly a function of over-all array length. This indicates that for a specified aperture, the gain is approximately independent of the number of elements, provided the spacing is not larger than 0.9λ .

The peculiar dips near the peaks of the gain curves of Fig. 1 are probably due to the transition stage where the secondary sidelobe level starts to become undesirable with increased spacing.³

* Manuscript received by the PGAP, February 6, 1958; revised manuscript received, November 17, 1958.

† Ramo-Wooldridge, a division of Thompson Ramo Wooldridge Inc., Los Angeles, Calif.

¹ Gain and directivity are used synonymously in this note.

² From the notes of R. W. Klopfenstein.

³ For example, see R. M. Foster, "Directive diagrams of antenna arrays," *Bell Sys. Tech. J.*, vol. 5, pp. 292-307; April, 1926.

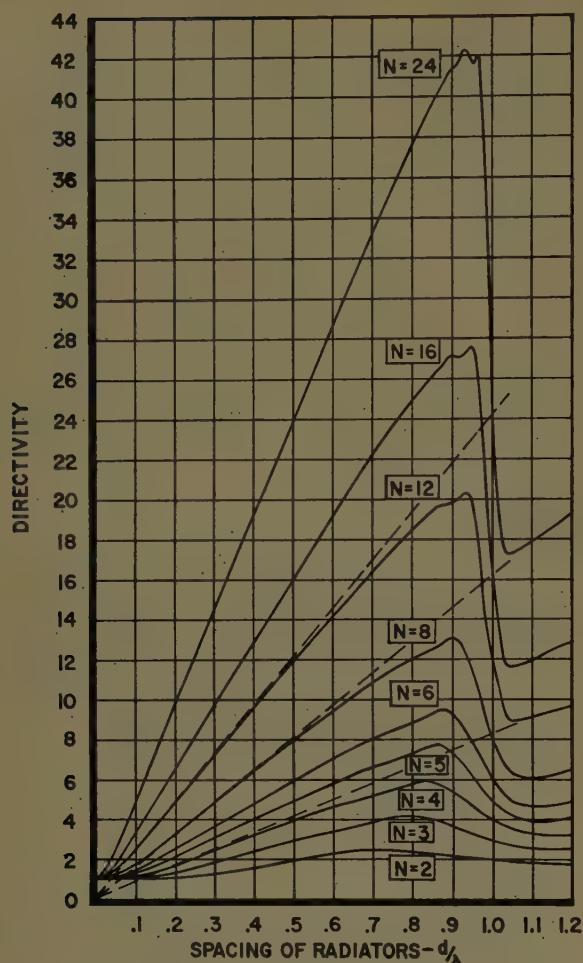


Fig. 1—Plot of directivity (relative to an isotropic radiator) of a uniform broadside array of N isotropic sources vs spacing. The dashed line is the directivity of a continuous line source with an aperture corresponding to $N=4, 8$ and 12 .

Fig. 1 should be compared to the directivity vs spacing curves presented by Kandoian⁴ for a uniform linear broadside array of individual sources possessing a sinusoidal unit pattern, e.g., loops. Prominent differences exist between the two sets of curves. The maximum gain is attained for the loop curves when the spacing is 1λ between successive elements. Also the peculiar dips do not exist in Kandoian's curves. However these distinctions appear to be reasonable since Kandoian has applied to (1) the effects of a directional element pattern. The higher secondary lobes that exist with the isotropic sources will be suppressed by the element pattern in the case of loops.

It is of interest to compare the gain of a discrete number of sources with the gain of a continuous line source, both having the same aperture. The dashed curves of Fig. 1 provide a comparison of the directivity of a continuous line source with the directivity for $N=4, 8$, and 12 isotropic sources. In the region where $d < 0.5\lambda$, the gain of an array of isotropic radiators can be estimated accurately from a continuous line source. For spacings larger than 0.5λ , the actual gain curves deviate from the asymptote to a greater extent. Nevertheless, the continuous line source provides a rough determination of gain for spacings up to approximately 0.9λ . A good empirical value for approximating the directivity of a uniform broadside array of isotropic sources in terms of its aperture, A , is

$$D = 1.9 \frac{A}{\lambda} \quad (2)$$

⁴ A. G. Kandoian, "Three new antenna types and their applications," *Proc. IRE*, vol. 34, pp. 70-75; February, 1946.

Modification of "Simplified Method for Computing Knife Edge Diffraction in the Shadow Region"*

L. J. ANDERSON† AND L. G. TROLESE†

CORRESPONDENCE between the authors of the above paper,¹ and J. H. Crysdale, DRTE, Ottawa, Can. and J. R. Wait, NBS, Boulder, Colo., has pointed out improvements which should be made in combining the phases of the reflected and unreflected rays. It turns out, as suggested by Crysdale, that this can best be done by changing the argument of expressions (9) and (10) to $2\pi\delta/\lambda$ instead of $v(v_0 + \Delta v/2)$

and re-labeling the abscissa of Fig. 5 in the same way. The δ 's are defined by (13). This not only improves the accuracy, but also simplifies the computations by eliminating the Δv 's.

Wait pointed out that the free-space distance traversed by the reflected and unreflected rays are slightly different and should be accounted for. This is also accomplished by the above modification.

The authors would like to express their appreciation to J. H. Crysdale and J. R. Wait for their suggestions, and the stimulating exchange of correspondence pertaining thereto.

* Manuscript received by the PGAP, January 22, 1959.

† Smyth Research Associates, San Diego, Calif.

¹ *IRE TRANS. ON ANTENNAS AND PROPAGATION*, vol. AP-6, pp. 281-286; July, 1958.

Effect of Surface Reflections on Rain Cancellation of Circularly Polarized Radars*

R. MCFEE† AND T. M. MAHER†

SURFACE reflections, along with many other factors, can prevent perfect cancellation of radar reflections from rain when circular-polarization techniques^{1,2} are used to suppress these returns. The purpose of this note is to present estimates of the reduction in cancellation which is due to this factor alone in the case where the radar overlooks the sea. The calculations are based on the reflection coefficients of sea water at two different frequencies, 500 mc and 3000 mc. The discussion is intended to apply primarily to ground-based search radars and not to radars with beams so directed that surface reflections are negligible.

Cancellation of rain reflections by circular-polarization techniques is attained ideally as follows. The transmitter power is divided and radiated in two equal components, one vertically polarized and the other horizontally polarized. One of these is delayed 90° in phase relative to the other before radiation. When these two components are radiated with equal gains in a given direction and undergo reflection by an *ideal* spherical raindrop, the reflections retain the original polarizations and have equal strengths. When they return to the antenna, the phase-shifted component is shifted again by 90°, after which both components are added together. Since they are now 180° out of phase and of equal magnitude, they cancel each other and the return from the raindrop is suppressed.

Ground reflections prevent this cancellation by destroying the equality of the antenna gains for the two components and by introducing extra phase shifts. As a result, the vertical and horizontal returns do not have the same amplitude and opposite phase, and therefore do not cancel when added.

Cancellation will also be upset by deficiencies in the power divider, phase shifter, and antenna of the radar, as well as by asymmetries in the reflecting rain drops or snow, and by multiple reflections in the rain cloud. Although assumed to be negligible in this analysis, these factors are by no means negligible in practice, and will deteriorate the cancellation substantially from the value given here where surface reflections are considered to be the sole disturbance.

In order to calculate the cancellation obtainable it is

necessary to define a quantitative index. This may be done in terms of the vertical and horizontal components, P_1 and P_2 respectively, of the power returned to the antenna. A third term, P_{12} , represents the received power level after the two return signals are added. If the voltages associated with P_1 and P_2 are equal and opposite in phase, then P_{12} will be zero. The cancellation ratio α is defined as the ratio of this received power P_{12} to the total incident power, P_1 plus P_2 .

$$\alpha = \frac{P_{12}}{P_1 + P_2} \quad (1)$$

Each of these powers is the sum of the returns from many raindrops at the same range but at different azimuths and elevations. It is assumed that the raindrops are uniformly distributed throughout this cross-section of the beam and that the phases of the returns from different raindrops are uncorrelated and thus that the powers may be added linearly.

The above expression can be put in a form suitable for numerical evaluation by introducing the concept of complex voltage gain. The complex voltage gain \bar{f} of a transmitting antenna is here taken as the quantity representing the magnitude and the phase angle of the voltage received at some point in the beam, relative to the voltage at a reference point located at the same distance from the antenna, in the center of the beam. By reciprocity, this gain is unchanged when the antenna is receiving.

In an ideal circularly polarized system, we will have $\bar{f}_1 = \bar{f}_2 = \bar{f}$, where each of these gains is a function of elevation angle θ and azimuth angle Φ . For antennas with free space patterns $\bar{f}(\theta, \Phi)$ having symmetry about the vertical and the horizontal axes, we will have to a good approximation,

$$f(\theta, \Phi) = g(\theta)h(\Phi). \quad (2)$$

Eq. (2) is known to be approximately correct for symmetrical antennas.

When the field at a remote point is due to a combination of a direct ray and the ray reflected from the earth's surface at a point *near* the antenna (Fig. 1), and when the reflection coefficient can be represented as $\Gamma e^{j\beta}$, the gains of the antenna for the vertical and the horizontal components are given to a close approximation by

$$\begin{aligned} \bar{f}_1(\theta, \Phi) &= h(\Phi)[g(\theta) + g(-\theta)\Gamma_1(\theta)e^{j\beta_1(\theta)}e^{j\Delta(\theta)}] \\ &= h(\Phi)\bar{G}_1(\theta) \end{aligned} \quad (3)$$

$$\begin{aligned} \bar{f}_2(\theta, \Phi) &= h(\Phi)[g(\theta) + g(-\theta)\Gamma_2(\theta)e^{j\beta_2(\theta)}e^{j\Delta(\theta)}] \\ &= h(\Phi)\bar{G}_2(\theta). \end{aligned} \quad (4)$$

* Manuscript received by the PGAP, May 27, 1958; revised manuscript received, December 22, 1958. This work sponsored by the U. S. Air Force, Rome Air Dev. Center, under contract AF-30(602)-1640.

† Dept. of Elec. Eng., Syracuse University, Syracuse, N. Y.
¹ L. N. Ridenour, "Radar System Engineering," McGraw-Hill Book Co., Inc., p. 84; 1947.

² W. D. White, "Circular radar cuts rain clutter," *Electronics*, vol. 27, pp. 158-160; 1954.

Here $\Delta(\theta)$ is the path length difference in wavelengths between the path taken by the direct ray and that taken by the reflected one. The new factors $\bar{G}_1(\theta)$ and $\bar{G}_2(\theta)$ are shorthand symbols for the terms in the square brackets and are functions of the elevation θ alone.

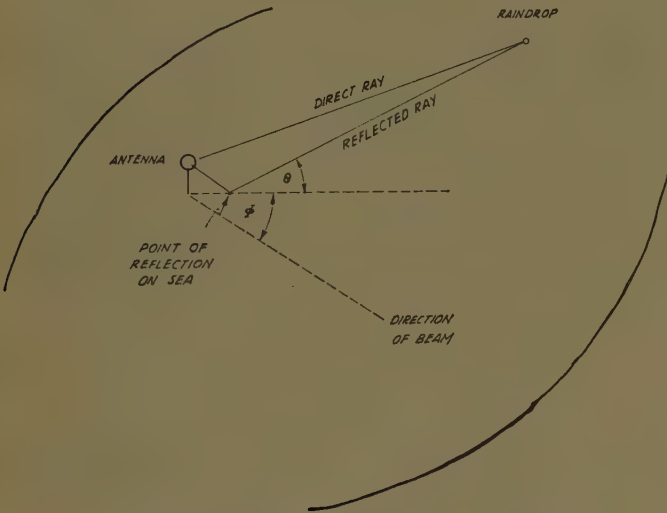


Fig. 1— θ is the elevation angle, and Φ is the azimuth angle.

The voltages of the returns will be proportional to the square of the voltage gains, since the path is traversed twice. The powers of the returns will be proportional to the absolute values of these voltages squared. This gives for (1),

$$\alpha = \frac{\frac{1}{2} \iint |\bar{f}_1^2 - \bar{f}_2^2|^2 d\theta d\Phi}{\iint (|\bar{f}_1|^4 + |\bar{f}_2|^4) d\theta d\Phi} \quad (5)$$

The integration limits are the boundaries of the beam, $0 < \theta < \theta_{\max}$ in elevation and $-\Phi_{\max} < \Phi < \Phi_{\max}$ in azimuth. There is a factor of one half in the numerator of this equation because, with proper matching, the resistance of the transmission line on which the voltages are added is twice the resistance of each of the two transmission lines feeding it. If (3) and (4) are substituted into the above equation and if the integration with respect to the azimuth Φ is carried out, the result is

$$\alpha = \frac{\frac{1}{2} \int |\bar{G}_1^2 - \bar{G}_2^2|^2 d\theta}{\int (|\bar{G}_1|^4 + |\bar{G}_2|^4) d\theta} \quad (6)$$

The problem now is to evaluate (6) from the given voltage gain pattern of the antenna $g(\theta)$ and the coefficients Γ_1 , Γ_2 , β_1 and β_2 , all of which are functions of θ .

A simplification of this equation can be made if it is recognized that the fluctuation due to the path length difference, $\Delta\theta$, is periodic and varies much more rapidly than the other quantities. As a result it can be averaged out first. We obtain, after substitutions and some manipulation,

$$\begin{aligned} & |\bar{G}_1^2 - \bar{G}_2^2|_{AV^2} \\ &= 4g^2(+\theta)g^2(-\theta)[\Gamma_1^2 + \Gamma_2^2 - 2\Gamma_1\Gamma_2 \cos(\beta_1 - \beta_2)] \quad (7) \\ & \quad g^4(-\theta)[\Gamma_1^4 + \Gamma_2^4 - 2\Gamma_1^2\Gamma_2^2 \cos 2(\beta_1 - \beta_2)], \end{aligned}$$

and

$$\begin{aligned} & |\bar{G}_1|_{AV^4} + |\bar{G}_2|_{AV^4} \\ &= [g^2(+\theta) + g^2(-\theta)\Gamma_1^2]^2 + [g^2(+\theta) + g^2(-\theta)\Gamma_2^2]^2 \\ & \quad + 2g^2(+\theta)g^2(-\theta)[\Gamma_1^2 + \Gamma_2^2]. \quad (8) \end{aligned}$$

The cancellation ratio is determined by numerical integration after substitution of these formulas into (6).

Figs. 2-4 show the values used for $g(\theta)$, Γ and β . The antenna beam is assumed to be pointed slightly upward, with its 3-db point on the horizon as is customary, and to have a 6° vertical beamwidth. Its free space voltage pattern $g(\theta)$ is assumed to be of the $\sin x/x$ type. Values of Γ and β are for sea water and have been taken from Burrows and Attwood's work.³ For numerical integration, values were calculated every $\frac{1}{2}^\circ$ from 0° to 10° .

Under the assumptions that rain drops are uniformly distributed throughout the beam cross section and that perfect cancellation would be achieved were it not for surface reflections, it was found that reflections from sea water yield the values, given in Table I, for the ratios of the power of returns reaching the receiver to the power of returns incident on the antenna:

TABLE I

Frequency	Power Cancellation Ratio	Power Cancellation Ratio in db
500 mc	1/37	-15.7 db
3000 mc	1/67	-18.3 db

These ratios are not influenced significantly by the shape of the beam or its width, but they will be quite sensitive to its elevation. Elevating the beam reduces the reflected power, hence improving the cancellation, but at the expense of low angle coverage.

As the reflecting properties of smooth earth to micro-

³ C. R. Burrows and S. S. Attwood, "Radio Wave Propagation," The Academic Press, Inc., New York, N. Y., vol. 3, ch. 4; 1949.

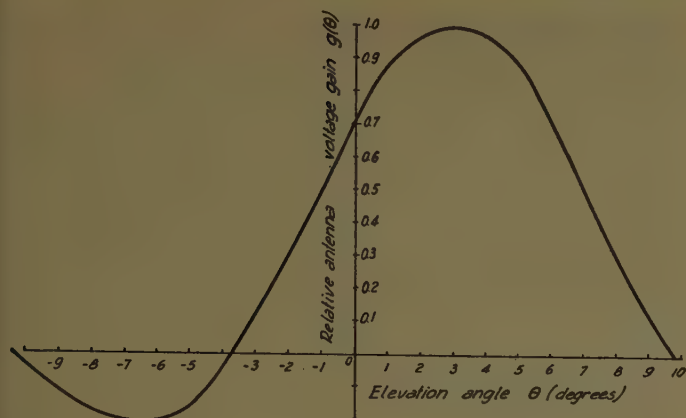
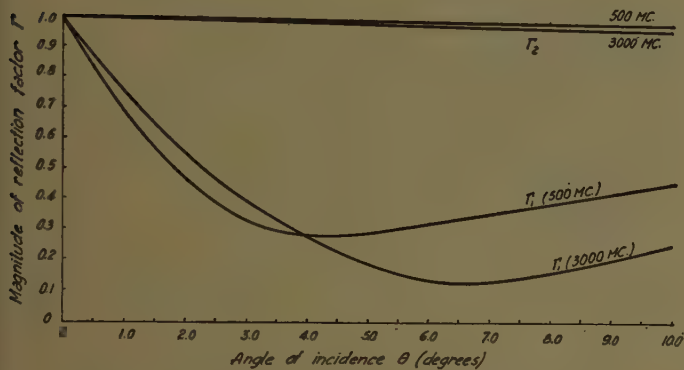
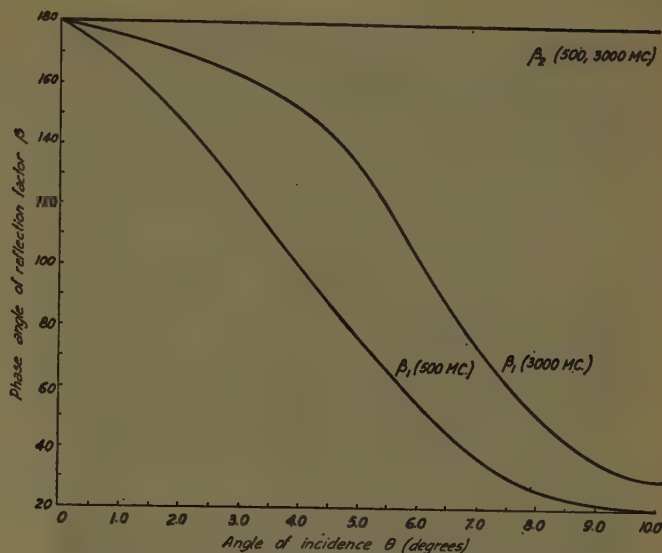


Fig. 2—Voltage gain of antenna in free space.

Fig. 3—Magnitude of reflection factor of sea water (Γ_1 vertical polarization, Γ_2 horizontal).Fig. 4—Phase angle of reflection factor of sea water (β_1 vertical polarization, β_2 horizontal).

waves are not unlike those of sea water,⁴ the cancellation ratios for radars sited in flat countryside will approximate those given in the above table.

It is evident from these results that, at best, only a moderate degree of cancellation of returns from rain can be achieved by using circular polarization techniques in search radars overlooking the sea or flat countryside.

⁴ Burrows and Attwood, *op. cit.*

Laboratory Development Notes Omnidirectional Vertically Polarized Paraboloid Antenna*

E. O. WILLOUGHBY† AND E. HEIDER†

THE problem of obtaining high-gain vertically-polarized antennas in the UHF region by arrays of vertical antennas is complicated by mutual couplings between the antennas themselves and the supporting mast. When, in addition, beam-tilt and wideband operation are attempted, the difficulties become almost insuperable.

Hence it was decided that for the problem of UHF communication to aircraft, there was much to be gained by having only one excitation point for a wide aperture

—8λ in this case—and a standard reflector system so designed that several such units could be stacked vertically to give more directivity. (See Fig. 1.)

DESCRIPTION

VP—360° omnidirectional UHF beacon TV antenna. Paraboloid of revolution about line parallel to directrix.

Excitation—from a focal circle, the initial excitation from the vertical axis of symmetry being expanded out from the axis by a very low impedance disk, or conical transmission line, and then redirected by a toroidal reflector to illuminate the two halves of the paraboloid.

* Manuscript received by the PGAP, October 3, 1958. This work was financed by the Australian Dept. of Civil Aviation. Patent filed Application No. 28443, June 6, 1957.

† University of Adelaide, Australia.



Fig. 1—Omnidirectional vertically polarized paraboloid antenna.

The construction of so large an antenna is of some interest. A paraboloid of revolution is the limiting case of a hyperbola of revolution, for a hyperbola has an eccentricity greater than 1, while the paraboloid has an eccentricity=1. Now a hyperboloid is a ruled surface and hence there is a chance that the paraboloid surface could be made of strips. This proved to be the case, and with the help of Dr. Brearley of the University Mathematics Department, it was shown that strips at 78° to the axis were less than 1 inch off straight out in 4 feet 0 inch, and by using parallel strips with a variable overlap, a very satisfactory paraboloid was made.

Clearly, however, if large numbers of such antennas were to be made, simpler methods of construction suited to production could be devised.

EXPERIMENTAL RESULTS

The paraboloid antenna and the pick up antenna for polar diagram tests were spaced 130 feet ($R=2D^2/\lambda$) and at a height of 15 feet, and placed on a test carriage capable of swinging from 9° below the horizon to 36° above. (See Fig. 2.)

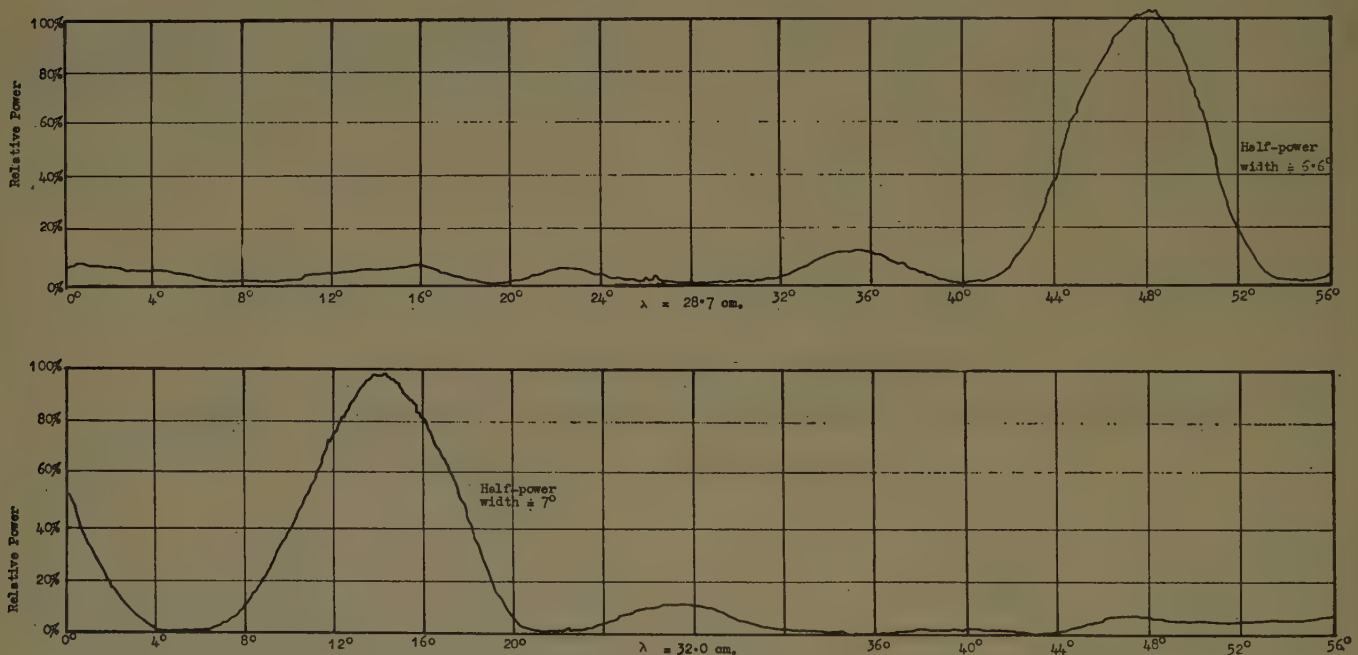


Fig. 2—Omnidirectional vertically polarized paraboloid antenna. Gain approximately 40 or 16 db.

In the somewhat elaborate experimental model, arrangements have been made to lift the focal circle to provide *beam tilts* up to about 4° (half the angle between maximum and zero of the main beam).

Operating wavelength = 28 cm = 11 inches
 Over-all length = 7 feet 6 inches
 Over-all diameter (of focal circle) = 8 feet 6 inches
 Maximum diameter paraboloid = 3 feet 9 inches
 Minimum diameter paraboloid = 1 foot 6 inches.

The dimensions of the antenna were such that it was not convenient to have the axis horizontal; and the test was arranged so that the interference of the sidelobes reflected in the ground plane would not appreciably affect the width determined for the main beam, although the apparent sidelobes were accentuated by this test procedure. The magnitude of the sidelobes is indicated by the asymmetry of the main lobe of the pattern, the side lobes being greater for the upper test result than

the lower, which were taken traversing through the respective main lobes in opposite directions.

The polar diagrams show the following results. Upper radiation pattern,

$\lambda = 29.7\text{ cm}$, angle between maximum and zero of main lobe $= 7.4^\circ$

$\lambda = 32.0\text{ cm}$, angle between maximum and zero of main lobe $= 7.7^\circ$.

As much work remains to be done, a comprehensive report dealing with the control of the antenna pattern, bandwidth, and beam tilt will be given at a later date; the latter in particular is expected to be important as nulls between the sidelobes are expected to be filled in, in a manner useful for aviation or TV patterns.

In conclusion, our thanks to our colleagues at the Weapons Research Establishment for making their measuring equipment available.

Contributors

Dimitri S. Bugnolo (S'52-A'53-M'59) was born in Atlantic City, N. J., on February 3, 1929. He received the B.S. degree in electrical engineering from the University of Pennsylvania, Philadelphia, in 1952.



D. S. BUGNOLO

From 1952 to 1954, Mr. Bugnolo was a research engineer with the Burroughs Corporation in Paoli, Pa. He joined the staff of Yale University as a teaching assistant and received the M.E. degree in 1955. In June, 1956, Mr. Bugnolo joined the staff of Columbia University as an instructor in electrical engineering. He is currently engaged in both teaching and research and is a candidate for the Dr. Eng. Sc. degree.



R. P. Decker was born on March 26, 1926, in Chicago, Ill. He received the B.S. degree in electrical engineering in 1948 from Northwestern University, Chicago, Ill.



R. P. DECKER

During the two-year period 1944 to 1946, he was in the Armed Forces and spent a considerable portion of his overseas period in an armored field artillery battalion.

In January, 1949, he joined the staff of the Collins Radio Company, Cedar Rapids, Iowa, as electrical engineer and was engaged in the development of control circuitry for high-power vacuum tubes and in 400-mc propagation studies and in the development of equipment for the analyzing and recording of propagation data. He then joined the antenna section where he participated in various phases of antenna development. He has made theoretical investigations with regard to rhombic antennas and is responsible for the development of the 37W-1 and the 37X-1 antennas. Other work includes waveguide filters, antenna feed system development, and low noise circuitry. He is presently engaged in the design of specialized equipment for propagation measurements and single sideband diversity reception.



Lorne H. Doherty (S'42-A'46-M'53-SM'58) was born in Montreal, Can., on August 22, 1922. He received the B.S. degree

in electrical engineering from McGill University, Montreal, in 1944, and the Ph.D. degree in electrical engineering from Cornell University, Ithaca, N. Y., in 1953.



L. H. DOHERTY

He joined the staff of the National Research Council of Canada in 1944, and was employed in radio wave propagation research in Ottawa, Ontario, and Suffield, Alberta. In 1948, while undertaking graduate studies, he was appointed Research Associate at Cornell University, and worked in the fields of radio astronomy, antennas, and radio wave propagation. In 1953, he rejoined the National Research Council, and has been engaged in radio wave propagation research since that date.

Dr. Doherty is a member of Sigma Xi.



Lambert T. Dolphin, Jr. (S'52-M'57) was born in Shoshone, Idaho, on May 24, 1932. He received the A.B. degree in physics in 1954, with considerable work in electronics, from San Diego State College, San Diego, Calif., in 1954. He has done two years of graduate work in physics at Stanford University, Stanford, Calif.



L. T. DOLPHIN, JR.

He joined the staff of Stanford Research Institute in 1956. He has been engaged in basic research of the upper atmosphere by radio and radar techniques, and in the development of radio propagation equipment, and has supervised a study of radio effects of nuclear detonations. At present, he is a research physicist with the Stanford Communication and Propagation Laboratory.

Mr. Dolphin is a member of Sigma Pi Sigma.



John D. Dyson (S'49-A'52-M'58) was born on August 9, 1918, in Lemmon, S. D. He received the B.S. degree in economics from South Dakota State College, Brookings, in 1940, was employed for one year as a sta-

tistician, and served on active duty with the U. S. Army from 1941-1946. He received the B.S. degree in electrical engineering from



J. D. DYSON

South Dakota State College in 1949, and the M.S. and Ph.D. degrees in electrical engineering from the University of Illinois, Urbana, in 1950 and 1957, respectively. He was a part time instructor at South Dakota State College in 1949 and was on the research staff of the Sandia Corporation, Albuquerque, N. M. in 1951 and 1952. Since October, 1952, he has been on the staff of the Antenna Laboratory of the University of Illinois where he is now a research assistant professor.

Dr. Dyson is a member of Sigma Xi, Eta Kappa Nu, Sigma Tau and Pi Mu Epsilon.



Leopold B. Felsen (S'47-A'53-M'54-SM'55) was born in Munich, Germany, on May 7, 1924. He received the B.E.E., M.E.E., and D.E.E. degrees from the Polytechnic Institute of Brooklyn, Brooklyn, N. Y., in 1948, 1949, and 1952, respectively.



L. B. FELSEN

He entered the United States in 1940, and during World War II was concerned with work on electronic ballistic calibration devices in the U. S. Army. Since 1948, he has been with the Microwave Research Institute of the Polytechnic Institute of Brooklyn and presently holds the position of research associate professor. His research work has been concerned chiefly with problems in electromagnetic diffraction, multimode propagation, and microwave network and measurement techniques. He has also been teaching graduate courses in the electrical engineering department.

Dr. Felsen is a member of the USA Commission 6 of URSI and of Eta Kappa Nu, Tau Beta Pi, and Sigma Xi.



Roger F. Harrington, for a photograph and biography, please see pp. 321-322 of the July, 1958, issue of these TRANSACTIONS.

Joseph B. Keller was born on July 31, 1923, in Paterson, N. J. He received the B.A. and M.S. degrees in physics in 1943 and 1946, respectively, and the Ph.D. degree in mathematics in 1948, all from New York University, New York, N. Y.

He was a physics instructor at Princeton University, Princeton, N. J., a research associate at the Columbia University Division of War Research, New

York, N. Y., and was Head of the Mathematics Branch of the Office of Naval Research. Since 1946, except for a year at ONR, he has been at New York University, where he is now research professor of mathematics. He has done research in acoustics, fluid dynamics, and electromagnetic theory. In recent years, he has been concentrating on diffraction problems.

Dr. Keller is a member of the American Physical Society.



Ray L. Leadabrand (S'49-A'52-M'54) was born in Pasadena, Calif., on October 12, 1927. He received the B.S. degree in communication engineering from San Jose State College, San Jose, Calif., in 1950, and the M.S. degree in electrical engineering from Stanford University, Stanford, Calif., in 1953.

From 1950 to 1952, he was a field engineer for the Philco Corp., in Japan and Korea. While with

Philco he was engaged in the installation and testing of antennas and communications equipment.

From 1952 to 1955, Mr. Leadabrand was on the staff of the Radio Propagation Laboratory at Stanford University, where he was engaged in research on auroras, sporadic E, meteors, and related problems. In October, 1955, he joined the staff of Stanford Research Institute as a research engineer in the Special Techniques Group of the Radio Systems Laboratory. Since that time he has been engaged in research on auroral and meteoric propagation.

Mr. Leadabrand is a member of Sigma Xi, and the U. S. Committee of URSI.



E. Levin was born in Los Angeles, Calif., on April 19, 1930. He attended the University of California at Los Angeles and

received the B.A. degree in physics with highest honors in 1950, the M.A. degree in physics in 1951, and the Ph.D. degree in mathematics in 1955. From 1953-1955, he was associated with the Institute for Numerical Analysis as a thesis fellow and research assistant.

In 1955, Dr. Levin joined the Ramo-Wooldridge Corporation where he served as group leader of the applied mathematics group and later as associated head of the mathematical analysis department. In 1958, he joined the aeronautics department of the RAND Corporation. Since 1955, he has also been engaged in teaching for the University of Southern California Extension Department, Los Angeles. His work in applied mathematics includes contributions in the fields of elasticity, plasticity, hydrodynamics, and orbit mechanics.

He is an associate member of the ASME, a member of the American Rocket Society, Sigma Xi, the American Mathematical Society, the Mathematical Association of America, and the Society for Industrial and Applied Mathematics.



L. Lewin was born on July 22, 1919, in Essex, England.

During World War II he was engaged at the Admiralty Signals Establishment on the design of radar antennas and waveguide components.

In 1946, he joined Standard Telecommunication Laboratories, becoming head of the microwave department in 1951. He is engaged in research into waveguides and components, antennas, noise and electromagnetic theory.

Mr. Lewin is a member of the Institution of Electrical Engineers.



R. B. Muchmore (S'39-A'40-SM'49) was born on July 8, 1917, in Augusta, Kan. He attended the University of California at Berkeley, receiving the B.S. degree in electrical engineering in 1939. He received the E.E. degree in communications engineering from Stanford University, Stanford, Calif., in 1942.

From 1942 to 1946, he was employed by the Sperry Gyroscope Co. as a project engineer working in the fields of antennas and microwave test equipment. In 1946, he

joined the staff of the Guided Missile Laboratory at the Hughes Aircraft Co., where he did systems and noise analysis. From 1954 to 1958, he was with the Ramo-Wooldridge Corporation as a senior member of the technical staff doing systems analysis and work in the field of radio propagation. He is now Director of the Space Technology Laboratories' Guidance Research Laboratory.

Mr. Muchmore is a member of Sigma Xi, RESA, the Acoustical Society of America, and U. S. Commission II, International Scientific Radio Union.



George Neal was born in Kingston, Ontario, Can., on February 13, 1928. He received the B.S. degree from Queen's University, Kingston, in 1951.

After graduation, he joined the staff of the National Research Council of Canada, at the Scarborough Field Station, where he was engaged in work on anomalous propagation at three centimeters across Lake Ontario, and on scatter

propagation at ten centimeters. Recently he has been working on navigational aids at the Radio and Electrical Engineering Laboratories of the National Research Council in Ottawa.



Arthur A. Oliner (M'47-SM'52) was born in Shanghai, China, on March 5, 1921. He received the B.A. degree from Brooklyn College, Brooklyn, N. Y., in 1941, and the Ph.D. degree in physics from Cornell University, Ithaca, N. Y., in 1946. While at Cornell, he held a graduate teaching assistantship in the physics department and also conducted research on an Office of Scientific Research and Development project.

Since 1946, Dr. Oliner has been with the Microwave Research Institute of the Polytechnic Institute of Brooklyn, where he has been engaged in research in a variety of



J. B. KELLER



E. LEVIN



R. B. MUCHMORE



R. L. LEADABRAND



L. LEWIN



G. NEAL



A. A. OLINER

topics in the microwave field. He has also taught graduate courses in physics and electrical engineering, and is a research professor at the Institute.

Dr. Oliner is a member of Commissions 1 and 6.3 of URSI, the American Physical Society, and Sigma Xi. He is also on the National Academy of Sciences Advisory Panel to the National Bureau of Standards.



Allen M. Peterson (M'56) was born in Santa Clara, Calif., on May 21, 1922. He attended San Jose State College, San Jose, Calif., from 1940 to 1942. He received the B.S. degree in 1948, the M.S. degree in 1949, and the Ph.D. degree in 1952, from Stanford University, Stanford, Calif., all in electrical engineering.



A. M. PETERSON

He was a member of the Electronics Group of the Sacramento Air Service Command from 1942 to 1944, and was on active duty with the U. S. Army Air Forces

from 1944 to 1946. Since 1947, he has been a staff member of the Radio Propagation Laboratory at Stanford, and is currently associate professor of electrical engineering. In 1953, he joined Stanford Research Institute, where he has been engaged in research on radio propagation, communications, and radio systems design. At present he is manager of the Communication and Propagation Laboratory.

Dr. Peterson is a member of the Scientific Research Society of America; Sigma Xi, the Society for Industrial and Applied Mathematics, Commission III of the United States Committee of URSI, and a National Science Foundation Panel charged with planning and reviewing aurora and ionospheric research programs being conducted during the present International Geophysical Year. Also in conjunction with the IGY, he heads a program in upper atmosphere studies by radio-sounding techniques being carried out at Stanford.



Walter Rotman (A'49-M'55) was born in St. Louis, Mo., on August 21, 1922. From 1942-1945, he served in the U. S. Army Air

Force working on radar equipment. He received the B.S. and the M.S. degrees from the Massachusetts Institute of Technology, Cambridge, in 1947 and 1948, respectively. While at M.I.T., he worked as a research assistant in the Research Laboratory of Electronics.



W. ROTMAN

In 1948, he joined the Electromagnetic Radiation Laboratory of the Air Force Cambridge Research Center, Bedford, Mass., where he is now in charge of the missile antenna section. His field of interest also includes progressive wave antennas and microwave optical systems.

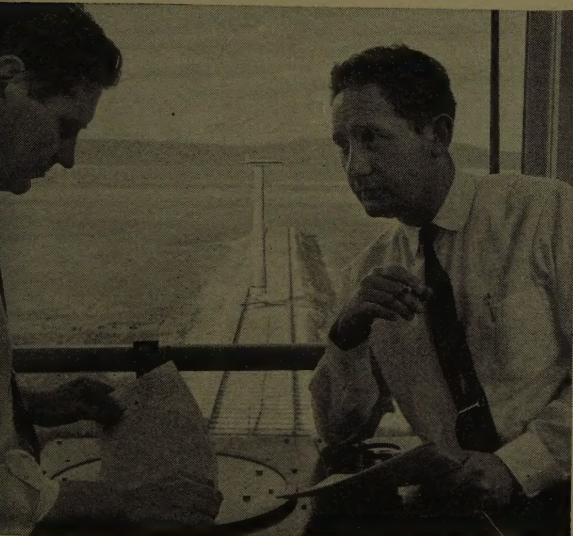
Mr. Rotman is a member of RESA and Sigma Xi.



A. D. Wheelon, for a photograph and biography, please see page 116 of the January, 1959 issue of these transactions.

(right) Lockheed Q-5 target missile features telemetry that registers miss-distance and theoretical hits in testing accuracy of other missiles.

ANTENNA— TELEMETRY



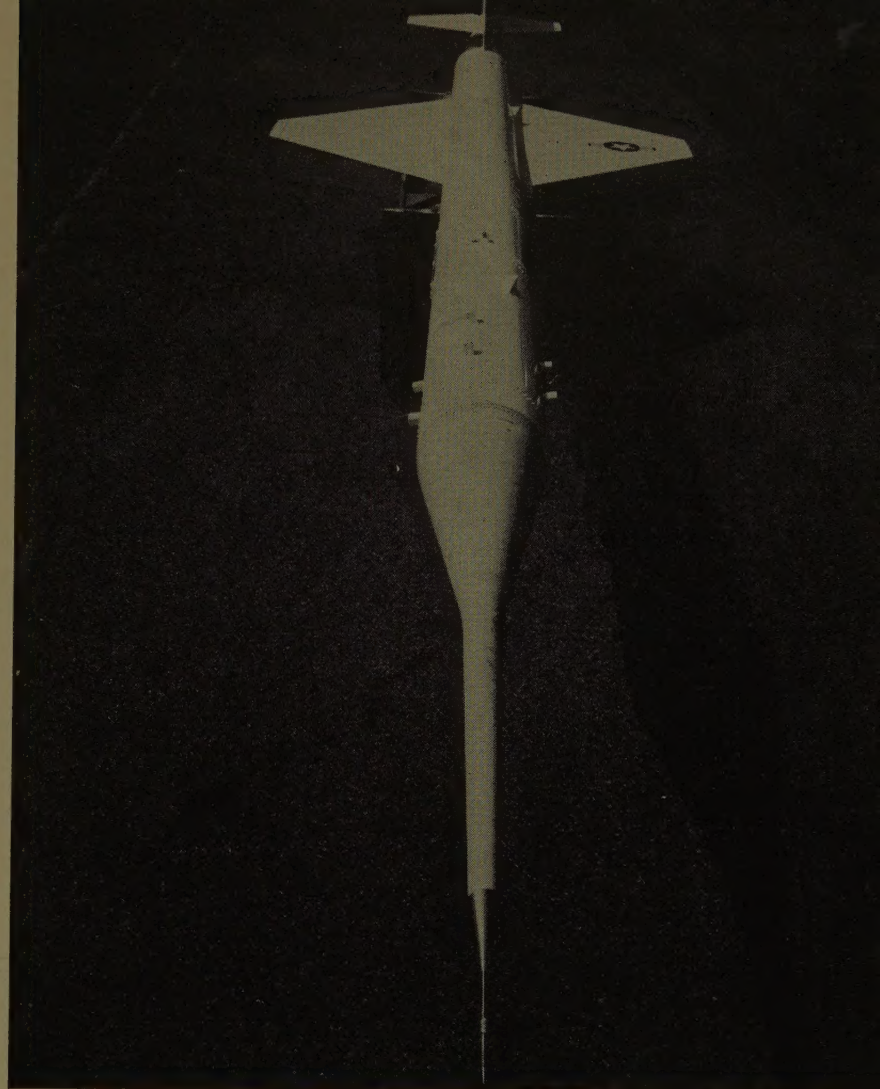
Studying results of antenna pattern measurements — part of the activity of the Space Communications laboratory.

Lockheed

**MISSILES AND SPACE
DIVISION**

SUNNYVALE, PALO ALTO, VAN NUYS,
SANTA CRUZ, SANTA MARIA, CALIFORNIA

CAPE CANAVERAL, FLORIDA • ALAMOGORDO, NEW MEXICO



Expanding the Frontiers of Space Technology

Lockheed maintains extensive research capabilities for the development of antennas and telemetering systems and spacecraft applications.

Laboratory studies in antennas and electromagnetic propagation include the application of solid state materials to microwave transmission line components; the design of antennas to survive the rigors of space flight; the effects of space on radio signals and radar detection; and the scattering from missile shapes and space vehicles. Research is also being conducted in the application of ferrites and MASERS; on problems of radio transmission between space vehicles and Earth, re-entry scattering and diffraction by man-made objects and ionized gases; and development of antennas for data link systems between satellites and ground stations.

Telemetering has been brought to a high degree of successful application in the integration of circuits and components into high-performance systems. A completely sub-miniaturized FM-FM system has been developed, along with a complete PAM-FM system characterized by highly efficient band-width utilization, low power consumption and economy of size and weight. This represents a significant achievement in the field of high capacity telemetry.

Scientists and engineers of outstanding talent and inquiring mind are invited to join us in the nation's most interesting and challenging basic research and development programs. Write: Research and Development Staff, Dept. D-56, 962 W. El Camino Real, Sunnyvale, California.

"The organization that contributed most in the past year to the advancement of the art of missiles and astronautics."

NATIONAL MISSILE INDUSTRY CONFERENCE AWARD

INSTITUTIONAL LISTINGS

The IRE Professional Group on Antennas and Propagation is grateful for the assistance given by the firms listed below, and invites application for Institutional Listing from other firms interested in the field of Antennas and Propagation.

ANDREW CORPORATION, 363 E. 75th St., Chicago 19, Ill.
Antennas, Antenna Systems, Transmission Lines, Development and Production.

ANTLAB, INC., 6330 Proprietors Rd., Worthington, Ohio
Antenna Pattern Range Systems—Recorders & Mounts.

BLAINE ELECTRONETICS, INC., 14757 Keswick St., Van Nuys, Calif.
Antennas, Paraboloids, Scale Models, Antenna Radiation Pattern Measurement Towers.

COMMUNICATION PRODUCTS COMPANY, INC., Marlboro, N. J.
Fixed Station and Vehicular Antennas and Associated Cable Systems

DEVELOPMENTAL ENGINEERING CORP., 1001 Conn. Ave. N.W., Washington, D. C. and Leesburg, Va.
Research, Development, Installation of Antennas and Antenna Equipment for Super Power Stations.

DORNE AND MARGOLIN, INC., 29 New York Ave., Westbury, L. I., N. Y.
Research, Development, and Manufacture of Airborne Antennas and Systems

THE GABRIEL LABORATORIES, Div. of the Gabriel Co., 135 Crescent Road, Needham Heights 94, Mass.
Research and Development of Antenna Equipment for Government and Industry.

HUGHES AIRCRAFT COMPANY, Culver City, Calif.
Research, Development, Mfr.: Radar, Missiles, Antennas, Radomes, Tubes, Solid State Physics, Computers.

I-T-E CIRCUIT BREAKER CO., Special Products Div., 601 E. Erie Ave., Philadelphia 34, Pa.
Design, Development and Manufacture of Antennas, and Related Equipment.

JANSKY & BAILEY, INC., 1339 Wisconsin Ave. N.W., Washington 7, D. C.
Radio & Electronic Engineering; Antenna Research & Propagation Measurements; Systems Design & Evaluation.

MARK PRODUCTS CO., 6412 W. Lincoln Ave., Morton Grove, Ill.
Multi Element Grid Parabolas, Antennas for Two-Way Communications, R & D.

THE RAMO-WOOLDRIDGE CORPORATION, Los Angeles 45, Calif.

TRANSCO PRODUCTS, INC., 12210 Nebraska Ave., Los Angeles 25, Calif.
Res., Design, Dev., & Mfr. of Antenna Systems & Components for Missile, Aircraft & Ground Installations.

WHEELER LABORATORIES, INC., 122 Cutter Mill Road, Great Neck, N. Y.
Consulting Services, Research and Development, Microwave Antennas and Waveguide Components.

WIND TURBINE COMPANY, West Chester, Pa.
Complete Antenna Systems and Towers

The charge for an Institutional Listing is \$25.00 per issue or \$75.00 for four consecutive issues. Application may be made to the Technical Secretary, The Institute of Radio Engineers, 1 East 79th Street, New York 21, N. Y.